POLITECNICO
MILANO 1863

Department of Aerospace Science and Technology
Doctoral Program in Aerospace Engineering

NON-IDEAL COMPRESSIBLE FLUID DYNAMICS of ORGANIC VAPORS:
from NOZZLE FLOWS to PRESSURE PROBES

Doctoral dissertation of:
Camilla C. Conti

Supervisor:
Prof. A. Guardone

Co-supervisors:
Prof. V. Dossena, Prof. A. Spinelli

Tutor:
Prof. M. Quadrio

The Chair of the Doctoral Program:
Prof. P. Masarati

April 2021 – Cycle XXXIII

To my Dad

ACKNOWLEDGEMENTS

This work would have never been possible without the precious support of many people.

First of all, I would like to express my sincere gratitude to Professors Alberto Guardone, Andrea Spinelli and Vincenzo Dossena for their supervision, mentoring and the opportunities they have given me, starting from this very doctoral position.

I would also like to thank the reviewers, Professors Fabrizio Fontaneto and Luca Sciacovelli, for taking the time to read this work and their valuable suggestions.

I feel as if I'm standing on the shoulders of giants. Every person I seeked advice from is a true expert in their field and has, humbly and with no hesitation, passed on to me invaluable knowledge that set the foundation for my work.

A huge thank you goes to Professors Paolo Gaetani and Giacomo Persico for the insightful discussions and their contributions to the many tricky aspects encountered while dealing with the TROVA.

Under this respect, a special recognition is also due to Technicians Dario Crema, Paolo Grigatti, Gabriele Campanardi and Donato Grassi for their practical help and ingenious solutions, to Alessandro Mora for his tips on how to tame ICEM and for his delicate crafting of the TotAle probe, and to Alberto Fusetti for his relentless contribution to endless lab days and his irreplaceable moral support.

You don't get through a Ph.D without great colleagues. Thank you to Alessandro, (Andrea) Giuseppe, (Andrea) NT, Marco, Davide, Gianluca, Giulio, Barbara, Bàrbara, Myles, Tommaso and Filippo for the jokes, sharing of ideas and occasional venting.

Thank you also to my Gechini friends Edo, Luca, Dario, Rich, Cristina, Sonia, Gioster and Bino for making any lunch break and movie night quite a lot of (much needed) fun.

A special mention goes to Giorgia, Marta and Simone, three generations of brilliant Ph.D. candidates with whom I had the privilege of working closely and share many joys and pains at CREA lab.

A heartfelt recognition goes to Gioele, my enthusiastic MSc. thesis student, for his invaluable contribution to Pitot tubes testing and, together with Alberto, for lightening up my days at CREA. Thank you also to Marco, for making lab hours much more fun for everyone.

I am very thankful to my closest friends Ludo, Ema, Chia, Monti, Mula, Pisa and Sara for all the adventures together and for being my pick-me up in these past years.

Last, but definitely not the least, I cannot put into words how grateful I am for the profound love from my beautiful Family, that supported me every single day of this challenge. I owe this achievement to You.

Camilla
Milano, April 2021

The big AHA of this piece was that there was no big AHA moment. Every step of the process consisted of benign and timid decisions. And even though it's pretty easy and obvious to explain how the final image works, there is no way I could have sketched it out on a piece of paper without walking down all the detours and dead ends.

– Christoph Niemann, *Sunday Sketching*

SUMMARY

Non-Ideal Compressible Fluid Dynamics (*NICFD*) is a branch of gasdynamics concerned with flows of dense vapors occurring close to the vapor-liquid equilibrium and the critical point, so in conditions in which the ideal gas law does not properly describe the thermodynamics involved. As a result and unlike an ideal gas, the flow field shows a marked dependance on process conditions. If molecularly complex fluids are considered, behaviours that are also qualitatively different with respect to an ideal gas are possible, such as the increase in speed of sound and non-monotone Mach number trends along isentropic expansions or a Mach number increase across oblique shocks.
Non-ideal flows occur in a wide range of engineering processes and the present work is specifically relevant for Organic Rankine Cycles (*ORCs*) in the power generation field. Fluids usually employed in *ORCs* feature high complexity and molecular weight, and turbine expansion occurs in the dense gas region near the saturation curve and the critical point. As a result, turbine flows are highly supersonic and show marked non-ideal flow effects.

Established studies on compressible flows are mostly based on the assumption of ideal gas behaviour. However, the latter model fails both quantitatively and qualitatively in describing non-ideal flows. Thus, a holistic approach involving theoretical, numerical and experimental aspects was carried out in the present work in order to contribute to the fundamental understanding of the relatively new field of *NICFD*.
Wind tunnel testing concerning non-ideal flows is intrinsically complex due to the high temperature and pressure conditions involved, as well as due to issues related to undesired vapor condensation. As a result, experimental data concerning such flows are scarcely available in literature for comparison with simulation and design tools. The large experimental data-set produced within this research includes subsonic and supersonic nozzle expansions and direct measures of normal shock losses, and contributes to filling the aforementioned literature gap.
Moreover, as a further consequence of the difficulties in experimentally reproducing non-ideal flows, many procedures routinely carried out in conventional wind tunnels with air are instead still in development here. The present work thus also contributes to establishing reliable methodologies for detailed nozzle flow characterization and pressure probes testing for non-ideal flows.

First of all, a theoretical calculation framework was implemented to investigate the non-ideal dependance of isentropic expansions on total conditions, with the aim of identifying similarity parameters that would provide further understanding of this peculiar behaviour and reduce the complexity of any problem in which non-ideal flows are encountered. Complex fluids in moderately high non-ideal conditions (representative of most engineering processes) were found to have similar expansions if total conditions share the same total compressibility factor Z_T because they also share similar volumetric and caloric behaviour throughout the process.
This was verified with extensive experimental campaigns on non-ideal supersonic nozzle flows on the *Test Rig for Organic VApors* (*TROVA*) at Politecnico di Milano, a blow-down wind tunnel specifically designed to reproduce non-ideal flows of organic vapours in conditions representative of *ORC* turbines operation. Tests were carried out covering a large portion of the vapor phase of fluid siloxane MM, commonly employed in high-temperature *ORCs*, from strongly non-ideal conditions

with $Z_T = 0.39$ to dilute ones at $Z_T = 0.98$. Pressure measurements and Mach number extraction from schlieren visualizations, in synergy with numerical simulations, not only highlighted the non-ideal dependance of isentropic expansions on total conditions, but most importantly confirmed the suitability of the total compressibility factor as a similarity parameter for conditions with $Z_T \geqslant 0.60$.

Experimental testing on the *TROVA* was then performed to characterize moderately non-ideal expansions in choked subsonic nozzles at different Mach numbers. Pressure measurements, with the support of Laser Doppler Velocimetry (*LDV*) and numerical simulations, allowed to assess the impact of flow non-ideality in subsonic conditions and to verify that it is more marked where compressibility effects are also more relevant.

Building on the knowledge of experimental testing and numerical simulation of elementary nozzle flows in the non-ideal regime, the focus was then shifted towards the development of experimental techniques for pressure probe testing in the *TROVA*. This is the initial step towards future pressure probes calibration and blade cascade testing in such flows, as well as towards reliable velocity, mass flow rate and performance measurements in industrial contexts where non-ideality is relevant. Several pneumatic lines configurations were assessed to overcome the most challenging experimental aspects, namely the transient nature of the *TROVA* operation and mass sink effects due to vapor condensation in the lines. A pneumatic scheme implementing nitrogen flushing was thus devised to allow pressure probes testing in subsonic and supersonic non-ideal flows. The optimal configuration was identified and several best practices were highlighted, such as keeping lines length to the minimum, considering the volume within employed transducers and performing lines dynamic testing.

An experimental campaign in the *TROVA* with Pitot tubes in non-ideal subsonic flows of organic vapors was then carried out to complete the pneumatic system commissioning and evaluate its performance for both total and static pressure measures against direct reference counterparts from the *TROVA* plant. Also, the campaign allowed to experimentally verify that flow non-ideality does not affect the behaviour of a Pitot tube in non-ideal subsonic flows, indicating that no particular calibration is required for this type of instrument in such compressible flow conditions.

Finally, Pitot tubes were employed to perform the first ever direct total pressure loss measurement across normal shock waves in non-ideal flows of siloxane MM vapors. This contributes to filling the current literature gap in available experimental results in *NICFD* and establishes a reliable methodology for such measurements, paving the way towards blade cascade testing in such flows and to pressure probes use in research and industrial contexts where non-ideality is relevant.

PUBLICATIONS

Parts of the content of this work also appear in:

- Conti, C. C., Spinelli, A. and Guardone, A. (2020). *"Similarity Parameters for Non-Ideal One-Dimensional Isentropic Expansions"*. NICFD 2020 Proceedings in the ERCOFTAC Book Series, Springer.
- Cammi, G., Conti, C. C., Spinelli, A. and Guardone, A. (2020). *"Experimental characterization of nozzle flow expansions of siloxane MM for ORC turbines applications"*. Energy. https://doi.org/10.1016/j.energy.2020.119249.
- Cammi, G., Conti, C. C., Spinelli, A., Cozzi, F., and Guardone, A. (2019). *"Experimental Characterization of Nozzle Flow Expansions of Siloxane MM for ORC Turbines Applications"*. ORC 2019 Proceedings.
- Spinelli, A., Cammi, G., Conti, C. C., Gallarini, S., Zocca, M., Cozzi, F., Gaetani, P., Dossena, V., and Guardone, A. (2019). *"Experimental observation and thermodynamic modeling of non-ideal expanding flows of siloxane MDM vapor for ORC applications"*. Energy, 168. https://doi.org/10.1016/j.energy.2018.11.071

The following works are in preparation:

- Conti, C. C., Spinelli, A., and Guardone, A. *"Shock Losses and Pitot Tube Measurements in Non-Ideal Subsonic and Supersonic Flows of Organic Vapors"* – in preparation for the *ORC 2021* conference.
- Conti, C. C., De Donati, G., Fusetti, A., Spinelli, A., and Guardone, A. *"Pneumatic Lines for Pressure Probe Measurements in Transient Flows of Non-Ideal Vapors Subject to Line Condensation"* - in preparation for journal submission (Measurements).
- Conti, C. C., Spinelli, A., and Guardone, A. *"Direct Total Pressure Loss Measure across Normal Shocks in Non-Ideal Flows of Organic Vapors"* – in preparation for journal submission (Exp. In Fluids).

CONTENTS

CHAPTER 1

INTRODUCTION

1.1 Context and Motivation

Non-Ideal Compressible Fluid Dynamics (*NICFD*) is a branch of gasdynamics that studies flows of dense vapors occurring in the close proximity of the vapor-liquid equilibrium and the critical point, so in conditions in which the ideal gas law does not properly describe the thermodynamics involved. *Compressibility factor* Z is defined in Equation (1.1) where P is pressure, T is temperature, ρ is density and R is the gas constant.

$$Z = \frac{P}{RT\rho} \tag{1.1}$$

It represents the departure of the fluid volumetric behavior from that of an ideal gas at same temperature and pressure. It is therefore identically equal to 1 in case of ideal gas behaviour and possibly differs from 1 otherwise: it is thus an indication of the level of non-ideality. The term *non-ideal* in *NICFD* indeed refers to this latter aspect, which has a number of direct gasdynamic "side-effects" distinctly separating such flows from those of ideal gases. For example, isentropic expansions show a non-ideal dependance on total conditions, a matter most extensively studied within the frame of this work from a theoretical, numerical and experimental point of view. Moreover, shock waves in non-ideal flows also depend on the upstream thermodynamic state and not only on the pre-shock Mach number.
In the frame of compressible fluid flows, it is also useful to consider the *fundamental derivative of gasdynamics* Γ, defined as the curvature of an isentrope in the $P - v$ thermodynamic plane, with $v = 1/\rho$ representing the specific volume. Manipulation yields:

$$\Gamma = 1 + \frac{c}{v}\left(\frac{\partial c}{\partial P}\right)_s \tag{1.2}$$

where c is speed of sound and s is specific entropy per unit mass. The fundamental derivative of gasdynamics can thus be interpreted as the dimensionless variation of the speed of sound along an isentropic process and its value determines the admissible flow behaviors. This is best illustrated for internal flows by resorting to the *quasi-one-dimensional* approach (see e.g. Thompson (1988)) describing the steady operation of an adiabatic nozzle where body forces are negligible, the curvature radius at any axial location is large compared to the cross-sectional length and the cross-sectional area distribution is smooth and gradual. With the further hypothesis of isentropic flow, manipulation of the governing equations allows to conveniently express streamwise gradients of flow variables as a function of the gradient of the known cross-sectional area A distribution along the nozzle axial coordinate x:

$$\frac{1}{u}\frac{\mathrm{d}u}{\mathrm{d}x} = \frac{1}{M^2-1}\frac{1}{A}\frac{\mathrm{d}A}{\mathrm{d}x} \tag{1.3}$$

$$\frac{1}{\rho}\frac{\mathrm{d}\rho}{\mathrm{d}x} = \frac{M^2}{1-M^2}\frac{1}{A}\frac{\mathrm{d}A}{\mathrm{d}x} \tag{1.4}$$

$$\frac{1}{P}\frac{\mathrm{d}P}{\mathrm{d}x} = \frac{1}{1-M^2}\frac{\rho u^2}{P}\frac{1}{A}\frac{\mathrm{d}A}{\mathrm{d}x} \tag{1.5}$$

$$\frac{1}{c}\frac{\mathrm{d}c}{\mathrm{d}x} = \frac{(\Gamma-1)M^2}{1-M^2}\frac{1}{A}\frac{\mathrm{d}A}{\mathrm{d}x} \tag{1.6}$$

$$\frac{1}{M}\frac{\mathrm{d}M}{\mathrm{d}x} = \frac{1+(\Gamma-1)M^2}{M^2-1}\frac{1}{A}\frac{\mathrm{d}A}{\mathrm{d}x} \tag{1.7}$$

The above relationships, where u is velocity and M is Mach number, are valid regardless of any thermodynamic model. They determine the well-known relationships between nozzle shape

(converging/diverging) and flow quantities depending on subsonic or supersonic flow regime, and the role of Γ is evident in the last two equations. For a Polytropic Ideal Gas (*PIG*), $\Gamma = (\gamma + 1)/2$, where γ is the specific heats ratio, meaning that $\Gamma > 1$ always. As a result, speed of sound decreases monotonically along expansions (Equation (1.6)) (Thompson, 1971).
If the fluid cannot be modeled as an ideal gas, namely if the thermodynamic state is not that of a dilute gas, then thermodynamic regions with $0 < \Gamma < 1$ are possible for those characterized by a *High Molecular Complexity* (*HMC*). Molecular complexity is defined as the number of active degrees of freedom of a molecule $N = 2\, M_m\, c_{v0}/R$, where M_m is the molecular mass and c_{v0} is the ideal gas specific heat at constant volume evaluated at critical temperature (Colonna and Guardone, 2006). For a polytropic van der Waals fluid, $0 < \Gamma < 1$ occurs for $N > 7.57$. *HMC* fluids are, for example, Octane with $N = 73.80$, siloxane MM with $N = 77.40$ and MDM with $N = 115$. As counter examples, water has $N = 6.87$, nitrogen $N = 5.00$, CO_2 $N = 7.00$: they are characterized by $\Gamma > 1$ and are classified as *Low Molecular Complexity* (*LMC*) fluids (Harinck et al., 2009).
In regions where $0 < \Gamma < 1$ the speed of sound c decreases with pressure, leading to an increase in c along isentropic expansions, oppositely to what happens for a *PIG* (Equation (1.6)). Depending on the particular flow conditions with certain values of Γ (Equation (1.7)), this might even result in a non-monotonic Mach number trend along an expansion (Thompson, 1971). Moreover, considering oblique shock waves, the non-ideal decrease in c along compressions leads to an increase in the tangential Mach number which, for certain stagnation conditions, can result in an increase in the Mach number across the shock (Vimercati et al., 2018).
Very molecularly complex fluids characterized by $N > 33.33$ that can exhibit regions with $\Gamma < 0$ are defined as *Bethe-Zel'dovich-Thompson* (*BZT*) fluids. So-called *non-classical* phenomena such as rarefaction shock waves can occur. These are outside the scope of the present work, which instead focuses on the characterization of non-ideal classical flows with $Z \leqslant 1$ and $0 < \Gamma < 1$.

Established studies on compressible flows are extensively based on the hypothesis of ideal gas behaviour. The ideal gas model is simple yet powerful, in that it is accurate enough for most applications and conveniently allows to write analytical forms of many flow configurations of practical interest. However, it fails both quantitatively and qualitatively in describing non-ideal classical flows. Part of the aim of this thesis work is to indeed provide further fundamental understanding of such flows by characterizing them with a multidisciplinary theoretical, numerical and experimental approach.

The present research project lies in the field of engineering and thus its motivation cannot be detached from its practical applications. *NICFD* flows occur in a vast range of engineering processes, from rocket propulsion to industrial chemical activities. Examples are the oil & gas, heat pumps and refrigeration fields and even pharmaceuticals production with the use of the rapid expansion of supercritical solutions (*RESS*) (Helfgen et al., 2003). In the power generation field, non-ideal flows occur in supercritical carbon dioxide (sCO_2) power cycles and in Organic Rankine Cycles (*ORCs*). The latter are preferred to conventional steam cycles when low to medium source temperature and low to medium power output are considered, thanks to their low cost, plant simplicity and thermodynamic efficiency. Fluids usually employed in *ORCs* feature high complexity and molecular weight, and turbine expansion occurs in the dense gas region near the saturation curve and the critical point. As a result, turbine flows are highly supersonic and show important non-ideal flow effects, requiring accurate design tools accounting for these aspects in order to achieve high turbine efficiency, which in turn strongly impacts cycle efficiency (Colonna et al., 2015; Macchi and Astolfi, 2016).
Unfortunately, comparison of numerical design and analysis tools, ranging from preliminary loss correlations to full computational fluid dynamics (*CFD*) simulations, with experiment is relatively rare. This is because detailed experimental data characterizing non-ideal flows for *ORC* applications are currently not widely available in the open literature due to the intrinsic difficulties

in running dedicated experimental facilities. ORC working fluids, like many others of interest in the *NICFD* field, are liquids at standard room temperature and pressure. Typical ORC inlet turbine flows are instead at saturated, superheated or supercritical conditions, with temperatures and pressures ranging from about 100 to 400 °C and 10 to 50 bar (Macchi and Astolfi, 2016). Thus, in order to reproduce realistic conditions in a wind tunnel, a closed gas cycle or a phase transition thermodynamic cycle must be put in place. These are noticeably more complicated and expensive with respect to operation with incondensable gases such as air, where compressed air storage tanks or continuous loops are often sufficient to carry out an experimental campaign. Moreover, measurement procedures are also more complex due to the high fluid temperature involved and condensation issues in pneumatic lines. Also, the non-ideal flow field dependance on stagnation conditions significantly increases the number of flows that have to be experimentally reproduced for a complete characterization.
Despite these difficulties, several active plants exist and are starting to provide valuable experimental data, mostly on relatively simple yet extremely useful geometries such as converging-diverging nozzles. These allow to reproduce elementary flows important for fundamental *NICFD* studies and are also the simplest geometry representative of turbine blade passages in ORC turbines. Amongst these so-called *nozzle-fitted facilities* is the *Test Rig for Organic VApors* (*TROVA*) (Spinelli et al., 2013) at the Laboratory of Compressible Fluid-dynamics for Renewable Energy Applications (CREA Lab) of Politecnico di Milano, where all the experimental campaigns concerning the present thesis were carried out. Other plants of this kind are the ORCHID (Head et al., 2016) at TU Delft, the CLOWT (Reinker et al., 2017) at Muenster University of Applied Sciences and the dense-gas blowdown facility at Imperial College London (Robertson et al., 2020).
Several turbine-fitted facilities instead including all typical components of an organic Rankine cycle also exist, such as the *LUT micro-ORC test rig* at Lappeenranta – Lahti University of Technology (Turunen-Saaresti et al., 2017). The ORCHID at TU Delft is designed to also operate with a turbine instead of a nozzle, but testing to date was performed with the latter only. These experimental test rigs are mainly devoted to performance measurement of the different components and of the overall thermodynamic cycle and are less suited to provide detailed flow information than nozzle-fitted facilities. Within this context, part of the objectives of this work are to establish reliable experimental procedures for the detailed characterization of non-ideal flows of particular interest for organic Rankine cycle applications and fill the present literature gap in available experimental data. To this end, several extensive experimental campaigns, supported by CFD calculation, were carried out on the *TROVA* employing converging and converging-diverging nozzles to reproduce subsonic and supersonic vapor flows of Siloxane MM, a fluid commonly employed in high temperature *ORCs*.

Due to the peculiarity of non-ideal vapor flows in *ORCs*, measurements such as velocity magnitude and direction, mass flow rate or turbine performance, which are routinely carried out in more standard cycles and turbomachinery (e.g. gas turbines operating with air and combustion gases), are not possible yet with available technologies. One of the main issues in real operating plants is indeed the closure of mass and energy balances due to the lack of reliable mass flow rate measures (Zanellato et al., 2017). Even blade cascade testing, quite common in the design process of gas and steam turbines, is instead significantly more complex in the case of non-ideal flows due to the previously mentioned difficulties in running dedicated wind tunnels. Cascade testing is only starting to take place for such flows. To the author's knowledge, the first experimental campaign of this kind was very recently carried out at Whittle Laboratories of Cambridge University in a newly modified transient wind tunnel of Ludwieg tube-type, where annular turbine cascade flows of R134a were characterized with static pressure measurements (Baumgärtner et al., 2019). Upon further upgrade of the test rig, wake measurements of R134a flows in the same cascade were performed with a wedge probe with substantial complementary use of CFD calculation. The latter

was necessary to overcome the unavailability of a Mach number measurement upstream of the probe allowing to calculate shock losses at the probe tip in order to retrieve the pre-shock total pressure and evaluate cascade losses (Baumgärtner et al., 2020).
One of the main reasons for the difficulties in real ORC plant measurements and in blade cascade testing is that no appropriately calibrated instrumentation for non-ideal conditions is currently available. Indeed, none of the previously mentioned wind tunnels for non-ideal flows is mature enough to be routinely employed as a dedicated calibration facility for pressure probes. Research efforts are now starting to move towards this direction. The first published works on the topic are from the *CLOWT* plant at Muenster University of Applied Sciences. Results on the performance of a rotatable cylinder Pitot probe in high subsonic flows with fluid Novec^{TM} 649 were very recently presented (Reinker et al., 2020) as part of a preliminary study in order to establish measurement techniques for determination of Mach numbers in high-subsonic and transonic organic vapor flow fields.
Thus, the last objective of this thesis work is the development and use of a measurement system for pressure probes operating with non-ideal flows of interest in the ORC field. L-shaped Pitot-type probes are employed in the present experimental campaigns for system commissioning and with a view of allowing immediate transposition in industrial applications. For this reason, they are here preferred to the more complex directional pressure probes usually involved in more research-oriented studies. Moreover, as it will be evident later on, Pitot tubes are a necessary intermediate step towards the calibration of directional probes for non-ideal flows and were therefore purposely chosen as the starting point for further developments in the field.
Concerning the present thesis work on the *TROVA*, subsonic testing is carried out with Siloxane MM in conditions representative of measurement sections in real *ORC* plants where Pitot-tubes can be employed for mass flow rate and performance measurement. Supersonic testing is also performed to measure directly, for the first time ever, total pressure losses across shocks of non-ideal flows of MM vapor. This sets the basis for future testing of blade cascades operating with such flows and also provides precious data for numerical tools comparison.
Attesting the growing interest in the field of pressure probes for non-ideal flows, the CREA Lab at Politecnico di Milano was awarded funding for the ERC Proof of Concept project *PROVA* (*Pitot pRobe for Organic VApours*) to develop and calibrate Pitot probes for flow measurements in subsonic and supersonic flows of organic vapors typical of ORCs. It is remarkable that this project raised the interest of leading ORC players representing over 90% of the market and of relevant manufacturers in close fields of applications (e.g. oil & gas and compressor manufacturing).

As perhaps evident by now, the motivations of the present work lie on several different levels. The field of non-ideal compressible fluid dynamics is relatively new with respect to the well known ideal gas world. As such, insights into the fundamentals of the topic are still useful and a first objective is to contribute under this aspect with a multidisciplinary approach that includes theoretical considerations, numerical calculation and experimental results.
On a second level, a significant part of the research effort is devoted to the development of reliable experimental methodologies for *NICFD* flows. This involves procedures for detailed nozzle flow characterization also including the complementary use of CFD to understand particular flow features and verify results. Building upon this experience, the necessary plant and procedure modifications are identified and implemented to allow probe testing in the challenging environment of high pressure, high temperature non-ideal flows. To this end, the first ever L-shaped Pitot tube testing is carried out in both subsonic and supersonic conditions to complete the system commissioning. This paves the way for the calibration of directional pressure probes and blade cascade characterization concerning non-ideal flows.
On a further level, experimental campaigns with Pitot tubes unlock the possibility of finally providing industry with the tools to perform reliable velocity, mass flow rate and performance

measurements in real operating plants where non-ideal flows are involved, such as in the field of organic Rankine cycles.
Finally, the large experimental data-set produced within this research includes subsonic and supersonic nozzle expansions as well as the first ever direct measurement of total pressure losses across normal shocks in non-ideal flows. This contributes to filling the current literature gap in available experimental results and provides precious information for numerical tools comparison.

1.2 Thesis Outline

The present thesis is structured as follows.
Part I introduces the employed theoretical and experimental frameworks.
Chapter 2 documents a theoretical study on the non-ideal dependance of isentropic expansions on total conditions. The aim is to provide a sound basis to address a matter that is relevant throughout this work, from nozzle flow characterization to pressure probes testing.
Chapter 3 provides a detailed description of the Test Rig for Organic VApors (*TROVA*) and the measurement techniques involved in the characterization of non-ideal flows of siloxane MM vapor.
Part II concerns the study of subsonic and supersonic nozzle flows in non-ideal conditions.
Chapter 4 reports the extensive experimental campaign performed with non-ideal supersonic nozzle flows together with a comparison with CFD calculation performed as a support for the interpretation and verification of experimental results.
Similarly, Chapter 5 covers experimental and numerical results of non-ideal flows in choked subsonic nozzles.
The focus is then shifted from nozzle flow characterization to Pitot tubes in non-ideal flows in Part III.
Chapter 6 presents the design of the pneumatic system for pressure probe testing with such flows.
Chapter 7 details the preliminary Pitot tube characterization with air followed by testing in non-ideal subsonic flows of organic vapors.
Chapter 8 instead reports the first ever experimental total pressure drop measurements across normal shock waves in non-ideal flows of siloxane MM vapor.
Finally, Chapter 9 draws the conclusions of the present work and reports suggestions for future developments.

PART I:

THEORETICAL AND EXPERIMENTAL FRAMEWORK

CHAPTER 2

SIMILARITY PARAMETERS FOR NON-IDEAL ONE-DIMENSIONAL ISENTROPIC EXPANSIONS

The fact that the polytropic ideal gas model (PIG) does not provide a satisfactory description of the thermodynamics involved in non-ideal flows has a certain number of gasdynamic side effects. The one that is most relevant throughout the present thesis work, both in the case of nozzle flow characterization and in pressure probes testing, is the non-ideal dependance of isentropic expansions on total conditions. The matter is therefore extensively studied from a theoretical stand point in this chapter. The aim is to identify similarity parameters that would provide further understanding of this peculiar behaviour and reduce the complexity of any problem in which non-ideal flows are encountered.

The identification of a similarity parameter in the context of non-ideal flows can indeed provide precious information to reduce the number of variables for the preliminary design of thermodynamic cycles and components (e.g. turbomachinery) in various fields of application, such as organic Rankine cycle (ORC) power systems. Moreover, and quite relevantly for the present thesis work, it can allow to drastically reduce the experimental effort for detailed wind tunnel characterization and for future calibration of pressure probes operating in the non-ideal compressible regime. Not all possible nozzle or probe operating conditions would have to be reproduced, but only selected ones sharing the same similarity variable as real conditions would be required, entailing very significant time and costs savings.

2.1 Thermal and Caloric Behavior Similarity

Consider a fixed nozzle geometry and pressure trends along its axis for several one-dimensional (1D) isentropic expansions having different total conditions, such as qualitatively represented in Figure 2.1a for a set generic fluid. If the fluid behaves as a polytropic ideal gas (*PIG*), then all curves collapse onto one another if the dimensionless pressure ratio P/P_T is considered (P is static pressure and P_T is the total one). That is, expansions are similar, regardless of the actual total conditions, as shown in Figure 2.1b. However, the same does not occur if such thermodynamic model is not suitable (Figure 2.1c). All of this is also true for other dimensionless quantities such as the Mach number M, temperature ratio T/T_T and density ratio ρ/ρ_T (where T represents temperature, ρ is density and subscript T identifies total conditions).

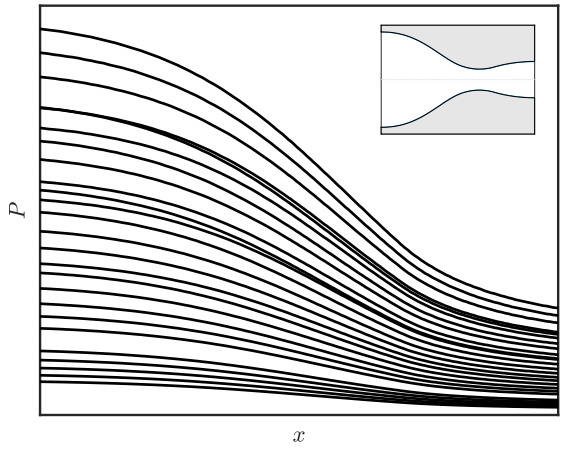

(a) Pressure.

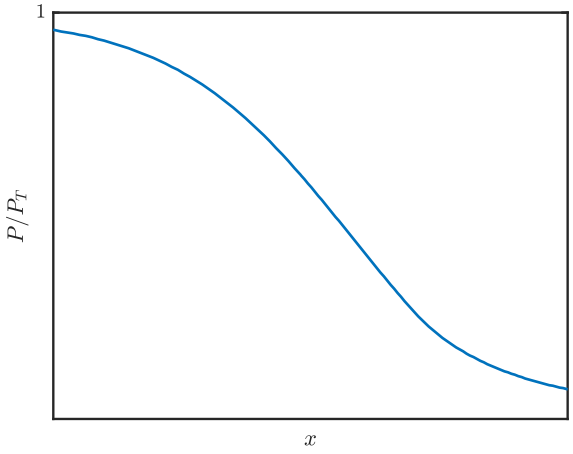

(b) Pressure ratio for a *PIG*.

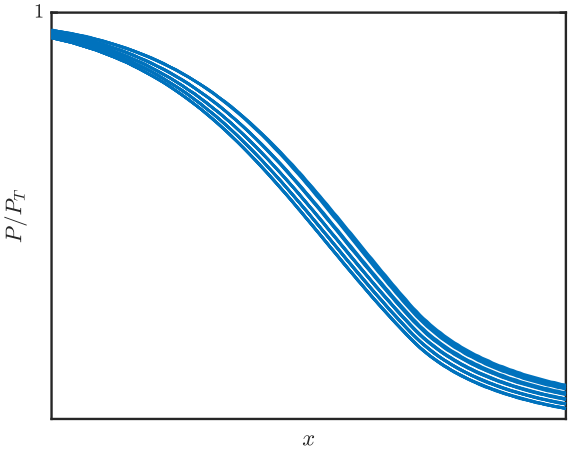

(c) Pressure ratio for a fluid not properly modeled by a *PIG*.

Figure 2.1. Qualitative representation of trends along a nozzle axis for several 1D isentropic expansions in a fixed geometry for a given fluid.

The reason for this is to be found in the particular volumetric and caloric behaviour of a polytropic ideal gas. As further detailed in Appendix A, a complete thermodynamic description of a single constituent fluid requires that either a fundamental relation or thermal and caloric equations of state be provided.
Compressibility factor Z can be considered as an indication of the volumetric behavior of a fluid with respect to that of an ideal gas at same temperature and pressure and is thus representative of the thermal equation of state, irrespectively of any process that the fluid might be undergoing. If an ideal gas is considered, the value of Z is always equal to one. Within the frame of isentropic expansions, this means that the volumetric behaviour of the fluid is always the same, regardless of the total and local flow conditions.
Considering the caloric equation of state, the fundamental derivative of gasdynamics Γ can be considered as a representative parameter in the case of isentropic expansions. Indeed, it is a quantitative measure of the variation of the speed of sound in isentropic transformations, so it is intrinsically defined to characterize the type of processes here analyzed as briefly recalled in Section 1. Moreover, it is explicitly dependent on molecular complexity (Harinck et al., 2009) so it accounts for the number of degrees of freedom in which a molecule can store energy during the expansion. This is precisely the information held in the caloric equation of state within the context of isentropic expansions. If a polytropic ideal gas is considered, the value of Γ is constant and only depends on the specific heats ratio γ: $\Gamma = \frac{\gamma+1}{2}$. It is therefore a constant value for a fixed fluid, meaning that the caloric behavior is independent of total and even local flow conditions in case isentropic expansions are considered.
As a result of the independence of both the volumetric and caloric behaviours on flow conditions, isentropic expansions for a certain *PIG* collapse onto a single curve if dimensionless quantities such as pressure ratio are considered. In case non-ideal flows are considered instead, neither Z nor Γ have fixed values a priori. Their local values at a certain point along an isentropic expansion depend on the local thermodynamic state, which in turn depends on total conditions. As a consequence, isentropic flows depend on total conditions too.

It is therefore natural to investigate the behaviour of compressibility factor and fundamental derivative of gasdynamics for non-ideal flows in order to understand the latter's dependance on total conditions. To this end, 1D isentropic expansions were studied and documented here, as next explained.

2.2 Calculation Framework

1D isentropic expansions were calculated for several total conditions chosen and classified in terms of their total compressibility factor Z_T, defined in Equation (2.1) where R is the gas constant, T_T is the total temperature and $\rho_T = \rho(T_T, P_T)$ is the stagnation density.

$$Z_T = \frac{P_T}{RT_T\rho_T} \tag{2.1}$$

Expansions were determined independently of any particular geometry by letting the pressure ratio P/P_T vary in the range $0.99 - 0.05$. Calculation was carried out for different levels of non-ideality, so for Z_T between 0.4 and 0.9, and for the pure fluids reported in Table 2.1. Twenty fluids from different families involving complex molecules (including Siloxanes, Alkanes, Cyclic Alkanes and Halocarbons) were considered. Simple molecules such as carbon dioxide, water and ammonia were also included in the analysis. Ten total conditions were considered for each Z_T. Total pressure and temperature (P_T, T_T) at same Z_T were chosen so as to cover the largest possible area in the vapor region of the $T - s$ thermodynamic plane of each fluid, where T and s are temperature and specific entropy. Figures 2.2a and 2.2b report chosen total conditions for

Type	Fluid	T_C $[°C]$	P_C $[bar]$	MW $[kg/kmol]$	N atoms	Chemical Formula
Siloxanes	MM	245.55	19.31	162.38	27	$C_6H_{18}OSi_2$
	MDM	292.21	14.38	236.53	37	$C_8H_{24}O_2Si_3$
	D4	313.34	13.32	296.62	40	$C_8H_{24}O_4Si_4$
	D6	372.63	9.61	444.92	67	$C_{14}H_{42}O_5Si_6$
Alkanes	Butane	151.98	37.96	58.12	14	C_4H_{10}
	Pentane	196.55	33.70	72.15	17	C_5H_{12}
	Hexane	234.67	30.34	86.18	20	C_6H_{14}
	Octane	296.17	24.97	114.23	26	C_8H_{18}
	Decane	344.55	21.03	142.28	32	$C_{10}H_{22}$
Cyclic Alkanes	Cyclopentane	238.57	45.71	70.13	15	C_5H_{10}
	Cyclohexane	280.45	40.81	84.16	18	C_6H_{12}
Alkenes	Isobutene	144.94	40.10	56.11	14	C_4H_{10}
	Benzene	288.87	49.07	78.11	12	C_6H_6
Other Hydrocarbons	Toluene	318.60	41.26	92.14	15	C_7H_8
	Acetone	234.95	47.00	58.08	10	C_3H_6O
Halocarbons	R1234yf	94.70	33.82	114.04	9	$C_3H_2F_4$
	R218	71.87	26.40	188.02	11	C_3F_8
	R1233zd	165.60	35.73	130.50	9	$C_3H_2ClF_3$
	R227ea	101.75	29.25	170.03	11	C_3HF_7
	RC318	115.23	27.78	200.04	12	C_4F_8
Other Fluids	Water	373.95	220.64	18.02	3	H_2O
	Carbon Dioxide	30.98	73.77	44.01	3	CO_2
	Ammonia	132.25	113.33	17.03	4	NH_3

Table 2.1. Fluids selected for analysis with critical temperature T_C, critical pressure P_C, molar weight MW, number of atoms and chemical formula.

exemplary fluids MM and CO_2 in their respective $T-s$ planes. The Helmoltz energy-based thermodynamic model with Span-Wagner functional form embedded in the *FluidProp* library was used to calculate all derived thermodynamic properties (see Appendix A). The maximum considered pressure was three times the critical one and the maximum considered temperature was set to the upper validity limit of the thermodynamic model. Care was taken to ensure no entering in the two-phase region during any expansion. This is why, for some fluids, $Z_T = 0.4$ had to be excluded from calculation or expansions had to be interrupted at the saturation curve.

For brevity, results will be shown only for exemplary fluids MM and CO_2, which were found to be well representative of high and low molecular complexity fluids, respectively. Indeed, qualitatively similar trends to MM were found for all investigated fluids except for those characterized by very low molecular complexity: water, carbon dioxide and ammonia. The behaviour of the latter three is instead well illustrated by the one of CO_2.

2.3 Z and Γ along Expansions

Figure 2.3 reports calculation results for fluids MM and CO_2. Z, Γ and area ratio A^*/A along expansions are plotted as a function of P/P_T. Each curve is an expansion evolving from $P/P_T = 1$ towards lower pressure ratios, with different colors corresponding to selected total compressibility values $Z_T = 0.4, 0.5, 0.6, 0.7, 0.8$ and 0.9. Considering carbon dioxide, several expansions were found to at least partially proceed in the two-phase region. Thus, plots in Figures 2.3b,2.3d and 2.3f were interrupted at the pressure ratio corresponding to two-phase region entry. In cases in which this occurred before the sonic condition, the whole expansion was instead removed.
It is remarkable that, considering a complex fluid, total conditions having same Z_T also have similar grouped Z and Γ trends and values along the expansion, as seen in Figures 2.3a and 2.3c,

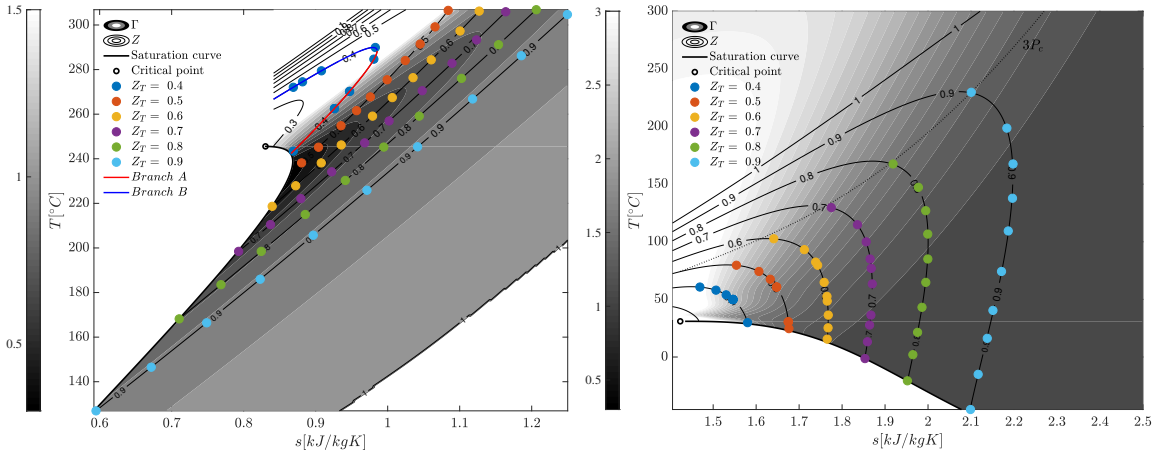

(a) $T - s$ diagram with Z and Γ contours for fluid MM.

(b) $T - s$ diagram with Z and Γ contours for CO_2.

Figure 2.2. Total conditions selected for expansion calculations for fluids MM and CO_2 are shown by dots in the $T - s$ plane. Each color corresponds to a selected Z_T value, consistently with plots in Figure 2.3.

indicating a similarity in volumetric and caloric behaviours. As less ideal conditions at lower Z_T are approached, however, larger differences in Γ and/or Z values are found. This is linked to the particular shape of compressibility factor and fundamental derivative isolines in the $T - s$ thermodynamic plane for complex fluids. Far away from the critical point, iso-Z are lines parallel to one another, as seen in the $T - s$ diagram in Figure 2.2a. Therefore, if expansions with different total conditions share the same Z_T, they also share close values of Z all along the process, since expansions are simply vertical lines in the $T - s$ plane. Moreover, iso-Γ curves are also parallel away from the critical point - not only between themselves, but also parallel to iso-Z curves. As a consequence, if expansions share the same Z_T, they not only share similar Z, but also similar Γ values along the process. At less ideal conditions, both Z and Γ isolines are no longer simple straight lines, but they form an enclosed region. Starting from the saturation curve and moving along an isoline into the vapor region, the path is initially a straight line towards higher temperature and entropy. This is exemplified as *Branch A* in Figure 2.2a on the $Z = 0.4$ isoline. A maximum entropy point is reached and the path along the isoline then bends back towards the saturation curve and lower entropy and temperature values (*Branch B* in Figure 2.2a). Iso-Γ curves show this enclosed region as the critical point is approached from low temperatures. Iso-Z curves instead show this behaviour close to the critical point aswell, but at higher pressures than iso-Γs. If expansions start on a point on *Branch B* of the iso-Γ or iso-Z line, then the trend in Γ or Z along the expansion will be non-monotone. Trends in Z and Γ are thus no longer similar to other expansions at same Z_T starting on *Branch A*. This can be seen in Figures 2.3a and 2.3c for $Z_T = 0.4$.

If simple molecules are considered instead, the compressibility factor trend along expansions sharing same Z_T is also comparable, whilst Γ does not show any common pattern.
Again, this is linked to the particular shape of the isolines in the $T - s$ thermodynamic plane, which is significantly different with respect to complex fluids. In the $T - s$ diagram in Figure 2.2b, iso-Z curves are still fairly parallel to one another along their *Branch A*, which is almost a vertical line. As a consequence, the value of Z does not vary much along an expansion, differently to what happens for complex fluids. This also why expansions with same Z_T have similar Z trends too. Considering iso-Γ curves instead, they are not at all parallel to iso-Zs, contrarily to complex fluids. This is responsible for the fact that total conditions sharing the same Z_T do not have similar values and trends of Γ if simple molecules are considered.

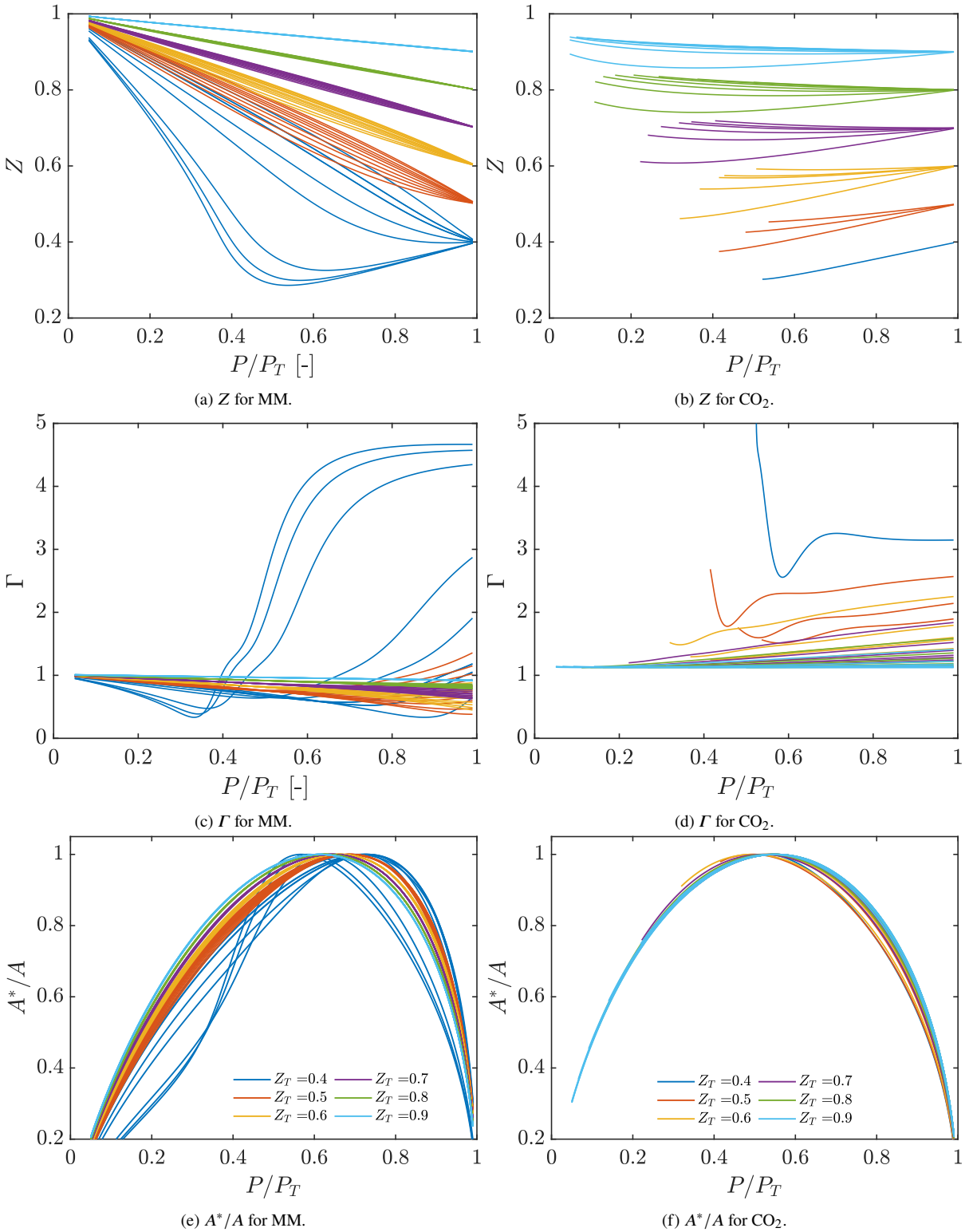

(a) Z for MM.

(b) Z for CO_2.

(c) Γ for MM.

(d) Γ for CO_2.

(e) A^*/A for MM.

(f) A^*/A for CO_2.

Figure 2.3. Compressibility factor Z, fundamental derivative of gasdynamics Γ and area ratio A^*/A along expansions for MM (left) and CO_2 (right) plotted as a function of pressure ratio P/P_T. Each color corresponds to a selected Z_T value as specified in area ratio plot legends and each line to a different total condition consistently with Figure 2.2.

2.4 P/P_T along Expansions

1D calculations confirm the non-ideal dependence of the expansions on total conditions for all selected fluids. This is illustrated for fluids MM and CO_2 in Figures 2.3e and 2.3f respectively, where the area ratio A^*/A along expansions is plotted as a function of P/P_T. As it can be seen, curves are not superposed, as would instead happen for an ideal gas behaviour.
Referring to Figure 2.3f, simple fluids show no particular pattern in expansions sharing the same total compressibility factor. In case of complex fluids instead (Figure 2.3e), A^*/A curves of expansions with the same Z_T are grouped together, except for strongly non-ideal conditions at $Z_T = 0.4$. In the latter case, although expansions are separated from other Z_T values, they are not superposed. The above observations indicate that expansion similarity is linked to similar trends and values in both the compressibility factor and the fundamental derivative. This occurs for complex fluids at moderately high levels of non-ideality for expansions sharing the same Z_T thanks to the particular shape of Z and Γ isolines. At strongly non-ideal conditions or when simple fluids are considered instead, having the same Z_T does not lead to similar Z and Γ along expansions, resulting in expansions that are not similar.
Considering molecularly complex fluids, the level of non-ideality has a non-negligible impact on isentropic expansions. For a fixed geometry, which for 1D calculation corresponds to fixing the area ratio A^*/A, pressure ratio is larger for expansions occurring at less ideal conditions (lower total compressibility factor). Table 2.2 reports average pressure ratios $\overline{P/P_T}$ for the expansions at chosen Z_T for three selected area ratios: $A^*/A = 0.8$ - subsonic, $A^*/A = 1$ - sonic and $A^*/A = 0.7$ - supersonic. These correspond to Mach numbers for MM of ~ 0.6, 1 and ~ 1.5, respectively. As a quantitative example, if sonic conditions are considered, pressure ratio can vary from an average $\overline{P/P_T} = 0.68$ at $Z_T = 0.4$ to $\overline{P/P_T} = 0.61$ at $Z_T = 0.9$ for fluid MM, so by a non-negligible 11.5%. Table 2.2 also shows that the average pressure ratio has larger variation with the level of non-ideality when compressibility effects become more important, so towards A^*/A corresponding to higher Mach numbers.

2.5 M, T/T_T and ρ/ρ_T along Expansions

The similarity considerations drawn above for pressure ratio are also valid for other dimensionless quantities such as the Mach number, temperature and density ratios. This is qualitatively visible in Figure 2.4 where they are plotted as a function of P/P_T along expansions. Considering complex fluid MM, similarity of expansions with different total conditions but same total compressibility factor $Z_T \geqslant 0.5$ is evident in Figure 2.4a for M, Figure 2.4c for T/T_T and Figure 2.4e for ρ/ρ_T. If a simple fluid such as CO_2 is instead considered, no similarity between expansions with same Z_T is present (Figures 2.4b, 2.4d and 2.4f), consistently with P/P_T, Z and Γ considerations above.
Amongst all dimensionless parameters, pressure ratio is the most important one when evaluating nozzle operation (e.g. in case of turbine blade cascades). Also, as it will be evident in the following, it is the main measured parameter in detailed nozzle expansions characterization. For these and for brevity reasons, the following quantitative analysis will focus on P/P_T only.

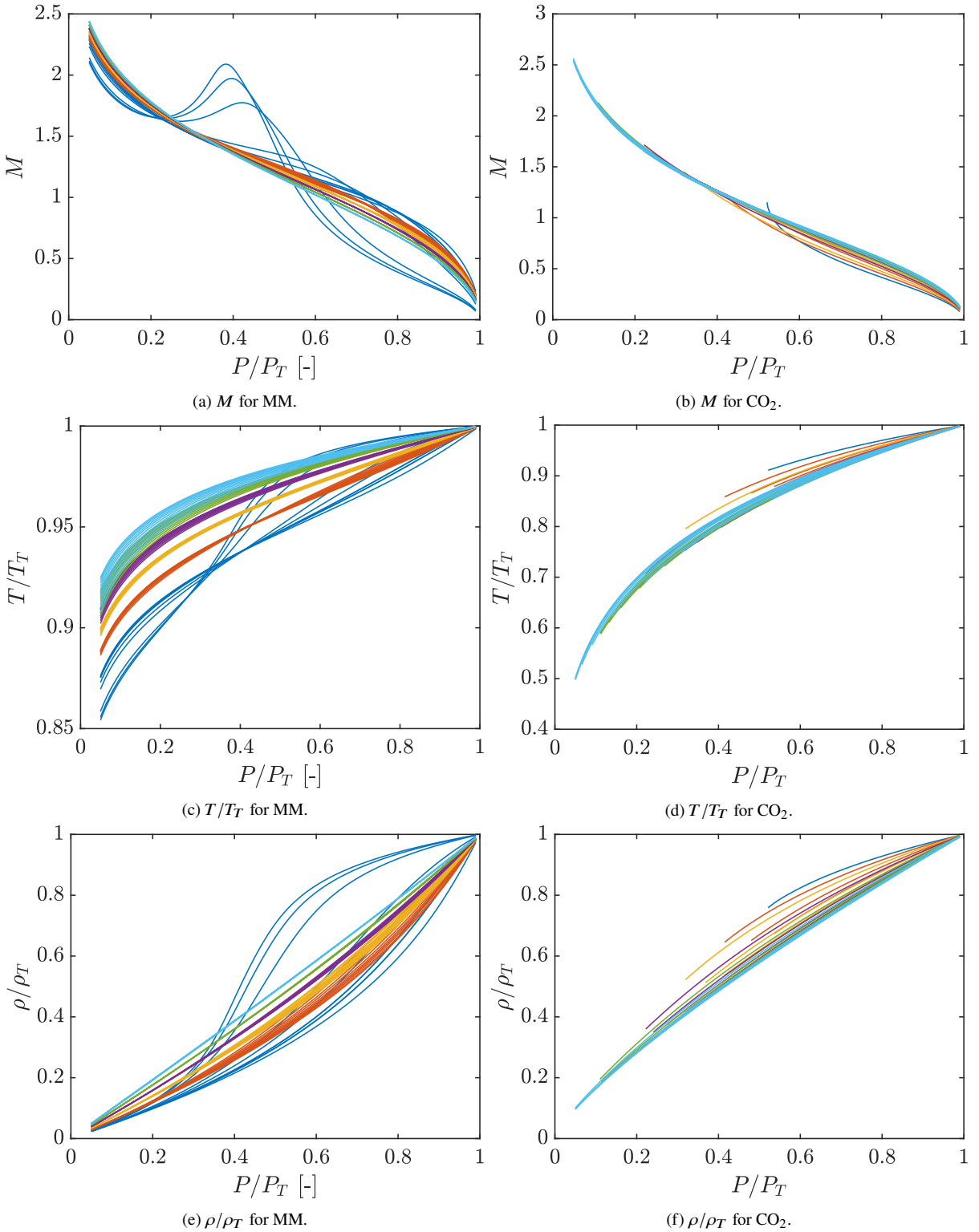

(a) M for MM.

(b) M for CO_2.

(c) T/T_T for MM.

(d) T/T_T for CO_2.

(e) ρ/ρ_T for MM.

(f) ρ/ρ_T for CO_2.

Figure 2.4. Mach number M, temperature ratio T/T_T and density ratio ρ/ρ_T along expansions for MM (left) and CO_2 (right) plotted as a function of pressure ratio P/P_T. Each color corresponds to a selected Z_T value as reported in legends in Figure 2.3 and each line to a different total condition consistently with Figure 2.2.

2.6 Z_T as Similarity Parameter for Molecularly Complex Fluids

To better visualize the findings above, it is useful to momentarily move from the area ratio employed in the calculation framework back to the initial generic nozzle geometry, as illustrated in Figure 2.5. Results show that expansions of a molecularly complex fluid in the non-ideal regime with different total conditions classified in terms of their total compressibility factor (Figure 2.5a) have pressure ratio curves that are well superposed if $Z_T \geqslant 0.5$ (Figure 2.5b). It can be concluded that isentropic expansions are *similar* if characterized by the same value of Z_T, which can therefore be considered as a suitable similarity parameter in these circumstances.
This was actually experimentally verified for flows of siloxane MM, as reported in Section 4 and published in Cammi et al. (2019, 2020). Pressure ratios of expansions in the same nozzle having different total conditions but same total compressibility factor were experimentally measured to be within error bars of one another for $Z_T \geqslant 0.6$.

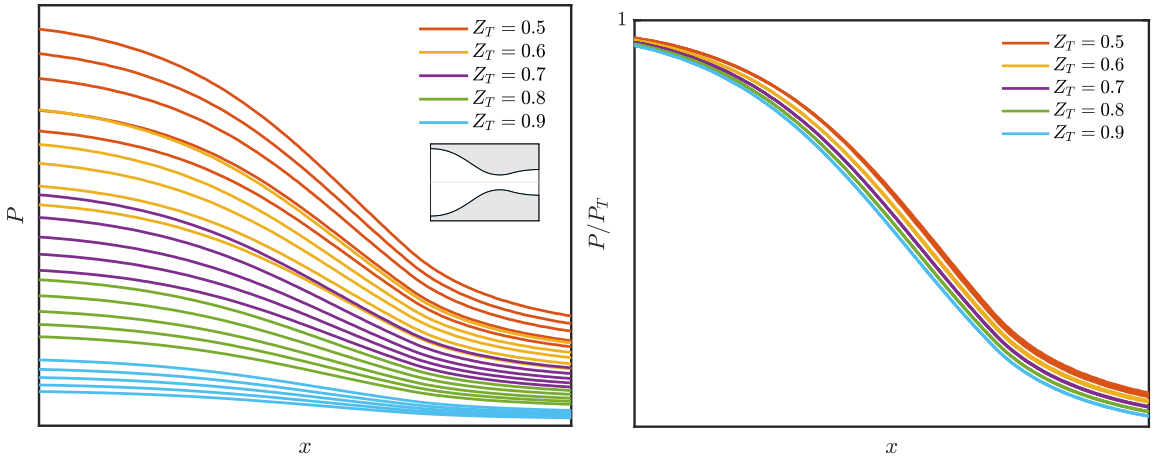

(a) Pressure.

(b) Pressure ratio.

Figure 2.5. Trends along a nozzle axis for several 1D isentropic expansions in a fixed geometry for a given molecularly complex fluid. Total conditions are classified in terms of their total compressibility factor Z_T.

Moving back to the generic area ratio frame of reference, to quantify the performance of Z_T as a similarity parameter for complex fluids, the maximum percentage pressure ratio variation $\Delta^{Z_T}_{P/P_T}$ is calculated as:

$$\Delta^{Z_T}_{P/P_T} = \frac{\max\left[P/P_T(Z_T)\right] - \min\left[P/P_T(Z_T)\right]}{\min\left[P/P_T(Z_T)\right]} \cdot 100 \tag{2.2}$$

where $\max\left[P/P_T(Z_T)\right]$ and $\min\left[P/P_T(Z_T)\right]$ refer to maximum and minimum values of pressure ratio registered at a specified A^*/A value among all expansions sharing the same Z_T. It is therefore an indication of the spread in pressure ratio values in a fixed geometry for expansions characterized by the same total compressibility factor but different (P_T, T_T). Considering Siloxane MM, Table 2.2 and Figure 2.6 report $\Delta^{Z_T}_{P/P_T}$ values at chosen Z_T for the three selected area ratios previously considered. At sonic conditions ($A^*/A = 1$), $\Delta^{Z_T}_{P/P_T} = 28.52\%$ at $Z_T = 0.4$, a very large value consistent with previous qualitative observations. As expected, there are significant improvements as more ideal conditions at higher total compressibility factor are approached, with $\Delta^{Z_T}_{P/P_T} = 0.57\%$ at $Z_T = 0.6$ and a further decrease to $\Delta^{Z_T}_{P/P_T} = 0.31\%$ at $Z_T = 0.9$. Considering other area ratios

MM	$Z_T = 0.4$		$Z_T = 0.5$		$Z_T = 0.6$		$Z_T = 0.7$		$Z_T = 0.8$		$Z_T = 0.9$	
	$\overline{P/P_T}$	$\Delta^{Z_T}_{P/P_T}$	$\overline{P/P_T}$	$\Delta^{Z_T}_{P/P_T}$	$\overline{P/P_T}$	$\Delta^{Z_T}_{P/P_T}$	$\overline{P/P_T}$	$\Delta^{Z_T}_{P/P_T}$	$\overline{P/P_T}$	$\Delta^{Z_T}_{P/P_T}$	$\overline{P/P_T}$	$\Delta^{Z_T}_{P/P_T}$
$A^*/A = 0.8$, **sub**	0.87	15.55	0.89	0.96	0.88	0.32	0.87	0.11	0.86	0.11	0.85	0.00
$A^*/A = 1$, **sonic**	0.68	28.52	0.69	1.38	0.66	0.57	0.64	0.29	0.63	0.15	0.61	0.31
$A^*/A = 0.7$, **sup**	0.37	35.02	0.32	9.62	0.30	3.88	0.28	1.68	0.27	0.70	0.26	0.73

Table 2.2. Average pressure ratio $\overline{P/P_T}$ and percentage difference in pressure ratio $\Delta^{Z_T}_{P/P_T}$ for fluid MM at different Z_T values and selected area ratios $A^*/A = 0.8$ - subsonic, $A^*/A = 1$ - sonic and $A^*/A = 0.7$ - supersonic.

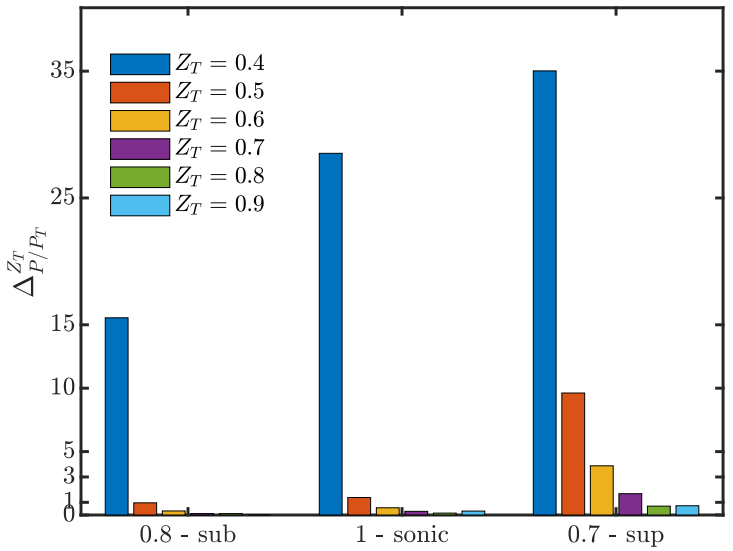

Figure 2.6. Percentage difference in pressure ratio $\Delta^{Z_T}_{P/P_T}$ for fluid MM at different Z_T values and selected area ratios $A^*/A = 0.8$ - subsonic, $A^*/A = 1$ - sonic and $A^*/A = 0.7$ - supersonic.

and the other investigated complex fluids, the same trend in $\Delta^{Z_T}_{P/P_T}$ with Z_T is evidenced. The percentage pressure ratio variation increases as the Mach number increases at same Z_T, also due to the lower value of the pressure ratio at the denominator (Equation (2.2)).
Siloxane MDM, a heavier fluid with higher complexity than MM, in its same family and with similar molecular structure, has overall lower values, with $\Delta^{Z_T}_{P/P_T} = 0.28\%$ at $Z_T = 0.6$ and $\Delta^{Z_T}_{P/P_T} = 0.15\%$ at $Z_T = 0.9$ for $A^*/A = 1$. Lower values of $\Delta^{Z_T}_{P/P_T}$ were also found for Siloxane D6 with respect to the simpler D4. Analogously, considering the Alkanes family, Z_T performance was found to improve as molecular mass and complexity increase leading to lower $\Delta^{Z_T}_{P/P_T}$ values, except at strongly non-ideal total conditions with $Z_T = 0.4$. In this case instead, total compressibility factor was found to perform worse for more complex fluids.
It should be pointed out that within other classes of complex fluids evaluated in the present analysis, this improvement with molecular complexity in the performance of Z_T as a similarity parameter was not as evident as for Siloxanes or Alkanes. This is because molecular structure can change significantly within the same fluid class (consider Halocarbons, for example), with important impacts on thermodynamic properties that make any analysis based only on molecular complexity misleading.

2.7 Conclusions and Future Developments

1D isentropic expansions for non-ideal flows of several different fluids with varying degree of molecular complexity were investigated. Findings indicate that, for complex fluids in moderately high non-ideal conditions ($Z_T \geqslant 0.5$), expansions are similar if total conditions share the same total compressibility factor. This is because trends and values of compressibility factor and fundamental derivative of gasdynamics are also similar along the process thanks to the particular shape of their isolines in the $T - s$ thermodynamic plane. These parameters are representative of information stored in thermal and caloric equations of state, suggesting that expansions are similar because they share similar volumetric and caloric behaviour throughout the process.

Although strongly non-ideal conditions do not share similar expansions, it must be pointed out that the present findings still have a relevant practical interest since most engineering processes involve expansions with typically $Z_T \geqslant 0.5$ (e.g. ORC turbines).

Further investigation of the topic is envisaged. Calculations using the *van der Waals* model should be carried out to better highlight the role of molecular complexity in flow similarity and possibly lead to a molecular interpretation of the similarity patterns reported here.

Nevertheless, as mentioned in the introduction to this chapter, the present results from theoretical calculation already provide very useful indications to possibly reduce the experimental effort required for non-ideal flow characterization. The campaign on supersonic nozzles reported in Section 4 will allow to experimentally verify these findings.

CHAPTER 3

THE TEST RIG FOR ORGANIC VAPORS (TROVA)

All experimental activities on non-ideal flows of organic vapors in the frame of this thesis were carried out on the Test Rig for Organic VApors (TROVA) located at the Laboratory of Compressible fluid dynamics for Renewable Energy Applications (CREA Lab) of Politecnico di Milano. Given its importance, this chapter is devoted to a detailed explanation of the plant layout, its main components and measurement instrumentation. Special focus is given to the description of the employed rear plates, nozzles and pressure probes. A typical test is also described together with the data processing procedure to analyze experimental results.

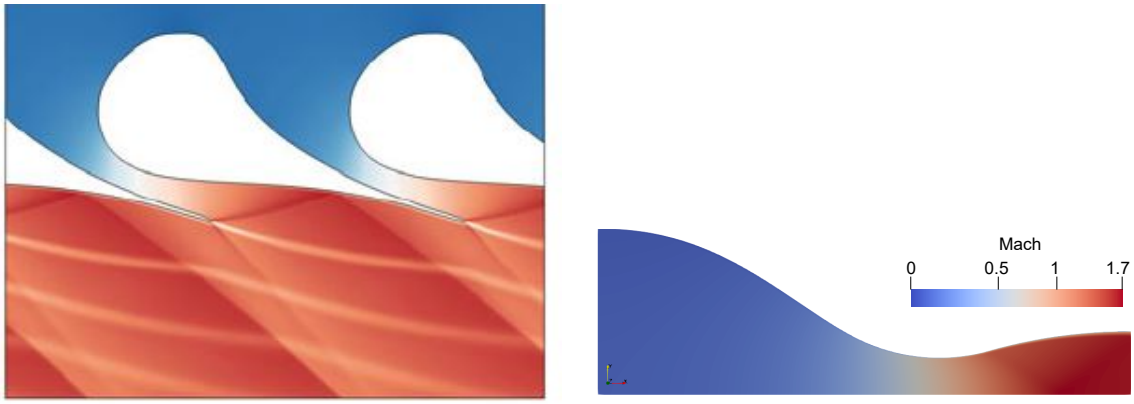

(a) Example of an ORC turbine stator flow field (Romei et al., 2020b).

(b) Example of a *TROVA* nozzle flow field.

Figure 3.1. Flow field Mach number from CFD simulations with siloxane MM. Blade channels in ORC turbines stators are well represented by the converging-diverging nozzle geometry employed in the *TROVA*.

3.1 The TROVA

The *TROVA* is a nozzle-fitted blow-down wind tunnel specifically designed to reproduce flows of organic vapors representative of those occurring in organic Rankine cycle turbines and experimentally characterize them with independent pressure, temperature and velocity measurements. A 2D planar straight-axis converging-diverging nozzle is the simplest geometry representative of a blade passage in an ORC turbine (Figure 3.1) allowing for pressure measurements without the need of calibrated pressure probes.
It is thus employed to investigate non-ideal flows in the *TROVA* test section. The nozzle is designed to exhibit a 2D expansion with a large isentropic core (the boundary layer in near-wall regions is very thin during an expansion): therefore, the flow field at the nozzle axis is fully characterized by simultaneous total temperature and pressure measures at the nozzle inlet and from static pressure measurements along the nozzle axis.
The plant was originally conceived in cooperation with a major ORC manufacturer to operate with different working fluids with minimal plant adjustments. The two design fluids were siloxane MDM, commonly employed in high temperature ORCs, and refrigerant pentafluoropropane (R245fa), used in low temperature ORCs. The first experimental campaigns starting from 2015 involved the use of MDM. It was later substituted in 2017 with siloxane MM, characterized by a higher thermal stability and saturation pressure which allowed a slightly easier plant management.
The batch configuration greatly reduces the required thermal power with respect to running a continuous phase-transition cycle and allows to explore a large range of test conditions, up to a maximum pressure of 50 bar and 400 °C. The thermal power involved in a continuous configuration ($\sim$ 2.5 MW) would be unsustainable due to the relatively large test section size, necessary to allow detailed flow measurements with pressure probes and ensure negligible blockage effects. Further information on the *TROVA* design can be found in Spinelli et al. (2013), while the next parts of this chapter present the experimental apparatus and the measuring techniques involved in this work.

3.2 Plant Layout and Thermodynamic Cycle

The TROVA operates with a batch Rankine cycle with an expansion occurring through the nozzle, so no useful work extraction takes place.
The plant layout can be found in Figure 3.2 and the corresponding thermodynamic cycle (for siloxane MM at exemplary operating conditions) in Figure 3.3.

The main plant components and thermodynamic processes are described next.

- The *High Pressure Vessel* (*HPV*) is a 1 m^3 volume where the organic fluid is stored and vaporized to the desired temperature and pressure conditions through an isochoric heating process (process $2 \rightarrow 4$ in Figure 3.3).
  The heating system is made of electrical band heaters located around the external wall of the cylindrical shell and heating wires at the top and bottom caps that heat and vaporize the fluid. The installed power is 37.5 kW and it is regulated by Proportional-Integral-Derivative (*PID*) controllers which act on a feedback signal from control thermocouples at the wall. The characteristic heating time is of $5 - 8$ hrs depending on desired operating conditions.
  Valves *V2*, *V3* and *BPCV* isolate the volume from the rest of the plant, whilst valves D1 and DR4 isolate it from the external environment. A safety valve with 50 bar maximum design pressure is also installed, with discharge in the *Low Pressure Vessel* (*LPV*).

- Valve *V3* is a ball valve operating to a maximum of 50 bar and 400 °C which isolates the *HPV* from the *Test Section*. It is operated via a dedicated *Labview*® software and is heated with electrical wires to avoid fluid condensation during tests.

- The *Main Control Valve* (*MCV*) is a throttoling valve that can be used to regulate vapor conditions from HPV conditions to an almost constant stagnation pressure in the plenum. In the present thesis work, however, the *MCV* is always kept completely open: the nozzle upstream conditions (h_{T6} - total enthalpy, P_{T6}- total pressure, T_{T6}- total temperature) and the mass flow rate $\dot{m}$ thus change in time due to *HPV* emptying. Figure 3.3 shows the thermodynamic cycle at the initial time of a test at typical conditions.
  The characteristic time of the change in nozzle inlet conditions is two orders of magnitude longer than the time needed for the flow to travel across the nozzle: nozzle flow can be considered as a sequence of steady states with varying boundary conditions, measured during the test. Therefore, by not regulating the *MCV*, different operating conditions (different non-ideality conditions) can be investigated in one single experimental run.
  Like valve *V3*, the *MCV* is heated with electrical wires to avoid fluid condensation during tests.

- The *plenum* is a settling chamber located upstream of the nozzle constituted by a 6 in pipe. Fluid velocity is very low (of the order of 1 m/s) so static quantities can be assumed equal to total ones. Total pressure ahead of the nozzle (P_{T6}) is therefore measured with a wall pressure tap and a flush-mounted transducer, being the kinetic energy contribution negligible. The total temperature (T_{T6}) is analogously measured by a statically calibrated thermocouple since the recovery factor can reasonably expected to be equal to one. The flow passes through a honeycomb to make it uniform and regular at the inlet of the nozzle.
  The *plenum* is also heated to avoid fluid condensation.

- The *Test Section* is the core of the TROVA, where the converging-diverging nozzle is located. After a smooth passage from the circular cross section in the plenum to a rectangular one, the fluid expands through the planar nozzle ($6 \rightarrow 7$) where static pressures along the axis are measured. The characteristic test time ranges from $\sim 20s$ to several minutes, depending on the operating conditions.

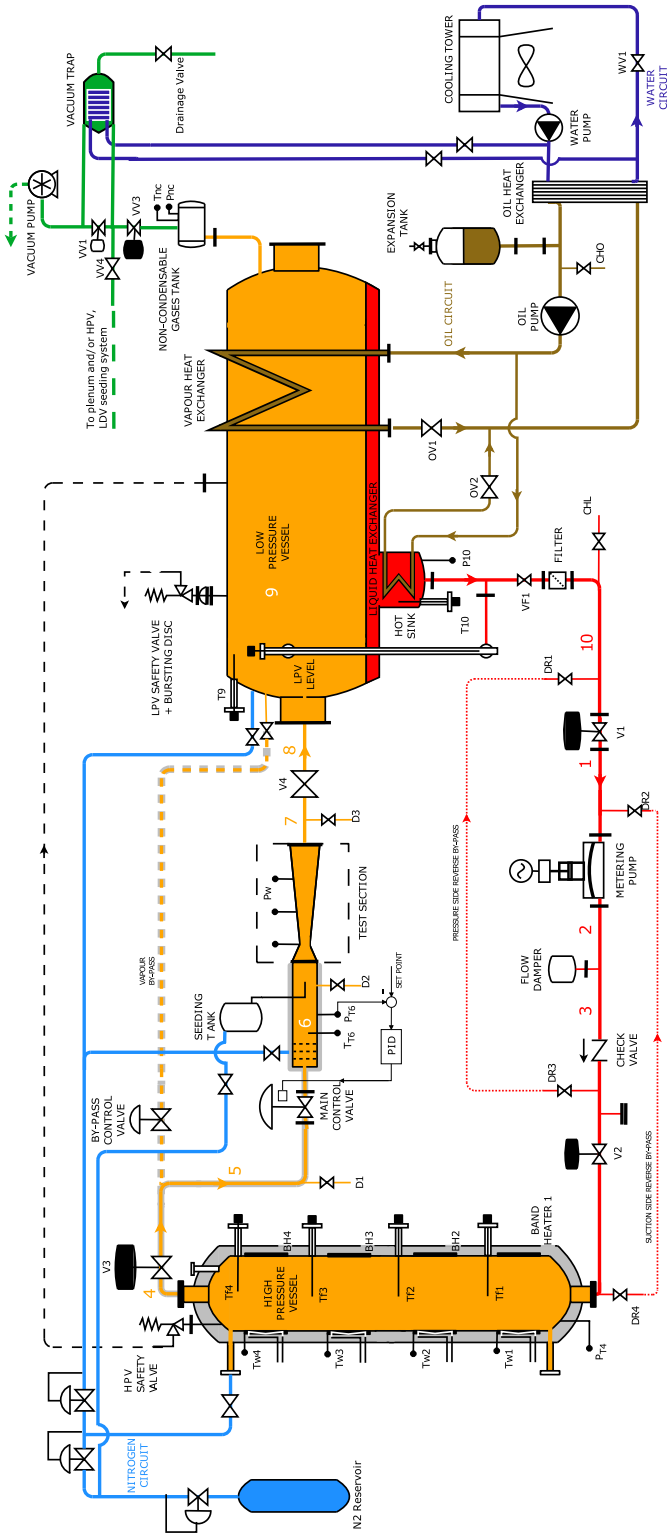

Figure 3.2. TROVA plant scheme. Numbers correspond to points on thermodynamic cycle in Figure 3.3.

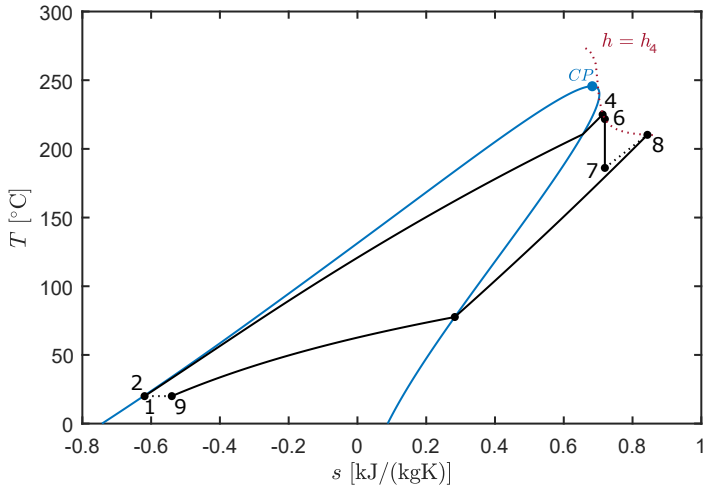

Figure 3.3. Thermodynamic cycle implemented by the TROVA (black lines). The light-blue line is the saturation curve, *CP* is the critical point and the red dotted line is the locus of points with $h = h_4$.

The test section is a modular flanged body (Figure 3.4), designed to accommodate different nozzle profiles and geometries. Its vertical sides are a quartz window (at the front) and a steel plate (at the back). The geometry is planar in order to easily accommodate the quartz window, that is the optical access designed to perform LDV measurements and schlieren visualizations of the flow field. The rear steel plate exhibits a series of taps for static pressure measurement along the nozzle axis. The plate is mirror-polished in order to provide the highly reflective surface needed for the schlieren technique implemented with the double-pass configuration (see Section 3.3.3).
The geometrical shape of the planar converging-diverging nozzle is provided by a pair of steel profiles mounted on the rear plate. By changing the profiles, different geometries can be mounted, so that different thermodynamic conditions can be explored. More detail on nozzle design and geometry is found in Section 3.6.

- The *Low Pressure Vessel* (*LPV*) is a 5.6 m^3 volume where the discharged expanded vapor is slowed down to rest (7 $\rightarrow$ 8), de-superheated and condensed (8 $\rightarrow$ 9) with isochoric processes. Points 7 and 8 change in time due to LPV filling and increase in pressure, although much more slowly than Point 6 (the *LPV* volume is six times larger than the *HPV*).
  No work extraction occurs in the test section, so all of the thermal energy supplied in the HPV needs to be removed in the LPV. This is done through a *Condensation System* consisting of a heat exchanger surrounding the vessel walls that de-superheats and condenses the vapor, and another heat exchanger in the hot well of the vessel (where the condensed liquid is stored) that cools the liquid. Both heat exchangers use diathermic oil, cooled by a water circuit with a cooling tower.
  Ball valve *V*4 separates the *LPV* from the test section during operations that require the latter disassembly (e.g. nozzle profiles or transducers substitution). A safety valve with 20 bar maximum design pressure is also installed and discharges in ambient air.
  The working fluid is stored here when the plant is not operating.

- The thermodynamic cycle and the piping circuit are completed by a metering pump that circulates the liquid from the *LPV* back to the *HPV* and compresses it to the initial *HPV*

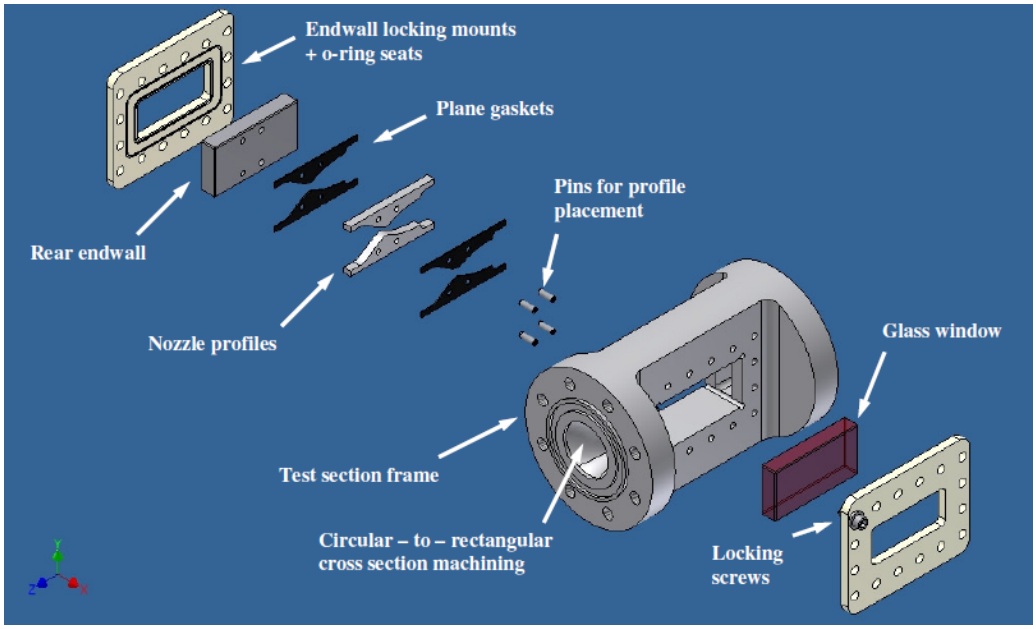

(a) Exploded view of test section components.

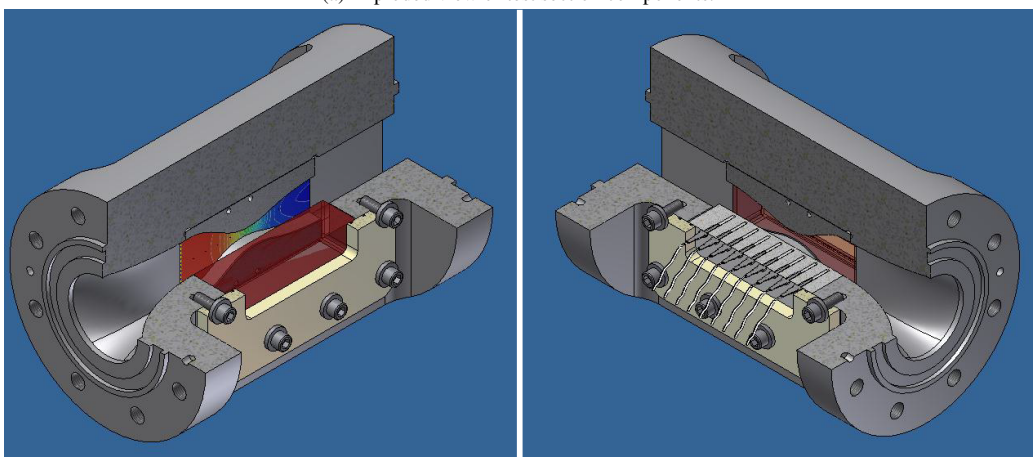

(b) Front (left) and back (right) 3D section view.

Figure 3.4. Test section arrangement.

pressure ($1 \rightarrow 2$).

- A by-pass circuit, parallel to valves *V3* and *MCV*, is operated by the *By-Pass Control Valve* (*BPCV*) and allows to discharge vapor into the *LPV* if excessive pressure is reached in the *HPV*.

- The plant includes a *Vacuum Pump* (*VP*) that can be connected to different parts of the *TROVA* through a valves system. Its maximum inlet operating conditions are 60 °C and 1.25 bar and it can reach a vacuum of a few mbar. It is used to evacuate the plant of all air prior to system filling with the working fluid and for air removal and uncondensables

deaeration during system operation. Indeed, dissolved gases in the working fluid may exit it during cooling and heating processes. It is used to vacuumize the *HPV* before the start of the heating process and remove air between valves *V3* and *V4* after test section disassembly. Moreover, the *LPV* is vacuumized down to ~ 50 mbar before test start to ensure longer test time in an under-expanded nozzle regime. A vacuum trap with a cross-flow heat exchanger is present just upstream of the vacuum pump to condensate and remove the plant working fluid diluted in nitrogen. This prevents it from entering the pump and mix with its oil, leading to lower viscosity and higher chances of pump failure. The vacuum circuit is colored in green in Figure 3.2.

- If the plant is not in operation, it is filled with inert nitrogen gas to a pressure slightly above the atmospheric one. This avoids air leakage into the plant, an undesirable situation considering the thermal decomposition catalyst effect of oxygen and water vapor in ambient air on siloxane fluids. An auxiliary *Nitrogen Plant* was purposely built after the first experimental campaigns with siloxane MDM highlighted a significant fluid decomposition with silica dioxide generation even though maximum operating temperatures were well below the known fluid thermal stability in clean conditions (Keulen et al., 2018). The auxiliary plant is constituted of a 0.8 m^3 nitrogen storage at 200 bar, distributed to several points of interest in the plant (*HPV, LPV* and Test Section) with dedicated lines and pressure reducers. The system also allows to fill the *HPV* to the desired pressure for ideal gas *TROVA* tests. It is also used for flow insemination in case the Laser Doppler Velocimetry (*LDV*) technique is implemented (Gallarini, 2020) or to flush pneumatic lines for probes testing as described in Section 6. The nitrogen gas circuit is colored in blue in Figure 3.2.

- Other auxiliary systems are the *Thermal Oil Circuit* and the *Water Circuit*, both part of the *Condensation System* in the *LPV*. The oil circuit (colored in brown in Figure 3.2) is used to cool down the superheated vapor in the *LPV* at the end of a test. It includes a centrifugal pump, a serpentine heat exchanger in the well where liquid organic fluid is found and a heat exchanger with the vapor phase at the external wall of the vessel. All of the heat is then discharged to the water circuit through a plate heat exchanger. The water circuit (purple in Figure 3.2) also gathers heat from the vacuum trap. With the use of a centrifugal pump, cooling water is circulated to a cooling tower to reject heat to ambient air.

A practical aspect of *TROVA* operation needs to be highlighted. The desired thermodynamic region in the vapor phase to be explored needs to be selected prior to the start of any test run. This determines the mass of fluid to be loaded in the *HPV* to reach the desired temperature T_{HPV} and pressure P_{HPV} at the end of the isochoric heating process. Experience over the years suggests, as best practice, to choose initial *HPV* conditions with at least a superheating of 10 °C to help prevent troublesome condensation in the plant during a test.
The amount of fluid to be transferred from the *LPV* to the *HPV* is monitored with a visual level meter. The conversion from geodetic height to fluid volume is possible with the use of a 3D CAD model of the *HPV*. The precision of the level meter is ~ 0.5 cm, which corresponds to ~ 0.2 dm^3 on the volume of fluid. Due to the manufacturing process, the real *HPV* volume is also slightly different with respect to the CAD one. All of this unfortunately introduces some uncertainties in the actual amount of fluid loaded in the *HPV*, meaning that conditions reached at the end of the heating process can be different with respect to the desired ones. The *BPCV* can be used to discharge pressure in the *HPV* without substantial temperature change.
Another key aspect that must be considered is that the actual total pressure and temperature in the *plenum* are not the same as P_{HPV} and T_{HPV} due to heat and pressure drops in pipes and valves towards the test section from the *HPV*. Moreover, the *MCV* has a ~ 2 s opening transient at the beginning of the test during which mass flow rate is discharged, proportionately to the nozzle throat

area. Useful data is acquired only after this transient, meaning that total conditions can differ significantly from the ones in the *HPV*, from ~ 0.5 to even ~ 5 bar.
It is therefore evident that, due to the nature of the plant, repeating tests at exactly the same conditions is not trivial. However, satisfactory repeatability can be achieved thanks to the plant management experience acquired at *CREA Lab* during past years of operation.

3.3 Measurement Techniques

3.3.1 Temperature Measurements

Thermocouples placed at the *plenum* axis are used to measure the total temperature at the inlet of the nozzle. Flow velocity is so low (~ 1 m/s) that a recovery factor equal to one is an acceptable approximation. One thermocouple of type K (*TCK*) with a hot junction diameter of 0.15 mm and one of type J (*TCJ*) with a hot junction diameter of 0.25 mm are employed after calibration in a thermostatic oven with a reference thermocouple, yielding an uncertainty of 1 °C. The thermocouples dynamic response was assessed to be fast enough so as not to require any signal reconstruction procedure from the measured temperature value, which is not constant in time due to the transient operation of the *TROVA*. Details can be found in Cammi (2019).

3.3.2 Pressure Measurements

Together with total temperature, total pressure is another fundamental quantity to characterize non-ideal nozzle flows. Total pressure P_t is measured with a static wall tap in the *plenum* because the kinetic head can be considered as negligible due to the low flow velocity. Static pressure P is instead measured through several wall taps drilled in the rear plate of the test section along the nozzle axis.
Both total and static pressures are measured with the use of miniaturized piezoresistive transducers with a sensing element 3.8 mm in diameter, directly flush mounted on the rear plate or *plenum*. This limits the spatial discretization of measures along the nozzle due transducers size with respect to a solution with long pneumatic lines exiting the plate from the back. However, this allows to limit the line-cavity pneumatic system to just two lines and a cavity, as shown in Figure 3.5, with an acceptable decrease in the frequency response compared to that of the simple sensor. The frequency response of transducers employed in the TROVA is in the range of $220 - 750\ kHz$, depending on their full-scales. Dynamic modeling of the complete line-cavity system and experimental testing (Antonini et al., 2008) have shown that it can correctly measure a signal with a frequency up to $200\ Hz$, a value that is more than appropriate for the present application since the energy content of the *TROVA* transient is well below 1 Hz.

The use of flush mounted transducers means that the whole pneumatic system is kept at the same temperature of the test section, thus avoiding condensation that would inevitably happen with long pneumatic lines. It would be very problematic due to possible measurement error linked to the presence of menisci at the vapor-liquid interface. Moreover, it would result in unacceptable measurement delay due to the *mass sink effect*, as extensively covered in Section 6.

Pressure sensors therefore face flows of siloxane vapors at high temperatures directly. For this reason, the employed transducers were specifically selected to have membranes resistant to silicone-based fluids and able to withstand a maximum operating temperature of 454 °C. Moreover, piezoresistive transducers are particularly sensitive to thermal effects because the electrical resistance is modified by the change in temperature of the sensor, leading to a non-negligible variation in both intercept and sensitivity of the calibration curve. This is accounted for by adding

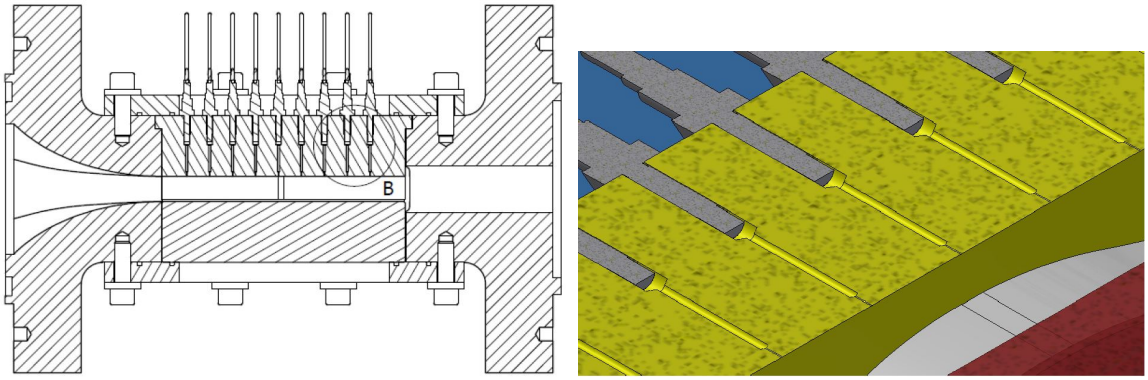

(a) Longitudinal section of the test section. Line-cavity system and transducers located at the rear plate.

(b) CAD detail of the test section and line-cavity system.

Figure 3.5. Test section and line-cavity system for flush-mounted transducers in the test section.

a compensation resistance to the voltage supply circuit of the Wheatstone bridge on the sensor. The voltage across the compensation resistance (V_T) exclusively depends on the current flowing through it, so on the temperature of the transducer but, unlike the output voltage $V_P = V_P(P,T)$, it is independent of the actual pressure. By exploiting this, transducers are calibrated in temperature as well as in pressure to ensure that thermal effects are considered when the voltage output is converted to a pressure reading. If temperature is constant, the relation between voltage output V_P and pressure P is linear: $P = mV_P + q$. The slope m and intercept q were experimentally verified to depend on the temperature voltage drop V_T through a second-order polynomial. Therefore, the calibration procedure no longer yields a curve, but its output is the surface described by:

$$P(V_P, V_T) = \underbrace{(a + bV_T + cV_T^2)}_{\text{m}} V_P + \underbrace{(d + eV_T + fV_T^2)}_{\text{q}} \tag{3.1}$$

The polynomial coefficients a, b, c, d, e and f are outputs of the complete calibration procedure. For each transducer, 21 pressure points equally spaced between atmospheric pressure and full scale were imposed, both with an increasing and decreasing step to account for possible hysteresis. This was repeated at five different temperatures from ambient temperature to 260 °C to cover the possible operating range during a test. In total, 105 sets of (V_P, V_T, P) points were obtained for a single transducer and were fitted with a least squares algorithm to obtain polynomial coefficients. The uncertainties in each one of the three quantities was propagated via an adaptive Monte Carlo method to calculate the uncertainty related to the pressure determined from Equation (3.1) during the measurement phase. Further details can be found in Cammi (2019).
The absolute pressure transducers employed in the present work are reported in Table 3.1 together with their uncertainties.

A previous thesis work (Tomasoni, 2013) highlighted that transducers calibration curves are affected by environmental conditions and by the various heating and cooling cycles of the plant. Fortunately, this only results in changes in coefficient d, so in a vertical shift of the calibration surface which can be easily corrected with an *on-line zero* procedure before each experimental run. A pressure transducer denominated *O175* with 1.75 bar full scale is connected to the plenum through a dedicated line and valves system which ensures that it always operates at room temperature - the only temperature at which it is therefore calibrated. The zero of this transducer is first performed by applying ambient pressure to it, measured with a high precision barometer. Transducer *O175* is

Model	full-scale FS $[bar]$	type	Uncertainty $[mbar]$	Uncertainty $[‰ FS]$
Kulite XTE	1.75	absolute	1.00	0.57
Kulite XTEH	3.5	absolute	13	3.71
Kulite XTEH	3.5	absolute	12	3.43
Kulite XTEH	7	absolute	7.58	1.08
Kulite XTEH	7	absolute	7.59	1.08
Kulite XTEH	7	absolute	7.82	1.12
Kulite XTEH	10	absolute	18.11	1.81
Kulite XTEH	14	absolute	17.76	1.27
Kulite XTEH	17	absolute	14.65	1.16
Kulite XTEH	21	absolute	23.47	1.12
Kulite XTEH	40	absolute	31.48	0.79

Table 3.1. Absolute pressure transducers employed in experimental campaigns on the *TROVA* with their uncertainties.

then put in communication with the plenum so that it can be used as a reference to acquire the zeros of all other transducers in the test section which cannot be put in direct communication with the ambient. Indeed, this procedure is carried out when the plant is at set point just prior to test start. The plant is sealed and subatmospheric conditions ($10 - 200$ mbar) are present in the test section. This on-line zero procedure introduces further uncertainties in the measurement chain which are accounted for in the final uncertainty of the pressure measurement by each transducer.

3.3.3 Schlieren Imaging

Visualization techniques were developed in order to extract qualitative and quantitative information in a non-intrusive way from often transparent fluid flows (Merzkirch, 1987). Methods can be grouped under three macro-categories:

- Fluid insemination with solid, liquid or gaseous tracers: information is gathered by tracking the particles flow, such as in Laser Doppler Velocimetry (*LDV*) and Particle Image Velocimetry (*PIV*). The *LDV* technique was successfully applied to non-ideal flows of siloxane MM during a previous Ph.D. thesis at *CREA Lab* (Gallarini, 2020);
- Visualizations of flows onto solid surfaces: oil or wool strings can be applied onto the body surface to highlight streamlines;
- Density-based techniques: light rays are deflected as they travel through a region with density changes, as in the case of compressible fluid flows, convective heat transfer, mixing, combustion and stratified flows. This effect is detected through appropriate optical apparatus and information on the flow field is extracted in the form of images of the occurring flow phenomena. The *schlieren*, *shadowgraph* and *interferometry* techniques all fall under this category, although each one is sensitive to a different aspect linked to density changes.

The optical technique here implemented is the density-based schlieren visualization method (Settles, 2001). It provides information on the whole flow field simultaneously and is therefore ideal to complement the discrete point-measurements provided by pressure transducers and thermocouples. Its main application is to provide qualitative information on flow structures such as shock waves and expansion fans. However, it was also employed in part of the present work to provide a direct quantitative measure of the flow Mach number.

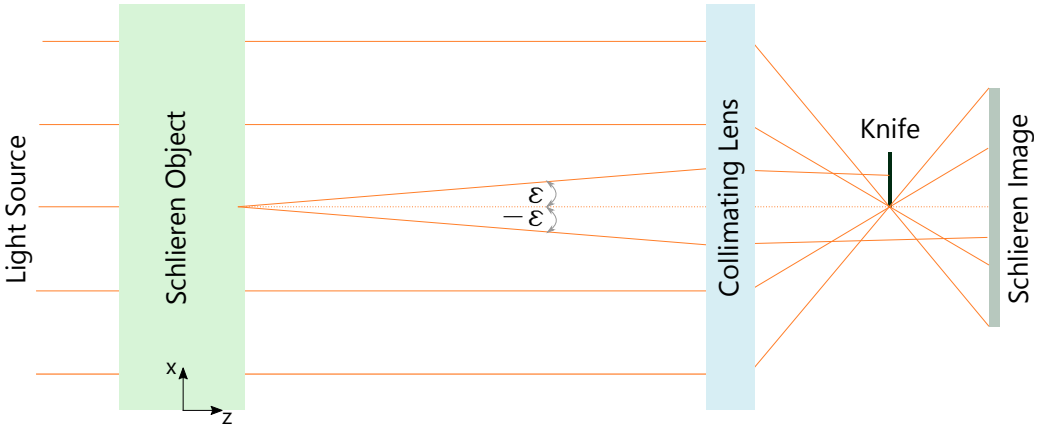

Figure 3.6. Illustration of the schlieren technique.

The schlieren technique exploits refractive index gradients due to spatial density gradients in order to visualize the latter in the flow. The *refractive Index n* is defined as the ratio between the speed of propagation of light radiation in a vacuum (a_0) to the speed of propagation of the same radiation in a generic transparent medium (a):

$$n(\rho, \lambda, medium) = \frac{a_0}{a} \tag{3.2}$$

This quantity is always greater than one and depends on density ρ, wavelength λ and medium. These relations are expressed in the Gladstone-Dale equation:

$$n = 1 + K\rho \tag{3.3}$$

where K is the substance and temperature-dependant Gladstone-Dale constant. The relation between density and refractive index gradients is evidenced by taking the derivatives of the above equation along direction x:

$$\frac{\partial n}{\partial x} = K\frac{\partial \rho}{\partial x} \tag{3.4}$$

It can be shown that light rays crossing a region where refractive index gradients are present along a certain direction x are subject to an angular deflection ϵ along the same direction that is proportional to the gradient:

$$\epsilon \propto \frac{\partial \rho}{\partial x} \tag{3.5}$$

The schlieren technique exploits exactly this aspect, as illustrated in Figure 3.6. Light rays from a light source pass through the test object where fluid flow is occurring, are subject to a deviation ϵ by density gradients in the flow field and finally impinge on a recording plane where the schlieren image is formed. Light rays deflected in one direction are selectively blocked by the knife edge, a key component of the optical system. They will not contribute to the schlieren image formation. Light rays deflected away from the knife edge instead reach the recording plane untouched by it. This will result in dark or bright regions at image positions corresponding to flow gradients responsible for rays deviation towards or away from the knife. The technique is sensitive to gradients perpendicular to the knife edge.

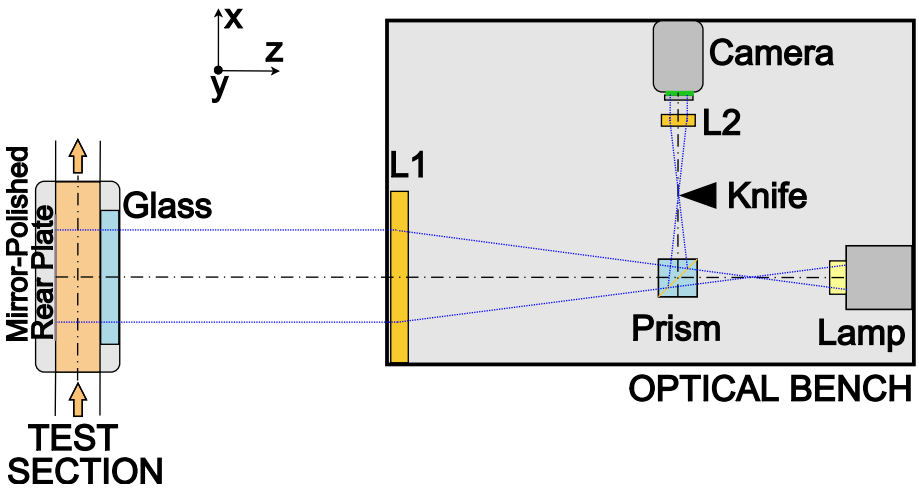

Figure 3.7. Optical bench used in the TROVA for schlieren visualizations.

Component	Characteristics
Light Source	Mercury vapors lamp, 100 W
	LED, 630 – 1120 mA, λ_{peak} = 460 nm
Camera	High-speed IDS uEye CP, CMOS 1936x1216 px
Lens L1	$f_1 = 1000\ mm$, $d_1 = 150\ mm$
Lens L2	$f_2 = 50\ mm$, $d_2 = 52\ mm$
	$f_2 = 75\ mm$, $d_2 = 52\ mm$
	$f_2 = 100\ mm$, $d_2 = 52\ mm$

Table 3.2. Main characteristics of the optical bench components. f is the focal length and d is the diameter of each lens. Lens L2 focal length can be varied from 50 to 100 mm.

TROVA Schlieren Bench

The optical bench for schlieren visualizations used in this work is schematized in Figure 3.7.

White light rays from the light source (a 100 W mercury vapor lamp or a LED) are collimated by a bi-convex lens (L1) and enter the test section perpendicularly to it. They are deflected by density gradients in the fluid flow and are reflected by the mirror-polished rear steel plate. The reflected beams cross the test section again and are focused by lens L1 (which therefore also constitutes the so-called schlieren head) at the knife edge, after a 90° rotation operated by a beam splitter cube. The schlieren image is then formed onto the sensor of a high-speed CMOS camera by a second lens (L2). The schlieren system used in this work thus employs a double-passage configuration. The limited available space at the back of the test section does not allow for a single-passage system. Also, the latter configuration would have required a second optical access in place of the steel rear plate of the test section, leading to a complicated configuration to accommodate pressure taps and nozzle profiles. Moreover, the double-passage configuration means that all optical components can be placed on a single optical bench, making system alignment (performed with a laser point light source) much more simple.
The most important characteristics of the optical bench components are summarized in Table 3.2.

The knife blocks the refracted rays that have a component perpendicular to its edge. Therefore, in order to visualize the horizontal density gradients (along the nozzle axis), the knife is set in the vertical direction. The exact 'aperture' position of the knife is set so as to ensure that density gradients are visualized with a satisfactory contrast. The position of the knife is such that positive density gradients (compressions and shock waves) appear dark whilst negative density gradients (expansions and expansion fans) appear bright.
The camera acquisition frame rate is set as the maximum one allowed by computer performance ($10 - 40\ fps$). The exposure time is a tradeoff between various aspects. A lower exposure time leads to higher definition images but also to overall darker images. The latter aspect can also be manipulated through the regulation of the light source. Therefore, exposure time and the mercury vapor lamp or LED were regulated so as to ensure high quality image and an appropriate brightness level. Indeed, the initial brightness level must ensure that no image saturation occurs during the test. Density gradients in the fluid flow cause an increase or a decrease in the brightness level in certain portions of the image: if the initial brightness level is too high, information loss occurs, because parts of the sensor may immediately become saturated and insensitive to stronger density gradients. Exposure time of about 1 ms was employed in the present experimental campaigns.

Application to Non-Ideal Flows

Schlieren visualizations of non-ideal nozzle flows of dense vapors present some measurement issues, as documented in Conti et al. (2017) for siloxane MDM and as verified for siloxane MM too in later experimental campaigns. Portions of the schlieren image expected to appear bright due to negative density gradients (expansion), were dark instead. This was attributed to the strong density gradients occurring in these non-ideal flows, causing refractions intense enough to deflect light onto some system aperture stop. Interestingly, these issues were found to decrease as the non-ideality of the flow decreased. Moreover, when the same nozzle geometry was used for analogous testing with air, these measuring-range issues were absent or noticeably reduced.
For an isentropic process (like the flow at the nozzle axis) the refractive index gradient can be conveniently rewritten highlighting compressibility ($1/c^2$) and pressure ratio along the nozzle (where P and P_T are static and total pressure, respectively) as:

$$\frac{\partial n}{\partial x} = K \frac{1}{c^2} P_T \frac{\partial (P/P_T)}{\partial x} \tag{3.6}$$

This equation clearly highlights the role of each quantity in determining the extent of light rays deflection and thus the intensity of measuring range issues. Total conditions are the most important variable in the value of the refractive index gradient when flows of the same fluid with different degrees of non-ideality are compared. Their direct impact is evident from Equation (3.6) but they also act indirectly by determining the extent of non-ideal gas effects and thus the value of compressibility. A more marked non-ideality results in stronger measuring range issues. When air and siloxane flows are compared, the very different value of compressibility (both due to molecular mass and non-ideal gas effects) and of the Gladstone-Dale constant determine a higher refractive index gradient for the latter, and thus, more intense measuring range issues.

Mach Number Measurement

The schlieren technique is usually employed as a useful qualitative support to other flow measurements. In this work, however, schlieren images are also quantitatively exploited to directly and independently measure the Mach number along the nozzle axis without the use of any thermodynamic model or hypothesis.
Peaks and troughs due to the surface roughness of nozzle profiles cause infinitely weak expansion

and compression waves in supersonic flow known as *Mach waves*. These are visible in schlieren images of the diverging portion of the nozzle as thin dark or bright lines and are especially evident in case of a rough surface finish of the profiles. At the axis of the nozzle the flow can reasonably be assumed as parallel to it due to symmetry. The slope of the Mach lines to the x-direction (μ) is therefore also their slope with respect to the flow, and is thus a direct measure of the Mach number M:

$$M = \frac{1}{\sin \mu} \tag{3.7}$$

An automated algorithm was implemented to identify Mach lines at the nozzle axis and measure their angle with respect to it. The schlieren image is divided into smaller sub-images which are enhanced to sharpen the Mach lines edges and converted to black and white from gray scale. The Hough tranform is applied to detect the set of lines lying in the black region corresponding to the Mach line and the best approximating line is chosen. The associated uncertainty on the Mach number is computed using the Taylor series method. Full details on the algorithm and its application to Mach lines, shock waves and expansion fans edges recognition can be found in Cammi (2019) and Cammi et al. (2021).

3.4 Test Description and Data Processing

All *TROVA* test runs share a similar time evolution, illustrated in Figures 3.8 and 3.9 for an exemplary test with siloxane MM. Once the *HPV* has reached the desired temperature and pressure and the *LPV* has been vacuumized, the test is operated via a dedicated *Labview*® routine. At instant $t = 0\ s$, two signals trigger the opening of valve *V3* and the recording of the schlieren images, so that the latter are synchronized with all other pressure and temperature measurements. Once *V3* is completely open, the *MCV* starts opening. After a short transient due to its opening time, the maximum pressure and the most non-ideal conditions are reached at each pressure tap. This is also when the lowest value of the compressibility factor evaluated at total conditions Z_T is recorded. Due to the blow down nature of the test and the absence of regulation on the *MCV*, total conditions change in time. Their evolution is shown in $P - T$ and $T - s$ diagrams in Figure 3.8. Static pressure at each tap continuously decreases in time as the *HPV* empties and conditions become more ideal with an increasing Z_T. Consistently with the expansion occurring in the nozzle, the pressure decreases from one tap to the next one along the x-axis at each moment in time. This can be seen in Figure 3.8c, where the spatial coordinate of each pressure tap is made explicit in the third dimension and in Figure 3.9a in which the spatial nozzle coordinate is instead implicit. The plot also shows total temperature, which instead does not decrease monotonically. This is reasonably due to a non-uniform temperature distribution inside the *HPV* at the beginning of the test, to heat exchange with piping from the *HPV* to the *plenum* and to heat radiation from *plenum* walls.

Due to the large pressure ratio between high and low pressure reservoirs, the nozzle operates in the under-expanded flow regime for most of the time. As the test proceeds, the *HPV* empties while the *LPV* fills, and nozzle operation shifts to adapted and then over-expanded regimes until the flow is unchoked and eventually stops. Shocks entering the nozzle divergent are detected from spikes at pressure taps and from schlieren images. The test ends with the closure of valves *V3* and *MCV* when pressure variation is no longer significant as equilibrium between *HPV* and *LPV* pressures is reached.

The data set from a *TROVA* test has an intrinsic time evolution, whilst nozzle flow is naturally analyzed according to its spatial coordinate along the axis, as indicated in Figure 3.8c. Cutting planes indicate selected time instants during a test at which pressure (and all other variables) are extracted, so as to show their trend along the x-coordinate of the nozzle axis as reported in Figure 3.9b. Se-

lected time instants are also reported in Figures 3.8b and 3.9a. As previously mentioned, each time instant can be considered as a steady nozzle flow. Meaningful extracted time instants typically correspond to different values of the total compressibility factor Z_T, so to different levels of non-ideality.

Data is acquired at a frequency of 1000 Hz and is then averaged in packages of 100 data points, giving an overall time resolution 0.1 s. This ensures a smoother signal by reducing disturbance but no information loss occurs because pressure decrease due to *HPV* emptying varies at a much lower frequency ($\sim$ 1 Hz).
All thermodynamic quantities at each averaged instant in time at each pressure tap (subscript i) at the nozzle axis can be calculated from total pressure P_t, total temperature T_t and static pressure P_i thanks to the hypothesis of isentropic flow. The latter is reasonable because the nozzle is designed to exhibit a large isentropic core (Section 3.6) and considered operating conditions are always in the under-expanded regime. Test data is discarded when shocks start entering the divergent. As better detailed in Appendix A, the Helmoltz energy-based thermodynamic model with Span-Wagner functional form embedded in the *FluidProp* library is employed here for experimental data post processing.

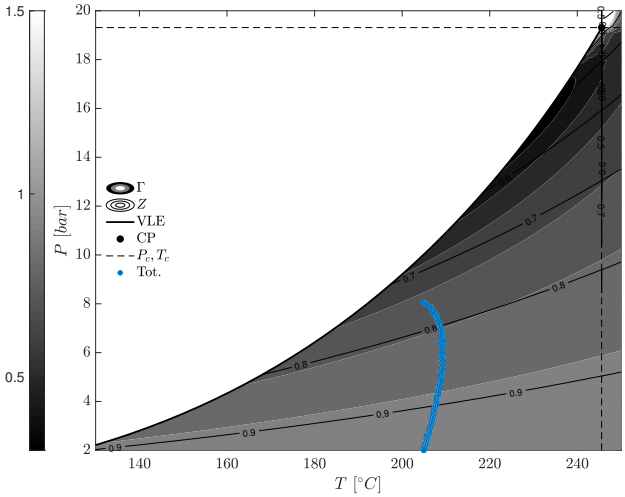

(a) Total conditions (*Tot.*) evolution during a test.

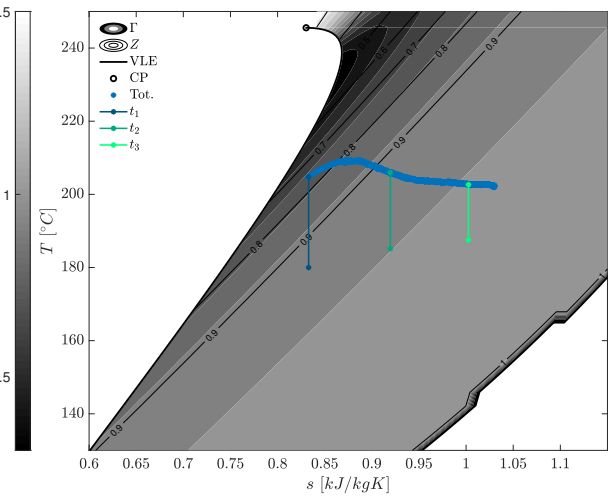

(b) Total conditions (*Tot.*) evolution during a test. Expansions at three selected time instants consistent with Figure 3.8c are also highlighted.

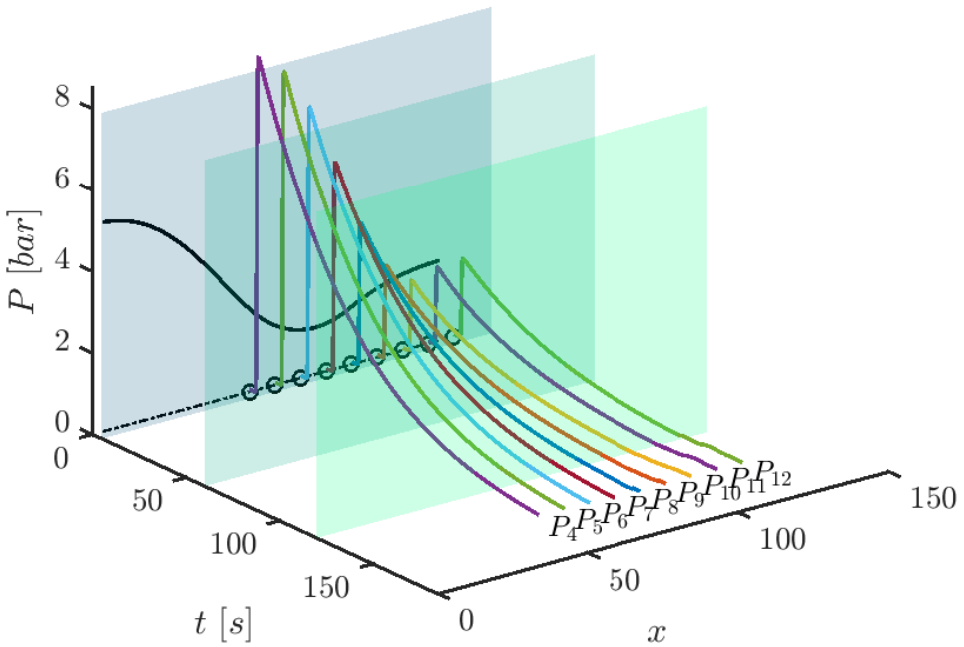

(c) 3D plot of test results. The spatial coordinate is explicit: each curve shows the pressure trend at a pressure tap along the nozzle (pressure taps before $n°4$ are not shown because no pressure transducers were mounted there for this test). Cutting planes indicate three selected time instants t_1, t_2, t_3 at which data is extracted.

Figure 3.8. Time evolution of a representative *TROVA* test with siloxane MM.

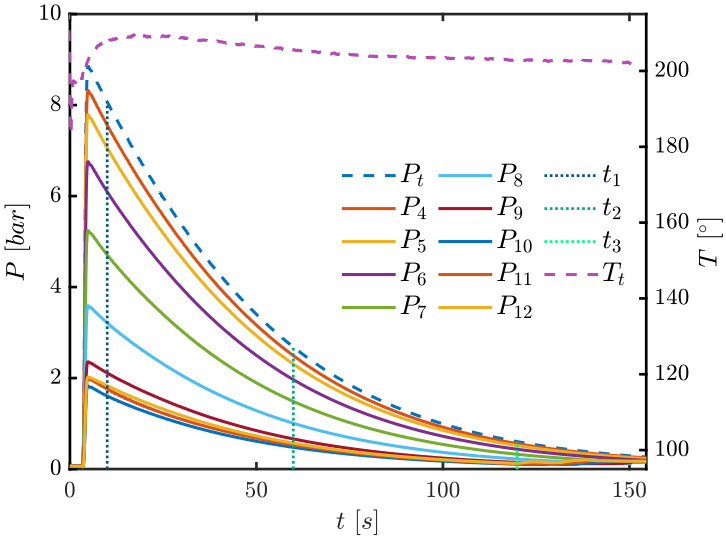

(a) Time evolution of pressure and total temperature signals. The three selected time instants consistent with Figure 3.8c are also reported.

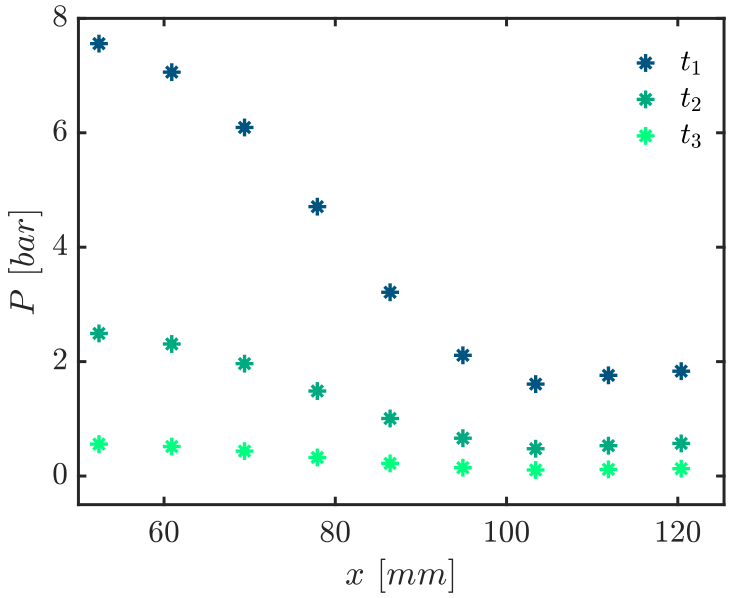

(b) Pressure along the nozzle axis for three selected time instants consistent with Figure 3.8c.

Figure 3.9. Example of typical *TROVA* test results with siloxane MM.

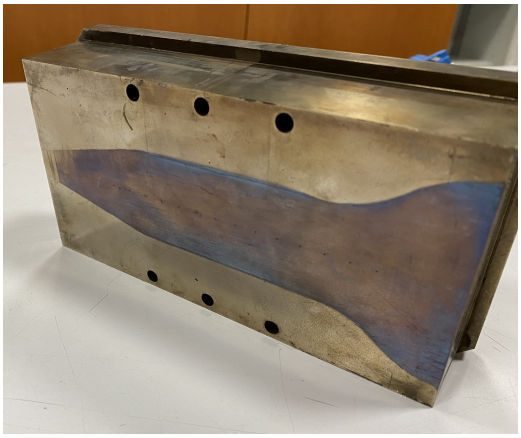

(a) Front of the plate. Pressure taps are visible as very small holes on the nozzle axis. Although no nozzle is mounted, its shape is still visible due to a different bluing linked to heating.

(b) Back of the plate with the characteristic triangular shape where transducers are mounted.

Figure 3.10. *JLo* rear plate.

3.5 Rear Plates

Three different rear plates were employed in the experimental campaigns considered here.
The *JLo* rear plate (Figure 3.10) is characterized by a peculiar triangular back section that allows to flush mount sixteen pressure transducers. Pressure taps have a diameter of 0.3 mm and are separated by a distance of 8.5 mm.

The *Pitot* rear plate is shown in Figure 3.11. It was designed and manufactured within the frame of the present work in order to accommodate pressure probes in the test section of the *TROVA*. The plate features four static pressure taps with a diameter of 0.3 *mm* and a hole with a diameter large enough to fit the stems of Pitot tubes considered here. The hole is located on the nozzle axis at 105 *mm* from the inlet, in the constant cross section region of the nozzles employed with this plate, as better explained in Section 3.6.
The probe support and alignment arm (visible in Figure 3.11) allows the manual regulation of the probe along the depth of the test section and ensures its alignment with the flow.
Static pressure taps 1 and 2 are located at 26 *mm* and 60 *mm* from the inlet, respectively. Tap 3 is in correspondence of the probe total pressure hole (79.6 mm from the inlet), tap 4 is in correspondence of the probe static pressure ring (92.3 mm from the inlet). Taps 2, 3 and 4 are all located in the constant cross section region of the employed nozzles (Section 3.6). Taps 3 and 4 have a spacing of 12.6 *mm* that does not allow the installation of flush mounted transducers like at the other taps. To overcome this problem, two Inox tubes with an outer diameter of 3 *mm* and length of 200 *mm* were welded onto the pressure taps holes to allow transducers installation at their end.
This experimental set-up does not allow probe rotation, which was a conscientious design choice for a number of reasons. First of all, Pitot tubes considered here are meant to work at close-to-zero incidence with the flow. They exhibit a certain angular insensitivity which conveniently eliminates the need for probe rotation to look for perfect flow alignment. In any case, due to the blow-down nature of the *TROVA*, probe movimentation is not even feasible during a test run. Rotation would only be possible before a test and only in the plane parallel to front and back test section walls, due to the planar configuration. Lastly, a design configuration allowing for probe movimentation would have resulted in a much more complicated and expensive system, with probable sealing issues.

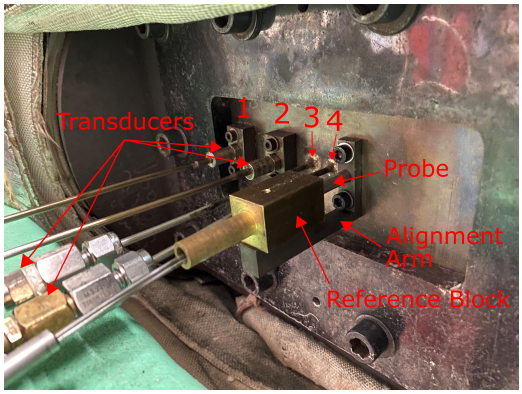

(a) Back of the plate, mounted on the test section. Pressure taps with mounted transducers and alignment arm are visible.

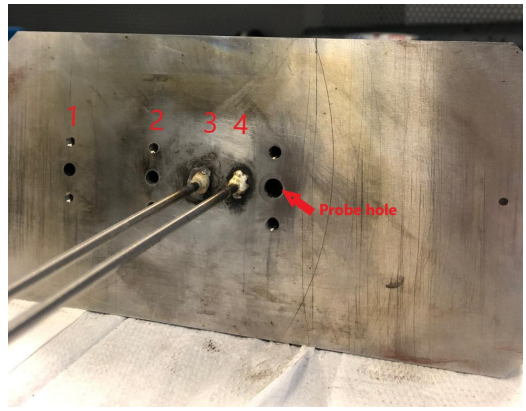

(b) Back of the plate.

Figure 3.11. *Pitot* rear plate.

With the present design, probe and flow alignment are ensured with the use of a simple alignment arm acting as probe support system, which was designed and produced together with the plate.

The *Wedge* rear plate (Figure 3.12) was designed together with the *nMDMwedge* nozzle (Section 3.6) to investigate non-ideal oblique shock waves on a diamond-shaped airfoil, as documented in Zocca et al. (2019). A removable shaft is located at the end of the plate in order to insert the aerodynamic profile in the flow. In the present case, a new shaft and and alignment arm were designed so as to instead accommodate Pitot tubes in the first ever experimental campaigns for direct pressure loss measurements across oblique shocks in non-ideal supersonic flows of siloxane MM (Section 8). The plate features six static pressure taps with a diameter of 0.3 *mm*, the last of which provides the so-called *free-stream* pressure before the shock (P_{fs}).

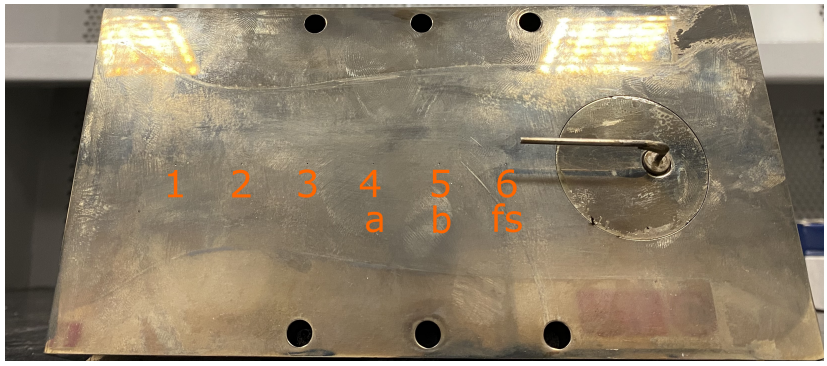

Figure 3.12. Front view of the *Wedge* rear plate with a Pitot tube mounted at its end. Only the three pressure taps indicated as *a,b,fs* were employed in experimental campaigns presented here. The last tap (fs) measures the *free-stream* pressure before the shock.

All rear plates are mirror-finished to allow the use of the double-passage schlieren configuration. However, as the images show, plant heating cycles are responsible for their bluing, which unfortunately deteriorates the quality of schlieren images. Rear plates are therefore periodically re-machined to achieve the necessary mirror quality finish.

3.6 Nozzles

Several different planar converging-diverging nozzles are employed in the present work. They are characterized by different size, exit Mach number, target fluid and design operating conditions, but they have all been designed according to the same procedure. Nozzle depth is imposed by the test section to 18.7 mm for all.
In the design process, viscous and thermal boundary layers are assumed to have a negligible thickness with respect to the nozzle height, so effects of viscosity and thermal conductivity are neglected. Under the above assumptions, the flow is described by the potential equation for irrotational compressible flows (Zucrow and Hoffman, 1977). The convergent section of the nozzle is designed using a fifth order polynomial, yielding a double concavity that provides gentle flow acceleration up to the throat H and reduces flow disuniformities. First and second derivatives are set equal to the diverging section ones at the throat. The diverging portion shape is determined through the *method of characteristics* (*MOC*), implemented according to Zucrow and Hoffman (1977) and coupled with a suitable thermodynamic model for non-ideal gases (see Guardone et al. (2013)). To provide the initial data curve for the *MOC*, transonic flow at the nozzle throat is computed by solving the transonic potential equation (Sauer, 1947). The expansion through the diverging section to the desired exit pressure is achieved through an initial circular profile, followed by the so-called *turning region*, in which the nozzle wall geometry is determined by imposing mass conservation at each cross section. Here, acceleration at the nozzle axis has ended and the flow in the rest of the cross section is simply made uniform and parallel to the axis.
This method yields coordinate points of the nozzle profile that are dimensionless with respect to the semi-height of the throat. The actual dimensional coordinates thus depend on the latter parameter, which is chosen by considering the following factors:

- the throat semi-height determines the throat cross sectional area A_t. This parameter must be larger than the minimum throat area avoiding blockage effects if a pressure probe or other components were to be inserted in the flow (Spinelli et al., 2013);
- the throat area determines the discharged mass flow rate, which in turn determines the pressure decrease from *HPV* to initial plenum total conditions due to the *MCV* opening transient and the duration of the experimental run. The semi-height must lead to an acceptable initial total pressure and to a reasonable test time (of the order of several seconds or a few minutes);
- the semi-height must lead to dimensional x- and y- coordinates that fit within the test section.

The nozzle flow resulting from the described procedure is characterized by a uniform Mach number and a velocity parallel to the nozzle axis at the exit section.
Due to the non-ideal nature of the considered flows, the resulting nozzle shape depends on total conditions and not only on the desired Mach number as in the case of a polytropic ideal gas. Therefore, each nozzle was designed for specific design total conditions but, due to the batch nature of the *TROVA*, it was tested in a wide range of operating conditions. Several nozzles were also tested with fluids different with respect to the design one, such as nitrogen instead of siloxane MM or siloxane MM instead of MDM.

Nozzle *nMM16* (Figure 3.13) was designed to achieve an exit Mach number $M = 1.6$ with siloxane MM, hence the name. It features a relatively small throat area, ensuring a low pressure loss during the *MCV* opening transient so that high total pressures and strongly non-ideal conditions can be achieved. It was therefore employed, together with rear plate *JLo*, to experimentally investigate non-ideal expansions with total conditions covering a relatively large range in the vapor phase of siloxane MM, even in supercritical conditions (Section 4). Its design conditions and geometrical characteristics are reported in Table 3.3.

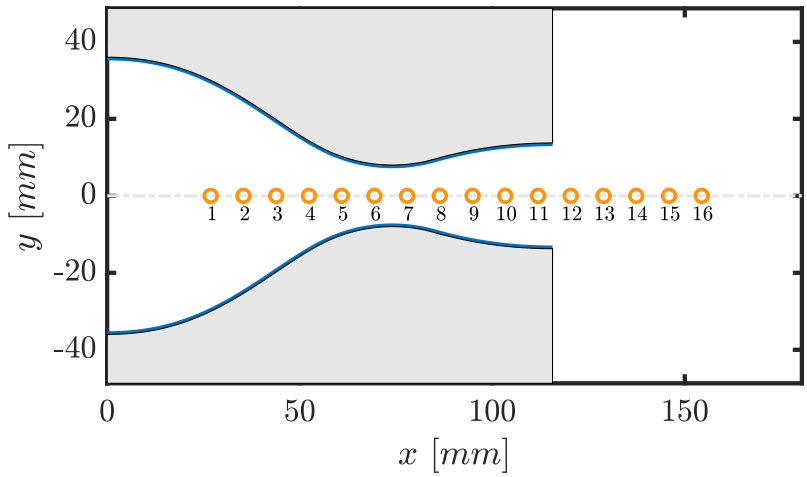

Figure 3.13. Schematic plot of nozzle *nMM16*. Pressure taps corresponding to those available on rear plate *JLo* are also shown.

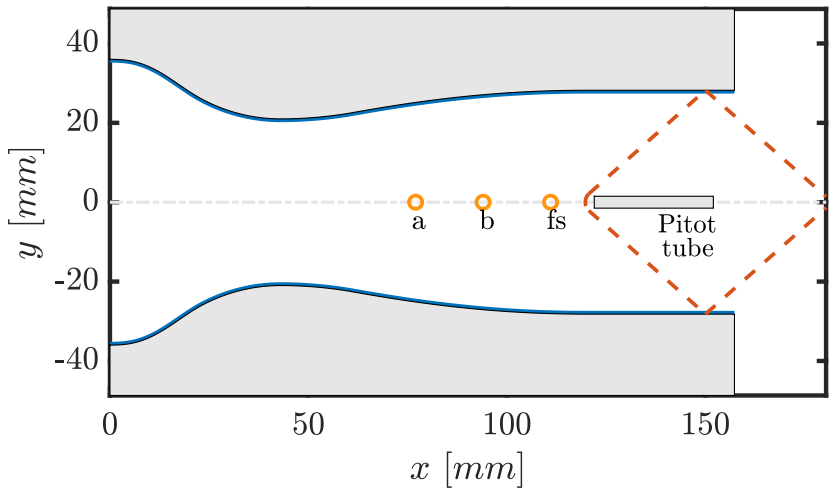

Figure 3.14. Nozzle *nMDMwedge* with pressure taps on the *Wedge* rear plate and Pitot tube. The expected bow shock in front of the latter is also sketched.

Nozzle *nMDMwedge* was designed to produce a uniform Mach number in the *turning region* (which includes the free-stream tap) of $M = 1.5$ with siloxane MDM, but it is used with MM in the experimental campaigns here presented. As previously mentioned, it was designed to investigate non-ideal oblique shock waves on a diamond shaped airfoil. It therefore features a discharge section with a constant-area where the aerodynamic profile can be placed. The nozzle throat is very large because the whole geometry is scaled so as to avoid blockage effects due to the airfoil presence. As a consequence, the pressure loss from the *HPV* to the plenum during the *MCV* opening transient is very large and can even reach ~ 4 bar. The nozzle design conditions and geometrical characteristics can also be found in Table 3.3.
As aforementioned, the airofoil is here substituted by a Pitot tube. The probe tip is placed in the uniform flow-region, as plotted in Figure 3.14.

Choked converging nozzles are also used in the present work to investigate non-ideal subsonic flows of siloxane MM and as a test section for Pitot tubes in view of future pressure probes calibration. These planar choked converging nozzles are characterized by a portion with constant cross-sectional area yielding design Mach numbers of 0.2, 0.5 and 0.7. For this reason, they were also exploited to test the Laser Doppler Velocimetry system in a region with limited velocity gradients during a past Ph.D. thesis (Gallarini, 2020). Nozzles are named according to their design Mach number as $cMM02$, $cMM05$ and $cMM07$, as represented in Figure 3.15. Like converging-diverging nozzles, their depth is imposed by the test section to 18.7 mm. The first convergent section of the nozzle is again designed using a fifth-order polynomial, with a double concavity and smooth acceleration up to the design Mach number. This portion and the constant cross-section one (semi-height $h = 19$ mm) are the same for all nozzles at different Mach numbers. The second convergent is a line of constant slope that ends with the throat, which is always choked due to the very low pressure in the *LPV*. The slope is the same for all Mach numbers but the length is such that the area ratio A^*/A between throat A^* and constant cross-section A corresponds to the desired Mach number for siloxane MM at total design conditions $P_t = 5$ bar and $T_t = 210\,°C$. Geometrical dimensions are reported in Table 3.3.
Choked convergent nozzles were tested with rear plate *JLo* during experimental campaigns to characterize subsonic nozzle flows (Section 5) and during the initial commissioning phase of pressure probes pneumatic lines (Section 6). They were instead mounted on the *Pitot* rear plate during Pitot tubes testing in subsonic flows of siloxane MM (Section 7). Figure 3.15 shows both configurations. The probe hole in the *Pitot* rear plate is located in the constant cross section region and sufficiently distant from both the first and second convergents in order to make sure that the probe tip lays in a position where the flow properties are reasonably uniform. The hole distance from the inlet was determined with the help of CFD simulations (Section 5.2.2).

A chocked nozzle configuration instead of a more conventional converging nozzle is the only possible option to consistently reproduce subsonic flows in the *TROVA*. Due to its blow-down nature, upstream nozzle pressure decreases and downstream ambient pressure increases during a single test. Very limited control on the pressure ratio across the nozzle is possible, making a simple convergent unable to maintain a chosen flow Mach number. Moreover, the upstream pressure is of several *bar* at the beginning of a test. The downstream ambient is vacuumized to few *mbar* and its pressure does not increase much during a test due to its very large volume. This means that pressure ratio between upstream and downstream ambients is much larger than the critical one, so the flow will be choked in the minimum area section of the plant. Pipes are several meters long before and after the test section and include various valves, and it is thus impossible to know where choking would occur and what the actual sonic area is. As a consequence, actual A^*/A in the nozzle would be unknown and the Mach number would be unpredictable. On the opposite, a throat at the nozzle exit ensures that the sonic section is fixed and that known Mach numbers are found in the nozzle.
Another peculiarity of these nozzles is their long section with constant cross-sectional area. Probe insertion in this portion will allow future calibration of pressure probes with flows of organic vapours at constant Mach number but varying levels of non-ideality and Reynolds number. In reality, due to non-ideal dependence on stagnation conditions, the Mach number varies slightly as P_T, T_T differ from design ones.

3.7 Pressure Probes

For reasons illustrated in the introduction, Pitot tubes are the probes of choice in the present work. A Pitot tube is a simple and relatively inexpensive instrument for fluid velocity measurement. It

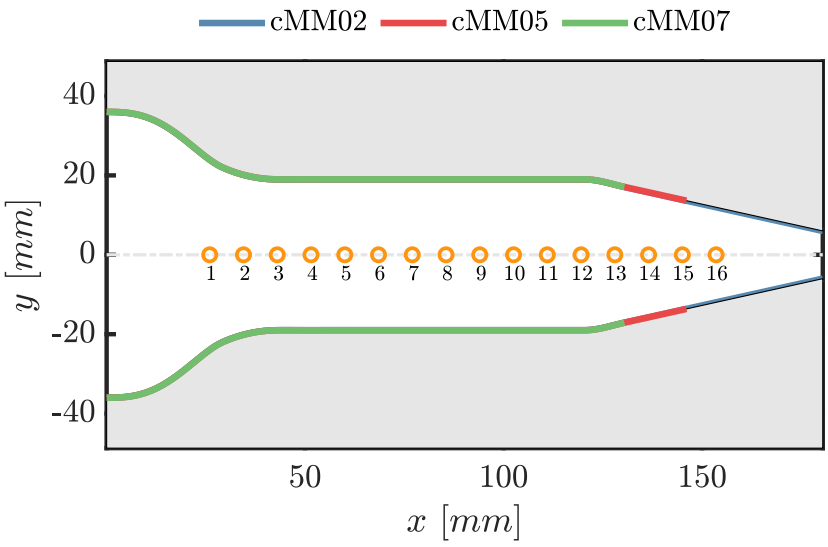

(a) Configuration with *JLo* rear plate.

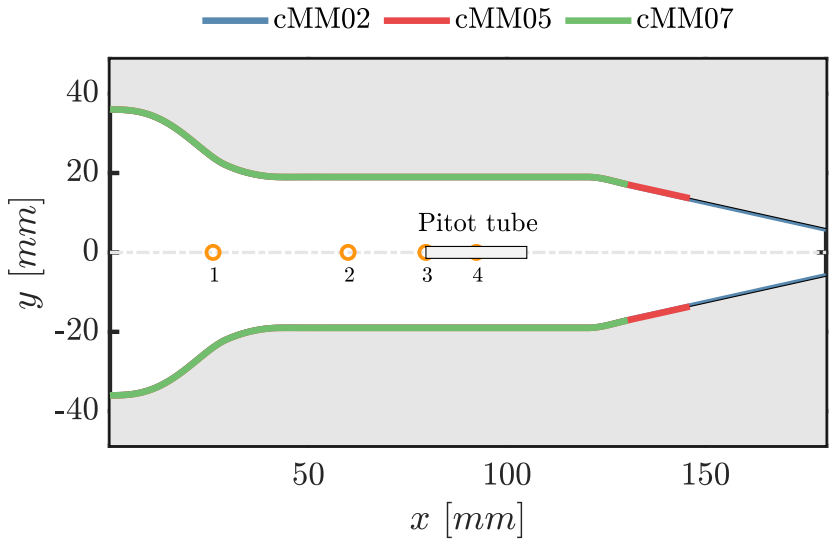

(b) Configuration with *Pitot* rear plate and Pitot tube.

Figure 3.15. Choked converging nozzles for three different Mach numbers $M = 0.2, 0.5, 0.7$ in the constant cross section part.

was invented by the French engineer Henry Pitot in 1732 but many improvements in its design were brought by Henry Darcy in the 19^{th} century, who was able to create the first working Pitot tube probe (Brown, 2001). Darcy's contribution was so relevant that his design for the instrument tip is still in use today. Nowadays, many other instruments for fluid dynamics applications are available. However, Pitot tubes are still largely used in many fields, such as in aircraft speed measurement and in power generation plants, thanks to their simplicity and reliability. As previously mentioned, they are still not widely employed in organic Rankine cycle plants due to difficulties linked to operating with non-ideal flows. Part of the objectives of the present work are indeed to begin testing of Pitot

Name	H_{th} $[mm]$	H_{in} $[mm]$	H_{out} $[mm]$	x_{out} $[mm]$	Fluid	P_t $[bar]$	T_t $[°C]$	M
nMM16	8.0	36	13.7	115.7	MM	21.4	254	1.6
nMDMwedge	21.0	36	28.2	157.3	MDM	10	277	1.5
cMM02	6.0	36	6.00	180.4	MM	5	210	0.2
cMM05	13.6	36	13.6	146.0	MM	5	210	0.5
cMM07	17.1	36	17.1	130.4	MM	5	210	0.7

Table 3.3. Nozzle semi-height at the throat, inlet and outlet and x-coordinate of the outlet section together with design fluid, total conditions and Mach number. The design Mach number is at the exit section for converging-diverging nozzles and at the constant cross-section region for choked converging ones.

tubes in such flows to allow flow velocity, mass flow rate and turbine performance measurements in *ORCs*.

The term *Pitot tube* actually encompasses different types of probes. A *simple* Pitot tube is a really only a total pressure probe, with a front pressure tap devoted to the measure of the flow total pressure. A *static* Pitot tube instead has pressure taps perpendicular to the flow direction that measure its static pressure. A *total-static* Pitot tube is a combination of the two instruments above, as illustrated in Figure 3.16. Total pressure P_t is measured by a pressure port located on the tip of the probe. Static pressure P is instead detected by the static ports, which are holes disposed perpendicularly to the flow velocity direction on a ring around the probe head. Pressure values are measured by pressure transducers installed at the end of the probe lines.

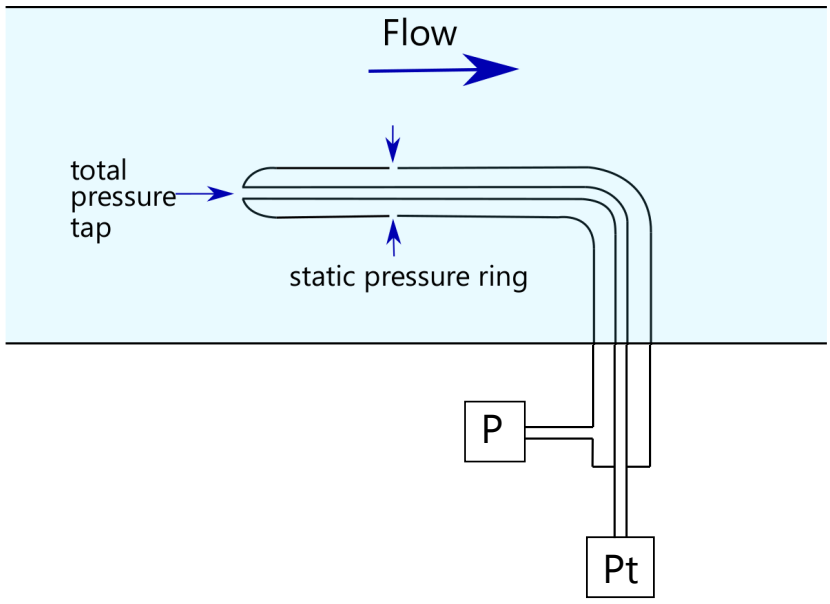

Figure 3.16. Schematization of a total-static Pitot Tube.

The difference $P_t - P$ between total and static pressures gives the kinetic head which, for incompressible flow, is directly related to the flow velocity through the value of density (Bernoulli's equation). If the subsonic flow velocity is high enough for significant compressibility effects, isentropic flow equations can be used to determine the flow conditions, since flow stop at the probe tip does not introduce total pressure losses. In case of an ideal gas flow, the pressure ratio

P/P_t between measured total and static pitot pressures can be used to directly determine the flow Mach number and temperature ratio through the explicit ideal gas isentropic flow relations. In order to calculate flow velocity, a total temperature measure is also required. If a non-ideal gas is considered instead, total temperature coupled with a suitable thermodynamic model is required to determine the flow Mach number too, due to the non-ideal dependence of isentropic expansions on total conditions (extensively covered in Section 2 from a theoretical point of view).
For high-subsonic operating regimes, calibration of Pitot tubes is suggested (Standard, 2008). In case of supersonic flow, a detached bow shock occurs at the tip and calibration is definitely needed to account for shock total pressure losses and determine the undisturbed flow conditions.

Geometrical characteristics that Pitot tubes should meet for accurate measurements are normed in ISO standards (Standard, 2008). The most important ones are that static-pressure holes shall not be larger than 1.6 mm, be at least six and placed not less than $6d$ from the tip of the nose and $8d$ from the axis of the stem, where d is the probe head diameter. If the static ring is too close to the probe tip, the measurement can be affected by flow overspeed around it, leading to a lower static pressure with respect to the undisturbed flow one. If the static ring is instead too close to the probe stem, the measurement can be affected by flow stagnation around it, resulting in a larger measured static pressure than the free-stream one. The best static ring position on the probe head is therefore where the two effects have subsided or compensate each other (Arts et al., 2001). The junction between the head and stem shall be either mitred or curved to a mean radius equal to $(3 \pm 0.5)d$. Finally, an alignment arm shall be fitted to the end of the stem away from the head, to ensure precise alignment and positioning within a conduit.

Three different L-shaped Pitot tubes were employed in the present work, featuring substantial differences in material, fabrication process, shape and pressure taps geometries. They are explained next. All probes feature a small probe tip size ($\sim$ 1.5 mm in outer diameter) in order to avoid blockage effects in the relatively small *TROVA* test section. For each probe, a brass reference block was purposely manufactured to be mounted on the probe and on the alignment arm as part of the probe support system to ensure alignment with the flow.

3.7.1 Aeroprobe Total - Static Pitot Tube

The Pitot tube most extensively used in this work was manufactured by company *Aeroprobe®*. It is identified with the acronym *AP* in the present work and is shown in Figure 3.17. It is a total-static Pitot tube manufactured in Inconel 718 out of two concentric tubes welded together. The inner tube starts from the tip of the probe with a pressure tap 0.6 *mm* in diameter, and is therefore devoted to total pressure measurement. The outer tube is used to measure static pressure and features six taps with a diameter of 0.25 *mm*, evenly angularly spaced around the *static ring* on the probe head at a distance of 12.7 mm from the tip. The six pressure taps are short-circuited in the circular sector between the two tubes, so the static pressure measured by the probe is the mean of those detected by all taps.
The alignment between the reference block and the probe tip is ensured by a flat machined on the stem.

3.7.2 Vectoflow Total - Static Pitot Tube

The second total-static Pitot tube employed in this work was manufactured by company *Vectoflow®* by 3D printing of AISI316 Stainless Steel. It is referred to with the acronym *VF* and is shown in Figure 3.18.
The probe tip shape is elliptical, with a tap diameter of 0.7 *mm*. Due to difficulties with the

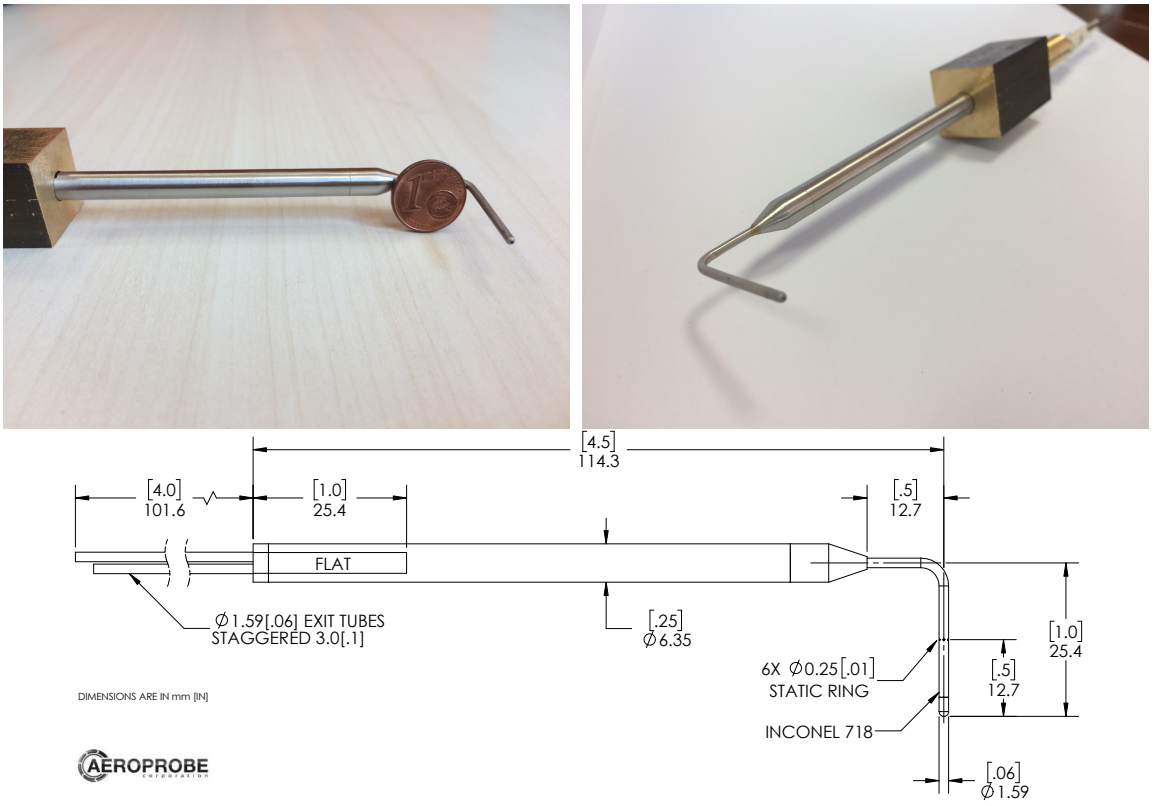

Figure 3.17. *Aeroprobe* Pitot tube. Photos with reference block and technical drawing.

manufacturing process, the probe only features two static pressure taps and does not rigorously meet the minimum required distance between static ring and probe tip (Standard, 2008). A stem extension with hexagonal shape was welded onto the body of the probe to provide reference surfaces for reference block mounting. However, due to imperfect welding, an offset angle of 6° between the reference block and the probe head is present.

3.7.3 TotAle Simple Pitot Tube

The third probe employed in this work is a simple Pitot tube, so a total pressure probe (Figure 3.19). It was manufactured in-house with a stainless-steel tube of outer diameter of 1.6 mm, so comparable to the other probes. The total pressure tap diameter is 0.6 mm and its distance from the stem is 30 mm. A reinforcement at the elbow was added to prevent bending due to aerodynamic loads.

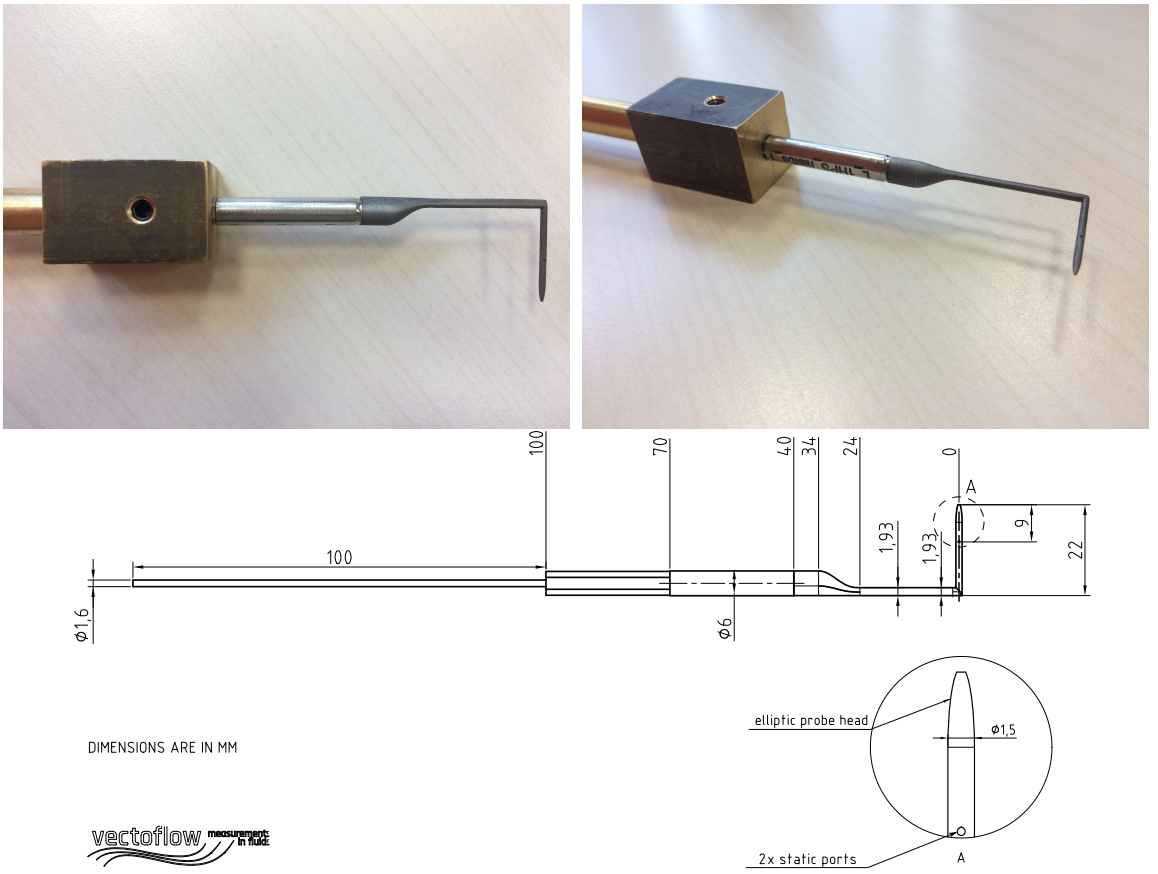

Figure 3.18. *Vectoflow* Pitot tube. Photos with reference block and technical drawing.

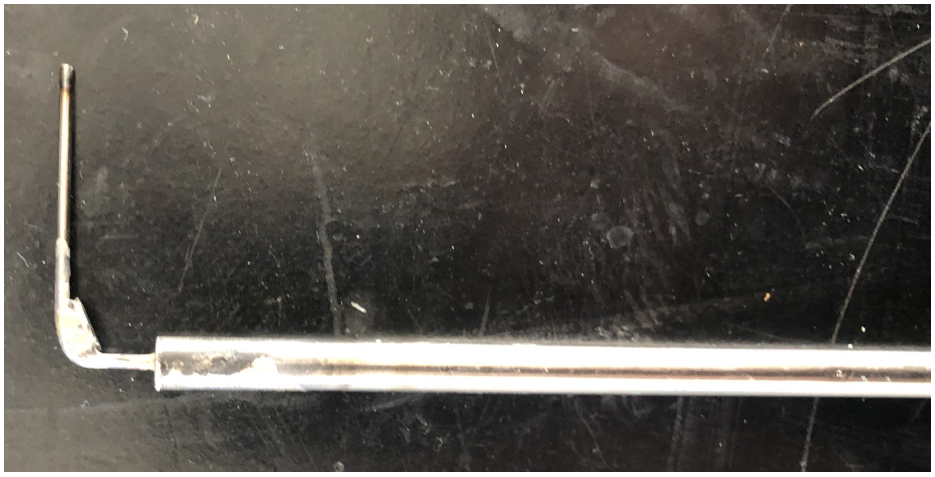

Figure 3.19. *TotAle* simple Pitot tube.

3.7.4 Performance Coefficients

To characterize Pitot tube performance, three coefficients were defined as follows:

$$\textbf{Total Pressure Coefficient}: \quad K_{Pt} = \frac{\Delta P_t}{\Delta P_{ts,ref}} = \frac{P_{t,ref} - P_{t,pitot}}{P_{t,ref} - P_{s,ref}} \tag{3.8}$$

$$\textbf{Static Pressure Coefficient}: \quad K_{Ps} = \frac{\Delta P_s}{\Delta P_{ts,ref}} = \frac{P_{s,ref} - P_{s,pitot}}{P_{t,ref} - P_{s,ref}} \tag{3.9}$$

$$\textbf{Kinetic Head Coefficient}: \quad K_{Pd} = \frac{\Delta P_{ts,pitot}}{\Delta P_{ts,ref}} = \frac{P_{t,pitot} - P_{s,pitot}}{P_{t,ref} - P_{s,ref}} \tag{3.10}$$

K_{Pt} represents the difference ΔP_t between the reference total pressure of the *TROVA* $P_{t,ref}$ and the one measured by the probe $P_{t,pitot}$. This coefficient can also be used for simple Pitot tubes/total pressure probes. K_{Ps} instead looks at the difference ΔP_s between reference and probe static pressures $P_{s,ref}$ and $P_{s,pitot}$, respectively. Both coefficients make the considered pressure difference dimensionless with respect to the reference kinetic head $\Delta P_{ts,ref} = P_{t,ref} - P_{s,ref}$. K_{Pd} is instead the ratio between the Pitot tube kinetic head $\Delta P_{ts,pitot} = P_{t,pitot} - P_{s,pitot}$ and the reference one, and is related to the other two coefficients through the expression: $K_{Pd} = 1 + K_{Ps} - K_{Pt}$.
If the Pitot tube were to work perfectly, coefficients values would be: $K_{Pt} = 0$, $K_{Ps} = 0$ and $K_{Pd} = 1$. However, these can be different from ideality due to probe misalignment, imperfect tap hole geometry or position on the probe head. Pitot tubes designed according to dimensions recommended in the norm (Standard, 2008) should show no particular issues under this aspect, but it is important to verify so, especially in the present case with very small probe size and compressible flow.

In order to minimize coefficients uncertainty, all pressures differences at the numerator and denominator are acquired with differential pressure transducers. Considering a function f of x_i independent variables, with i any positive integer. The uncertainty associated with f is then given by the formula:

$$i(f(x_i)) = \sqrt{\sum \left(\frac{\partial f}{\partial x_i} i_{x_i} \right)^2} \tag{3.11}$$

With the chosen differential measurement system, the coefficients uncertainties $i_{K_{Pt}}, i_{K_{Ps}}$ and $i_{K_{Pd}}$ are analytically determined by the following equations, where i is the uncertainty of the transducer measuring the quantity indicated in the subscript:

$$i_{K_{Pt}} = \sqrt{\left(\frac{1}{\Delta P_{ts,ref}} \right)^2 \left(i_{\Delta P_t} \right)^2 + \left(\frac{-\Delta P_t}{\Delta P_{ts,ref}^2} \right)^2 \left(i_{\Delta P_{ts,ref}} \right)^2} \tag{3.12}$$

$$i_{K_{Ps}} = \sqrt{\left(\frac{1}{\Delta P_{ts,ref}} \right)^2 \left(i_{\Delta P_s} \right)^2 + \left(\frac{-\Delta P_s}{\Delta P_{ts,ref}^2} \right)^2 \left(i_{\Delta P_{ts,ref}} \right)^2} \tag{3.13}$$

$$i_{K_{Pd}} = \sqrt{\left(\frac{1}{\Delta P_{ts,ref}} \right)^2 \left(i_{\Delta P_{ts,pitot}} \right)^2 + \left(\frac{-\Delta P_{ts,pitot}}{\Delta P_{ts,ref}^2} \right)^2 \left(i_{\Delta P_{ts,ref}} \right)^2} \tag{3.14}$$

It should be noted that all uncertainties are inversely proportional to the reference kinetic head $\Delta P_{ts,ref}$, leading to larger uncertainties at lower Mach numbers and pressure levels.

PART II:

CHARACTERIZATION OF NON-IDEAL NOZZLE FLOWS OF ORGANIC VAPORS

This second part of the thesis documents the detailed characterization of supersonic (Chapter 4) and subsonic (Chapter 5) nozzle flows in non-ideal conditions. Results from extensive experimental campaigns on the Test Rig for Organic Vapors (TROVA) are reported together with CFD calculation as a support for the interpretation and verification of experimental results.
The study of elementary nozzle flows provides an insight into the fundamentals of non-ideal compressible fluid dynamics and widens the data-set available in literature for comparison with numerical tools.

CHAPTER 4

NON-IDEAL SUPERSONIC NOZZLE EXPANSIONS

This chapter reports extensive experimental results characterizing the supersonic expansion of siloxane MM in nozzle nMM16. A wide range of total conditions were explored to systematically cover the vapor phase from highly non-ideal conditions at $Z_T = 0.39$ to dilute conditions at $Z_T = 0.98$. This allowed to verify the non-ideal dependence of isentropic expansions on total conditions and to assess the suitability of Z_T as a similarity parameter, following the theoretical approach in Section 2.

As well as providing insights into the physics of non-ideal flows and establishing experimental methodologies for nozzle flow characterization, the present experimental investigation provides significant validation data for the improvement of numerical design and simulation tools involving such flows. Given that the considered fluid, test conditions and nozzle geometry are representative of turbines in organic Rankine cycles, results are of particular interest in the field.

CFD simulations are also presented as support to experimental results to understand key flow features and as comparison.

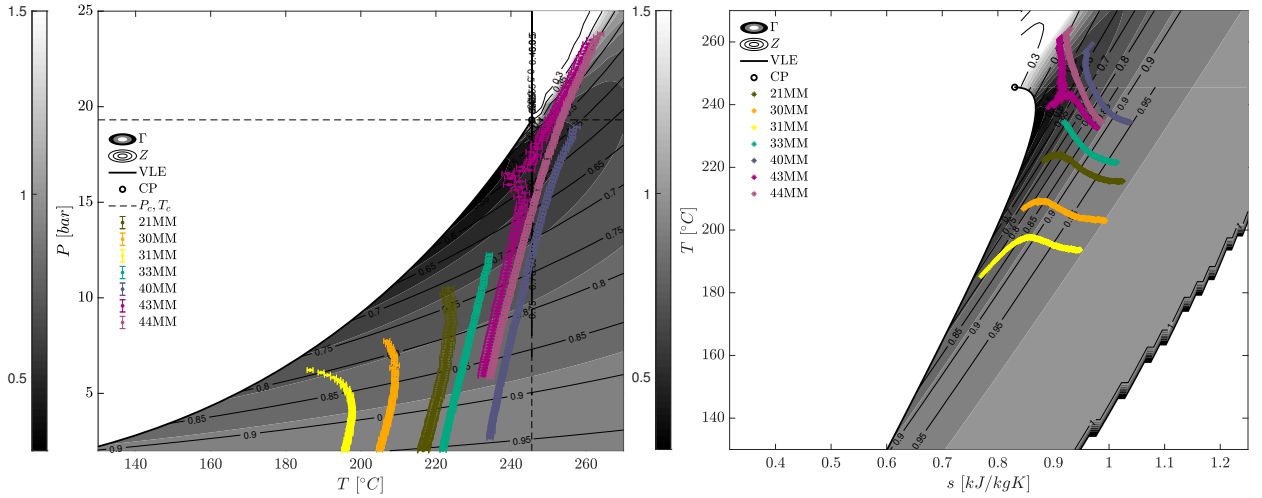

(a) $P - T$ plane.

(b) $T - s$ plane.

Figure 4.1. Evolution of total conditions during each test selected for analysis in the experimental campaign with siloxane MM and nozzle *nMM16*.

Test ID	Nozzle	Most non-ideal condition			Least non-ideal condition		
		$P_T\ [bar]$	$T_T\ [°C]$	Z_T	$P_T\ [bar]$	$T_T\ [°C]$	Z_T
21MM	*nMM16*	10.58	222.1	0.71	0.84	215.5	0.98
30MM	*nMM16*	7.80	206.8	0.77	0.57	202.9	0.99
31MM	*nMM16*	6.27	185.3	0.78	0.65	193.5	0.98
33MM	*nMM16*	12.29	234.5	0.69	1.61	221.7	0.96
40MM	*nMM16*	18.97	259.4	0.57	2.63	234.5	0.95
43MM	*nMM16*	23.54	262.4	0.39	5.85	232.6	0.87
44MM	*nMM16*	23.93	264.9	0.40	5.71	236.6	0.88

Table 4.1. Total conditions of tests selected for analysis in the experimental campaign with siloxane MM and nozzle *nMM16*.

4.1 Test Conditions

More than 20 tests, each taking up to one full day for preparation, were carried out in the experimental campaign with siloxane MM on nozzle *nMM16*. Table 4.1 reports those selected for analysis here. Each test run represents a sequence of steady state expansions evolving from the most non-ideal to the most ideal states documented in the table. Figure 4.1 reports the evolution of total conditions during each selected experimental run. It illustrates the wide region investigated in the vapor phase which also includes supercritical conditions, with total temperatures between $\sim$ 195 and 267 °C and total pressures in the range $\sim$ 0.5 – 24 bar. Each test with a certain set of initial total conditions was repeated at least twice. Consistency and repeatability were assessed as illustrated in Section 4.2 and only one test is analyzed here for each set of initial total conditions. Conclusions are therefore based on repeated measurements.

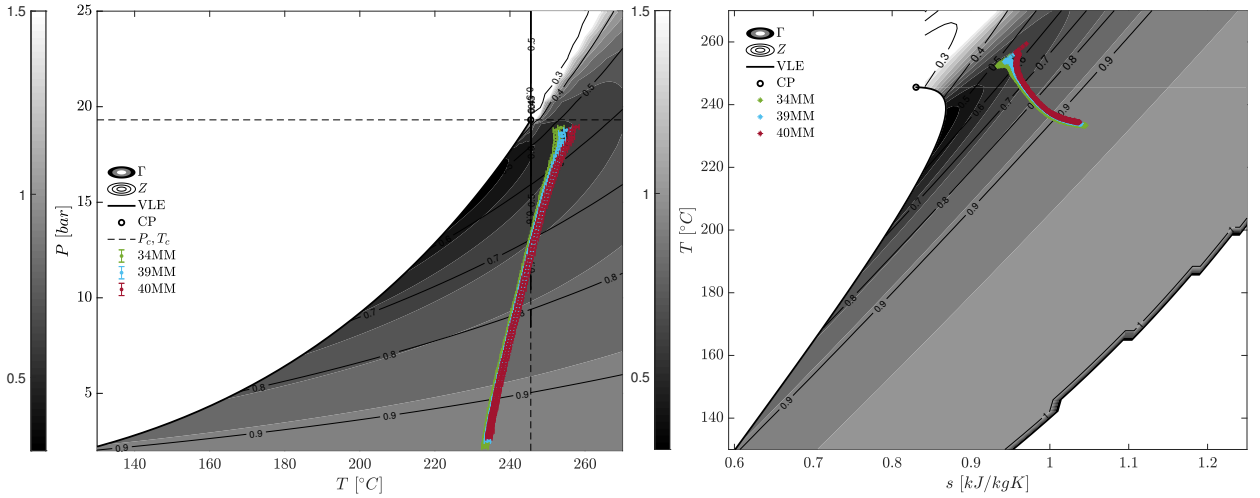

(a) $P-T$ plane.

(b) $T-s$ plane.

Figure 4.2. Evolution of total conditions during repeated tests $34MM, 39MM$ and $40MM$.

4.2 Consistency and Repeatability

Selected test $40MM$ is chosen here to illustrate the procedure by which the consistency and repeatability of an experimental run in the non-ideal regime on the *TROVA* is assessed. Test $40MM$ is the third repetition of a test run with its same initial total conditions. The other two tests are $34MM$ and $39MM$. Figure 4.2 reports the evolution of the three tests total conditions. A slightly different *HPV* emptying dynamics determined some difference between conditions at the very test beginning, but all three tests are within error bars of one another as they proceed.

Due to the non-ideal dependence of expansions on total conditions, test repeatability between different experimental runs can be investigated only by comparing static pressures at each pressure tap at same total pressure and temperature, as shown in Figure 4.3a. At the highest pressures, total temperature is slightly different between the three tests, as already mentioned above. Comparison at lower pressure levels (from $\sim$ 15 bar) is instead used to assess repeatability, given the good agreement between tests total temperatures. This is better illustrated by the zooms at pressure taps 5 and 7 in Figures 4.3b and 4.3c, respectively. Tests $39MM$ and $40MM$ show excellent agreement whilst $34MM$ is instead separated, as especially evident in tap 7. This disagreement was found to occur at all pressure taps and to increase along the nozzle (although zoomed details are not reported here for brevity). Test $34MM$ was therefore discarded and results from $40MM$, as confirmed by $39MM$, were considered for further nozzle flow analysis.
As previously mentioned, an analogous evaluation was performed for all initial total conditions considered in the present experimental campaign.

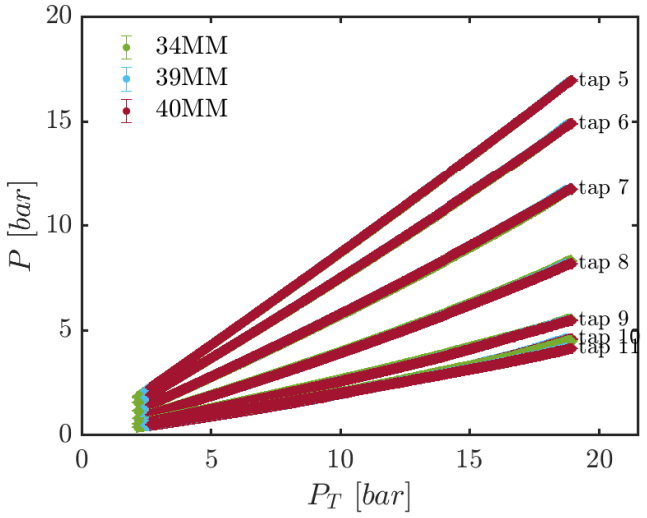

(a) Static pressure P at each tap as a function of total pressure P_T.

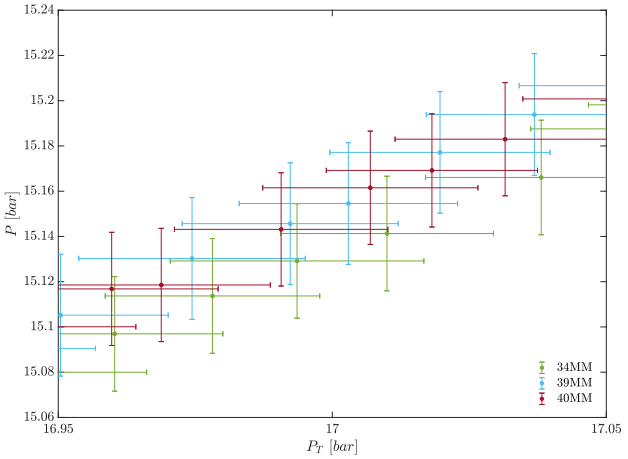

(b) Zoom at tap 5.

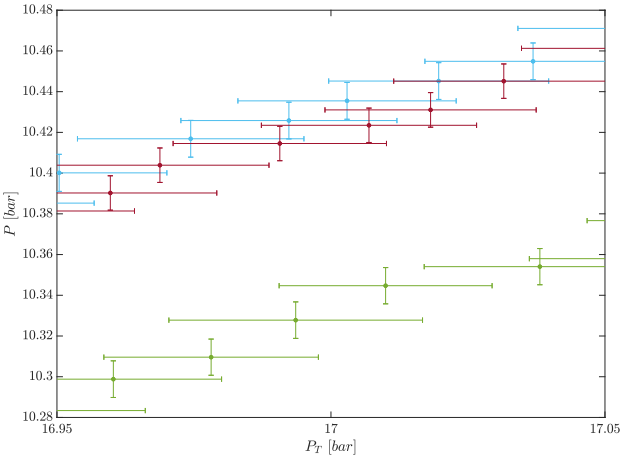

(c) Zoom at tap 7.

Figure 4.3. Repeatability assessment for tests $34MM, 39MM$ and $40MM$.

4.3 Non-Ideal Pressure Ratio Dependance on Total Conditions

Amongst all tests in the experimental campaign, $44MM$ achieved the most extreme conditions. It is used here to illustrate the non-ideal dependance of the pressure ratio along isentropic expansions on total conditions with experimental results. Nozzle expansions characterized by a total compressibility factor in the range $Z_T = 0.4 - 0.85$ were extracted. Corresponding total conditions are reported in Figures 4.4a and 4.4b with labels from b to k at increasing values of Z_T. Figure 4.4b also shows corresponding isentropic expansions.

Figure 4.4c shows the measured pressure ratio along the nozzle axis at extracted total conditions. P/P_T decreases from the most non-ideal condition ($44MMb$) to the most ideal one ($44MMp$). The pressure tap located at $x = 77.9$ mm is just downstream of the geometrical throat. Here, the pressure ratio at the lowest available Z_T is ~ 1.2 times that at the highest total compressibility factor.

The extent of non-ideal effects is quantified in Figure 4.4d where the percentage difference Δ_{P/P_T} between pressure ratio at minimum available total compressibility factor $P/P_T(Z_{T,min})$ and pressure ratio at maximum available total compressibility factor $P/P_T(Z_{T,max})$ is reported for each pressure tap along the nozzle. Δ_{P/P_T} and its uncertainty (calculated by propagating experimental data uncertainty and also reported in Figure 4.4d) are defined in Equations (4.1) and (4.2):

$$\Delta_{P/P_T} = \frac{P/P_T(Z_{T,min}) - P/P_T(Z_{T,max})}{P/P_T(Z_{T,max})} \cdot 100 \tag{4.1}$$

$$U_{\Delta_{P/P_T}} = \sqrt{U^2_{P/P_T(Z_{T,max})} + \left(\frac{P/P_T(Z_{T,min})}{P/P_T(Z_{T,max})}\right)^2 U^2_{P/P_T(Z_{T,min})}} \frac{1}{P/P_T(Z_{T,max})^2} \cdot 100 \tag{4.2}$$

In general, at all axial locations where pressure measurements are available except at the last two taps at nozzle exit, pressure ratios at most non-ideal conditions are between $10 - 30\,\%$ higher than those at the most ideal ones. From an experimental point of view, since this pressure ratio difference is one order of magnitude larger than measurement uncertainty, it can only be ascribed to non-ideal compressible flow effects. These results are in very good qualitative and quantitative agreement with 1D isentropic expansions presented in Section 2.4.

A particular feature of the last part of the nozzle expansion is to be pointed out. Nozzle *nMM16* was designed to achieve uniform outlet conditions. Thus, the last part of the divergent defines the so-called *turning region*: expansion at the axis has concluded and nozzle profiles only provide flow turning in the rest of the cross section to provide a uniform velocity profile. However, this exactly occurs only at nozzle design point which, due to the non-ideal nature of the flow, also depends on total conditions (Table 3.3). The particular design P_T and T_T for nozzle *nMM16* are never met during test $44MM$, resulting in an imperfect flow turning and a mild re-compression at the last two taps in the nozzle, and in higher values of Δ_{P/P_T}.

Figures 4.4e and 4.4f respectively show the trends in compressibility factor and fundamental derivative of gasdynamics along the nozzle axis for the expansions at different non-ideality level. Due to the different values of P_T and T_T, trends and values in both quantities are significantly different between the various expansions. These are not superposed as a result, consistently with the different volumetric and caloric behavior, as explained in Section 2.4

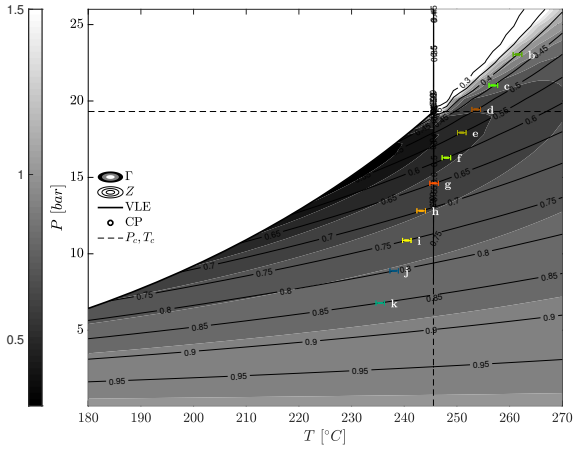

(a) $P-T$ plane with total conditions at extracted values of Z_T.

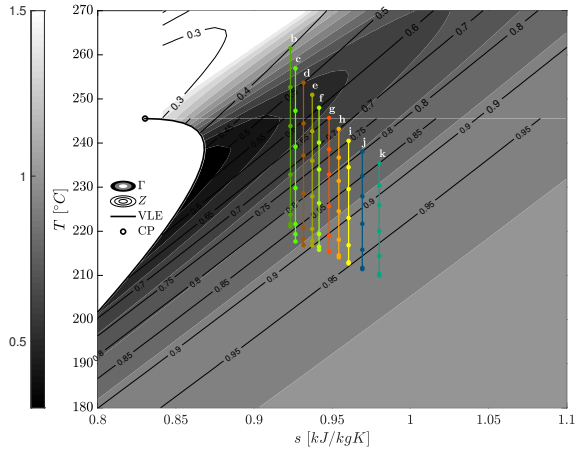

(b) $T-s$ plane with total conditions at extracted values of Z_T. Each expansion is also shown, wits dots representing static pressure measures at each active tap.

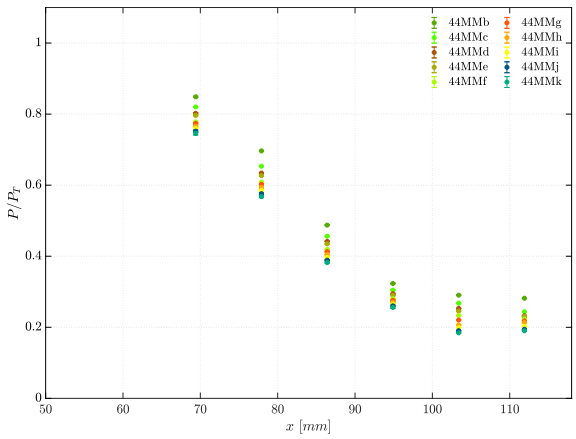

(c) Pressure ratio P/P_T along the nozzle axis during expansions with different Z_T.

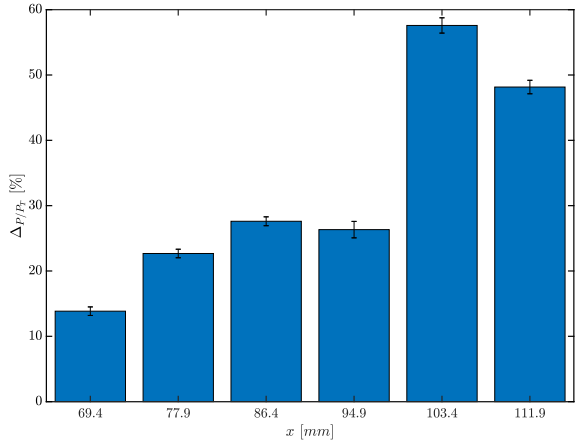

(d) Percentage difference Δ_{P/P_T} between pressure ratios at most and least ideal conditions at each tap along the nozzle axis.

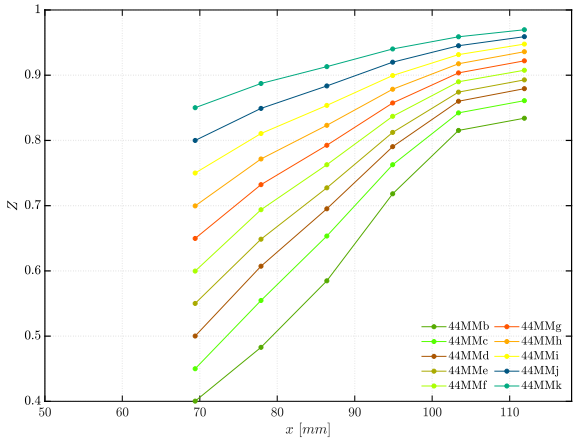

(e) Compressibility factor Z along the nozzle axis during expansions with different Z_T.

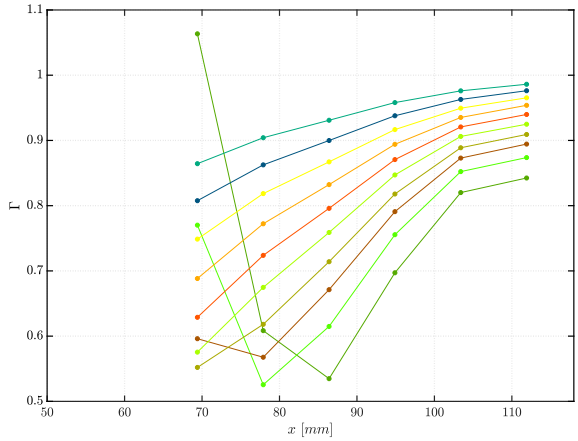

(f) Fundamental derivative of gasdynamics Γ along the nozzle axis during expansions with different Z_T. Non-monotonic trends are visible for the most extreme conditions.

Figure 4.4. Results from test $44MM$. Each letter and color identify different total conditions, with letters from b to k at increasing values of Z_T.

4.4 Non-Ideal Mach Number Dependance on Total Conditions

Non-ideal effects can also be observed through direct measurement of the Mach number thanks to the quantitative use of schlieren visualizations, as detailed in Section 3.3.3. Mach lines were identified in schlieren images corresponding to time instants during test *44MM* at the different values of total compressibility factor considered in the previous section. Figures 4.5a and 4.5b report the extracted Mach lines superposed to original schlieren images for the two exemplary conditions *44MMb* at $Z_T = 0.40$ and *44MMj* at $Z_T = 0.80$.
The schlieren image for condition *44MMb* is overall much darker than *44MMj*, especially from nozzle inlet until some distance after the throat, meaning that Mach lines recognition was possible for a smaller portion of the nozzle than condition *44MMj*. As explained in Section 3.3.3, the higher total pressure and level of non-ideality at $Z_T = 0.40$ are responsible for stronger refractive index gradients than for condition *44MMj*. This leads to a much darker image for the imposed camera lens aperture, exposure time and knife position, which are set so as to have acceptable image brightness and contrast throughout the test. If these parameters were varied for a brighter image at the beginning of the test, then later time instants could result too bright and even saturate the camera sensor. Nevertheless, Mach lines could be identified for a significant part of the nozzle and even after its discharge until expansion fans. As a side note, the latter are also extremely dark instead of being bright due to the strong refractive index gradients in the *44MMb* condition, leading to measuring range issues in which light rays are so deviated as to be blocked onto some optical system aperture stop (Section 3.3.3).
Once Mach lines are identified, their slope provides a direct measure of the Mach number along the nozzle (Section 3.3.3), as reported in Figure 4.5c together with the Mach number calculated at taps from static pressure measurements (see Section 3.4 for details on the calculation procedure). Uncertainty in the latter calculated values was also determined through a *Monte Carlo* approach but was found to be so small as to fall within the markers in the plot, and was thus not reported for graphical clarity.
Although characterized by a non-negligible associated uncertainty, Mach number values determined from schlieren visualizations show very good agreement with pressure measurements. Being the two sets of data independent of one another, their accordance positively indicates the reliability of the experimental results reported here.
Non-ideal gas effects are clearly illustrated in Figure 4.5c, given that the Mach number trends along the nozzle are not superposed for the two considered total conditions. The Mach number is overall higher for the most ideal case, consistently with the lower pressure ratio evidenced in the previous section. Considering the first tap in the *turning region* at $x = 103.4$ mm, the Mach number is $\sim 17\%$ higher in condition *44MMj* with respect to *44MMb*.

Condition *44MMb*, with $P_T = 23.05$ bar and $T_T = 263.9\,^{\circ}$C, is much closer to design point (Table 3.3) than *44MMj* having $P_T = 8.89$ bar and $T_T = 240.2\,^{\circ}$C. This is the reason why the nozzle *turning region* shows a much more constant Mach number for $Z_T = 0.40$ with respect to $Z_T = 0.80$, as highlighted in Figure 4.5c. In the latter case a significant recompression is evident due to the strong off-design regime of the nozzle.

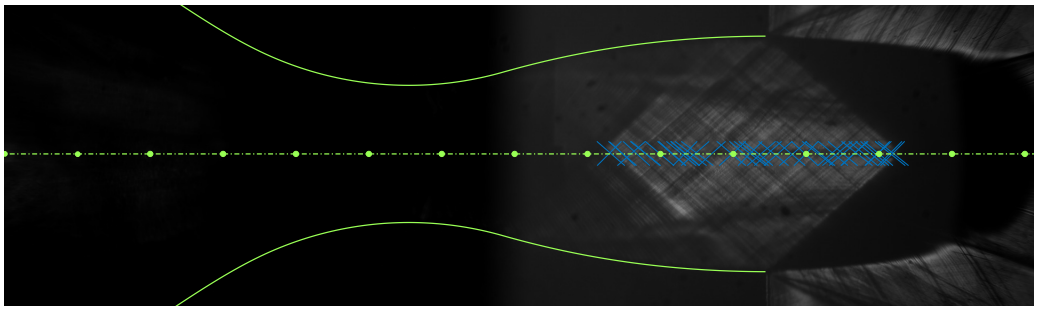

(a) Schlieren image with superposed identified Mach lines for condition $44MMb$ at $Z_T = 0.40$. Nozzle profile and pressure taps are also contoured.

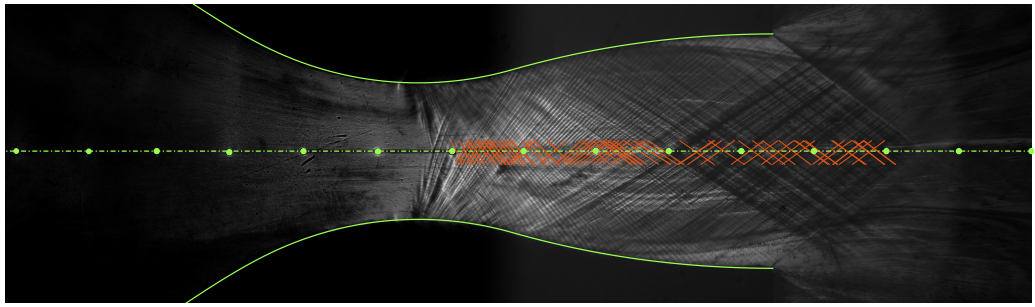

(b) Schlieren image with superposed identified Mach lines for condition $44MMj$ at $Z_T = 0.80$. Nozzle profile and pressure taps are also contoured.

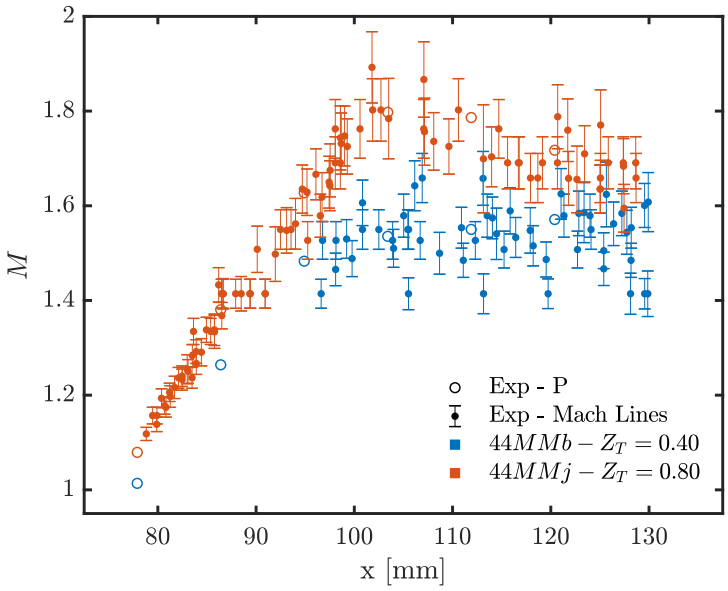

(c) Mach number determined from pressure measurements and from Mach lines in schlieren images. The plot is zoomed in the divergent: the tap at $x = 77.9$ mm is just after the geometrical throat.

Figure 4.5. Mach number extraction from schlieren images for conditions $44MMb$ at $Z_T = 0.40$ and $44MMj$ at $Z_T = 0.80$.

4.5 Z_T as a Similarity Parameter

Sets of expansions from different tests sharing the same value of total compressibility factor but different total pressure and temperature are here considered. The objective is to evaluate the suitability of Z_T as a similarity parameter for non-ideal isentropic expansions and provide an experimental verification of findings from theoretical calculation in Section 2.
Figure 4.6 reports total conditions of selected nozzle flows. Expansions having same Z_T are labeled with the same letter, starting from a at $Z_T = 0.39$ to n at $Z_T = 0.98$.

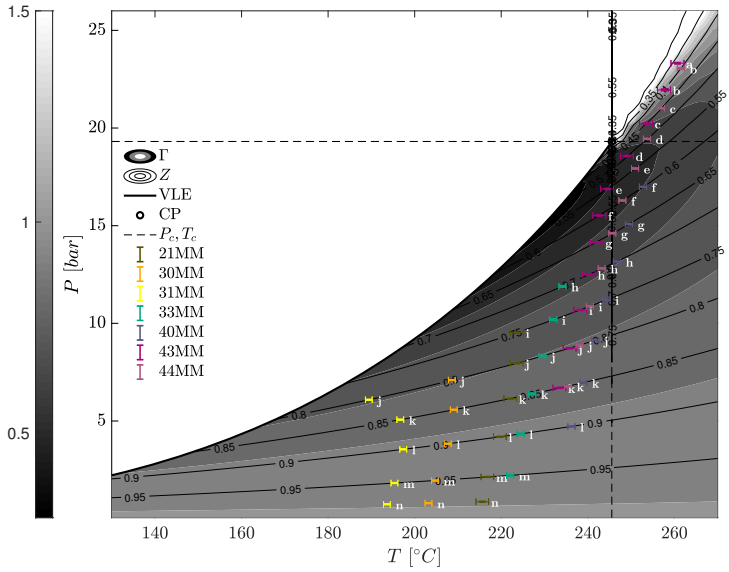

Figure 4.6. $P - T$ diagram with Z and Γ contours with total conditions of expansions sharing the same Z_T. Each color identifies a single test.

Comparison between pressure ratio profiles of expansions with different total conditions but same total compressibility factor can be found in Figure 4.7 for selected $Z_T = 0.40, 0.50, 0.70, 0.80, 0.90$ and 0.95. Experimentally measured pressure ratios are within error bars of one another if the total compressibility factor is the same. Appreciable differences are visible only for fairly extreme conditions with $Z_T = 0.40, 0.50$ and 0.60, qualitatively confirming findings from Section 2.
Some discrepancies at the last two taps are visible in certain cases even at moderately ideal conditions (e.g. $Z_T = 0.80$). This is attributed to the previously mentioned off-design nozzle operation, which cannot be characterized in terms of Z_T, and not to non-ideal gas effects, since conditions at nozzle exit are overall rather dilute.

The performance of Z_T as a similarity parameter can again be quantified with the percentage pressure ratio $\Delta^{Z_T}_{P/P_T}$ defined analogously to Section 2 in Equation (4.3). Its uncertainty is calculated by propagating experimental data uncertainty U, as defined in Equation (4.4).

$$\Delta^{Z_T}_{P/P_T} = \frac{\max\left[P/P_T(Z_T)\right] - \min\left[P/P_T(Z_T)\right]}{\min\left[P/P_T(Z_T)\right]} \cdot 100 \tag{4.3}$$

$$U_{\Delta^{Z_T}_{P/P_T}} = \sqrt{U^2_{\max[P/P_T(Z_T)]} + \left(\frac{\max\left[P/P_T(Z_T)\right]}{\min\left[P/P_T(Z_T)\right]}\right)^2 U^2_{\min[P/P_T(Z_T)]}} \frac{1}{\min\left[P/P_T(Z_T)\right]} \cdot 100 \tag{4.4}$$

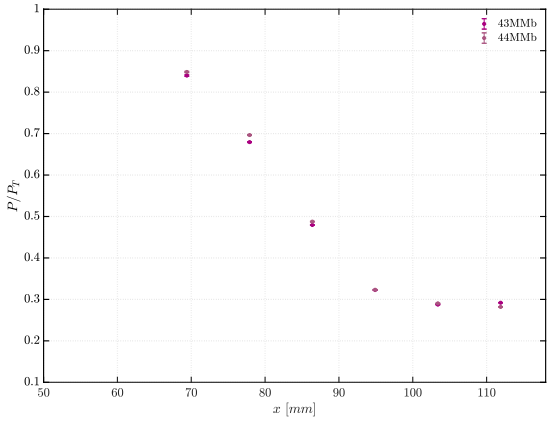

(a) $Z_T = 0.40$

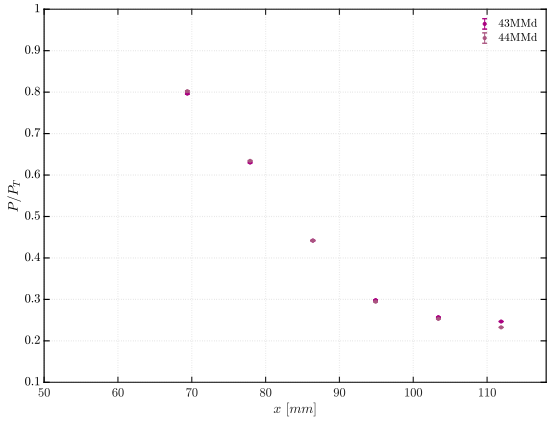

(b) $Z_T = 0.50$

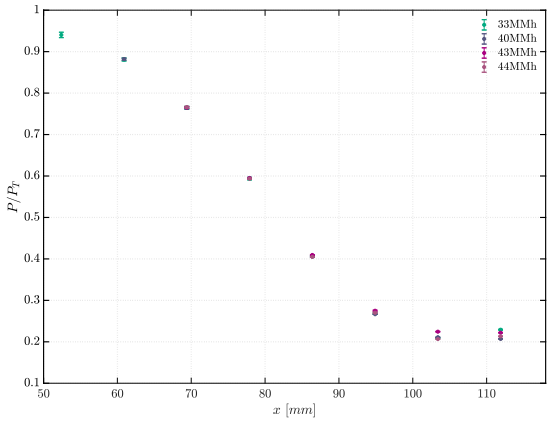

(c) $Z_T = 0.70$

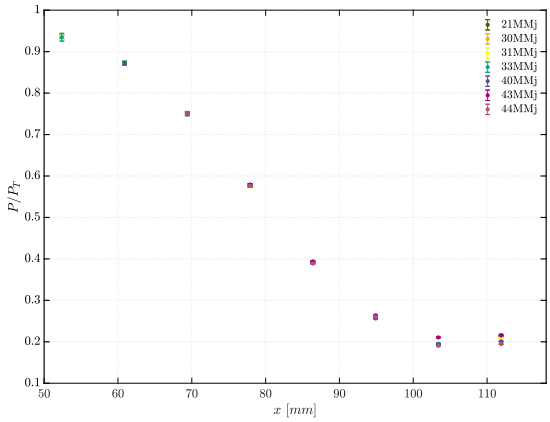

(d) $Z_T = 0.80$

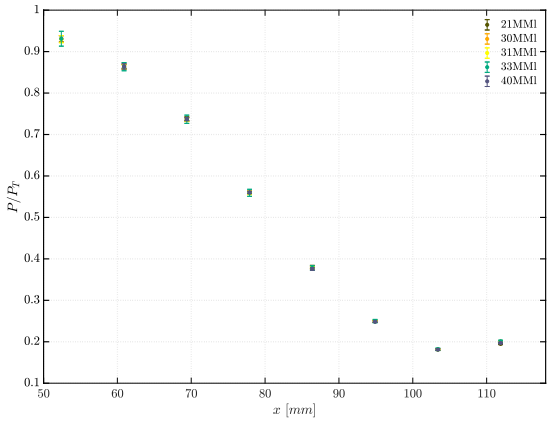

(e) $Z_T = 0.90$

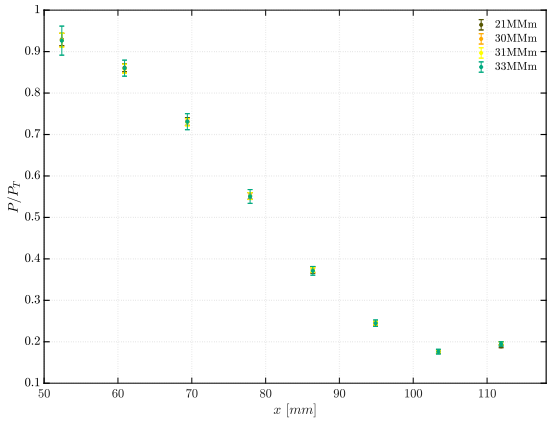

(f) $Z_T = 0.95$

Figure 4.7. Pressure ratio P/P_T along the nozzle axis for all different total conditions sharing selected values of Z_T.

max $[P/P_T(Z_T)]$ and min $[P/P_T(Z_T)]$ refer to the maximum and minimum values of pressure ratio registered at a specific axial location amongst all expansions sharing the same Z_T. Figure 4.8 reports percentage pressure difference $\Delta^{Z_T}_{P/P_T}$ with its uncertainty at the four central pressure taps. The last two taps were not considered due to the previously mentioned dependance on the nozzle operating regime. The first two taps were also not included because measurements were not available there at tests with most extreme initial conditions due to the unavailability of pressure transducers with a high enough full scale. Taps at $x = 69.4, 86.4, 94.9$ mm correspond to locations closest respectively to $A^*/A = 0.8$ - subsonic, $A^*/A = 1$ - sonic and $A^*/A = 0.7$ - supersonic, consistently with the analysis in Section 2 and Figure 2.6.

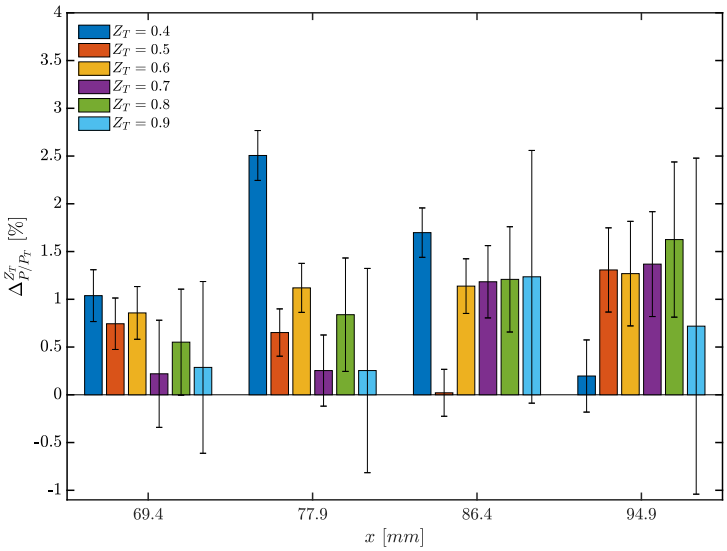

Figure 4.8. Percentage difference in pressure ratio $\Delta^{Z_T}_{P/P_T}$ with error bars for different Z_T values and selected pressure taps. Taps at $x = 69.4, 86.4, 94.9$ mm are locations respectively closest to area ratios $A^*/A = 0.8$ - subsonic, $A^*/A = 1$ - sonic and $A^*/A = 0.7$ - supersonic, consistently with the analysis in Section 2 and Figure 2.6.

Expansions grouped in terms of their Z_T show an experimental $\Delta^{Z_T}_{P/P_T}$ always well below 3%, confirming the suitability of the total compressibility factor as a similarity parameter to characterize isentropic expansions. Experimental $\Delta^{Z_T}_{P/P_T}$ values are noticeably lower with respect to those found with 1D calculation in Section 2 and Figure 2.6 at the most non-ideal conditions with $Z_T = 0.40$. This is due to the fact that the explored vapor phase area is much narrower in the experimental case with respect to the theoretical one, where temperatures ranged between 120 and 300 °C and maximum total pressure was up to three times the critical one. The various experimental total conditions are overall closer to one another resulting in a mitigated impact on expansions.

Consistently with results in Section 2 and Figure 2.6, $\Delta^{Z_T}_{P/P_T}$ overall decreases towards more dilute conditions from $Z_T = 0.40$ and increases along the nozzle. However, trends are not so clear-cut as for 1D calculation due to inevitable noise in experimental data. This is especially true in more dilute conditions, both at higher values of Z_T and towards the nozzle exit. Error bars here become very large because transducers operate at lower overall pressure levels, so further away from their full scale. Uncertainties in some cases become even larger than the value of $\Delta^{Z_T}_{P/P_T}$ itself. This unfortunately makes it difficult to draw definite conclusions on the trends of pressure ratio percentage difference. However, the good performance of the total compressibility factor as a similarity parameter for $Z_T \geqslant 0.60$ was already evidenced in measured pressure ratios in Figure 4.7.

Figure 4.9 reports comparisons between compressibility factors along the nozzle axis for expansions with different total conditions but same Z_T. Analogously, Figure 4.10 illustrates the fundamental derivative of gasdynamics. Expansions with $Z_T \geqslant 0.60$ have superposed profiles of both Z and Γ along the nozzle. For more non-ideal conditions instead, their trends show differences between the various expansions, particularly at the first axial locations. Considering $Z_T = 0.40$, a non-monotone trend in the fundamental derivative is quite evident for test $44MM$ with respect to test $43MM$ at same total compressibility factor. Although the two total conditions are fairly close in terms of pressure and temperature, the expansion in test $44MM$ proceeds in a region where the closing-in of iso-Γ curves is more pronounced, resulting in a more marked non-monotone fundamental derivative trend.

Consistently with findings in Section 2, pressure ratio profiles are not superposed between expansions with same Z_T when one or both Z and Γ profiles are most different. Expansions are no longer similar as a consequence of the different volumetric and caloric behaviour and Z_T cannot be considered a suitable similarity parameter here.

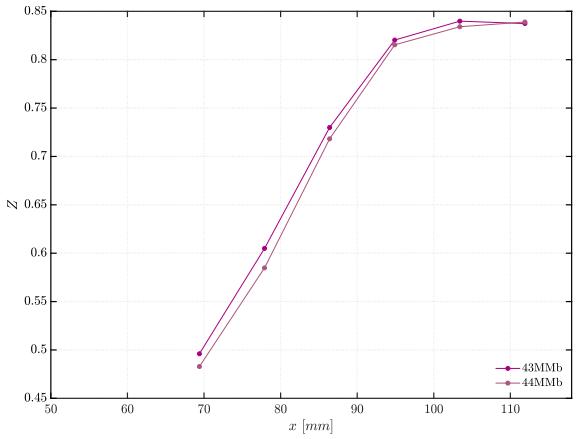

(a) $Z_T = 0.40$

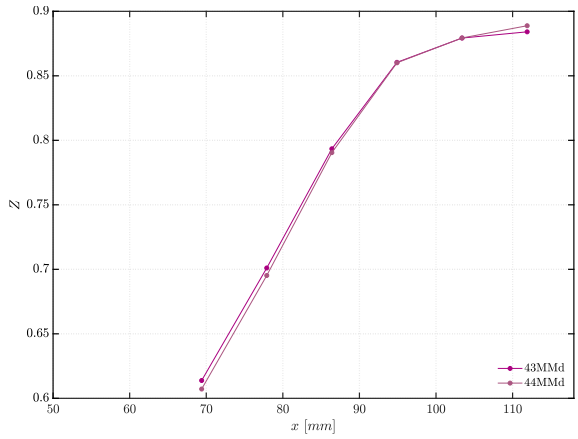

(b) $Z_T = 0.50$

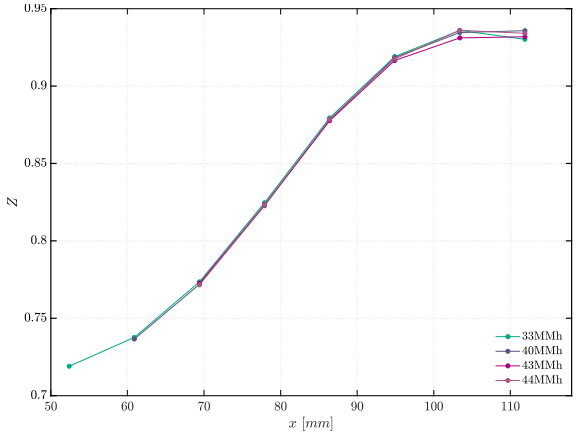

(c) $Z_T = 0.70$

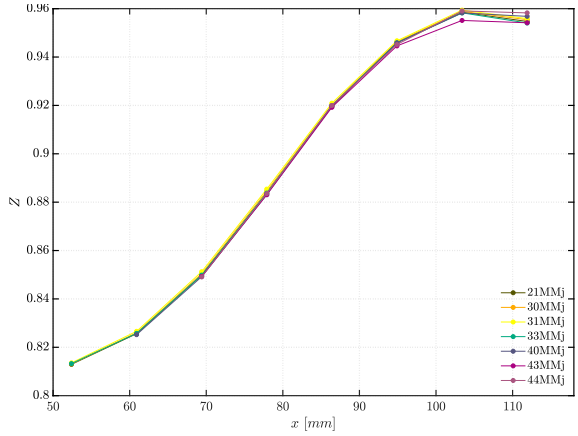

(d) $Z_T = 0.80$

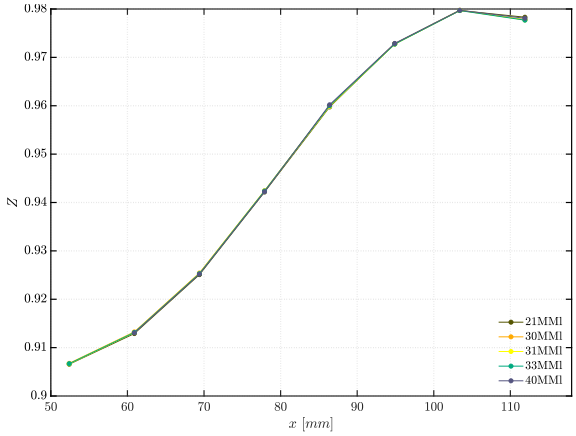

(e) $Z_T = 0.90$

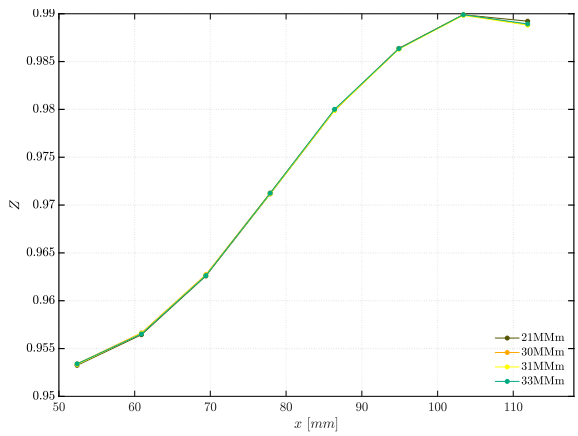

(f) $Z_T = 0.95$

Figure 4.9. Compressibility factor Z along the nozzle axis for all different total conditions sharing selected values of Z_T.

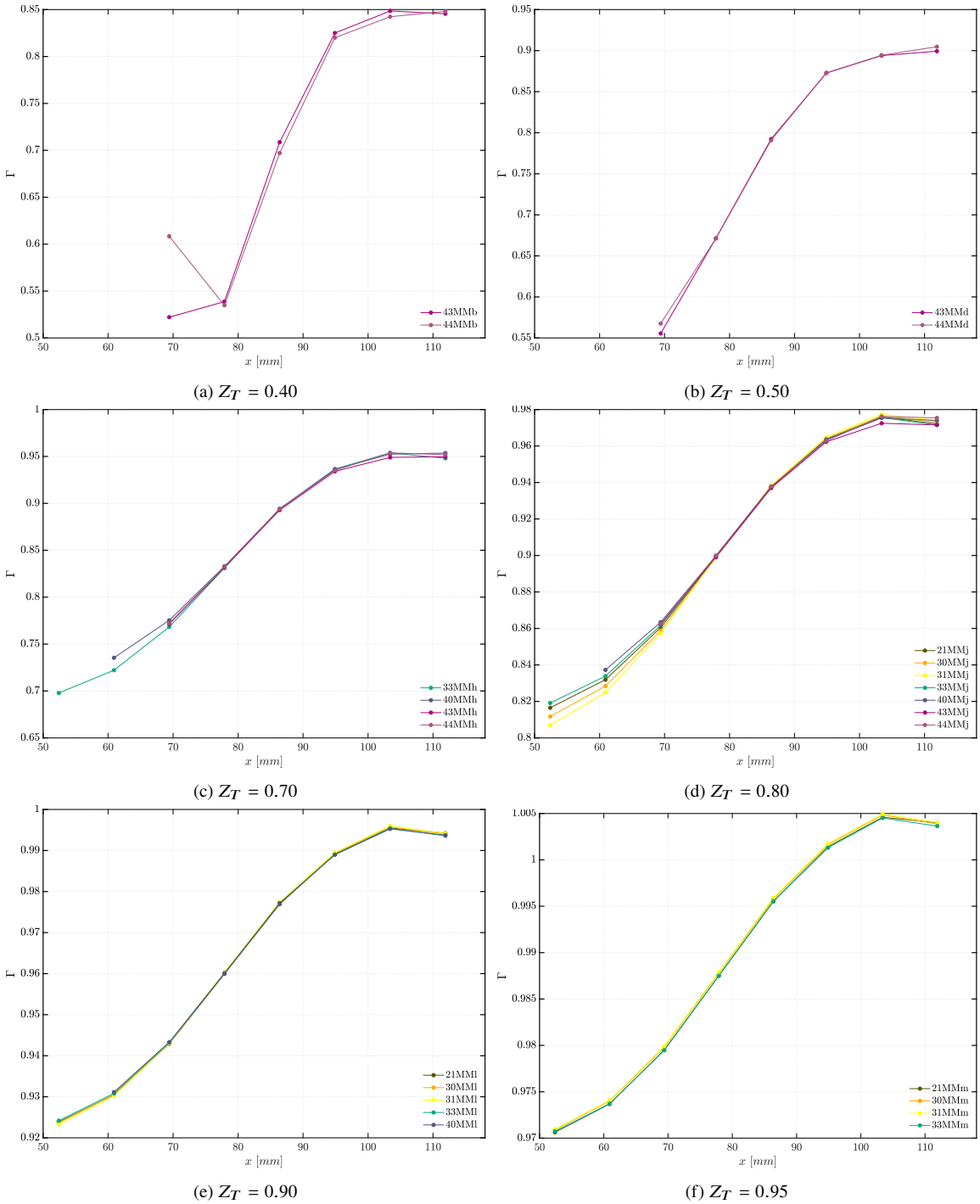

(a) $Z_T = 0.40$

(b) $Z_T = 0.50$

(c) $Z_T = 0.70$

(d) $Z_T = 0.80$

(e) $Z_T = 0.90$

(f) $Z_T = 0.95$

Figure 4.10. Fundamental derivative of gasdynamics Γ along the nozzle axis for all different total conditions sharing selected values of Z_T.

4.6 Numerical Simulations of Non-Ideal Supersonic Expansions of Siloxane MM

4.6.1 Solver Setup and Numerical Domain

CFD calculation are carried out using code *SU2 - v7.0.1* and the embedded improved Peng-Robinson-Stryjek-Vera (*iPRSV*) equation of state in polytropic form. Experimental results are instead processed using the Span-Wagner functional form through the *FluidProp* library (Appendix A), which has a comparable accuracy although slightly higher especially closer to the critical point. However, the *iPRSV* equation of state is directly coded within *SU2*, while the *FluidProp* library needs to be called upon externally, leading to a significant increase in calculation time. For this reason, the *iPRSV* equation of state is here employed.
For viscous calculation, the $k-\omega$ *SST* turbulence model is used. Viscosity and thermal conductivity are assumed constant and equal to the values calculated using the *FluidProp* library at the considered nozzle stagnation conditions. In all cases, the solution is time-marched with an implicit Euler scheme. A second-order accurate MUSCL scheme of Roe type is employed with Venkatakrishnan flux limiter. The Green-Gauss formula is used to compute gradients at cell interfaces.

The whole nozzle *nMM16* geometry was simulated and no symmetries were exploited to reduce calculation time. Given the planar nozzle geometry, a 2D numerical domain was considered.

Riemann boundary conditions were applied, with total conditions at the inlet and outlet pressure set at the outlet of the nozzle. No-slip conditions were imposed at top and bottom nozzle walls. The flow was considered adiabatic, with no heat exchange to/from walls.

4.6.2 Simulated Test Conditions

Simulated conditions correspond to time instants at selected total compressibility factor values during test $44MM$, as reported in Table 4.2. The imposed nozzle outlet pressure was taken as 80% of the one measured at the last available tap.
A grid dependence analysis was performed on the $44MMb$ at $Z_T = 0.40$ condition only. The other selected test $44MM$ conditions were then simulated with the grid-independent 2D viscous mesh only.

Name	P_T $[bar]$	T_T $[^\circ C]$	Z_T $[-]$
$44MMb$	23.30	262.7	0.40
$44MMf$	16.53	249.1	0.60
$44MMj$	9.13	238.8	0.80

Table 4.2. Selected test conditions from test *44MM* for CFD simulations.

4.6.3 2D Viscous Calculation on Structured Meshes

Several structured meshes were generated to perform a grid dependence analysis, all having a first cell height of 0.5×10^{-7} m to keep the y^+ coordinate at the wall below 1. Figure 4.11 illustrates an exemplary mesh and Table 4.3 reports mesh names, number of elements and points.

A Mach number contour of the solution on mesh $2d-A$ is reported in Figure 4.12a. Figures 4.13a and 4.13b are instead plots of pressure and Mach number trends along the nozzle axis for the different meshes. For comparison, experimental data from pressure measurements and from Mach lines in schlieren visualizations are reported. Different meshes have almost perfectly

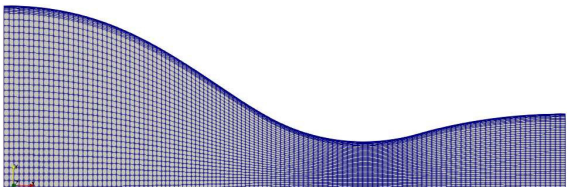

Figure 4.11. Structured mesh $2d - A$ for viscous calculation. Zoom on the upper half of the domain.

Grid Name	elements	points
$2d - A$	11k	11k
$2d - B$	22k	23k
$2d - C$	40k	40k
$2d - D$	83k	83k

Table 4.3. Meshes for grid dependence study for 2D viscous simulations on nozzle *nMM16*.

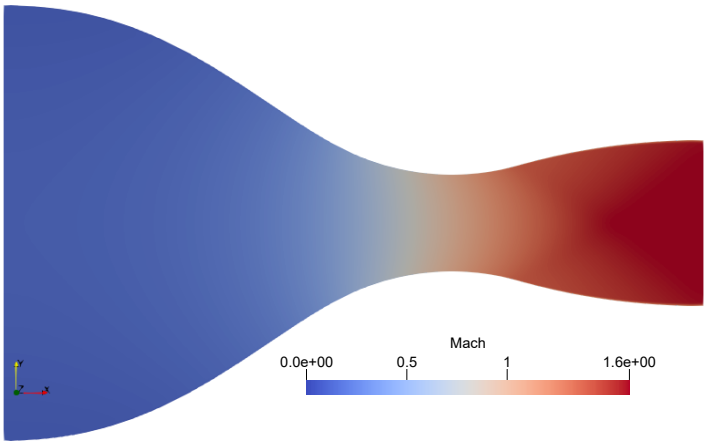

(a) Mach number contour of the solution on mesh $2d - A$.

superimposed curves of pressure and Mach number, with pressure difference between roughest and finest mesh below 0.1 % all along the nozzle except at the beginning of the turning region, where the discrepancy is larger but still well below 2 %.
Entropy and total enthalpy trends along the nozzle axis can be found in Figures 4.13c and 4.13d and are almost perfectly superimposed for all meshes. For both quantities, the percentage variation with respect to the inlet value is reported. Since the flow is adiabatic, total enthalpy should stay constant. Also, since the core of the flow at the axis is predominantly inviscid, entropy is expected to stay constant too. However, both change along the nozzle. This can be linked to numerical dissipation, in particular related to the strong curvatures present at nozzle profiles (Gori et al., 2019b). Nevertheless, both entropy and total enthalpy vary by less than 1% with respect to inlet values, implying limited numerical dissipation effects in line with findings in Gori et al. (2019b).
Figure 4.13e shows the mass flow rate for the different meshes. The trend is asymptotic for viscous calculation as mesh size increases, but all values are within 0.07% of the finest mesh.
To evaluate the accordance between numerical and experimental results, the percentage pressure deviation $\Delta P_{CFD-exp}$ is defined in Equation 4.5 and reported in Figure 4.13f. It is calculated at all pressure taps. The percentage deviation uncertainty $U_{\Delta P_{CFD-exp}}$ is also considered as per Equation 4.6, with the assumption of no uncertainty in CFD computations.

$$\Delta P_{CFD-exp} = \frac{P_{CFD} - P_{exp}}{P_{exp}} \cdot 100 \tag{4.5}$$

$$U_{\Delta P_{CFD-exp}} = \sqrt{\left(\frac{P_{CFD}}{P_{exp}}\right)^2 \cdot U_{P_{exp}}^2 \frac{1}{P_{exp}}} \cdot 100 \tag{4.6}$$

Overall, CFD tends to underestimate pressure and overestimate the Mach number with respect

to experimental results, and agreement worsens along the nozzle. Peculiarly, the absolute value of $\Delta P_{CFD-exp}$ is below 8% until the flow on the axis is accelerated and then almost doubles in the turning region to around 15%. These trends and values are in line with similar analyses on non-ideal supersonic nozzle expansions of siloxane MDM (Cammi, 2019; Gallarini, 2020; Spinelli et al., 2019) and refrigerant R1233zd(E) (Robertson et al., 2020).
No remarkable differences are evident between the different meshes in the grid dependence study. Plots in Figure 4.13 also report results from an inviscid simulation (labeled as *eul*) performed on mesh *2d-C*. Curves are well superposed to those of viscous calculation, suggesting that boundary layer growth has here a negligible impact on effective passage area and on flow expansion. 3d calculation are envisaged in the future to further assess this aspect by considering front and back test section walls, as well as top and bottom nozzle profiles.

4.6.4 Verification of Non-Ideal Expansions Dependance on Total Conditions

The already extensively discussed non-ideal dependance of expansions on total conditions is confirmed by numerical results, presented together with experimental data from the three selected test *44MM* conditions in Figure 4.14. As particularly clear by looking at CFD pressure ratio trends in Figure 4.14a, less ideal conditions show a higher pressure ratio. The percentage difference between pressure ratios at least and most ideal conditions calculated from numerical results is in agreement with the one from experimental data, as reported in Section 4.3.
CFD results correctly capture values of compressibility factor and fundamental derivative along the nozzle, including the non-monotone Γ trend for the most non-ideal condition *44MMb* at $Z_T = 0.40$. Z and Γ trends and values differ depending on total conditions, again highlighting the different volumetric and caloric behaviour responsible for the non-ideal expansions dependance on P_T and T_T.
Numerical simulations also highlight the significant flow difference in the *turning region* between expansions at different total conditions, given the different extents of flow recompression.
Figure 5.18e reports the percentage pressure ratio deviation $\Delta(P/P_T)_{CFD-exp}$ between experimental and numerical results. Agreement radically improves as more ideal conditions are approached compared to *44MMb* (previously discussed in the grid convergence study), with values overall well below 5%. This could be ascribed to a decrease in accuracy in the thermodynamic model as less ideal conditions are considered, leading to a larger difference between experiment and CFD.

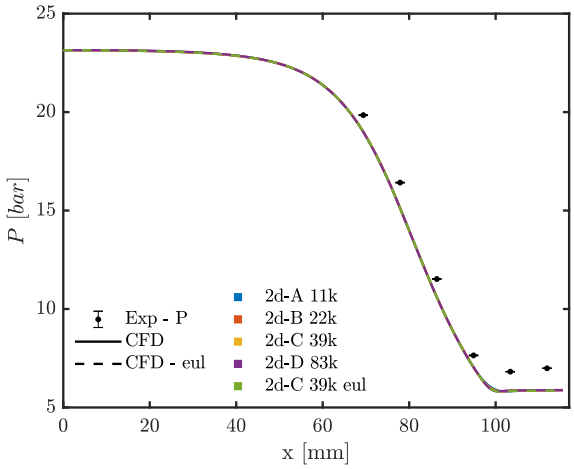

(a) Pressure along the nozzle axis.

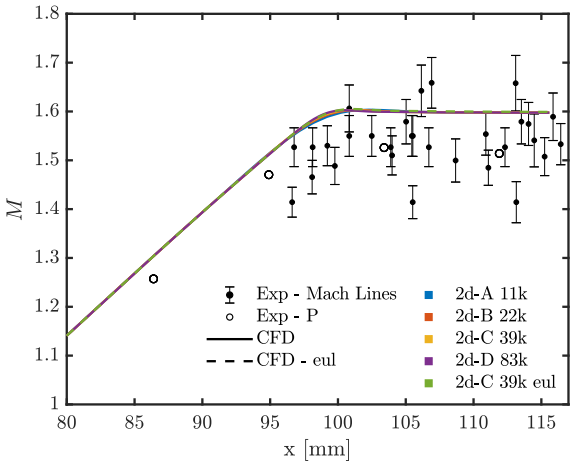

(b) Mach number along the nozzle axis. Zoom at the end of the divergent.

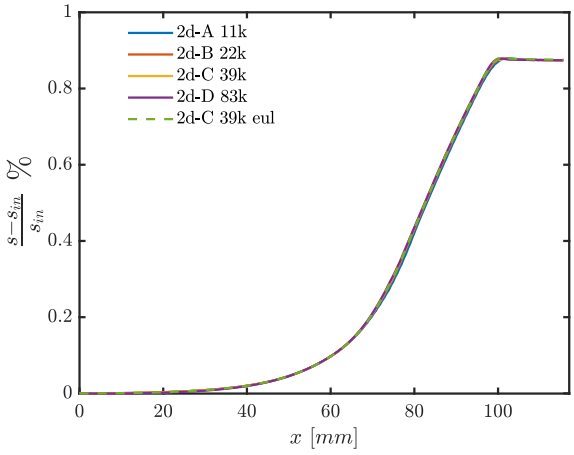

(c) Entropy along the nozzle axis.

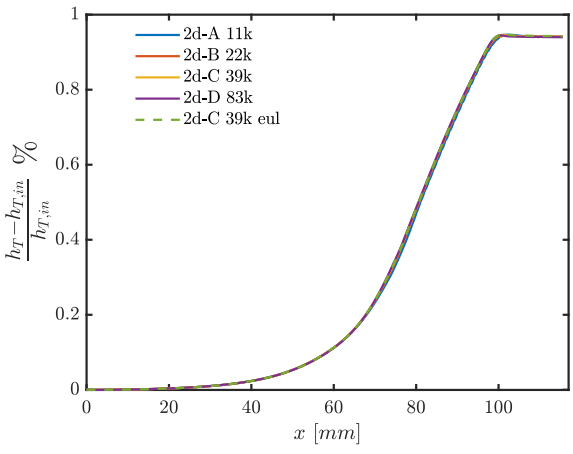

(d) Total enthalpy along the nozzle axis.

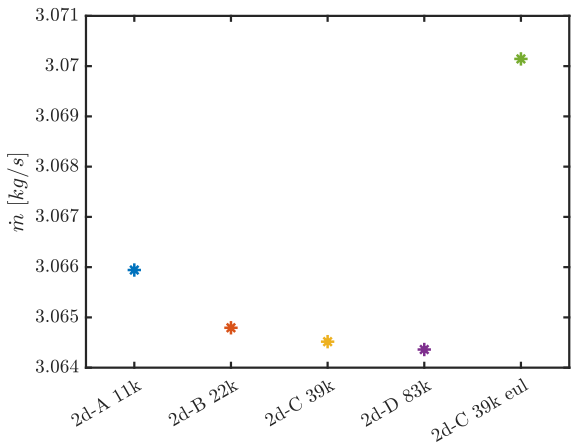

(e) Mass flow rate.

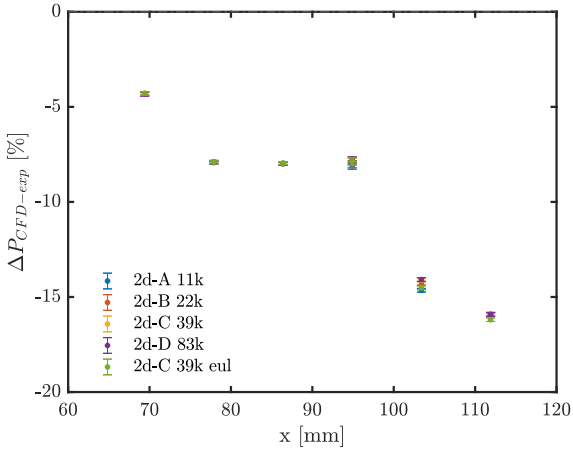

(f) Percentage pressure deviation between CFD and experimental results.

Figure 4.13. Grid dependence study for 2D viscous simulations on condition $44MMb - Z_T = 0.40$. A 2d inviscid simulation is also included for comparison.

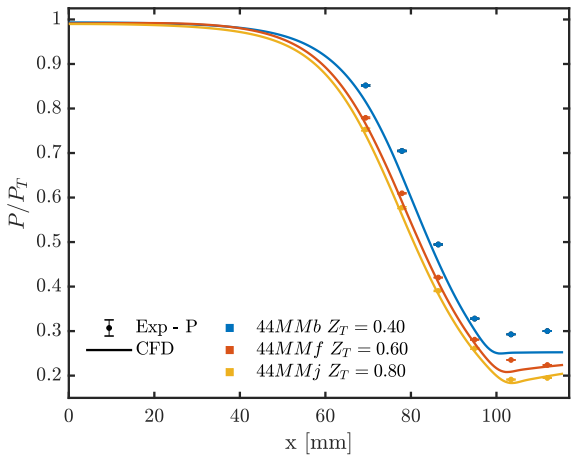

(a) Pressure ratio along the nozzle axis.

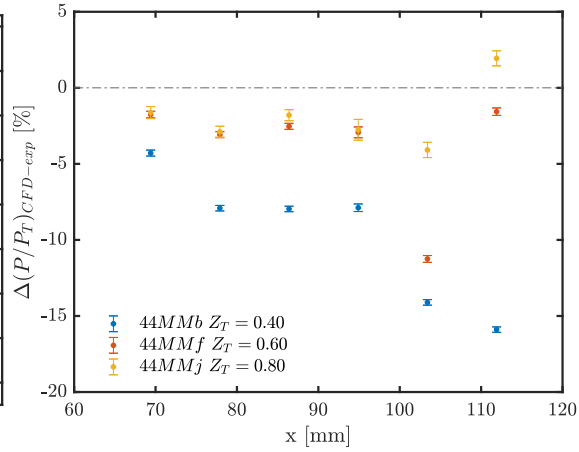

(b) Percentage pressure ratio deviation between CFD and experimental results.

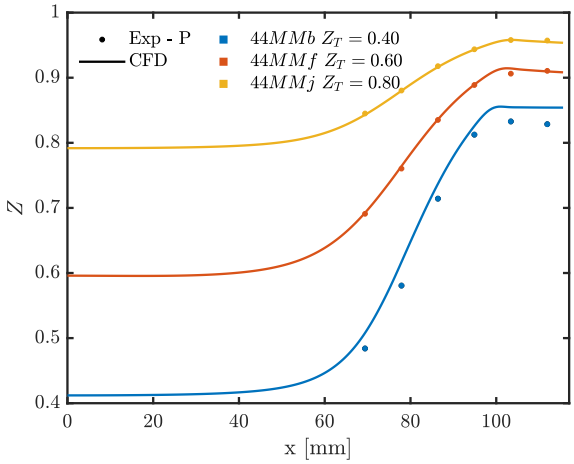

(c) Compressibility factor along the nozzle axis.

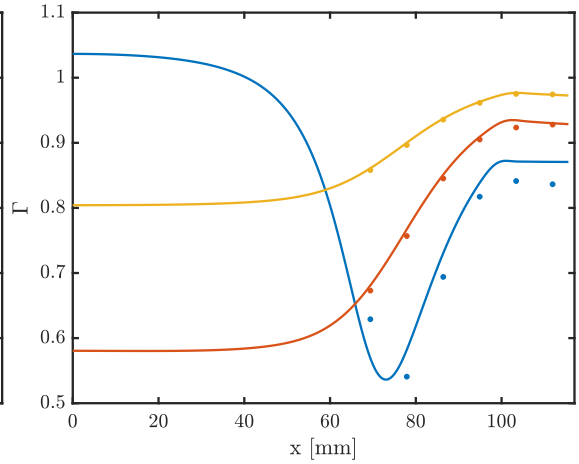

(d) Fundamental derivative of gasdynamics along the nozzle axis.

Figure 4.14. Comparison of conditions during test $44MM$.

4.7 Conclusions

This chapter presented results from an extensive experimental campaign concerning supersonic non-ideal flows of siloxane MM from strongly non-ideal conditions at $Z_T = 0.39$ to dilute ones at $Z_T = 0.98$. The non-ideal dependance of isentropic expansions on total conditions was experimentally verified with pressure measurements and Mach number extraction from schlieren visualizations, and was verified with CFD calculation.
The latter also allowed to assess the negligible impact of boundary layer on nozzle flow and evidence the different extent of flow recompression in the turning region depending on operating conditions. The effect of boundary layer growth should be analyzed in better detail in the future with the use of 3d simulation considering front and back test section walls aswell. It could be more relevant in strongly off-design nozzle conditions in which the flow is significantly recompressed in the *turning region* at the end of the nozzle, possibly contributing to an increased boundary layer growth. Moreover, adiabatic conditions were considered for CFD calculation. This is a reasonable hypothesis, considering that the test section is heated and insulated with respect to the ambient temperature and that the relatively small nozzle size means a low flow crossing time and a reduced heat transfer area. However, the test section is heated to wall temperatures that are actually $5 - 10\,°C$ higher than the expected total temperature in order to avoid possible flow condensation on the test section walls. It is thus possible that heat transfer to the fluid is infact not negligible. This could be verified by performing full 3d simulations including the experimental temperature gradient between the wall and the fluid.
Experimental tests covered a significant part of the vapor phase of fluid siloxane MM, allowing to gather data of expansions sharing the same total compressibility factor but markedly different total conditions. This allowed to experimentally verify the suitability of Z_T as a similarity parameter for conditions with $Z_T \geqslant 0.60$, confirming theoretical findings presented in Section 2.

CHAPTER 5

NON-IDEAL SUBSONIC CHOKED NOZZLE EXPANSIONS

This chapter reports experimental results characterizing the subsonic expansion of siloxane MM in nozzles cMM07, cMM05 and cMM02. Non-ideal effects were thoroughly experimentally investigated in supersonic conditions only until now, because these are the operating regimes attracting most research interest in the field of unconventional turbomachinery (e.g. turbines in ORCs). In subsonic conditions, much less experimental evidence was instead gathered due to the comparatively small subsonic region in the employed converging-diverging nozzle nMM16 and a consequent low number of pressure taps there. The experimental campaign reported here focuses on non-ideal subsonic flows because they are anyways relevant in the NICFD field and in engineering applications. Indeed, whilst compressibility effects are less pronounced with respect to the supersonic regime, thermodynamic non-ideality is stronger compared to supersonic flow at same total conditions since the flow is less expanded. Moreover, non-ideal subsonic flows occur in sections of organic Rankine cycle plants where mass flow rate or performance measurements would be performed if appropriate instrumentation were widely available, such as turbine inlet sections, and it is thus useful to investigate non-ideal subsonic conditions further.

As explained in Section 3.6, the employed choked converging nozzles were specifically designed with a large portion of constant cross sectional area. This provides a region with reasonably uniform flow properties and Mach number in which pressure probes can be inserted for calibration in non-ideal flows. For this reason, the present experimental campaign is essential in preparation for Pitot tubes testing in non-ideal flows in order to characterize the wind tunnel at different subsonic Mach numbers before probe insertion in the test section.

One set of initial total pressure and temperature was considered for each one of the three nozzles, with conditions ranging from mildly non-ideal at $Z_T = 0.80$ *to dilute at* $Z_T = 0.98$*. CFD calculation were also carried out as support and comparison to experimental results and to understand key flow features.*

Test ID	Nozzle	Most non-ideal condition			Least non-ideal condition		
		P_T $[bar]$	T_T $[°C]$	Z_T	P_T $[bar]$	T_T $[°C]$	Z_T
81MM	*cMM07*	8.58	212.0	0.75	0.83	198.4	0.98
212MM	*cMM05*	6.34	194.3	0.80	1.12	195.3	0.97
58MM	*cMM02*	7.30	206.6	0.79	0.34	194.3	0.99

Table 5.1. Least and most ideal total conditions of tests selected for analysis in the experimental campaign with siloxane MM and choked subsonic nozzles.

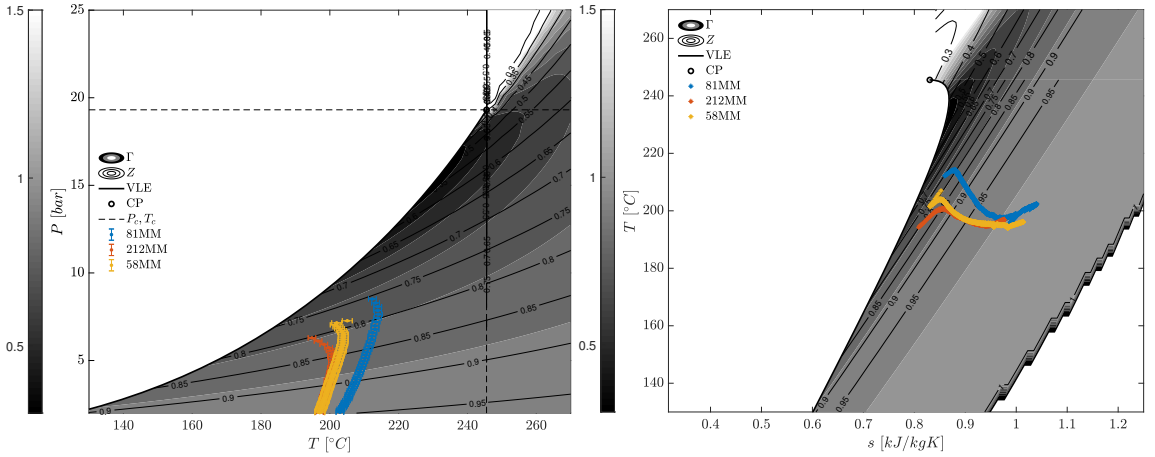

(a) $P - T$ plane.

(b) $T - s$ plane.

Figure 5.1. Evolution of total conditions during tests selected for analysis in the experimental campaign with siloxane MM and choked subsonic nozzles *cMM07*, *cMM05*, *cMM02*.

5.1 Test Conditions

An average of $4 - 5$ tests were repeated for each subsonic nozzle, each taking up to one full day for preparation. Consistency and repeatability were assessed as illustrated in Section 4.2 for supersonic conditions, although the complete analysis will not be reported here for brevity. Conclusions are therefore based on repeated measurements and only one test is analyzed here for each nozzle and set of initial total conditions, as reported in Table 5.1. The evolution of total conditions is reported for all tests in $P - T$ and $T - s$ diagrams in Figure 5.1.
Experimental results, together with CFD calculation, will be reported in the following sections for each choked subsonic nozzle.

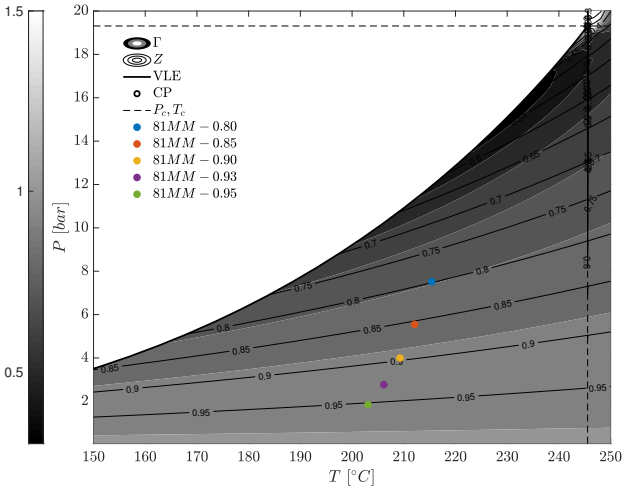

Figure 5.2. $P-T$ diagram with Z and Γ contours with total conditions of expansions selected from test *81MM*.

Name	P_T $[bar]$	T_T $[°C]$	Z_T $[-]$
81MM-0.80	7.52	215.41	0.80
81MM-0.85	5.55	212.11	0.85
81MM-0.90	4.00	209.28	0.90
81MM-0.93	2.77	206.14	0.93
81MM-0.95	1.85	203.08	0.95

Table 5.2. Selected test conditions during Test *81MM*.

5.2 Nozzle cMM07

The present section reports the chosen experimental conditions during representative test on nozzle *cMM07*, followed by a detailed explanation of the implemented 2D and 3D CFD calculation framework. Experimental and numerical results are finally presented together for analysis. CFD simulations of non-ideal choked subsonic expansions of siloxane vapor MM are compared against pressure and Laser Doppler Velocimetry (LDV) measurements. The latter were performed on nozzle *cMM07* in synergy with a past Ph.D. thesis (Gallarini, 2020). Pressure from LDV results was retrieved using measured total pressure and temperature, and the energy conservation equation together with the assumption of isentropic flow.
Quasi-1D calculations are also reported as further theoretical reference.

5.2.1 Experimental Dataset

Figure 5.2 and Table 5.2 report the total conditions extracted at different values of the total compressibility factor during test *81MM*.
These will be considered for experimental and CFD results analysis.

5.2.2 CFD Calculation Framework

Solver Setup

Analogously to simulations on supersonic nozzle *nMM16*, CFD calculation are carried out using code *SU2 - v7.0.1* and the embedded Peng-Robinson equation of state in polytropic form.
For viscous calculation, the $k-\omega$ *SST* turbulence model is used. Viscosity and thermal conductivity are assumed constant and equal to the values calculated using the *FluidProp* library at the considered nozzle stagnation conditions. In all cases, the solution is time-marched with an implicit Euler scheme. A second-order accurate MUSCL scheme of Roe type is employed with Venkatakrishnan flux limiter. The Green-Gauss formula is used to compute gradients at cell interfaces.

Grid Name	elements	points
$2d - A$	22k	22k
$2d - B$	49k	49k
$2d - C$	87k	88k
$2d - D$	165k	166k
$2d - E$	354k	355k

Table 5.3. Meshes for grid dependence study for 2D viscous simulations.

Nozzle Geometry and Numerical Domain

The choked subsonic nozzle geometry is described in detail in Section 3.6. Differently to calculation in supersonic nozzles however, CFD simulation of the nozzle here considered requires including a portion of the downstream volume in the numerical domain. The mere choked nozzle geometry is inappropriate because part of the physical phenomenon is lost, since the sonic throat extending in the downstream volume is not simulated. A preliminary 2D viscous simulation was performed on a domain including the convergent only. Full results will not be presented here for brevity, but the simulation was indeed found to be not representative of the actual flow field because the flow was not choked. As a consequence, the Mach number in the constant cross-section was not the expected one (~ 0.7) and results were in complete disagreement with quasi-1D theory and experimental measurements.
Thus, a downstream volume of size about twice the nozzle length was included in the numerical domain, as illustrated in Figure 5.3. The downstream volume geometry was simplified with respect to the real one, allowing to greatly reduce the computational burden. The real downstream volume has a slight enlargement (few *mm*) in the direction perpendicular to the plane at a certain distance after the geometrical throat which depends on nozzle length. Also, the geometry transitions to a circular cross section and is no longer planar. The numerical domain is instead assumed to be planar everywhere, so that, in case of 3D simulations, the model is simply an extrusion of the 2D domain by a depth equal to the test section one.
No symmetries were exploited to reduce calculation time due to issues with symmetry boundary conditions in the code. The flow was considered adiabatic, with no heat exchange to/from walls.

Simulated Test Conditions

Simulated conditions correspond to time instants at selected total compressibility factor values during test $81MM$, as reported in Table 5.2. The downstream ambient pressure imposed as boundary condition was taken from experimental results and was never larger than 0.5 bar, consistently with the fact that *HPV* pressure is always significantly larger than the *LPV* one, since the latter vessel is vacuumized before each test run and its volume is about ~ 6 times larger than the *HPV*.
Grid dependence analysis was performed, both in 2D and 3D domains, with the $81MM - 0.80$ condition only. Different test $81MM$ conditions were then simulated with the grid-independent 3D viscous mesh only.

5.2.3 2D Viscous Calculation on Structured Meshes

Exploiting the planar geometry of the numerical domain, 2D simulations were first considered. Several structured meshes were generated to perform a grid dependence analysis, all having a first cell height of 1×10^{-7} m to keep the y^+ coordinate at the wall below 1. Table 5.3 reports mesh names, number of elements and points, and Figure 5.3 illustrates an exemplary mesh.

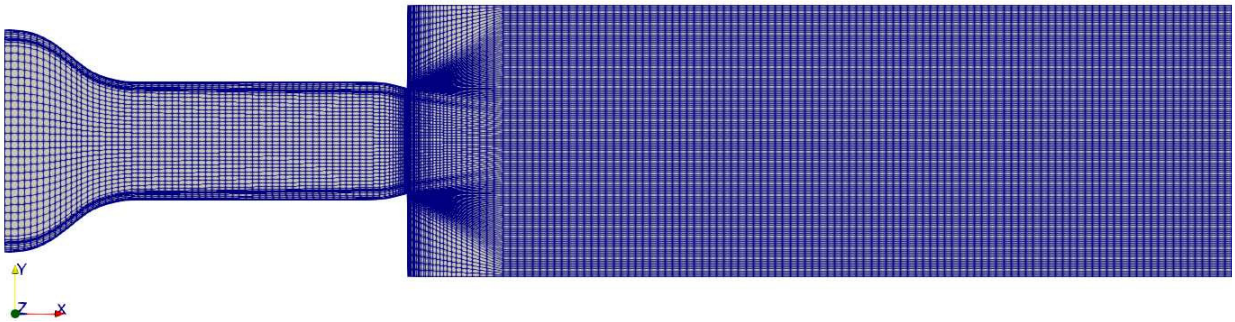

Figure 5.3. Viscous mesh $2d - A$ including the downstream volume.

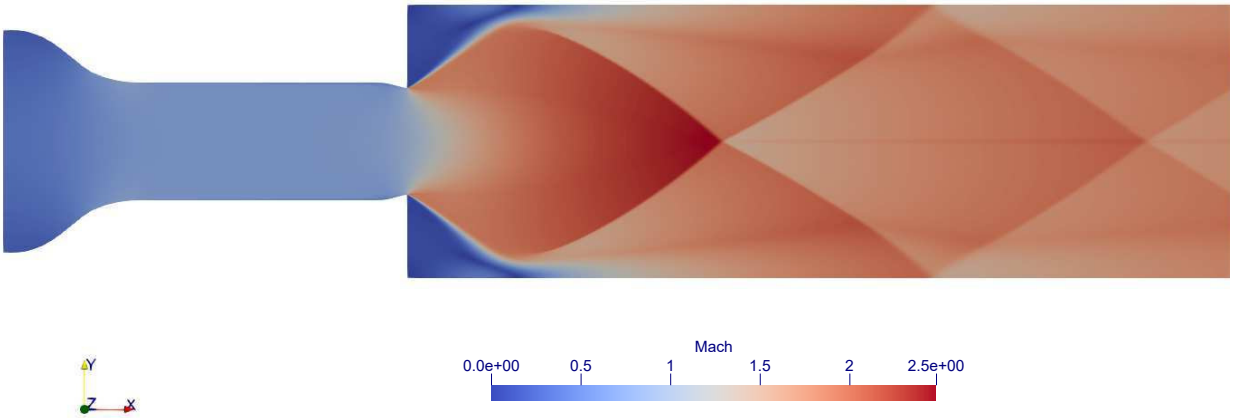

Figure 5.4. Mach contour for the flow field including the downstream volume with mesh $2d - D$.

Riemann boundary conditions were applied, with total conditions at the inlet and downstream pressure set at the outlet of the downstream volume. No-slip conditions were applied at all nozzle walls. All walls in the downstream volume were instead assumed as euler walls.

The Mach number contour for the flow field including the downstream volume can be found in Figure 5.4. A strong post expansion occurs after the throat due to the very low outlet pressure. Expansion fans reflect off the downstream volume walls giving rise to a weak shocks pattern which propagates to the outlet.

As evident in Figure 5.5, the boundary layer growth along the nozzle length is significant, so as to lead to a non-negligible passage area reduction and a change in pressure in the nozzle constant area section.

Figures 5.6a and 5.6b are plots of pressure and velocity trends along the nozzle axis for the different meshes. For comparison, 1D calculation and experimental data from pressure and LDV measurements are reported. Different meshes have almost perfectly superimposed curves, with pressure difference between roughest and finest mesh below 2 mbar (corresponding to less than 0.03 %) and velocity differences of the order of 0.1%.
All meshes are capable of capturing the effect of boundary layer growth, since pressure and velocity trends indicate an acceleration in the constant cross-section region due to the reduction in effective passage area.

The percentage variation with respect to the total condition value at nozzle inlet is reported for

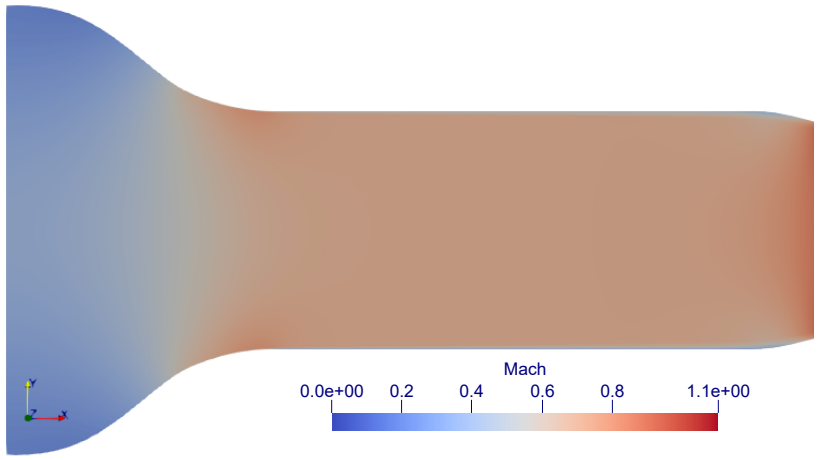

Figure 5.5. Detail of the Mach number in the nozzle for the 2D domain with mesh $2d - D$. Boundary layer growth is evident.

entropy and total enthalpy along the axis in Figures 5.6c and 5.6d. Curves are almost perfectly superimposed for all meshes. Both quantities vary by less than 0.07% with respect to stagnation values from nozzle inlet to throat, implying limited numerical dissipation effects (Gori et al., 2019b).
Figure 5.6e shows the mass flow rate for the different meshes. The trend is asymptotic as mesh size increases, but all values are within 0.1% of the finest mesh.
The accordance between numerical and experimental results is evaluated by means of the percentage pressure deviation $\Delta P_{CFD-exp}$, defined in Equation 4.5 and reported in Figure 5.6f. It is calculated at all pressure taps and at the LDV measuring position (using pressure determined from the velocity measure). The percentage deviation uncertainty $U_{\Delta P_{CFD-exp}}$ is also considered as per Equation 4.6, with the assumption of no uncertainty in CFD computations and in pressure from LDV.

Overall, 2D viscous calculation on structured meshes are in good agreement with experimental measurements, with a percentage pressure deviation always well below 2%, although discrepancies are larger than experimental uncertainty. No remarkable differences are evident between the different meshes in the grid dependence study.
Pressure from numerical simulations is within errorbars of the measured one at only one pressure tap ($\sim$ 80 mm). At the LDV measuring point, CFD pressure is 50 mbar higher than the one calculated from LDV measures, resulting in a percentage difference below 0.8 %. Also, CFD velocity is 2 m/s lower than LDV, corresponding to a 2% difference.

Comparison with Viscous calculation on Unstructured Meshes

Viscous calculation on unstructured meshes were also carried out. Results and grid convergence study are not reported here because they were found to be equivalent to the structured grid results above. Indeed, comparison between grid independent results on structured and unstructured meshes showed a pressure difference below 0.07 % and a velocity percentage difference well below 0.2%.

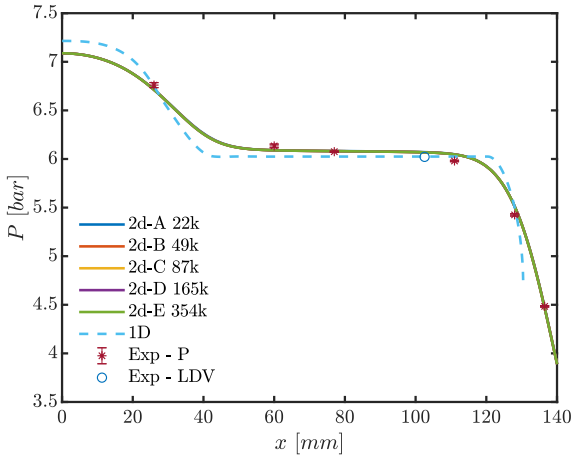

(a) Pressure along the nozzle axis.

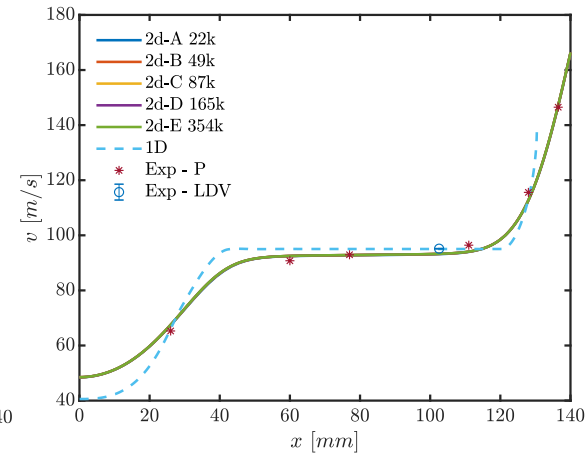

(b) Velocity along the nozzle axis.

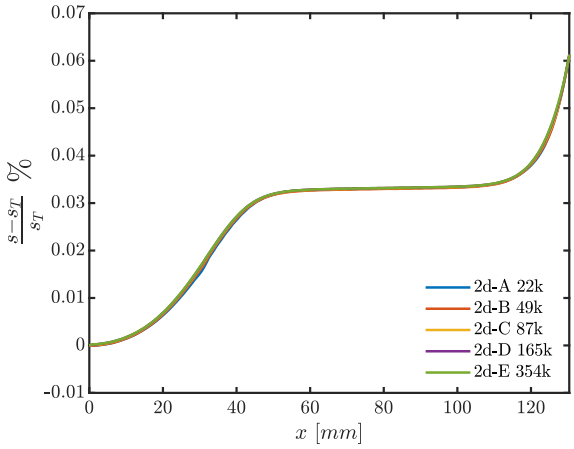

(c) Entropy along the nozzle axis.

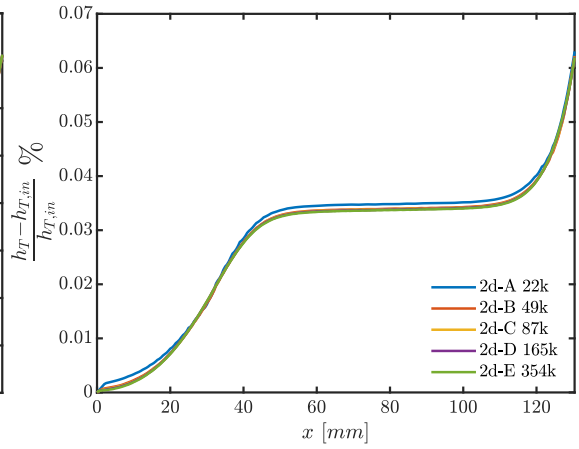

(d) Total enthalpy along the nozzle axis.

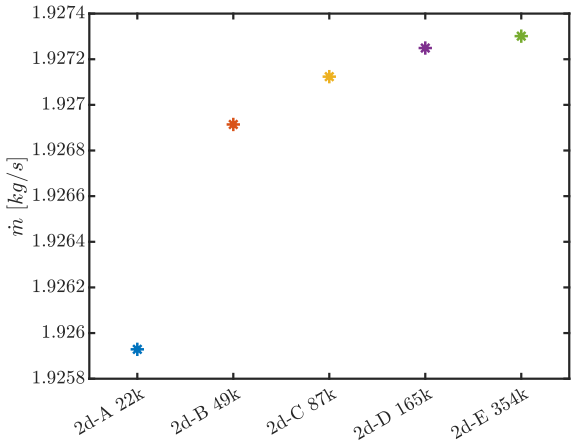

(e) Mass flow rate

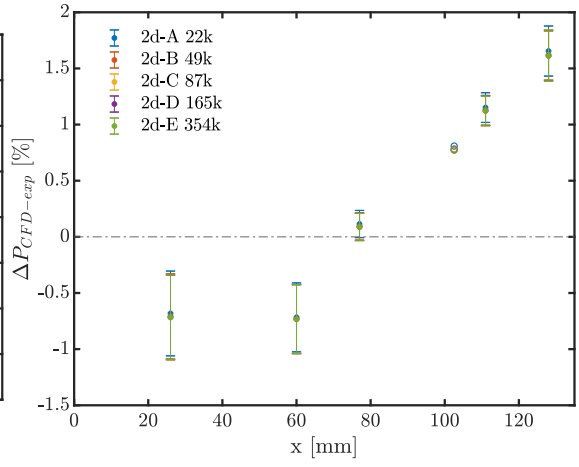

(f) Percentage pressure deviation between CFD and experimental results. The empty dot represent the LDV measure.

Figure 5.6. Grid dependence study for 2D viscous simulations on $81MM - 0.80$ conditions.

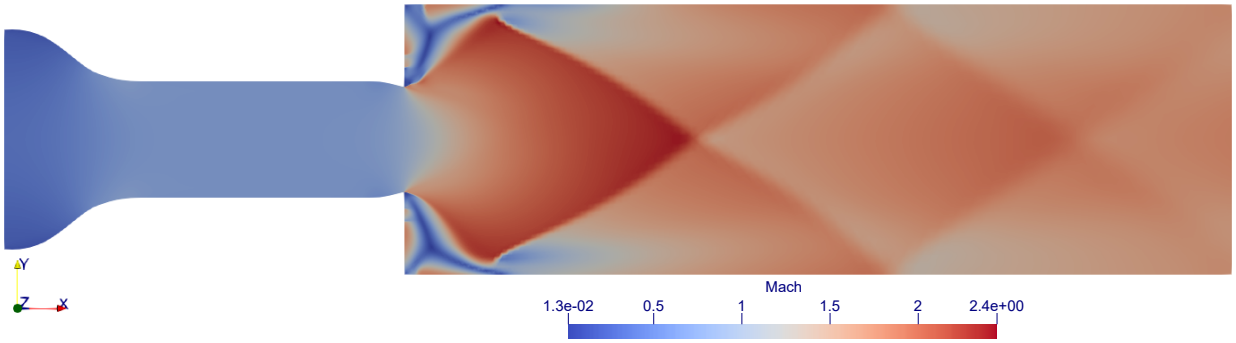

Figure 5.7. Mach contour for 2D inviscid calculation.

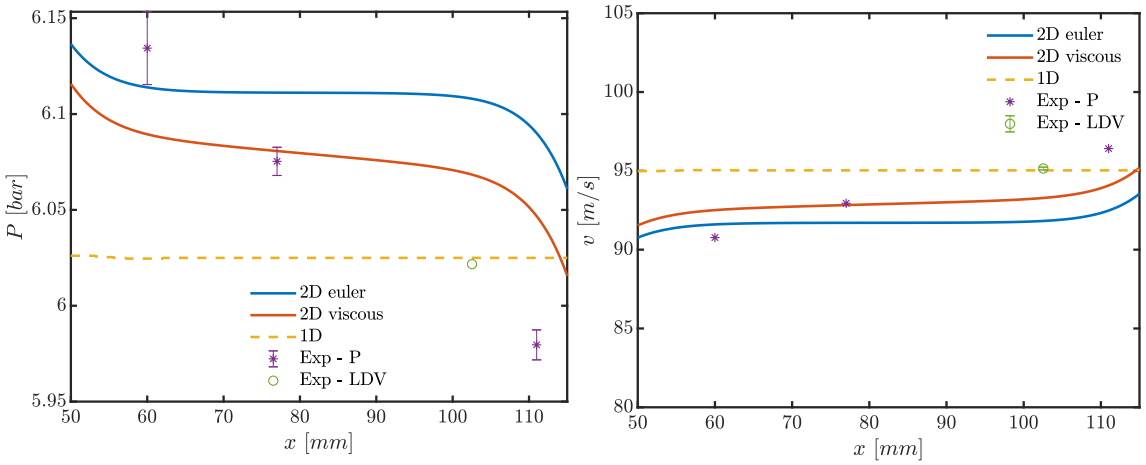

(a) Pressure.

(b) Velocity.

Figure 5.8. Comparison of axis trends between 2D viscous and inviscid simulations. The figure is zoomed on the constant cross-section part of the nozzle.

Comparison with Inviscid calculation on Unstructured Meshes

Grid independent solutions were compared for 2d viscous calculation on structured meshes and inviscid calculation on unstructured grids. Figure 5.7 reports the Mach number contour for the computed inviscid flow field. If compared to Figure 5.4, the shape of the sonic throat and expansion fans do not show significant differences. However, it is clear that no boundary layer is present on the nozzle wall in this case.

The discrepancy between viscous and inviscid axis solutions in Figures 5.8a and 5.8b indicates that viscous effects related to boundary layer growth have a significant impact on the flow field. Indeed, inviscid results show stronger disagreement with experimental results because the effective passage area decrease due to boundary layer is not accounted for.

Since viscous effects were found to be non-negligible in the 2D case, it is natural to hypothesize that boundary layers on the whole depth of the test section and on the front and rear walls might also have an impact on the flow field. For this reason, 3D CFD calculations were also carried out.

Grid Name	elements	points
$3d - A$	453k	476k
$3d - B$	1.5M	1.6M
$3d - C$	2.8M	2.9M
$3d - D$	6.5M	6.6M

Table 5.4. Meshes for grid dependence study for 3D viscous simulations.

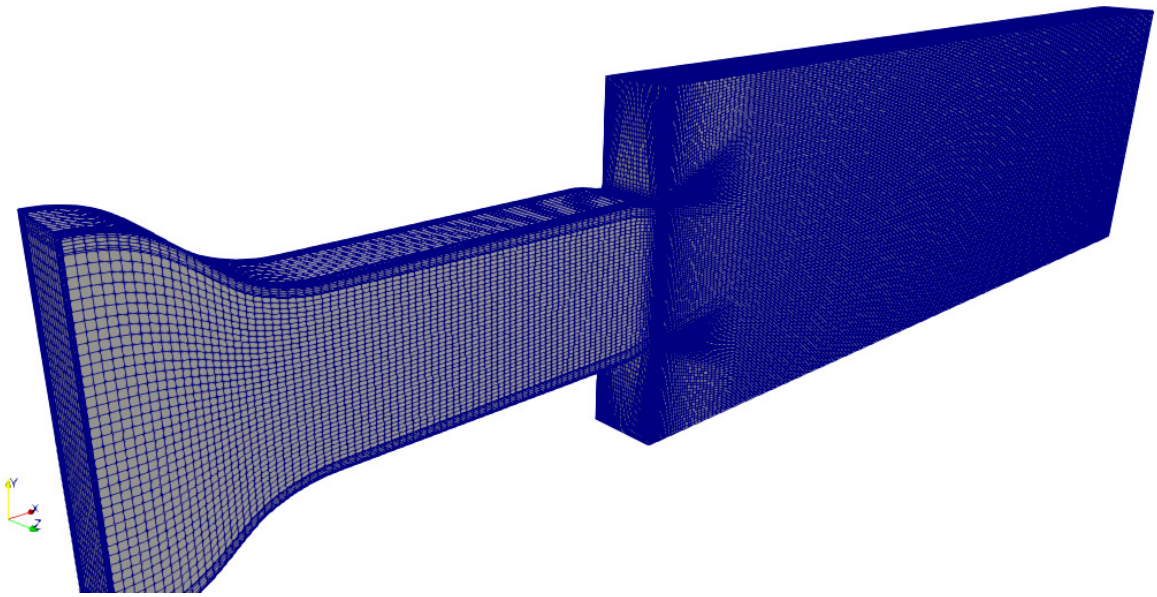

Figure 5.9. Structured mesh for viscous calculation $3d - B$.

5.2.4 3D Viscous Calculation on Structured Meshes

As aforementioned, the 3D numerical domain is an extrusion of the 2D one along the test section depth. The same boundary conditions as in the 2D case were applied, with the addition of no-slip conditions on front and back nozzle walls. Analogously to 2D viscous calculation, several structured meshes were generated to perform a grid dependence analysis, all having a first cell height of 1×10^{-7} m to keep the y^+ coordinate at the wall below 1. Table 5.4 reports mesh names, number of elements and points and an exemplary mesh can be found in Figure 5.9.

Figure 5.10 shows the Mach countour for the 3D flow field including the downstream volume, which is analogous to the 2D counterpart.

Figures 5.11a, 5.11b and 5.11c, 5.11d are plots of pressure and velocity trends along the nozzle axis for the different meshes. For comparison, 1D calculation and experimental data from pressure and LDV measurements are reported.
Different meshes have almost perfectly superimposed curves, with pressure difference between roughest and finest mesh below 0.08% and velocity differences of the order of 0.2%.
Figures 5.11e and 5.11f show entropy and total enthalpy trends along the nozzle axis, which are again well superimposed for all meshes. For both quantities, the percentage variation with respect to the total condition value is reported. Just like in the 2D case, entropy and total enthalpy vary by less than 0.06% from nozzle inlet to throat, implying limited numerical dissipation effects.
Figure 5.12a shows the mass flow rate for the different meshes. The trend is not asymptotic as

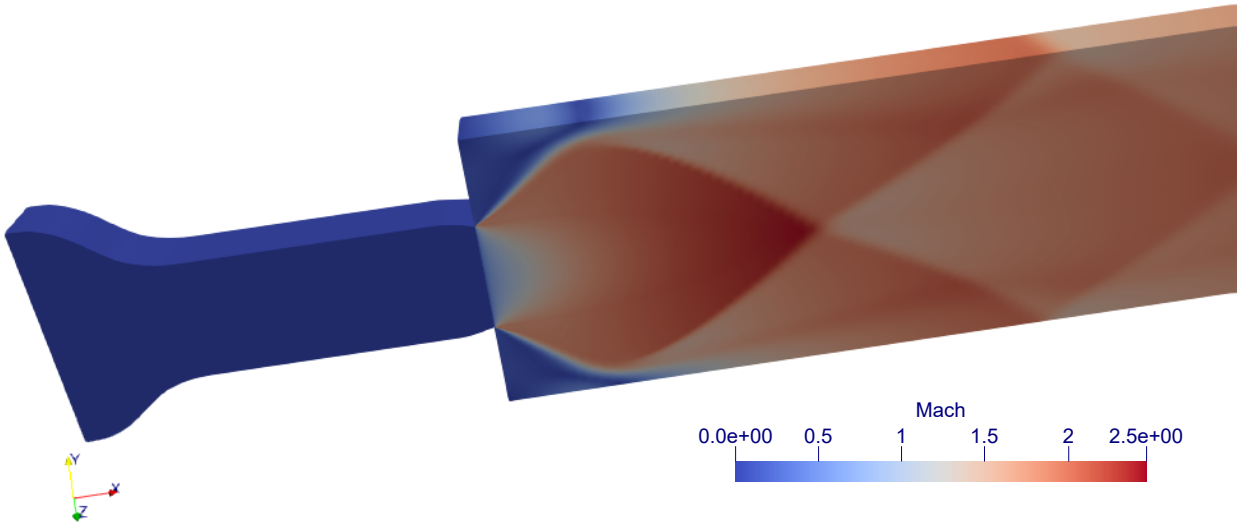

Figure 5.10. Mach contour for the 3D flow field.

mesh size increases, but all values are within 0.0015% of the finest mesh.
The percentage pressure deviation between numerical and experimental results, as defined in Equation 4.5, is reported in Figure 5.12b. Overall, the value of $\Delta P_{CFD-exp}$ is always well below 1.5%. Differences with respect to experimental measurements are generally larger than uncertainty, analogously but with better agreement compared to 2D simulations. Pressure is within errorbars from the measured one at only one pressure tap (~ 80 mm). At the LDV measuring point, CFD pressure is 20 mbar ($\sim 0.3\%$) higher than the one calculated from LDV measures. Also, CFD velocity is < 1 m/s lower than LDV, corresponding to $< 1\%$ difference.

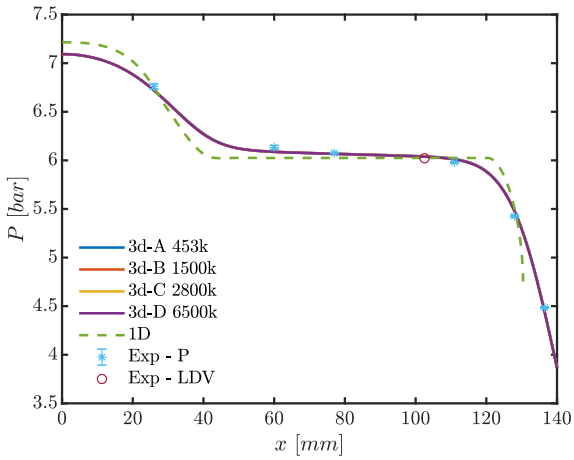

(a) Pressure along the nozzle axis.

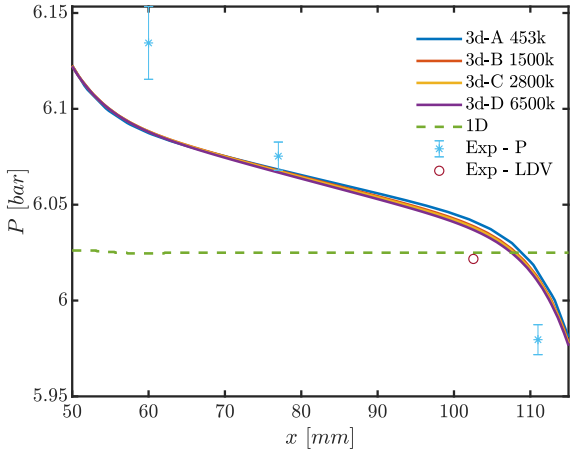

(b) Pressure along the nozzle axis. Zoom at the constant cross sectional area.

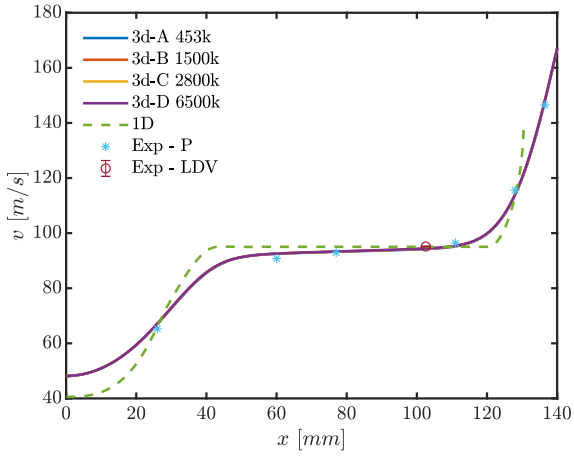

(c) Velocity along the nozzle axis.

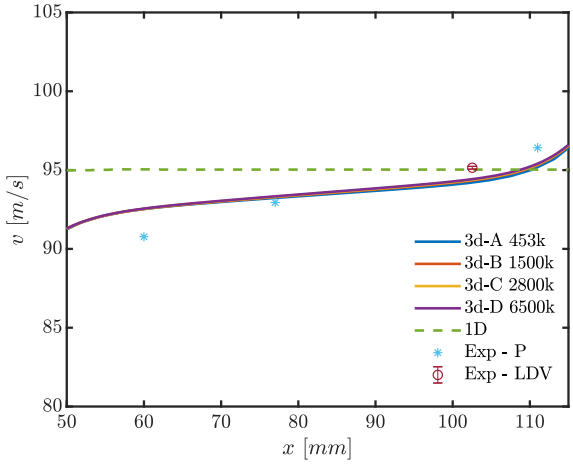

(d) Velocity along the nozzle axis. Zoom at the constant cross sectional area.

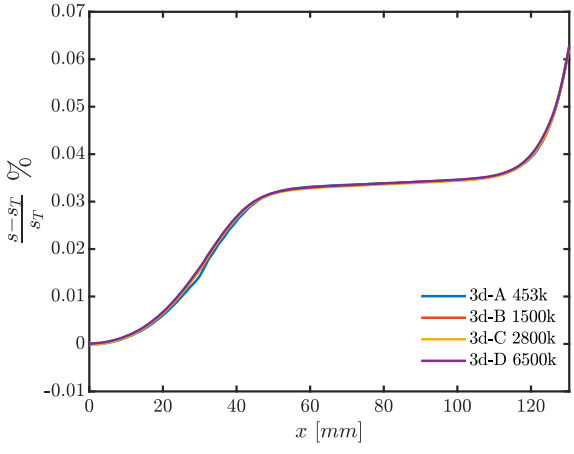

(e) Entropy along the nozzle axis.

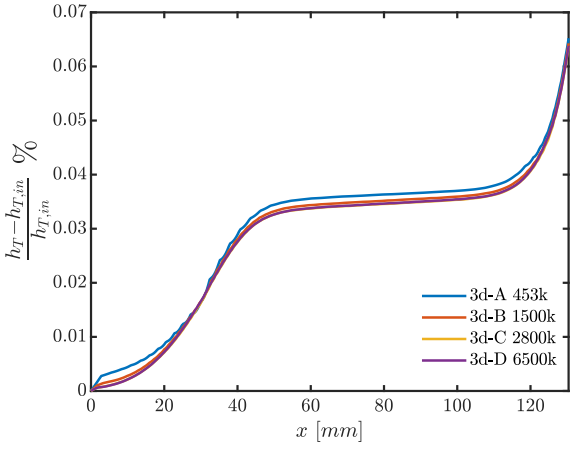

(f) Total enthalpy along the nozzle axis.

Figure 5.11. Grid dependence study for 3D viscous simulations including the downstream volume.

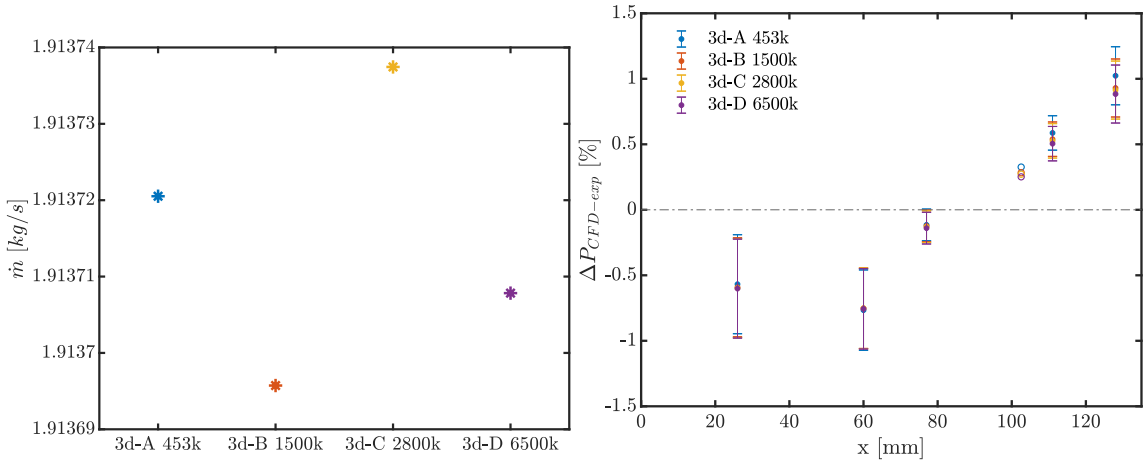

(a) Mass flow rate

(b) Percentage pressure deviation between CFD and experimental results. The empty dot represents the LDV measure.

Figure 5.12. Grid dependence study for 3D viscous simulations including the downstream volume.

5.2.5 3D vs. 2D Calculation

Viscous grid independent solutions are compared in 2D and 3D cases in Figure 5.13. There is a noticeable difference in nozzle axis pressure and velocity trends between the two cases due to the impact of boundary layer on the effective passage area, which leads to slightly stronger flow expansion in the constant area region in the 3D case. For this reason, the latter shows better agreement between CFD and experiment, as evident in the percentage pressure deviation in Figure 5.13e, especially towards the end of the nozzle where boundary layer thickness is larger and its impact is therefore more significant.

This indicates that boundary layer needs to be properly accounted for, both with the use of turbulence models and with the full 3D numerical domain, to produce accurate simulations of the problem here considered, as evident in Figure 5.14.

Pressure difference between the beginning and end of the constant cross-section region is of the order of 50 mbar. Whilst in percentage terms this corresponds to a $\sim 1\%$ variation, in absolute terms it is larger than transducers uncertainty ($\sim 7 - 10$ mbar) and is thus significant from an experimental point of view. For example, this is important in case pressure probes are inserted in the constant area portion of the nozzle for calibration. Since a reference static pressure is needed, a wall tap in correspondence of the probe holes will have to be considered. In common practice, probes calibration in air takes place in semi-confined nozzles and a tap upstream of the nozzle exit is taken as reference. If a static tap too far upstream were considered here, the effect of boundary layer in such relatively small and confined test section would result in assuming the wrong reference pressure and possible inaccurate probe calibration.

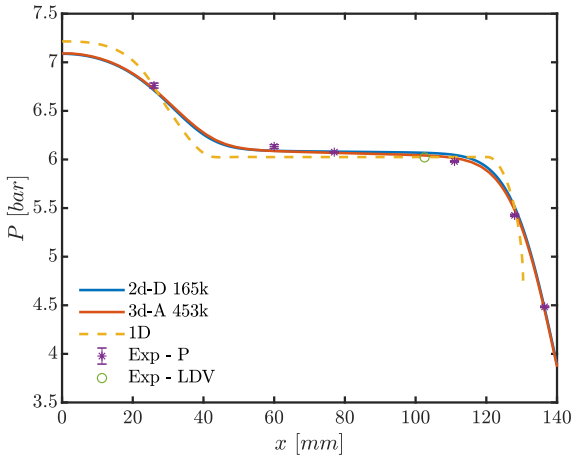

(a) Pressure - entire nozzle.

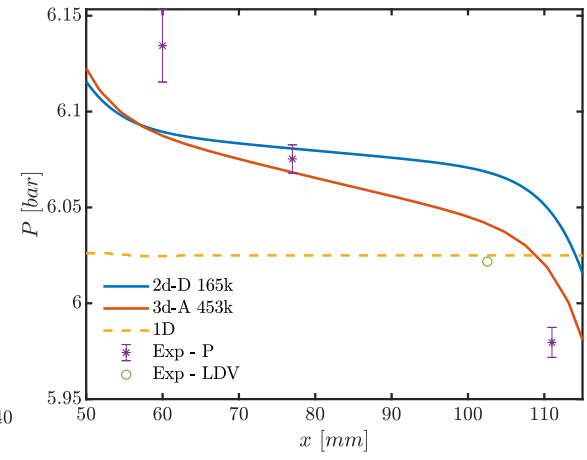

(b) Pressure - zoom in the constant area portion.

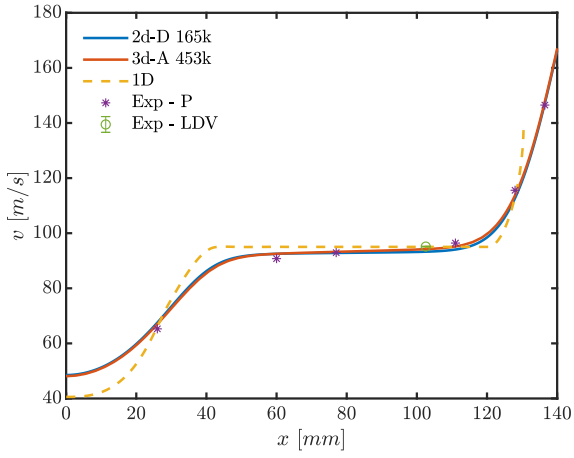

(c) Velocity - entire nozzle.

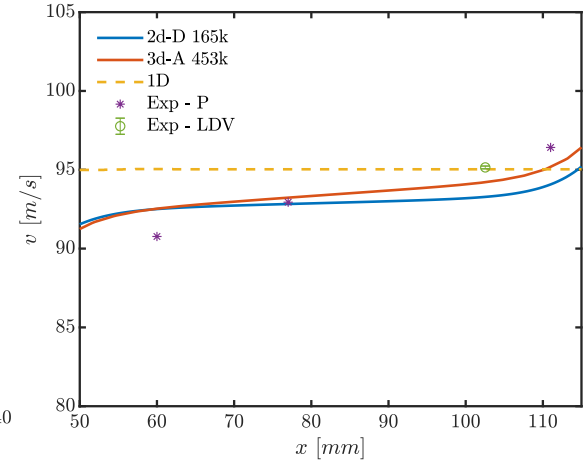

(d) Velocity - zoom in the constant area portion.

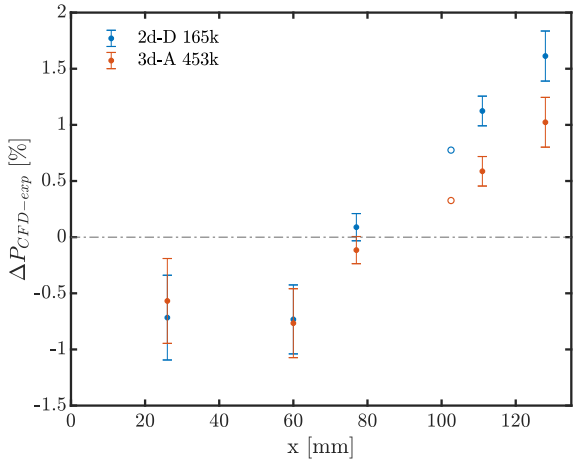

(e) Percentage pressure deviation between CFD and experimental results. The empty dot represent the LDV measure.

Figure 5.13. Pressure, velocity and percentage pressure deviation along the nozzle axis for 2D and 3D simulations.

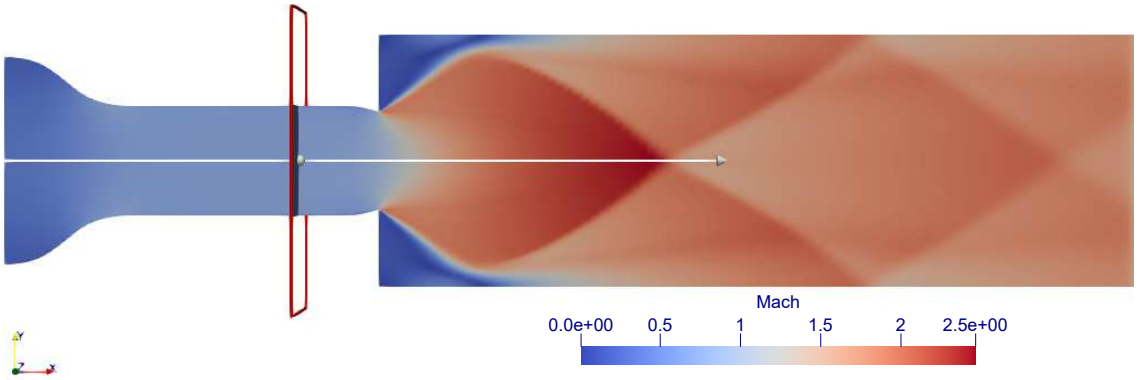

(a) Mach number flowfield with cutting plane at 102.5 mm (LDV measurement point).

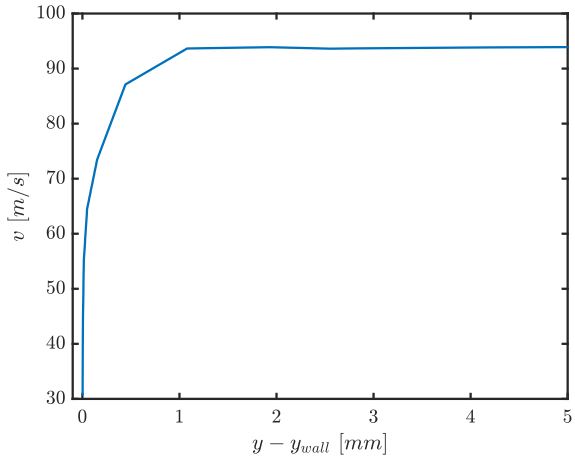

(b) Velocity in the cutting plane as a function of distance from the wall in the y-direction, with constant $z = 0$ mm.

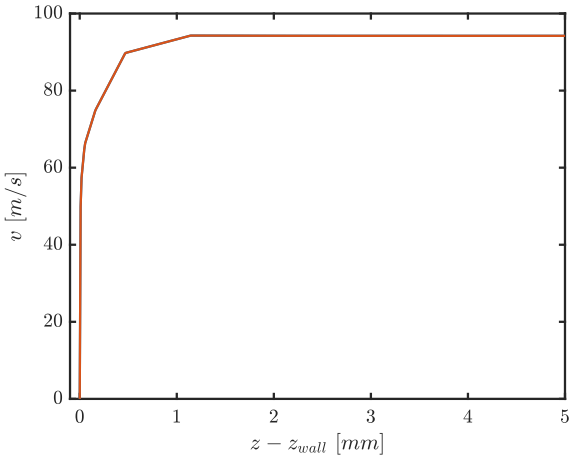

(c) Velocity in the cutting plane as a function of distance from the wall in the z-direction, with constant $y = 0$ mm.

Figure 5.14. Cutting plane at 102.5 mm (LDV measurement point), with plots of velocity in the cutting plane as a function of wall distance in y- and z-directions, indicating a boundary layer thickness ~ 1 mm.

5.2.6 Non-Ideal Expansion Dependance on Total Conditions

CFD calculation were performed for all other selected conditions from test $81MM$ in order to verify the effects of non-ideality. Given the long calculation time, the roughest available mesh $3d - A$ was employed. The value of the y^+ coordinate at the wall was verified to be below 1 for all considered cases. For condition *81MM-0.93*, calculation was also performed on the finest mesh $3d - D$ in order to verify grid independence results for *81MM-0.80*. Indeed, very little difference between solutions on coarsest and finest meshes was found, confirming the suitability of mesh $3d - A$ for the current study and leading to considerable time savings.

Both experimental and numerical results highlight the non-ideal dependance of the expansion on total conditions. Less ideal conditions show a higher pressure ratio (Figures 5.15a and 5.15b) meaning that, given the same geometry, the flow is less expanded. The percentage pressure ratio difference between least and most ideal conditions in the constant cross-section region is about 2% with respect to the most ideal case. This is not insignificant, especially considering that the most non-ideal conditions have a value of $Z_T = 0.80$, which is not so extreme.
Counter-intuitively, the Mach number (Figures 5.15c and 5.15d) is also higher for less ideal conditions due to the much lower speed of sound, which more than counterbalances the lower flow velocity. The maximum Mach number difference between least and most ideal conditions is about 0.01 or 1.5% with respect to the most ideal case.
Compressibility factor and fundamental derivative trends and values differ for different total conditions. This indicates a different volumetric and caloric behaviour, which is consistent with the variation in pressure ratio and Mach number trends characterizing expansions.
The effect of boundary layer on pressure ratio seems to be constant across all levels of ideality. The difference between CFD pressure ratios at coordinates $x = 60\,\text{mm}$ and $x = 102.5\,\text{mm}$, corresponding respectively to the location of the first pressure tap in the constant are region and the position of the LDV measurement point, is ~ 0.007 for all total conditions. Depending on the actual total pressure level, however, this will result in a more or less noticeable pressure variation in the constant cross-section region due to the boundary layer. More extreme conditions at higher total pressure will therefore have a stronger impact in absolute terms. As an example, the pressure variation is $\sim 50\,\text{mbar}$ for the *81MM-0.80* condition having $P_T = 7.52\,\text{bar}$ whilst it reduces to $\sim 15\,\text{mbar}$ for *81MM-0.95* at $P_T = 1.85\,\text{bar}$.

Figure 5.16 reports the percentage pressure ratio deviation $\Delta(P/P_T)_{CFD-exp}$ between experimental and numerical results. It is defined, together with its uncertainty, analogously to the percentage pressure deviation in Equation 4.5. Here pressure is substituted by pressure ratio to be consistent with the comparison between expansions with different total conditions. It is evident that the level of agreement between CFD and experimental results does not significantly change with respect to *81MM-0.80* as more ideal conditions are approached. Compared to simulated conditions for supersonic nozzle *nMM16* where the minimum considered total compressibility factor was $Z_T = 0.40$, here it is $Z_T = 0.80$. Thus, the decrease in thermodynamic model accuracy with non-ideality surely has a much lower, or possibly negligible, impact here.

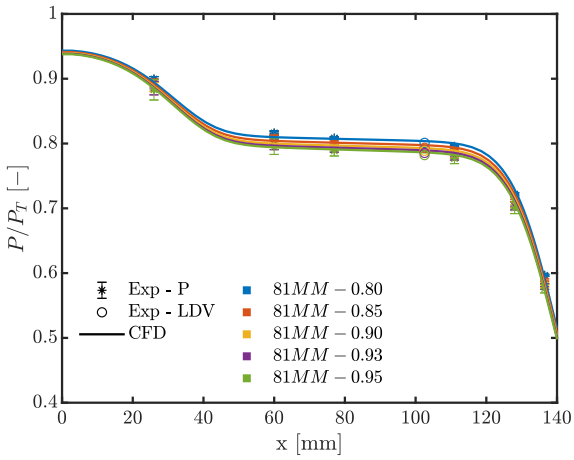

(a) Pressure ratio along the nozzle axis.

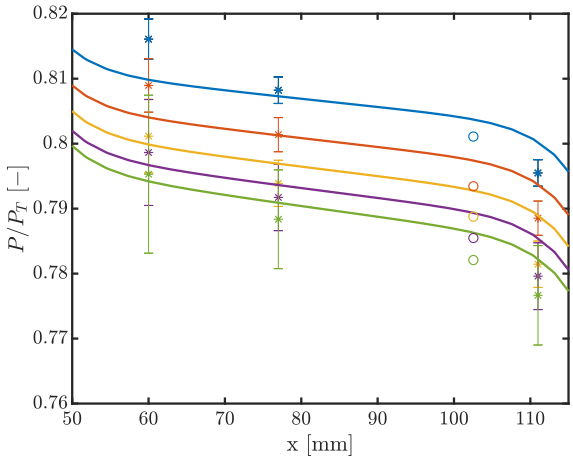

(b) Pressure ratio along the nozzle axis. Zoom at the constant cross sectional area.

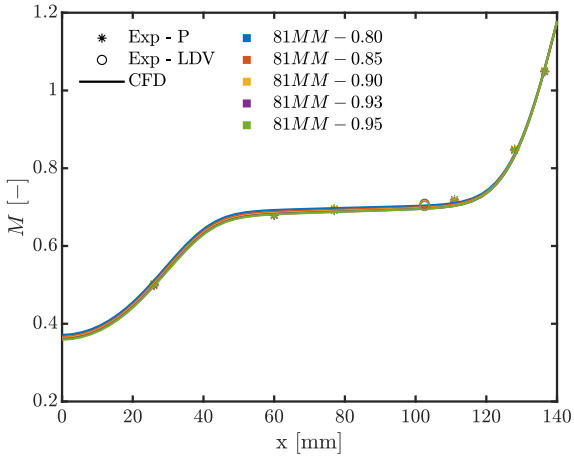

(c) Mach number along the nozzle axis.

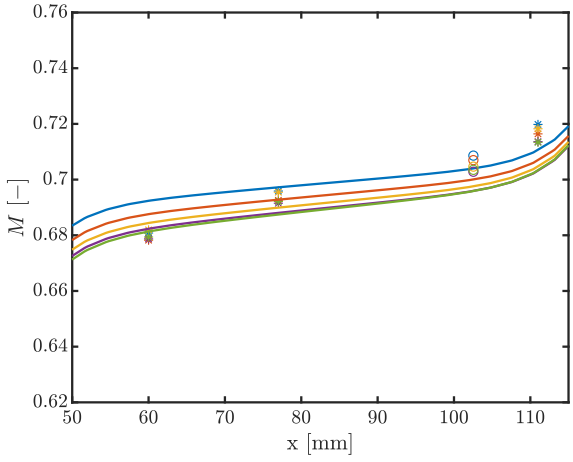

(d) Mach number along the nozzle axis. Zoom at the constant cross sectional area.

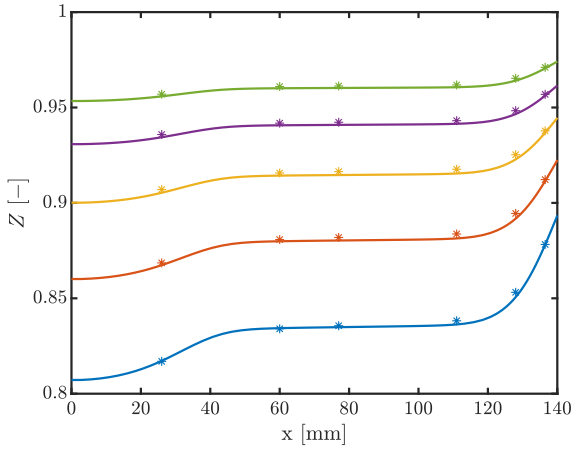

(e) Compressibility factor along the nozzle axis. LDV results not shown here.

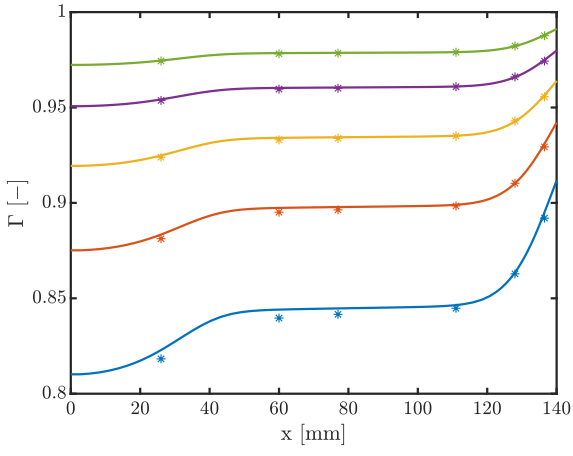

(f) Fundamental derivative of gasdynamics along the nozzle axis. LDV results not shown here.

Figure 5.15. Comparison of expansions at conditions during test $81MM$.

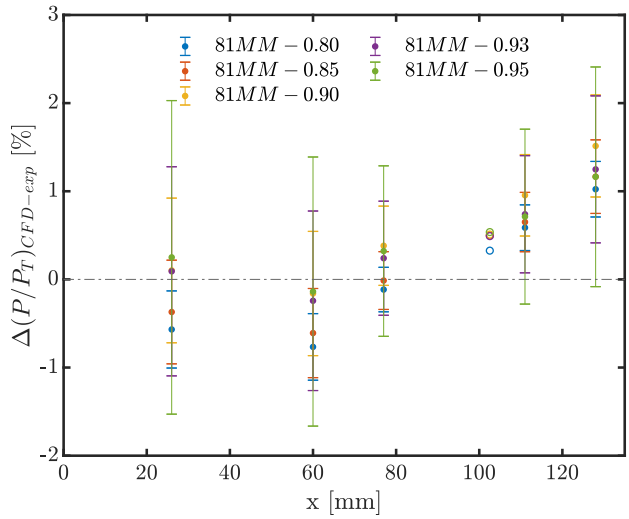

Figure 5.16. Percentage pressure ratio deviation between CFD and experimental results.

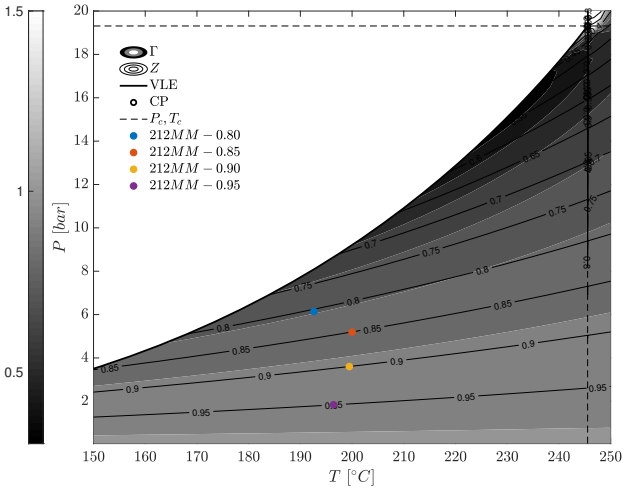

Figure 5.17. $P-T$ diagram with Z and Γ contours with total conditions of expansions selected from test *212MM*.

Name	P_T $[bar]$	T_T $[°C]$	Z_T $[-]$
212MM-0.80	6.34	194.6	0.80
212MM-0.85	5.22	200.5	0.85
212MM-0.90	3.60	199.3	0.90
212MM-0.95	1.84	196.7	0.95

Table 5.5. Selected test conditions during Test *212MM*.

5.3 Nozzle cMM05

5.3.1 Experimental Dataset

Figure 5.17 and Table 5.5 report the total conditions extracted at different values of the total compressibility factor during test *212MM* which will be considered for experimental and CFD results analysis.
No LDV measurements were performed on this nozzle.

5.3.2 CFD Calculation Framework

The same code, solver setup and numerical domain modeling as for nozzle *cMM07* were here employed for *cMM05* too. Building upon results for *cMM07*, calculation were performed directly on a 3D mesh with $567k$ elements created using the same cell spacing (including first cell height and growth law at the wall) as grid *3d-A*. Given that nozzle *cMM05* is longer than *cMM07*, the number of elements is slightly higher with respect to *3d-A* ($453k$).
The value of the y^+ coordinate at the wall was verified to be below 1 for all simulated conditions.

5.3.3 Non-Ideal Expansion Dependance on Total Conditions

Numerical and experimental data from all test *212MM* conditions are reported in Figure 5.18, illustrating the non-ideal dependance of expansions on total conditions. As particularly clear by looking at CFD pressure ratio trends in Figures 5.18a and 5.18b, less ideal conditions show a higher pressure ratio. However, the percentage pressure ratio difference between least and most ideal conditions in the constant cross-section region is of the order of 1% with respect to the most ideal case. This is about half of what was found for *cMM07*, confirming 1D calculation findings (Section 2) that non-ideality effects are less pronounced where compressibility is less important.
Considering the experimental pressure ratio, the associated uncertainty does not allow to draw clear-cut conclusions as with numerical results, because pressure ratios at all levels of non-ideality fall within error-bars of one another.

Nevertheless, compressibility factor and fundamental derivative trends and values differ depending on total conditions, again highlighting the different volumetric and caloric behaviour responsible for the non-ideal expansions dependance on P_T and T_T.

CFD results allow to assess the effect of boundary layer on pressure ratio which, analogously to *cMM07*, seems to be constant across all levels of ideality. The difference between CFD pressure ratios at coordinates $x = 60\,\text{mm}$ and $x = 102.5\,\text{mm}$ in the constant cross-section region is ~ 0.003 for all total conditions. Thus, in absolute terms, pressure change will be larger in less ideal cases at higher total pressure, with a value of $\sim 20\,\text{mbar}$ for *212MM-0.80* ($P_T = 6.34\,\text{bar}$) and of $\sim 7\,\text{mbar}$ for *212MM-0.95* at $P_T = 1.84\,\text{bar}$. Whilst this is still larger than transducers uncertainty, it is evident that boundary layer impact is here much weaker with respect to nozzle *cMM07*. This is due to the fact that flow in the constant area section of the latter is closer to sonic conditions compared to *cMM05* and is thus more sensitive to passage area changes.
Figure 5.18e reports the percentage pressure ratio deviation $\Delta(P/P_T)_{CFD-exp}$. It indicates an overall good level of agreement between CFD and experimental results. The value of $\Delta(P/P_T)_{CFD-exp}$ is always below 1.5% and does not seem to be impacted by the level of flow non-ideality in a significant way.

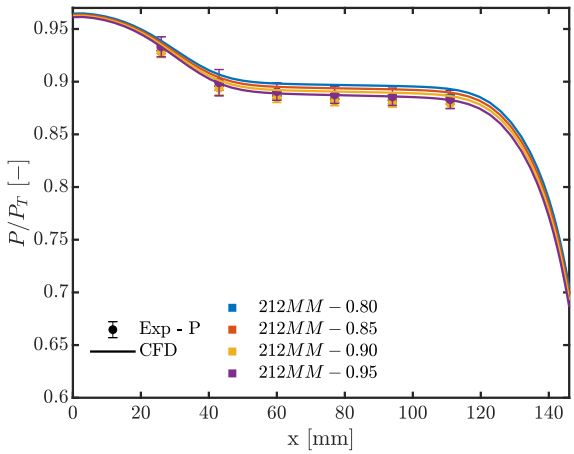

(a) Pressure ratio along the nozzle axis.

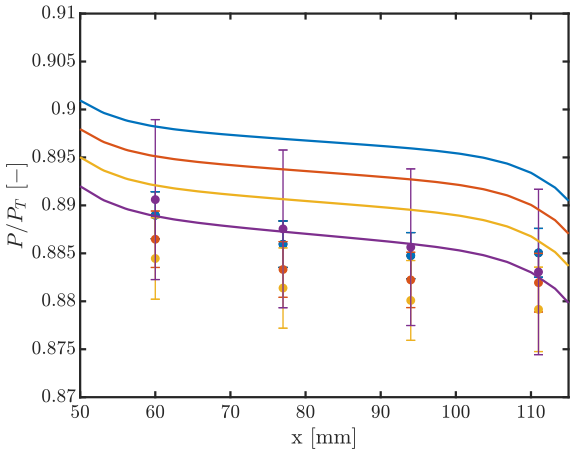

(b) Pressure ratio along the nozzle axis. Zoom at the constant cross sectional area.

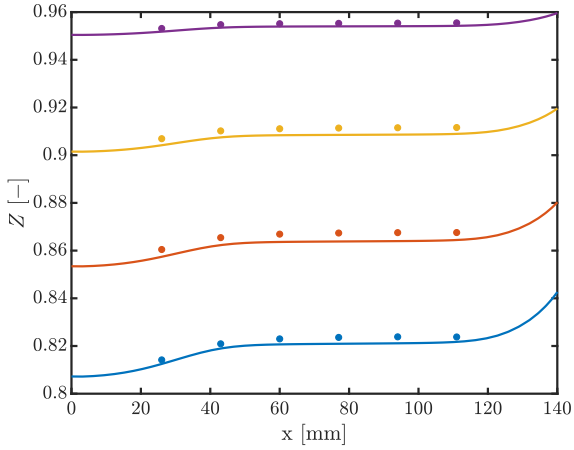

(c) Compressibility factor along the nozzle axis. LDV results not shown here.

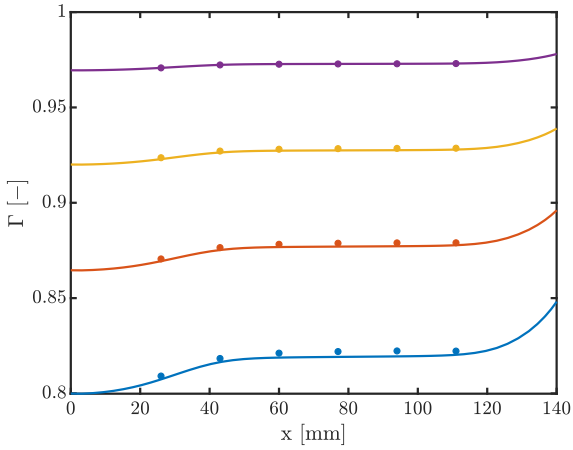

(d) Fundamental derivative of gasdynamics along the nozzle axis. LDV results not shown here.

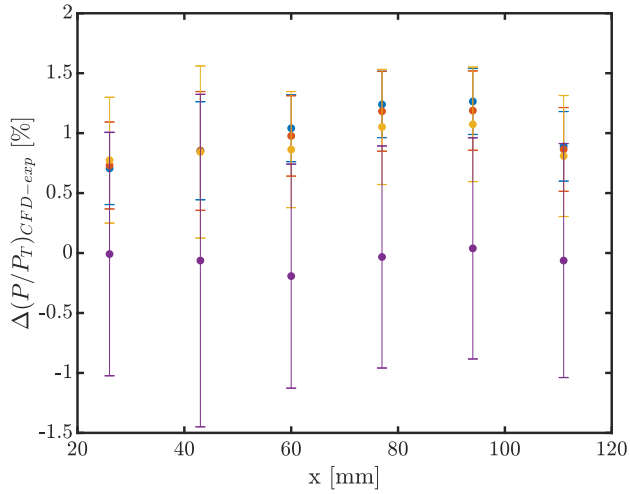

(e) Percentage pressure ratio deviation between CFD and experimental results.

Figure 5.18. Comparison of expansions at conditions during test $212MM$.

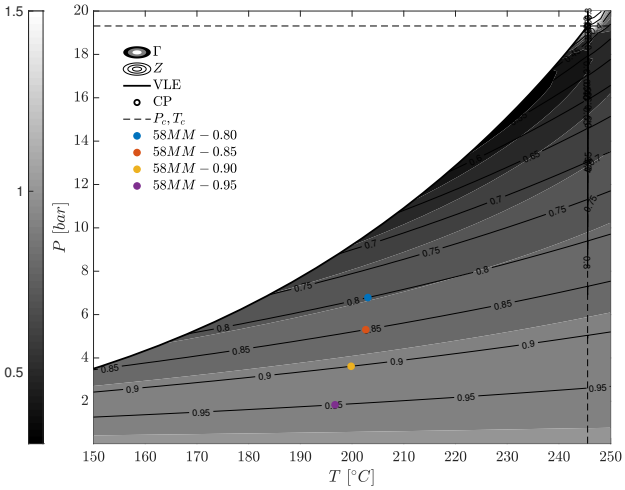

Figure 5.19. $P-T$ diagram with Z and Γ contours with total conditions of expansions selected from test *58MM*.

Name	P_T $[bar]$	T_T $[°C]$	Z_T $[-]$
58MM-0.80	6.78	203.1	0.80
58MM-0.85	5.30	202.6	0.85
58MM-0.90	3.62	199.8	0.90
58MM-0.95	1.84	196.7	0.95

Table 5.6. Selected test conditions during Test *58MM*.

5.4 Nozzle cMM02

5.4.1 Experimental Dataset

Figure 5.19 and Table 5.6 report the total conditions extracted at different values of the total compressibility factor during test *58MM* on nozzle *cMM02*. No LDV measurements and CFD calculation were performed on this nozzle, so the analysis here reported is focused on pressure measures.

5.4.2 Non-Ideal Expansion Dependance on Total Conditions

Results from all test *58MM* conditions are reported in Figure 5.20. Pressure ratios for different levels of non-ideality in Figures 5.20a and 5.20b are not perfectly superposed, suggesting a non-ideal dependance on total conditions. However, pressure ratios fall within error-bars of one another, confirming that non-ideality effects are so weak due to low flow compressibility as to fall within experimental uncertainty.
Nevertheless, compressibility factor and fundamental derivative trends differ depending on total conditions analogously to *cMM05* and *cMM07* nozzles, again indicating the different volumetric and caloric behaviour responsible for the non-ideal expansions dependance on P_T and T_T.
CFD results are not available to clearly assess the effect of boundary layer on pressure ratio. However, pressure ratio measures in the constant cross-section region are markedly constant with respect to *cMM05* and *cMM07* nozzles in Figures 5.15b and 5.18b, respectively. It can therefore be concluded that boundary layer growth has a negligible impact in case of nozzle *cMM02*, consistently with a low sensitivity to passage area changes in flows so distant from sonic conditions.

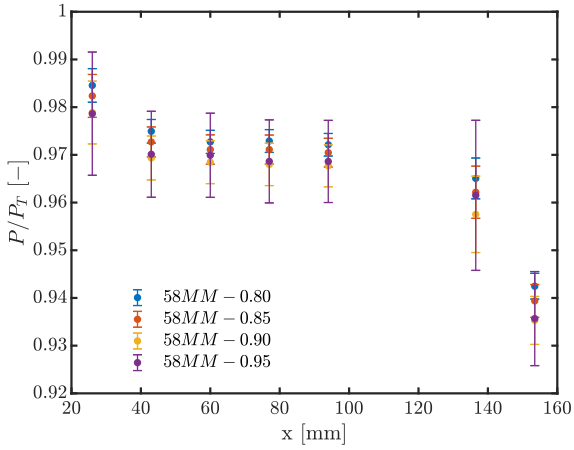

(a) Pressure ratio along the nozzle axis.

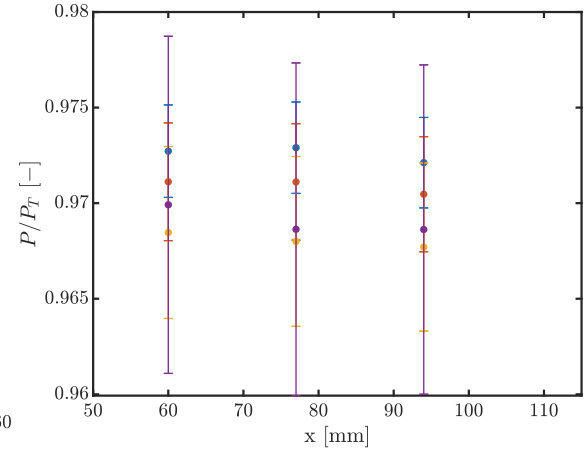

(b) Pressure ratio along the nozzle axis. Zoom at the constant cross sectional area.

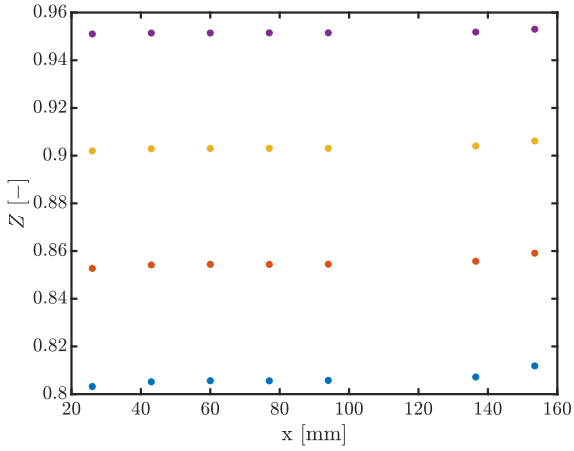

(c) Compressibility factor along the nozzle axis.

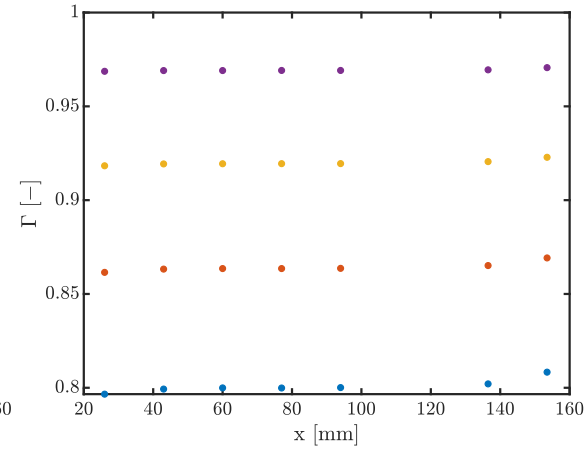

(d) Fundamental derivative of gasdynamics along the nozzle axis.

Figure 5.20. Comparison of expansions at conditions during test $58MM$.

5.5 Conclusions

The present chapter reports the characterization of three choked subsonic nozzles at different Mach numbers operating with moderately non-ideal flows. Experimental results in synergy with numerical calculation were used to assess key flow aspects, such as nozzle expansions dependance on total conditions and the impact of boundary layer growth in the constant cross-section portion of the nozzles.
Non-ideal effects were verified to be more important where compressibility effects are also more relevant.
Boundary layer growth was found to have a stronger impact at Mach numbers closer to sonic conditions due to the higher sensitivity to passage area variations. The level of non-ideality does not have an impact on the pressure ratio decrease induced by the presence of the boundary layer. However, its effects increase in terms of absolute pressure change as the total pressure increases.
These are all precious information in view of the use of choked subsonic nozzles as calibration wind tunnels for pressure probes in the non-ideal regime, because a correct choice of the reference static pressure is now possible to enable accurate calibration.

PART III:

PITOT TUBES IN NON-IDEAL FLOWS OF ORGANIC VAPORS

This third and last part of the thesis builds upon the experience matured in nozzle flow characterization on the Test Rig for Organic Vapors (TROVA) and presents one of the first ever experimental campaigns with pressure probes employed in non-ideal flows of organic vapors. This is the initial step towards future pressure probes calibration and blade cascade testing in such flows, as well as towards reliable velocity, mass flow rate and performance measurements in industrial contexts where non-ideality is relevant.
The development of a pneumatic system allowing pressure probes insertion in the TROVA test section is described in Chapter 6. The pneumatic system commissioning is then completed with the insertion of Pitot tubes in subsonic flows of organic vapors, as documented in Chapter 7. Chapter 8 reports the first ever experimental campaign with Pitot tubes in non-ideal supersonic flows of organic vapors for the direct measurement of normal shock total pressure losses.

CHAPTER 6

PNEUMATIC LINES FOR PRESSURE PROBE MEASUREMENTS IN NON-IDEAL FLOWS OF ORGANIC VAPORS

This chapter presents the development and testing of a pneumatic system for pressure measurements that will enable future use and calibration of probes operating with subsonic and supersonic non-ideal flows.

The pneumatic system is composed of lines and cavities of different shapes and sizes connecting pressure taps at the measuring point with pressure transducers mounted at line ending. It is implemented in the Test Rig for Organic VApors (TROVA), where testing with fluid siloxane MM (hexamethyldisiloxane, $C_6H_{18}OSi_2$) was carried out. An outline of the experimental apparatus is presented in Section 6.1. Pneumatic lines are subject to condensation unless heating is supplied. This can lead to poor pressure measurements quality related to presence of vapor-liquid menisci, hydrostatic head and mass-sink effects. These challenges were evaluated by means of theoretical calculation and experiments in the context of TROVA operation and are detailed in Sections 6.2 and 6.3. A pneumatic system configuration involving nitrogen flushing of the line was found to be the optimal setup to overcome all aforementioned difficulties, as reported in Section 6.4. An application of this pneumatic line configuration to differential measurements for future employment in probes calibration and shock losses is found in Section 6.5. The final lines setup for Pitot tube testing in subsonic flows of Siloxane MM is reported in Section 6.6.

6.1 Experimental Setup

The present experimental campaign was carried out on the *TROVA* with siloxane MM with the implementation of minor modifications to the plant. A key aspect of the facility, here recalled, is that it is a blow-down wind tunnel. As such, *TROVA* operation is intrinsically transient. After test start (t_{start}), a peak is reached and then pressure decreases in time with a low frequency content (below 1 Hz) related to the emptying of the High Pressure Vessel *HPV*.

6.1.1 Employed Nozzles and Rear Plates

The present testing on pneumatic lines was performed using planar choked converging nozzles *cMM02, cMM05* and *cMM07*, characterized by a portion with constant cross-sectional area yielding design Mach numbers of ~ 0.2, 0.5 and 0.7, as described in detail in Section 3.

Probe insertion in the constant cross-section portion will allow future calibration of pressure probes with subsonic flows of organic vapors at constant Mach number but varying levels of non-ideality and Reynolds number. During the present pneumatic lines commissioning phase, this nozzle design allows instead the evaluation of system performance by direct comparison of pressure measures at the end of the pneumatic line with flush mounted transducers in adjacent taps. Indeed, compared measurement points are all located in the constant cross-section portion of the nozzle, so the same pressure should be found, except for possible boundary layer effects as described in Section 5.
The *JLo* rear plate was used for all preliminary pneumatic system testing prior to probe insertion. The complete system including the Pitot tube instead employed the purposely developed *Pitot* rear plate. Both rear plates are described in more thorough detail in Section 3.

6.1.2 Unheated Pneumatic Lines

All pressure measures in the *TROVA* to date were performed with the use of flush mounted absolute transducers. This solution ensures response times well below the characteristic *HPV* emptying time and avoids possible condensation issues in pneumatic lines. The downsides are more expensive transducers due to high temperature operation and time-consuming calibration in temperature as well as pressure. However, if probes are employed, differential pressure measures are carried out between the various probe taps so as to minimize the final measurement uncertainty. Also, if Pitot tubes are tested, the difference between reference *TROVA* pressure and the one measured by the instrument is also to be acquired (both total and static quantities). A differential configuration is not possible if transducers are flush mounted: lines connected to wall pressure taps, exiting the back of the test section and meeting at the two ends of the differential transducer are needed as shown in Figure 6.1. The length of these lines can vary depending on the distance between measurement points.

Since fluid MM is liquid at room temperature and considered operating pressures during tests, pneumatic lines are subject to condensation unless heating is supplied. The latter solution is complicated due to small line diameter necessary for reduced response times (2 mm internal, $3 - 4$ mm external), is expensive, cumbersome and not flexible in case line length is varied. Moreover, if the line is unheated the fluid at the transducer sensor will be significantly cooler than at the measurement point. This is positive, because differential transducers able to withstand high temperatures are not readily available on the market. Also, temperature calibration is no longer required. For these reasons, line heating was not pursued. Rather, the focus was on overcoming practical challenges linked to line condensation, as explained in the following.

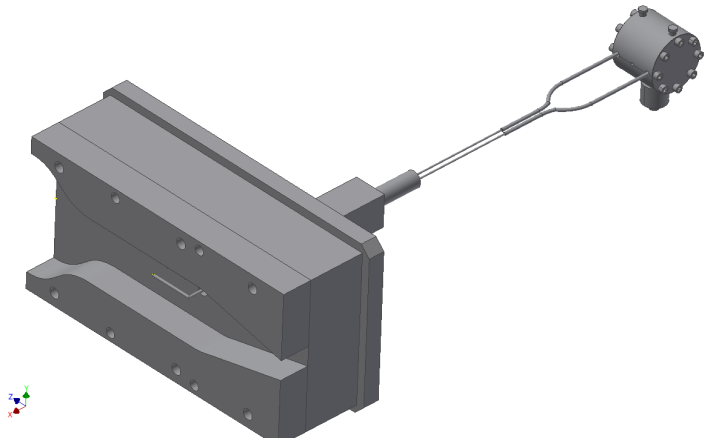

Figure 6.1. Differential pneumatic lines for pressure probe measurements. In this example, Pitot tube kinetic head (difference between its total and static pressures) is being measured.

6.2 Pneumatic Line with Condensation

Preliminary testing was carried out on a single pneumatic line of 2 mm internal diameter and 200 mm long. This length is the estimated minimum one during future probe testing.
To verify that condensation does take place and determine the possible fluid temperature at which sensors might be exposed, a thermocouple was first placed at the end of the line. The latter was connected to the wall tap in the plenum where total pressure is measured because this is where maximum temperature occurs. The peak temperature read by the thermocouple for all tests was less than 40 °C, confirming that condensation occurs immediately as the fluid enters the line and that sensors can expect a fluid temperature not far from ambient one, considering that lines will likely be longer in the final probe testing configuration. Initial total conditions for these preliminary tests were well representative of future Pitot tube experimental campaigns.
Condensation can be problematic, even during steady measures, for two reasons: menisci presence and hydrostatic head. The presence of vapour and liquid phases in the line implies the existence of menisci and a consequent pressure difference across the interface which can alter the reading at the sensor at the end of the line. This pressure difference was estimated using the Laplace-Young law and experimentally verified values of surface tension and contact angle for fluid MM with a stainless steel surface ($\sim 0\,°$). The calculated value was 32 Pa, largely below transducers uncertainty. Moreover, since it is impossible to predict where in the line condensation starts, liquid formation could create a hydrostatic head between the vapour-liquid interface and the transducer location. This effect is considered negligible if the pressure difference caused by the hydrostatic head is lower than the transducer uncertainty. Calculation for liquid MM showed that this occurs if the geodetic head is lower than 70 mm. Particular care was thus taken to ensure this during line installation.

For all further testing, the thermocouple at the end of the line was replaced by an absolute transducer. Signal from the latter was compared with a flush mounted transducer at another identical wall pressure tap in the plenum.
The line transducer is expected to correctly measure flow pressure once the whole line volume V_{line} is filled with MM. The corresponding time delay, defined as the time taken from test start for the line and flush mounted transducer signals to be within error bars of one another, can be estimated as follows. Vapour flow through wall tap to the line is assumed choked at the minimum

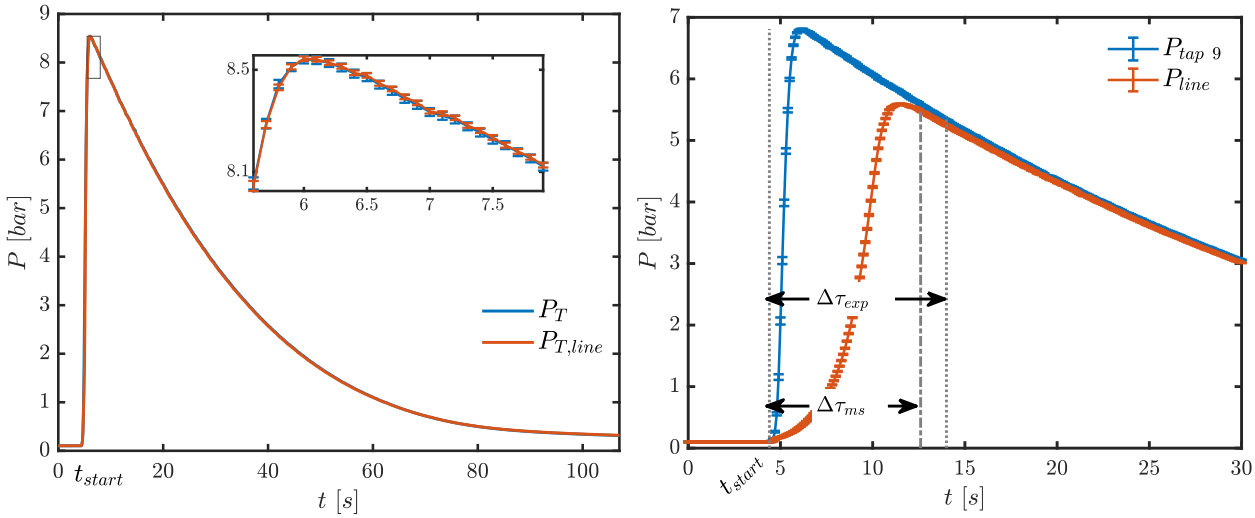

(a) *Test A*. Error bars are included in the zoom.

(b) *Test B*. The first 30 s only are shown here for plot clarity.

Figure 6.2. Pressure measures during *Test A* and *Test B*.

cross section A_{min}. This is a realistic hypothesis at the beginning of a test when lines are under vacuum conditions. The total pressure tap is large, so here A_{min} corresponds to the line internal diameter. The time delay $\Delta\tau$ is determined from the balance $V_{line} = \dot{V}_{vap}\Delta\tau = C_d c A_{min}\Delta\tau$ where $\dot{V}_{vap}$ is the volumetric flow rate and C_d is the discharge coefficient taken as 0.65 for small and sharp edged orifices (Shawney, 2013). Speed of sound c is calculated from total pressure and total temperature using a Helmoltz energy based fundamental relation of Span-Wagner type embedded in the *FluidProp* library. The calculated time delay of the line was found to be two orders of magnitude below the dataset time resolution of 0.1 s (see Section 3 for details).
Figure 6.2a shows results for an exemplary test (*Test A*) having initial $P_T = 8.5$ bar and $T_T = 215$ °C and carried out on nozzle $cMM07$. Perfect overlap between the two pressure readings was found, without any delay effects due to the line filling and no menisci or hydrostatic head effects.
The pneumatic line was then connected to the static pressure tap number 11 located in the constant area region of the nozzle and pressure signal was compared with flush mounted transducers at wall tap 9 in the same region. The two static taps are only 17 mm apart and boundary layer effects are expected to be only slightly noticeable outside of transducers uncertainty at the beginning of the test, when pressure levels are higher (Section 5.2).
The time delay of this line was estimated in the same way as *Test A*. Thermodynamic quantities at the static tap were found using total pressure, total temperature and the isentropic flow hypothesis coupled with the aforementioned thermodynamic model. The minimum area in this case is the tap hole (0.3 mm in diameter), leading to larger time delay with respect to the previous configuration, but still well below the dataset time resolution. As Figure 6.2b shows for an exemplary test (*Test B*) having the same nozzle and initial total conditions as *Test A*, there is instead a significant time delay between signals ($\Delta\tau_{exp} \sim 9.6$ s) which is orders of magnitude higher than the estimated one. As explained in the following section, it is attributable to the *mass sink effect* linked to condensation.

6.3 Mass Sink Effect

As the test begins and MM enters the line as vapour, the sensor at its end is unable to correctly measure flow pressure until the whole line volume V_{line} is filled with liquid, given condensation. This change of state was neglected in previous delay estimates and is the reason for their disagreement with *Test B* experimental results. Indeed, the higher liquid density means that a larger MM mass will be needed to fill the line although the entering mass flow rate is still limited by the lower vapor density. This leads to much larger delay times with respect to no line condensation.
To verify this phenomenon a simple model for delay time estimate was developed and verified against experimental data.
Pressure signal from a flush-mounted transducer is discretized into z time steps of equal size Δt. Thermodynamic properties at each time instant are calculated as described in Section 6.2 and flow through wall tap to the line is again assumed choked at the minimum cross section A_{min}. The vapor mass entering the line at each time step is $dm = d\dot{m}\Delta t = C_d \rho c A_{min} \Delta t$. When the total vapor mass $m_{vap} = \sum_{i=0}^{z} dm_i$ that has entered the line equals the liquid mass $m_{liq} = \rho_{liq} V_{line}$ that can be contained in it, the transducer at the end of the line should start reading the correct pressure. The time instant at which this occurs can be determined by numerically solving the equation $m_{vap} = m_{liq}$ for the value of z. Time delay due to mass sink $\Delta\tau_{ms} = z\Delta t$ is proportional to vapor density, speed of sound and to minimum area size. Thus, it is expected to decrease for larger orifices, at higher pressure levels and lower Mach numbers due to the higher local density at the pressure tap.
Figure 6.2b shows that time delay predicted with the above procedure for *Test B* is $\Delta\tau_{ms} = 8.2\,\mathrm{s}$ and is in good agreement with experimental data having $\Delta\tau_{exp} \sim 9.6\,\mathrm{s}$, confirming the mass sink mechanism occurrence. Discrepancy between predicted and actual value is attributable predominantly to the choked flow assumption. In reality, as the line fills and its pressure gets closer to the flow one, inflow into the pneumatic system will no longer be choked and the system will fill more slowly.
Considering *Test A* on the total pressure tap, calculated time delay due to mass sink is negligible as pressure signals are always within measurement uncertainty of one another. This is because density is higher at the total pressure tap and, most of all, due to the much larger A_{min}. A roughly ten-fold increase in the minimum diameter corresponds to a two orders of magnitude decrease in time delay.

If steady state measures were performed, it would be possible to wait until the line is full of liquid and discard initial test instants. However, the TROVA operates in transient mode due to its batch nature so steady measurements are not possible. Also, initial test time cannot be discarded because this is when the flow is most non-ideal (due to higher pressure) and where the most interesting research data is to be gathered. Thus, a line nitrogen flushing solution is put in place to overcome line condensation and avoid time delay due to mass sink effects.

6.4 Pneumatic Line with Nitrogen Flushing

The scheme of preliminary tests with one flushed line connected to a static wall tap is shown in Figure 6.3. The line is directly connected to nitrogen storage tanks and pressure is regulated through a pressure reducer to just above the maximum expected one during the test. The line pressure transducer is mounted just downstream a solenoid electrovalve (*EV*) at a distance of $\sim 1\,\mathrm{m}$ from the measurement point. Line length is here representative of the longest expected lines for future Pitot tubes testing. The valve is actuated by a *Labview*® program to open as the test is triggered and close right after the pressure peak is reached in the test section. This ensures that the line only contains nitrogen at all times during a test and no MM vapor enters it, so as to avoid condensation. As the test proceeds, nitrogen exits the line from the static tap into the test section as

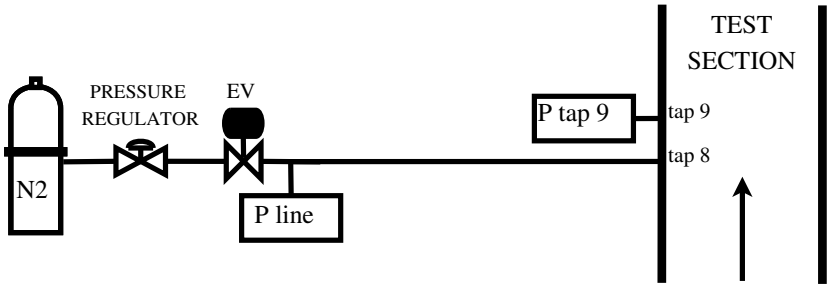

Figure 6.3. Single pneumatic line with nitrogen flushing.

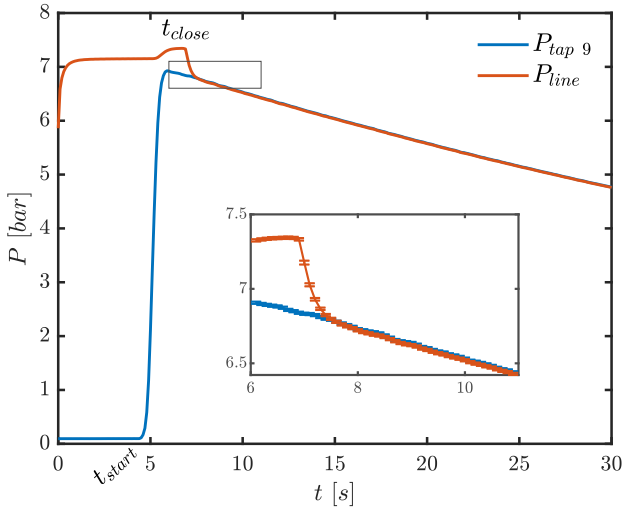

Figure 6.4. Pressure measures during *Test C*. The first 30 s only are shown here for plot clarity.

line pressure tends to equilibrium with the decreasing test section one. Results of exemplary *Test C* on nozzle $cMM02$ with initial total conditions $P_T = 7$ bar and $T_T = 200$ °C are here reported. The line was mounted in the constant area region on tap 8 and pressure signals were compared with a sensor flush mounted on the adjacent active tap 9. Boundary layer is here not expected to cause any significant difference between static pressures at the two taps, given that the two are only 8.5 mm apart and that conditions are far away from sonic ones (Section 5.4).
As Figure 6.4 shows, pressure in the line decreases and is within error bars from flow pressure in under 1 s after the solenoid valve is closed at t_{close}. Even lower time delay could be achieved by fine-tuning line nitrogen pressure and t_{close} parameters. This result is an excellent improvement with respect to measurements involving condensation in the line, especially considering that the line in *Test C* is about five times longer than in *Test B*. Indeed, tests with condensation in the same *Test C* configuration (not reported here for brevity) showed a time delay ~ 60 s.

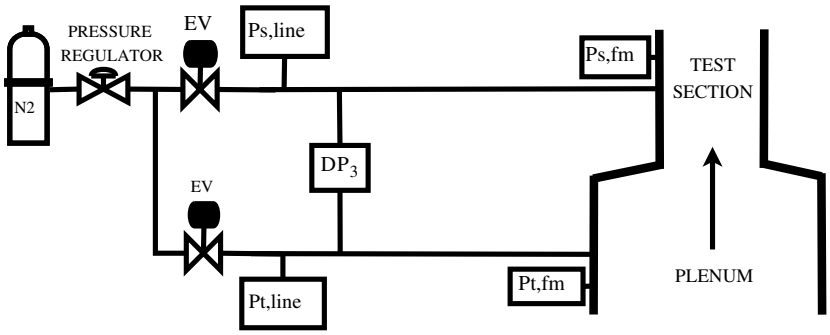

Figure 6.5. Differential pneumatic system with nitrogen flushing.

6.5 Flushed Pneumatic Lines in Differential Configuration

As previously explained, probes calibration requires differential pressure measurements to minimize uncertainty. Preliminary tests on a nitrogen flushed pneumatic line for differential pressure measures were carried out with the configuration shown in Figure 6.5. Overall line length is about 1 m in view of future Pitot tubes testing. One line was installed at the total pressure tap in the plenum and the other one at tap 8 in the constant area region of the nozzle to reproduce a similar setup to differential pressure measures between reference TROVA and Pitot tube total pressures. Differential static pressure will also be measured between the Pitot tube static port and static pressure wall taps, but lines length will be significantly shorter.

The objective of these preliminary tests was to compare the kinetic head measured with flush mounted transducers $\Delta P_1 = (P_t - P_s)_{fm}$ with the reading ΔP_3 of the differential transducer. The wall mounted pressure sensor is placed at tap 7 in the constant area section. Boundary layer effect is here again expected to be negligible, for the same reasons above.
In order to better identify possible issues with either one of the lines, absolute pressure transducers were also mounted on each line and the pressure difference $\Delta P_2 = (P_t - P_s)_{line}$ was calculated. Figure 6.6 reports results for *Test D* with same initial total conditions and nozzle as *Test C*, showing the excellent overlap between kinetic heads measured in the three different ways. It can be concluded that the nitrogen-flushed pneumatic system is able to correctly measure in differential mode aswell, given the complete agreement between the differential transducer and absolute flush mounted ones. This aspect is of fundamental importance to achieve accurate pressure probe calibration with a low experimental uncertainty in the future. Moverover, given its correct functioning, an analogous pneumatic lines setup was employed for total pressure losses measurement across shocks in non-ideal flows of Siloxane MM, as reported in Section 8.

6.6 Flushed Pneumatic Lines for Pitot Tube Measurements in Subsonic Flows of Siloxane MM

The complete pneumatic lines configuration for probes testing here presented is specifically devised so that each quantity measured by the probe can be compared against plant references. Under this aspect, this is only possible with the use of a Pitot tube because its static pressure should agree with the plant reference one and thus allows to check the proper functioning of the dedicated line. This would not be possible if directional probes were employed instead, making Pitot tube testing a key preparatory step for their use.

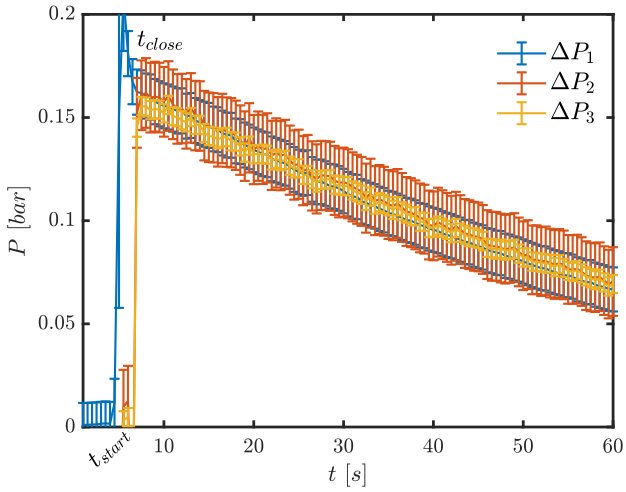

Figure 6.6. Kinetic head measurement during *Test D*.

The quantities of interest to be measured during *TROVA* testing of Pitot tubes in subsonic flows of Siloxane MM are:

- $P_{t,ref}$: reference total pressure in the TROVA plenum, measured with a flush mounted absolute transducer;
- $P_{s,ref}$: reference static pressure in the constant cross section part of the subsonic choked nozzle, measured with a flush mounted absolute transducer;
- $P_{t,line}$: total pressure measured in the line exiting a pressure tap in the plenum;
- $P_{s,line}$: static pressure measured in the line exiting the static wall tap in the constant cross-section region of the nozzle at the $x-$coordinate in correspondance of the Pitot tube static ring;
- $P_{t,pitot}$: total pressure measured in the line connected to the total pressure port of the Pitot tube;
- $P_{s,pitot}$: static pressure measured in the line connected to the static ring of the Pitot tube;
- $\Delta P_{ts,line}$: kinetic head directly measured with a differential transducer between a total pressure tap in the plenum and a static wall tap in the constant cross section of the nozzle in correspondence of the Pitot tube static ring. Given that this differential transducer is mounted on lines, its extremities are not exactly subject to $P_{t,ref}$ and $P_{s,ref}$, but actually to $P_{t,line}$ and $P_{s,line}$. This is why the subscript *line* is used although this is taken as reference kinetic head of the plant;
- ΔP_t: total pressure difference directly measured with a differential transducer between a pressure tap in the plenum and the Pitot tube and should thus correspond to $P_{t,line} - P_{t,pitot}$. It is the numerator of the total pressure coefficient K_{Pt} defined in Equation 3.8;
- ΔP_s: static pressure difference directly measured with a differential transducer between a static wall tap in the constant cross section of the nozzle in correspondence of the Pitot tube

Measured Quantity	Model	full-scale *FS* [*bar*]	type	Uncertainty [*mbar*]	Uncertainty [‰*FS*]
$\Delta P_{ts,line}$	Schaevitz P2100 Series	2.0	differential	6.06	3.3
$\Delta P_{ts,pitot}$	Schaevitz P2100 Series	2.0	differential	3.63	1.8
ΔP_t	Schaevitz P2100 Series	0.7	differential	1.35	1.9
ΔP_s	Schaevitz P2100 Series	0.7	differential	1.20	1.7

Table 6.1. Differential pressure transducers employed in the experimental campaign on the *TROVA* with their uncertainties after calibration on the plant acquisition system.

static ring and the Pitot tube itself. It should thus correspond to $P_{s,line} - P_{s,pitot}$. It is the numerator of the static pressure coefficient K_{Ps} defined in Equation 3.9;

- $\Delta P_{ts,pitot}$: kinetic head directly measured with a differential transducer by the Pitot tube. It should thus correspond to $P_{t,pitot} - P_{s,pitot}$ and is the numerator of the kinetic head coefficient K_{Pd} defined in Equation 3.10.

The last four quantities are acquired in differential mode to minimize uncertainties in the coefficients defining the Pitot probe performance, as defined in Section 3.7.4. Table 6.1 reports the differential transducers employed for each measured quantity, together with their uncertainties. The two 2 bar transducers were employed for preliminary Pitot tube characterization on the *Safety Valves Test Rig* at *LFM* aswell, as described in Section 7.1. They display a larger uncertainty after calibration on the *TROVA* with respect to calibration at *LFM*. This is probably linked to different measurement chains in the two plants acquisition systems. In particular, the on-line zero procedure is applied to transducers that are in sub-atmospheric conditions just before test start, and thus involves the use of one transducer more than at the *Safety Valves Test Rig*, where the zeros are taken at atmospheric pressure with the use of a simple barometer.

The pneumatic lines scheme used for subsonic Pitot tube testing is shown in Figure 6.7 and builds upon the nitrogen flushed system developed and tested in the previous sections, with the addition of several lines to allow the simultaneous acquisition of all pressures of interest. Absolute pressure transducer are installed on each line to help pinpoint possible issues with any of them. This is why pressures $P_{t,line}$, $P_{s,line}$, $P_{t,pitot}$ and $P_{s,pitot}$ are also acquired with absolute transducers having the most suitable full-scale amongst those listed in Table 3.1.
It must be pointed out that $P_{s,ref}$ is labeled as a *reference* pressure against which Pitot tube and line readings can be compared because it is acquired with the consolidated flush-mounted technique already extensively used for nozzle characterization, and thus does not include any possible measurement changes induced by line presence, such as delay, as later covered in better detail. However, the effect of boundary layer, whose intensity depends on operating conditions and employed nozzle as investigated in Section 5, might mean that $P_{s,ref}$ is non-negligibly larger than $P_{s,line}$ or $P_{s,pitot}$. This should be accounted for when evaluating the performance of the pneumatic system.

Particular care was taken during system design and components positioning to minimize lines length and fittings volume, so as to decrease the overall response time as much as possible. After testing many different configurations, including stainless steel tubing and related compression fittings, the best configuration in terms of flexibility and leakages was found to be with hydraulic tubing with 4 mm in outer diameter and hydraulic quick couplers by *Legris*®. To decrease the lines volume, a smaller tube with 2 mm outer diameter was inserted in the hydraulic tubing.

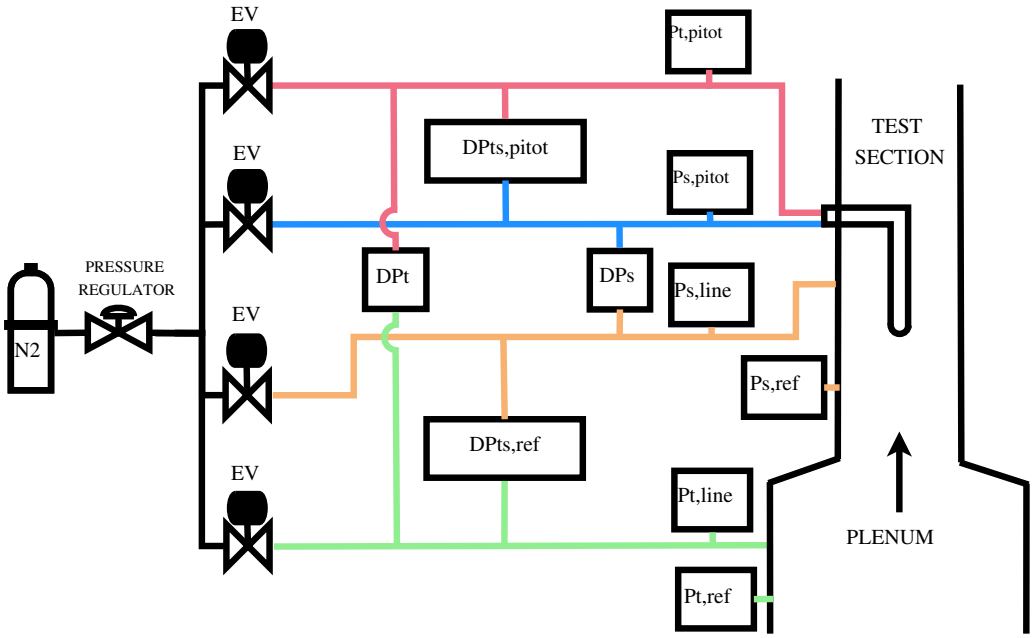

Figure 6.7. Flushed pneumatic lines scheme for Pitot tube testing in subsonic flows of Siloxane MM. Rectangular boxes represent pressure transducers.

6.7 Conclusions

The present chapter documented the experimental effort having the aim of identifying the best possible pneumatic lines configuration for pressure probes testing in the *TROVA* with non-ideal flows of organic vapors. Twelve tests with siloxane MM were carried out (each taking at least one day for preparation), together with more than twenty tests with nitrogen (about half an hour each). The most challenging aspects were the transient nature of plant operation coupled with inevitable vapor condensation in the lines, which was responsible for a mass sink effect unacceptably delaying the pneumatic system response time. A lines scheme involving nitrogen flushing was thus found to be the optimal setup. Testing was performed on configurations allowing absolute and differential pressure measures, building towards the final application for pressure probes testing in subsonic and supersonic non-ideal flows.

CHAPTER 7

PITOT TUBES IN NON-IDEAL SUBSONIC FLOWS OF ORGANIC VAPORS

This chapter presents the results of an experimental campaign involving Pitot tubes in non-ideal subsonic flows of organic vapors. The main objective is to complete the commissioning of the pneumatic system developed in Section 6 for pressure probes testing in such flows. The acquired experience should develop the related experimental techniques and establish best practices for pressure probes calibration and shock losses measures in cases where non-ideality is important. To this end, a Pitot tube and subsonic flows were purposely chosen because, together, they allow to have a direct reference counterpart for the probe total and static measures. This therefore permits the evaluation of the correct performance of the overall pneumatic system, something which would not be possible if directional probes and/or supersonic conditions were considered.

A second aim of the present experimental campaign is to verify the proper functioning of Pitot tubes with flows of siloxane MM, a fluid that is significantly different with respect to more conventional air and which exhibits a marked non-ideal behaviour in the explored vapor region. This would have relevant practical implications by enabling velocity, mass flow rate and turbomachinery loss measurements in systems involving non-ideal flows of organic vapors, such as organic Rankine cycle (ORC) plants.

7.1 Preliminary Pitot Tube Characterization in Air

Preliminary Pitot tube testing in subsonic flows was carried out with air at the *Laboratory of Fluid Machines* (*LFM*) on the *Safety Valves Test Rig*. The objective was to verify the proper functioning of *Vectoflow* and *Aeroprobe* Pitot tubes and assess their sensitivity to flow yaw angle φ, Mach number M and Reynolds number Re. Knowing probes behaviour is important information in view of Pitot tubes insertion in the *TROVA* for pneumatic lines testing.

7.1.1 Safety Valves Test Rig

The air available at the *Safety Valves Test Rig* is stored in 18 pressure vessels with maximum working pressure in the range $80 - 180$ bar with the use of an alternative compressor with nominal flow rate of $400\,\mathrm{Nm^3/h}$. Air to the test section is preheated by an oil heater at 100 °C and its pressure is set by means of a regulator in the range $0 \div 20\,\mathrm{bar_r}$. A 4 ” line connects the reducer to a vessel with capacity 1500 l that acts as plenum to the nozzle test section mounted on it. Total pressure in the plenum is measured with a wall pressure tap. A tube bundle flow straightener and a honeycomb are installed to ensure flow uniformity and axial direction in the test section.

7.1.2 Test Section and Regulation

The test section is composed by the nozzle with the Pitot tube mounted on it.
The particular nozzle employed in this campaign is a choked convergent discharging in ambient air, which allows the independent variation of flow Mach and Reynolds numbers. The nozzle geometry, shown in Figure 7.1, is planar with a short convergent part joining the plenum to a very long section with constant cross sectional area where wall pressure taps for reference static pressure are found. An adjustable shutter is positioned at the constant section end, providing the minimum cross section at the discharge.

Given that the plenum total pressure is always high enough with respect to ambient pressure to ensure choked nozzle operation, the shutter position fixes the Mach number in the constant area region (with area A) according to the corresponding area ratio A/A^* with the throat (with area A^*). Mach numbers ranging from 0.1 to 0.8 were obtained by changing the position of the shutter, as indicated in Figure 7.1. The Reynolds number is instead determined by the overall pressure level - identified by the static pressure value relative to the ambient - which affects flow density. The static pressure level is varied from ambient up to the maximum possible one in steps of 1 or 2 bar. The maximum pressure level that can be reached at each M is limited by the maximum flow rate of the *Safety Valves Test Rig*, and it therefore decreases with increasing Mach number. At larger M, when only a small pressure range is possible, static pressure is varied in steps of 0.5 bar.
The probe is installed in a region sufficiently far from the first convergent and from the outlet shutter so as to ensure uniform and undisturbed flow. Due to the relatively large dimensions of the constant cross section portion ($80\,\mathrm{mm} \times 50\,\mathrm{mm}$, much larger with respect to the *TROVA*), no blockage effects are expected on the probe and boundary layer growth can be considered negligible. In order to assess the probe angular sensitivity, it is rotated so as to vary the flow incidence angle. Figure 7.2a considers a reference system consistent with the probe and defines the plane containing stem axis and the probe head as the *pitch plane*, and that perpendicular to it and containing the probe head axis as the *yaw plane*. The present testing only considered yaw angle φ variations since, due to the nozzle shape, it is impossible to rotate the probe in the pitch plane. The same is true in the TROVA plant aswell, where only tests at 0° were performed (Section 7.2). Here, rotation of the Pitot tube is operated by a *MICOS-VT80* slide rigidly mounted to the nozzle, as shown in Figure 7.2b and controlled via a dedicated *Labview*® routine. An angular range between −16° and 16° with a 2° step was investigated at each Mach number and pressure level. The probe head angular

Figure 7.1. Choked convergent nozzle employed in the experimental campaign at the *Safety Valves Test Rig*.

position was verified with a digital level with 0.1° accuracy.
The first test point is acquired at $\varphi = 0°$. The Pitot tube is then rotated towards positive yaw angles. Once the maximum yaw is reached, the probe is taken back to null incidence and an additional test point is acquired. It is then rotated towards negative yaw angles until the minimum, and taken again back to zero incidence where another additional test point is acquired.
To avoid that at high Mach number and pressures the aerodynamic load prevents probe rotation due to bending, a bearing was installed between the probe stem and the hole in the nozzle where it is installed.

7.1.3 Pneumatic Lines and Pressure Transducers

The pneumatic lines configuration is shown in Figure 7.3. It is analogous to the complete one for subsonic testing of Pitot tubes in the *TROVA* (Figure 6.7), except that no nitrogen flushing is necessary here, so the related components are not present in the scheme. Moreover, no absolute transducers are mounted on the lines. Only a relative (with respect to the ambient) transducer measuring the reference total pressure $P_{t,ref}$ is employed here. The same quantities defined in Section 6.6 are acquired ($\Delta P_{ts,line}$ is here referred to as $\Delta P_{ts,ref}$).

The lines that connect pressure taps to transducers are several meters long in this experimental setup. This is not an issue here, unlike in the *TROVA*, because plant operation is steady. A change in operating conditions during an experimental run at a certain M number and pressure level only occurs when the probe is rotated. To avoid the occurrence of dynamic stall, which could cause non-symmetrical behaviour around $\varphi = 0°$, a waiting time of 3 s was imposed between rotation and measurement acquisition.

Considering reference total pressure $P_{t,ref}$, the transducer was chosen amongst available

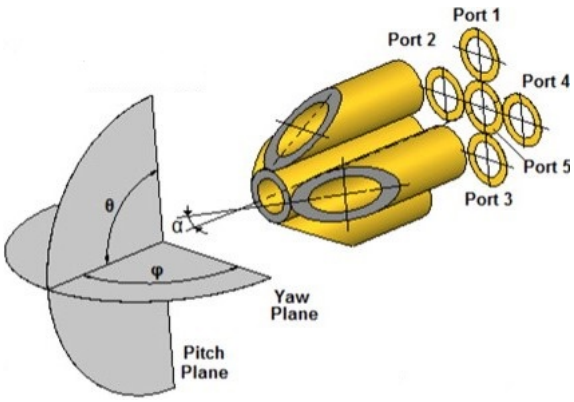

(a) Probe reference system defining *pitch* and *yaw* planes. The figure is for a five hole probe but it is valid for a Pitot tube aswell.

(b) *MICOS-VT80* slide for probe rotation.

Figure 7.2. Probe reference system and slide used for Pitot tube rotation during the experimental campaign at the *Safety Valves Test Rig*.

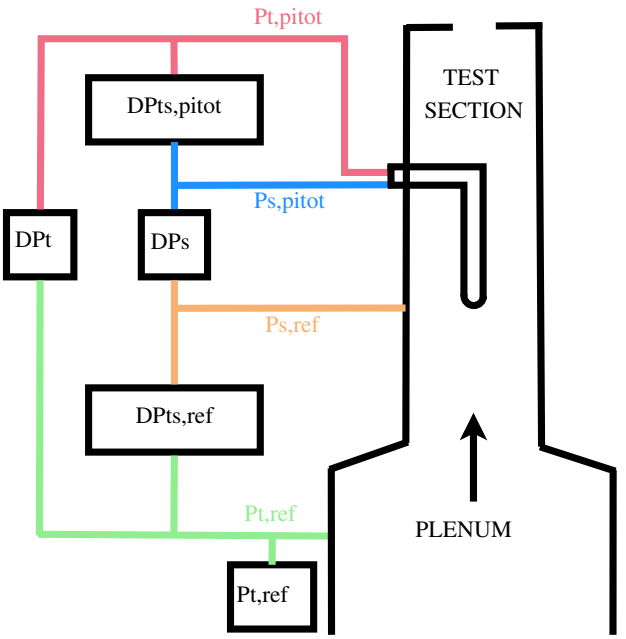

Figure 7.3. Pneumatic lines scheme for subsonic Pitot tube testing with air at the *Safety Valves Test Rig*. Rectangular boxes represent pressure transducers.

relative ones with full-scale 2.5, 5, 10 bar depending on the chosen test pressure level.
Except for the reference total pressure, all other transducers operate in differential mode to minimize measurement uncertainty. For the same reason, transducers full scale was chosen as close as possible to the expected pressure difference value. Pressure transducers employed for each measured quantity, together with their uncertainties, are reported in Table 7.1.

Measured Quantity	Model	full-scale *FS* [*bar*]	type	Uncertainty [*mbar*]	Uncertainty [‰ *FS*]
ΔP_t	Schaevitz P2100 Series	1.0	differential	1.00	1.0
$\Delta P_{ts,pitot}$	Schaevitz P2100 Series	1.5	differential	2.30	1.5
ΔP_s	Schaevitz P2100 Series	2.0	differential	2.07	1.0
$\Delta P_{ts,ref}$	Schaevitz P2100 Series	2.0	differential	1.92	1.0
$P_{t,ref}$	Schaevitz P2100 Series	2.5	relative	4.08	1.6
$P_{t,ref}$	Schaevitz P2100 Series	5.0	relative	10.48	2.1
$P_{t,ref}$	Schaevitz P2100 Series	10.0	relative	9.15	1.0

Table 7.1. Pressure transducers employed in the experimental campaign at the *Safety Valves Test Rig* with their uncertainties.

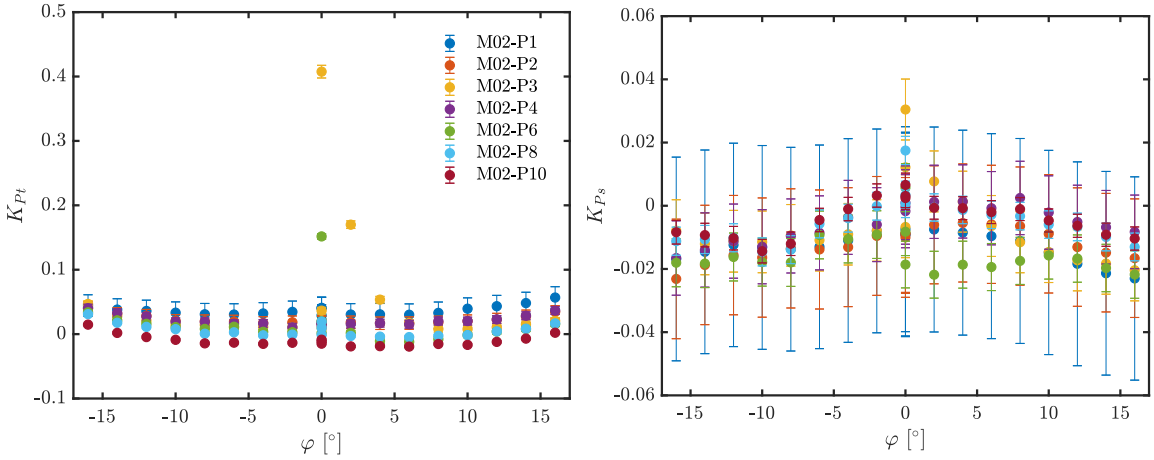

(a) K_{Pt}. (b) K_{Ps}.

Figure 7.4. K_{Pt} and K_{Ps} for the *Vectoflow* Pitot tube as a function of φ at $M = 0.2$ and different static pressure levels. Nominal relative static pressure value in $[bar_r]$ is indicated by the number in the legend after the symbol P for pressure.

7.1.4 Vectoflow Pitot Tube

This section reports test results for the *Vectoflow* Pitot Tube. Only total and static pressure coefficients K_{Pt} and K_{Ps} are here reported, whilst the kinetic head coefficient K_{Pd} is here left out for brevity since it is directly dependent on the previous two.
It was quickly observed that, especially at static pressure levels higher than ambient, the total pressure tap response time was extremely long, of the order of ~ 10 s. This is most likely due to an occlusion in the internal channel of the total pressure line due to manufacturing imperfections in the $3D$ printing process, and clearly makes the probe unfit for use in the *TROVA*. As a consequence of this delay, coefficients were found to be non-symmetric with respect to the yaw angle and unacceptably large in absolute value at any φ, as shown in Figure 7.4 reporting plots of K_{Pt} and K_{Ps} as a function of φ at $M = 0.2$ and different static pressure levels. Plots report three experimental points at $\varphi = 0°$ for each test condition because three null incidence points are acquired, as previously mentioned: at test start and after the probe is brought back to $\varphi = 0°$ after maximum positive and negative yaw angles are reached.
Due to the evidenced issues, testing of the *Vectoflow* Pitot tube was interrupted.

7.1.5 Aeroprobe Pitot Tube

Test results on the *Aeroprobe* Pitot tube are here analyzed to investigate the range of yaw angles at which it is insensitive and to understand if the Reynolds number Re, varied independently of the Mach number through the static pressure level, has an impact on probe behavior. The value of Re (defined on the probe head diameter) was found to vary between 1.5×10^4 and 1.5×10^5 across all explored conditions.
Total and static pressure coefficients (K_{Pt} and K_{Ps}) as a function of the yaw angle at different static pressure levels are plotted at exemplary nominal Mach numbers $M = 0.2,\ 0.5,\ 0.7$ in Figure 7.5. As previously mentioned for the *Vectoflow* Pitot tube, K_{Pd} is not reported here.
Not all tested M are shown for brevity. The chosen three can be considered as representative of the Pitot tube behaviour in incompressible, mid-subsonic compressible and high-subsonic compressible flow regimes, respectively. The nominal pressure is indicated in legends after the letter P and is equal to the relative static pressure of the nozzle $P_{s,ref}$ rounded up to the closest integer. At the beginning of every test run, the plenum total pressure is regulated to bring the nozzle static pressure as close as possible to the nominal one. As explained before regarding the *Vectoflow* Pitot tube, plots report three experimental points at $\varphi = 0°$ for each test condition.

Measurement uncertainty decreases with increasing Mach number and pressure level, as highlighted in Section 3.7.4. As reported in Figure 7.5, for all considered tests in the yaw angle range $-10° \leqslant \varphi \leqslant 10°$, the total pressure coefficient K_{Pt} is always lower than 0.02 and the K_{Ps} lower than 0.04 in absolute value. Restricting the yaw angle to $-6° \leqslant \varphi \leqslant 6°$, total and static pressure coefficients are fairly constant, with a maximum absolute value of 0.01 for K_{Pt} and 0.02 for K_{Ps}. Lower overall coefficients values are found for higher Mach numbers due to the larger kinetic head at the denominator. The *Aeroprobe* Pitot tube can thus be considered insensitive to flow direction in this angular range. Moreover, such coefficients values translate into a measurement error in total and static pressures which is respectively $\leqslant 1\%$ and $\leqslant 2\%$ of the kinetic head. If the most extreme condition at $M = 0.2$ is considered ($P_{s,ref} = 10\,\mathrm{bar_r}$), the difference between reference and Pitot tube total pressures ΔP_t is lower than 3 mbar. Static pressures difference ΔP_s is instead of the order of 6 mbar. Considering $M = 0.5$ at $P_{s,ref} = 7\,\mathrm{bar_r}$, $\Delta P_t \leqslant 11$ mbar and $\Delta P_s \leqslant 22$ mbar. For $M = 0.7$ at $P_{s,ref} = 2.5\,\mathrm{bar_r}$, $\Delta P_t \leqslant 7$ mbar and $\Delta P_s \leqslant 14$ mbar.
Figure 7.5 also illustrates how the Reynolds number variation has practically no noticeable effects on probe behaviour. For each tested Mach number, all experimental points having same yaw angle at different pressures are within error bars of one another.
The effects of compressibility on Pitot tube performance can also be isolated by considering results of tests at different Mach number but same Reynolds one. This was investigated for Re values ranging between 1.5×10^4 and 1.5×10^5 considering test conditions within a 10% tolerance of the chosen nominal Reynolds number. The full set of results is not reported here for brevity. Experimental points from test runs having different M but sharing the same Reynolds numbers are within error bars of one another, meaning that compressibility effects have a negligible impact on probe behaviour.
It can therefore be concluded that the probe is insensitive in the yaw angle range $-6° \leqslant \varphi \leqslant 6°$. Moreover, it was verified that it operates correctly independently of flow Reynolds and Mach numbers, as should be with all Pitot tubes designed according to normed guidelines (Standard, 2008). However, especially given the very small size of the probes employed in this work and the different compressibility regimes in which it will operate, it was deemed appropriate to verify this experimentally.

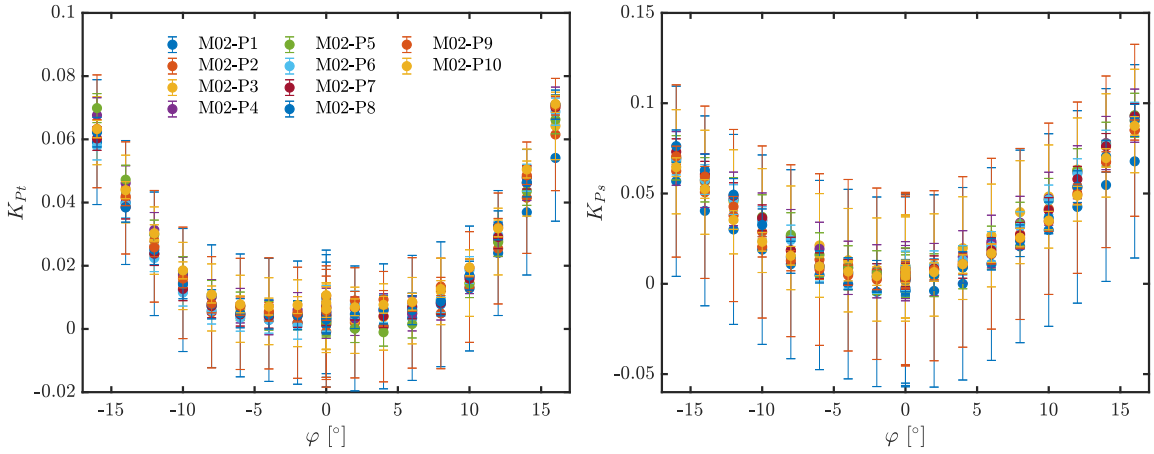

(a) K_{Pt} at $M = 0.2$.

(b) K_{Ps} at $M = 0.2$.

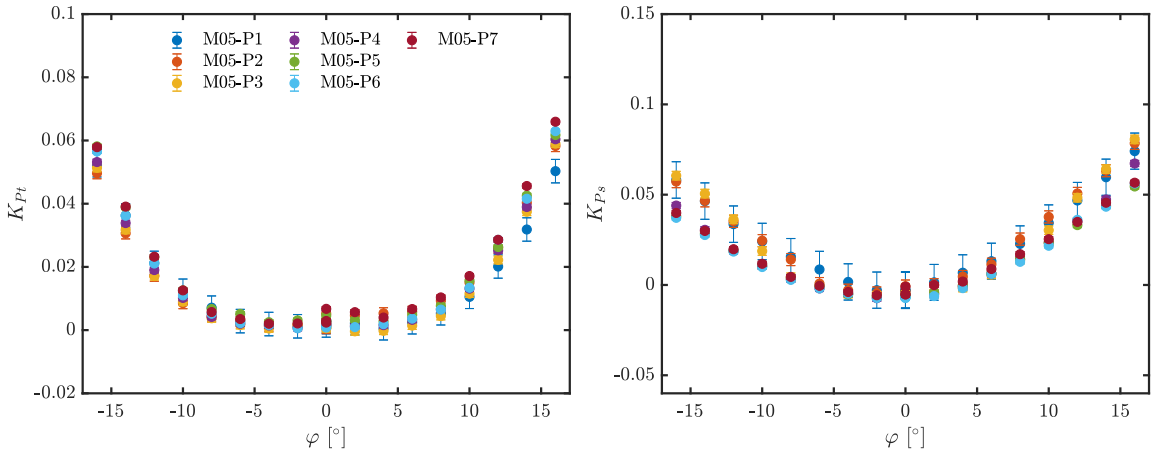

(c) K_{Pt} at $M = 0.5$.

(d) K_{Ps} at $M = 0.5$.

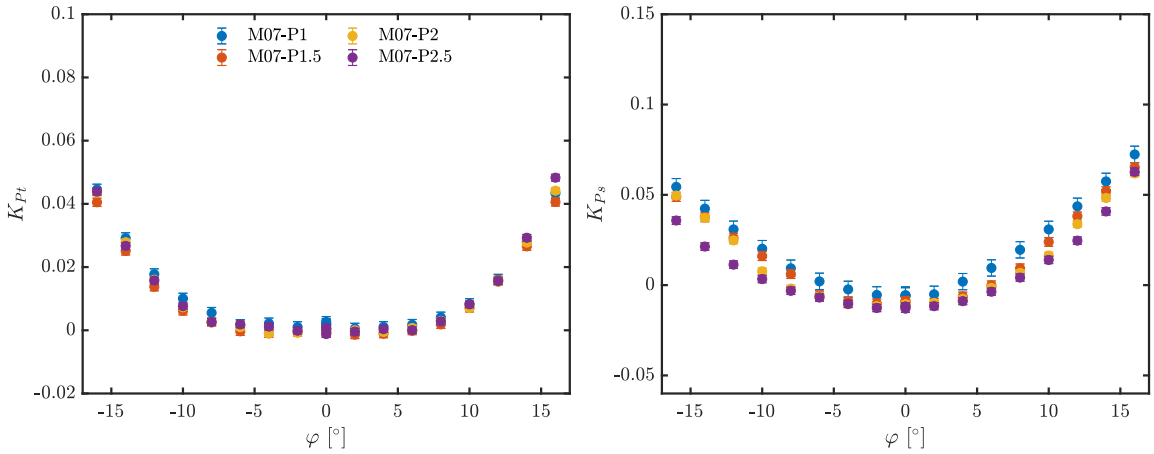

(e) K_{Pt} at $M = 0.7$.

(f) K_{Ps} at $M = 0.7$.

Figure 7.5. K_{Pt} and K_{Ps} for the *Aeroprobe* Pitot tube as a function of φ at different static pressure levels for Mach numbers $M = 0.2,\ 0.5,\ 0.7$. Legends are consistent between K_{Pt} and K_{Ps} plot pairs at each M.

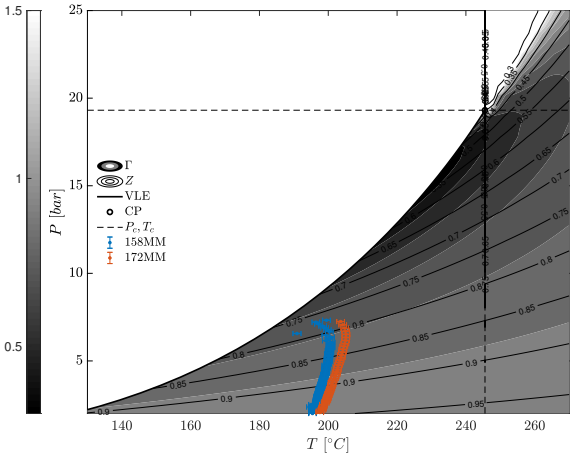

Figure 7.6. $P-T$ diagram with Z and Γ contours with total conditions during subsonic testing of the *Aeroprobe* Pitot tube with siloxane MM in the *TROVA*.

Name	Nozzle	P_T $[bar]$	T_T $[°C]$	Z_T $[-]$
158MM	*cMM02*	7.36	202	0.78
173MM	*cMM05*	7.40	210	0.79

Table 7.2. Initial total conditions of subsonic tests on the *TROVA* with fluid MM and the *Aeroprobe* Pitot tube.

7.2 Pitot Tube Testing in Non-Ideal Flows of Siloxane MM Vapor

After preliminary characterization in air, testing of the *Aeroprobe* Pitot tube with flows of Siloxane MM vapor at nominal Mach numbers $M = 0.2$ and 0.5 was carried out on the *TROVA*. The main objective was testing the complete pneumatic system for future directional probes and shock losses measures in non-ideal flows of organic vapors. Moreover, possible effects of the level of non-ideality on the Pitot tube performance are also considered.
The *Pitot* rear plate and subsonic choked nozzles *cMM02* and *cMM05* were employed. Nozzle *cMM07* was instead not considered here because 1D calculation indicated that the probe presence in the test section would cause non-negligible blockage effects, possibly leading to transonic flow conditions that might complicate the evaluation of the pneumatic system functioning.
A description of the pneumatic lines system and employed pressure transducers is found in Section 6.6.

One set of initial total conditions in the *HPV* was considered for each nozzle, as reported in Table 7.2, together with the name of the chosen exemplary test for each considered condition. Indeed, consistency and repeatability were assessed analogously to previous campaigns for supersonic and subsonic nozzles characterization, but the complete analysis will not be reported here for brevity.

7.2.1 $M = 0.2$

Results from test *158MM* presented in Figure 7.7 allow to evaluate the system performance at subsonic conditions with a Mach number $M \simeq 0.2$.
All acquired absolute pressures are plotted as a function of time in Figure 7.7a. The reference total pressure measured with a flush-mounted transducer is superposed to $P_{t,line}$ and $P_{t,pitot}$. The total pressure difference ΔP_t, directly measured with a differential transducer, is ~ 7 mbar at test beginning and decreases down to 1 mbar at the end, confirming the excellent agreement. This is evident in Figure 7.7c, where ΔP_t is reported together with pressure computed from absolute transducers. All three quantities agree, although the calculated pressure differences have a very large error-bar due to the large uncertainty propagated from absolute measures. This also highlights the importance of using differential transducers instead of absolute ones in the present case.

Quite analogously, the three measured static pressures $P_{s,ref}, P_{s,line}$ and $P_{s,pitot}$ in Figure 7.7a are also superposed. $P_{s,ref}$ is measured with a flush-mounted transducer at a pressure tap upstream of the other two pressures axial location, but it is superposed to the latter because boundary layer growth has a negligible impact (Section 5). Consistently, the static pressure difference ΔP_s in Figure 7.7d is a mere 3 mbar at test start and decreases to less than 1 mbar at the end, and its trend agrees very well with the difference between absolute transducers.
Given the good measurement performance in both total and static quantities, the kinetic head reported in Figure 7.7b shows a perfect overlap between readings from all differential and absolute transducers.
Total and static pressure coefficients are reported in Figure 7.7e. The absolute value of K_{Pt} is below 0.03 for most of the test. K_{Ps} is instead less than 0.015 at the beginning and then increases to 0.04 at the end of the test. However, the error-bar size also increases dramatically, with an uncertainty of ± 0.1, so larger than the coefficient value itself. Although limited, the increase in both K_{Pt} and K_{Ps} absolute values and in their uncertainty is unfortunately physiological due to the decrease in the kinetic head at the coefficients denominator as the test proceeds, and does not correspond to an increase in pressure differences ΔP_t or ΔP_s.
Nevertheless, overall K_{Pt} and K_{Ps} values are fairly constant and quite in line with findings during characterization in air, indicating an adequate performance of the complete pneumatic system in non-ideal flows of siloxane MM at $M \simeq 0.2$ for total, static and kinetic head measurements.

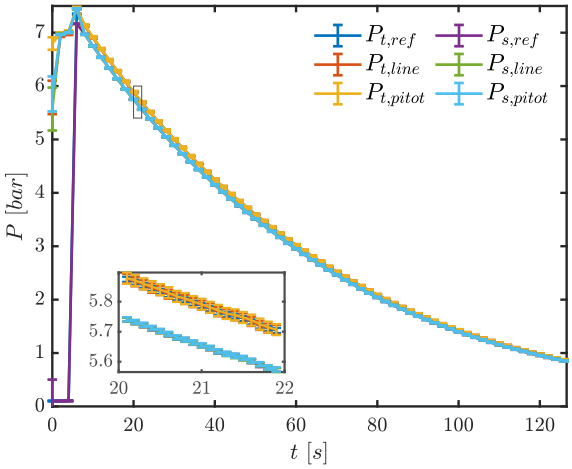

(a) Absolute pressures.

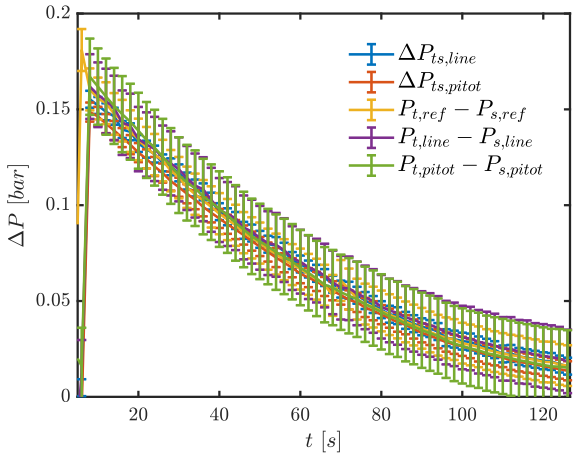

(b) Kinetic head.

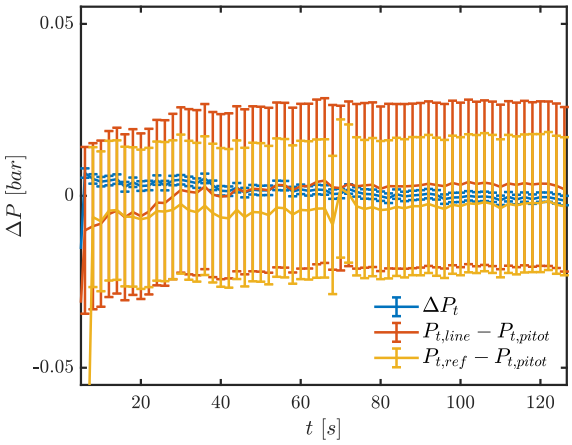

(c) Total pressure difference.

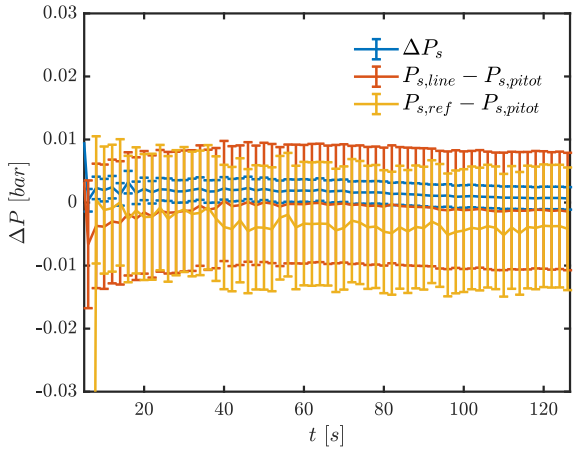

(d) Static pressure difference.

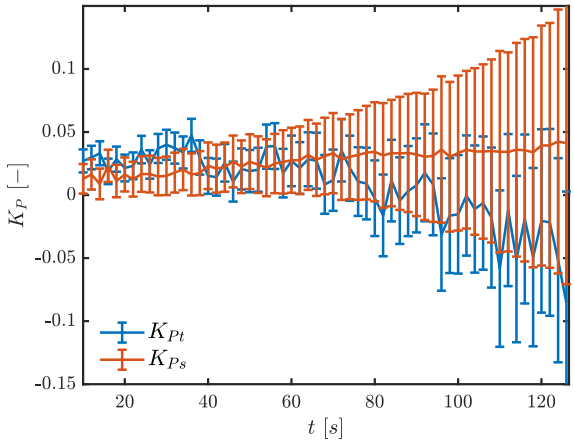

(e) Performance coefficients.

Figure 7.7. Results from test *158MM* with nozzle *cMM02*. Pressure differences directly measured with differential transducers are also compared to the ones calculated from absolute transducers.

7.2.2 $M = 0.5$

Figure 7.8 reports results from test *172MM* with the complete pneumatic system operating in non-ideal flows at $M \simeq 0.5$.
Differently with respect to testing at $M \simeq 0.2$, the Pitot tube total pressure $P_{t,pitot}$ is not well superposed with respect to reference and line total pressures. This is particularly evident in the red zoom box in Figure 7.8a where, although $P_{t,pitot}$ is still within errobars of the other two, it is overall significantly higher. This is reflected in a negative total pressure difference ΔP_t in Figure 7.8c with an average value of ~ -10 mbar. The negative measure by the differential transducer is confirmed by the difference between absolute pressures, albeit with much larger uncertainties.
Considering static pressures in Figure 7.8a, $P_{s,ref}$ is slightly higher than the line and Pitot one at the beginning of the test, consistently with the limited but not negligible boundary layer effect occurring at higher pressure levels (Section 5). $P_{s,line}$ and $P_{s,pitot}$ are instead well superposed, consistently with a ΔP_s value in Figure 7.8d always well below 3 mbar.
Consistently with the absolute pressures plot, the kinetic head in Figure 7.8b linked to reference flush mounted transducers is slightly lower due to the higher $P_{s,ref}$, whilst that related to the Pitot tube is a little larger. However, even though a difference in nominal values is present, all curves are actually within error-bars of one another.
Total and static pressure coefficients are reported in Figure 7.8e. The value of K_{Ps} is in line with air testing because it is always lower than 0.01, even though error bars become very large towards the end of the test, as previously mentioned. K_{Pt} values are instead always negative due to the larger Pitot tube total pressure and become very large in absolute value towards the end of the test due to the decrease in kinetic head at the coefficient denominator. Indeed, the total pressure difference ΔP_t is fairly constant throughout the test, but its relative importance increases as the pressure level decreases.
It is evident that the pneumatic system is adequate for static pressure measures, but an issue on the Pitot tube total pressure line is present, as further investigated next.

7.2.3 Measurement Delay

Pitot tube testing with nozzle *cMM05* has shown that its total pressure $P_{t,pitot}$ is evidently larger than the total reference and line ones. The only physically possible explanation for this, which is also consistent with the emptying dynamics in which the pneumatic line operates, is of a measurement delay. Line pressure is unable to readily adapt to the decreasing pressure in the test section, meaning that at any given time instant, the pressure in the total pressure line of the Pitot tube is larger than the reference one, leading to errors in both absolute and differential measures.
The extent of the delay was found to increase when nozzles with larger throat area were employed ($cMM05$ with respect to $cMM02$, in which case the delay was not noticeable) and when nitrogen was used instead of MM, so when the emptying dynamics of the HPV was faster. Nitrogen tests are not reported in the present work, but they were carried out prior to any testing with siloxane MM.
This delay was somewhat unexpected, given that no such issues were evident during preliminary lines testing without the probe described in Section 6. Given that the Pitot tube was indeed absent during such tests, the delay was initially attributed to a possible contraction in the total pressure inner channel. However, probe inspection with an harmonic thread indicated that the line was actually clear. The reason for the measurement delay is instead to be found in a different overall lines volume between the pneumatic systems for testing without and with the probe. This was because the former preliminary campaign was carried out with nozzle *nMM02*, involving a slow emptying *HPV* dynamics, and with only one differential transducer on each line. The complete system for probes testing instead features two differential sensors on each line, either measuring a kinetic head or the difference between Pitot tube and line static or total pressures. As evident in

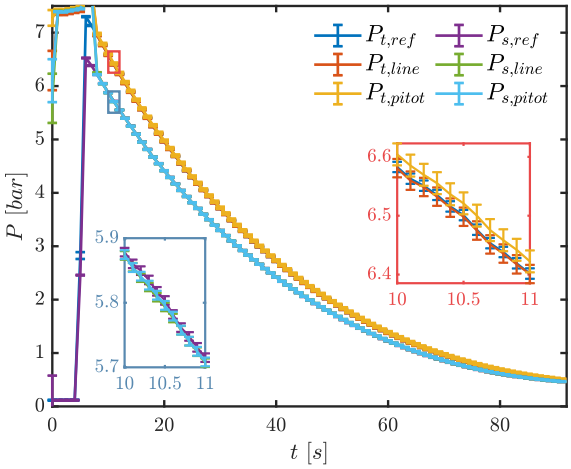

(a) Absolute pressures.

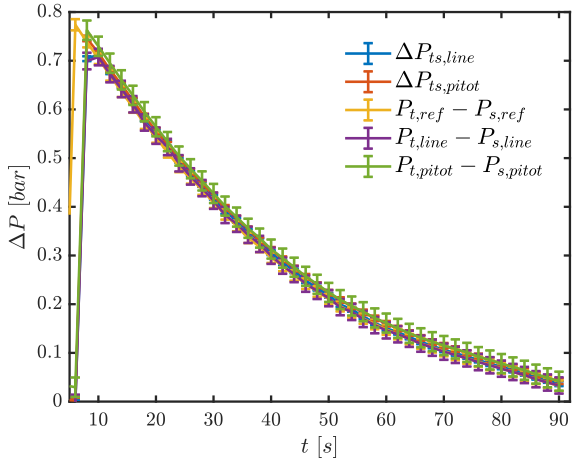

(b) Kinetic head.

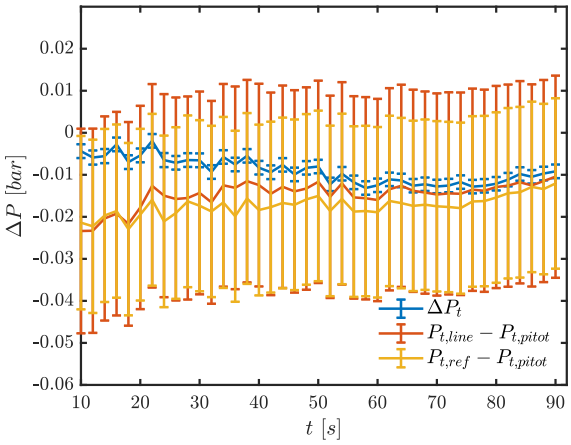

(c) Total pressure difference.

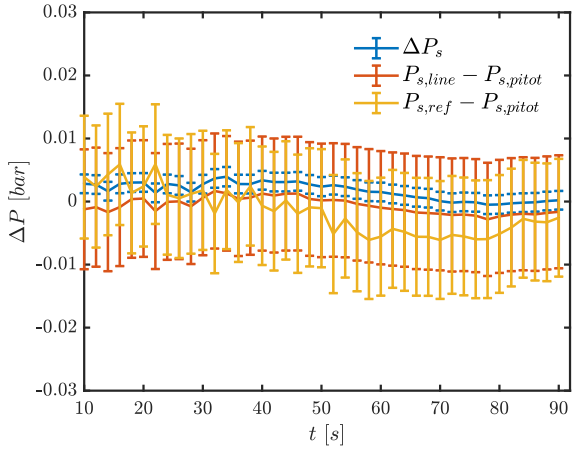

(d) Static pressure difference.

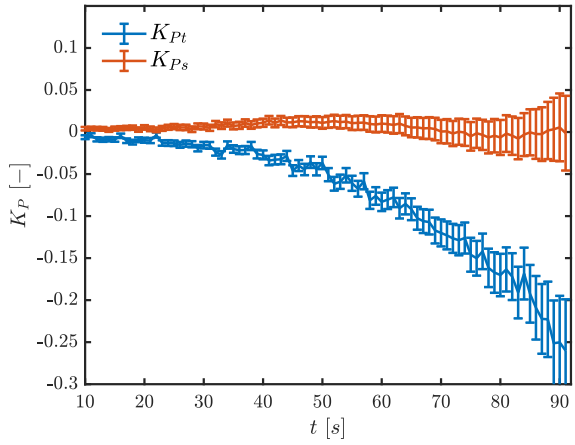

(e) Performance coefficients.

Figure 7.8. Results from test *172MM* with nozzle *cMM05*. Pressure differences directly measured with differential transducers are also compared to the ones calculated from absolute transducers.

Figure 7.9. Internal membrane chamber of a *Schaevitz* differential pressure transducer.

Figure 7.9, differential transducers are characterized by a relatively large internal volume in the membrane chamber leading to a 'hidden' but significant increase in the overall lines volume. This dramatically increases the pneumatic line nitrogen discharge time during tests and is responsible for the larger total pressure measured by the Pitot tube.
Pneumatic system dynamic testing, next described, allowed to confirm the source of the unwanted measurement delay and identify best practices to reduce the issue.

7.3 Pneumatic Lines Dynamic Testing

Just before a typical *TROVA* test start, pneumatic lines are loaded with nitrogen. It is then is discharged into the test section as the lines empty as the test proceeds, due to the transient nature of the plant. Therefore, the aim of the dynamic testing procedure is to assess the Pitot tube total pressure line response as it empties.
To this end, the scheme shown in Figure 7.10a is employed. The probe total pressure pneumatic system, complete with electrovalve *VV1* and absolute and differential transducers, is the same as during actual tests so as to account for the real lines volume. The other end of differential transducers ΔP_1 and ΔP_2 is left open to ambient conditions. An absolute reference transducer and an electrovalve *VV2* are added at the probe tip.
The dynamic testing procedure is as follows. The total pressure line is pressurized by opening electrovalve *VV1* while *VV2* is closed. *VV1* is then closed after a desired constant pressure is reached. In this case, line pressurization up to $\sim 250\,\mathrm{mbar_r}$ was considered sufficient, since line discharge during tests occurs over very small pressure differences with the test section (except at the very first test instants just after electrovalves closure). *VV2* is then opened, imposing a negative step input to the line as it discharges into the atmosphere from the probe tip, analogously to what happens during test time. Pressure read by transducers at the end of the line P_{line} is compared to the reference transducer at the probe tip P_{tip}, as shown in Figure 7.11a in order to determine the line response.
It must be pointed out that electrovalve *VV2* is not a fast-opening valve. However, its opening time is orders of magnitude lower than the characteristic time of pressure decrease due to *HPV*

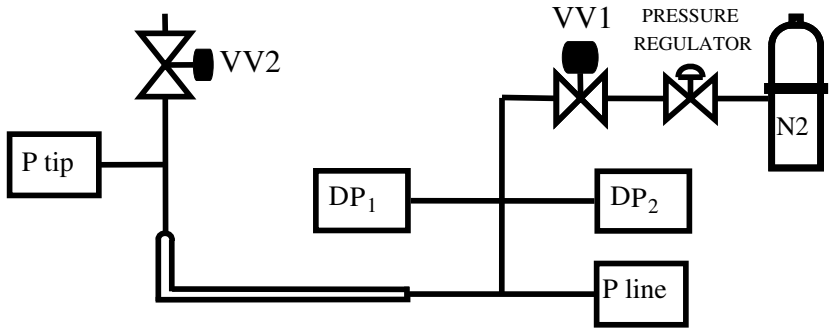

(a) Pneumatic lines scheme for dynamic testing of the probe total pressure line.

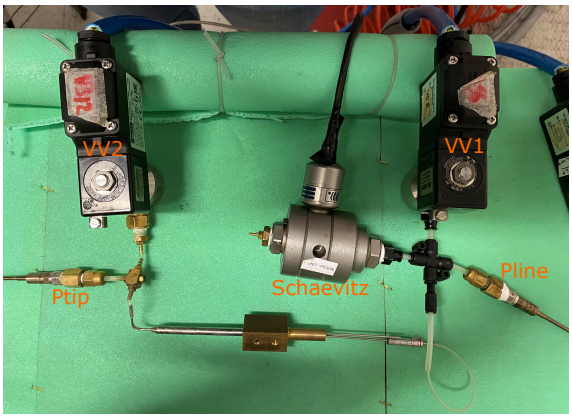

(b) Example of a configuration including one differential *Schaevitz* transducer.

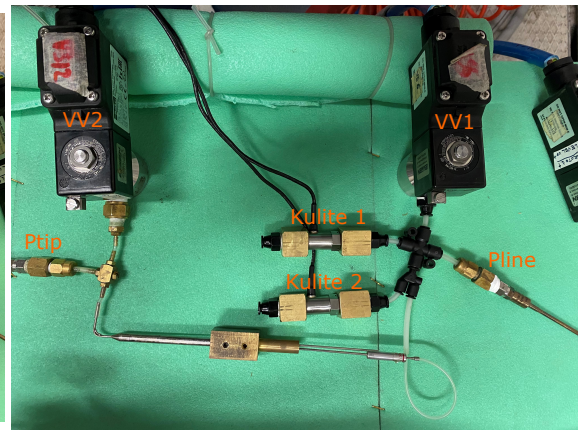

(c) Example of a configuration including two differential *Kulite* transducers. Their much smaller volume is eloquent.

Figure 7.10. Scheme and examples of different lines configurations for dynamic testing.

emptying during a test. It was therefore considered sufficiently fast to represent a step input in the present case.

For comparison (as for example in Figures 7.10b and 7.10c), various line configurations were also tested, featuring only one or no mounted differential transducers, and even using the *TotAle* probe instead of the *Aeroprobe* Pitot tube. Given that the excessive chamber volume of the employed *Schaevitz* transducers is the culprit for measurement delay, *Kulite* differential sensors of *XTL-3-375 (M)* series were identified as candidate substitutes given their significantly smaller size. Therefore, the lines dynamic response was also tested in configurations including the latter.
Figure 7.11a reports the step response for all tested line configurations, as indicated in the legend. Abbreviation *AP* represents all cases involving the *Aeroprobe* Pitot tube, *TA* stands for *TotAle* total pressure probe, *Sch* for *Schaevitz* differential transducers and *Ku* for *Kulite* ones. The number of transducers is also indicated, whilst in case no transducer type is specified, the line does not have any mounted sensor.
A $\sim 250\,\mathrm{mbar_r}$ step was applied in all cases, but the plotted pressure trend was normalized with respect to the exact imposed one for comparison purposes. The value of P_{line} is plotted for all configurations, as well as the tip pressure P_{tip} for reference.
Results quite self-evidently provide the explanation for the measurement delay issues identified on the *Aeroprobe* Pitot tube total pressure line. The use of two *Schaevitz* differential transducers

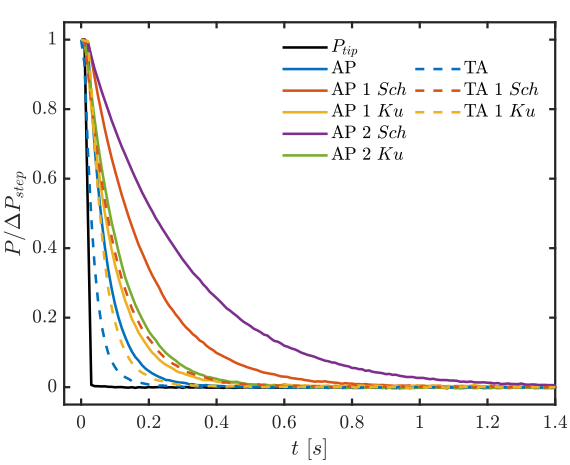

(a) Step pressure response.

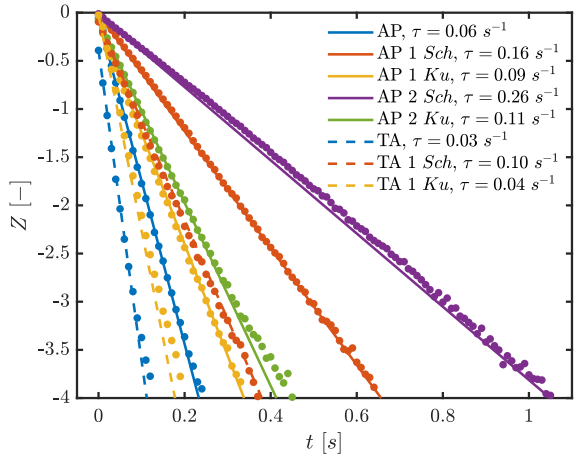

(b) Quantity Z as a function of time and data fitting by straight lines with slope $-1/\tau$.

Figure 7.11. Dynamic testing of several total pressure line configurations, starting at $t = 0\ s$, when electrovalve *VV2* is opened.

significantly slows down the system response, given that the line pressure does not reach the tip one before 1.4 s after the step is applied. This is significantly later with respect to the configuration with one transducer only, which indeed was the one used during preliminary pneumatic line testing prior to probe insertion in the test section.
Kulite transducers instead provide much less measurement delay and are therefore envisaged for use in pressure probes testing instead of *Schaevitz* ones.
Comparison between *Aeroprobe* Pitot tube and *TotAle* total pressure probes also illustrates that the latter has a noticeably faster dynamics thanks to the slightly larger tap diameter. For this reason, it was the preferred instrument for shock loss measurements in Section 8.

Even though line-cavity systems are usually of $2^{nd}-$order, Figure 7.11a indicates that the total pressure line is so over-damped that its response closely resembles that of a $1^{st}-$order system. As such, its response is determined by the *static sensitivity* K and its *time constant* τ. Since $P_{line} = P_{tip}$ after the transient has expired, then it can be assumed that $K = 1$. The time constant can be estimated by plotting quantity $Z(t) = \ln\left(1 - \frac{P_{line}(t)}{KP_{tip}(t)}\right)$ as a function of time, as shown in Figure 7.11b. The straight line slope is then related to the time constant: $\frac{dZ}{dt} = \frac{-1}{\tau}$. Data points fall very close to a straight line, confirming that the line response is of $1^{st}-$order type (Doeblin, 1990). The best fit line for all configurations was determined, giving the respective time constant values, as indicated in the legend, and allowing to quantify the different response speeds. The use of one *Schaevitz* transducer more than doubles the response time with respect to the line-only case for both probes. Adding a further sensor of the same type further increases it by a factor of ~ 1.5.
For comparison, one *Kulite* transducer instead increases the time constant of the single line by only $\sim 50\%$.
Given these findings, testing with nozzle *cMM05* was repeated by limiting the overall volume on the *Aeroprobe* Pitot tube total pressure line to the very minimum. The differential transducer devoted to direct probe kinetic head measure was removed since it was thought best to focus on achieving an accurate total pressure measurement. Also, the *Schaevitz* sensor measuring the total pressure difference was substituted with a *Kulite* one with a comparably low full scale of

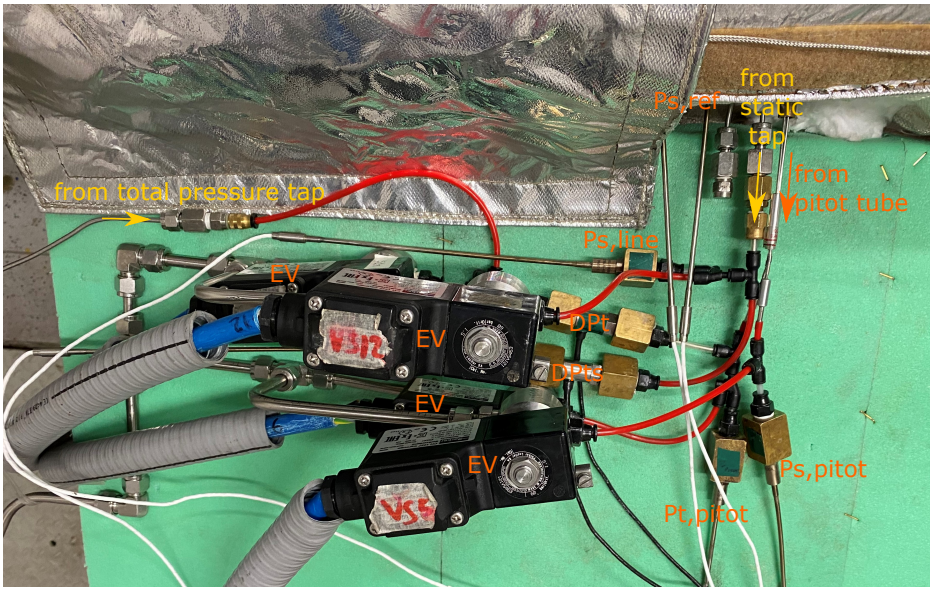

Figure 7.12. Pneumatic lines configuration for Pitot tube testing in subsonic flows of Siloxane MM with minimal volume where only two *Kulite* differential transducers are employed. The absolute transducer measuring $P_{t,line}$ is covered by the electrovalves (*EV*).

0.7 bar and uncertainty of 1.7 mbar. The *Schaevitz* differential transducer measuring $\Delta P_{ts,line}$ was instead replaced by a *Kulite* sensor with 5.9 bar full scale and an uncertainty of 10 mbar. The final configuration is shown in Figure 7.12.

7.4 Reduced Delay at $M = 0.5$

Results concerning total pressure measures of tests with the reduced volume configuration are reported in Figure 7.13. Repeatability was assessed as in all previous cases and only one test is here reported (test *206MM*).
Things have improved considerably, given that the Pitot tube total pressure is always superposed to $P_{t,ref}$ and $P_{t,line}$, as visible in Figure 7.13a. This is confirmed by the total pressure difference ΔP_t in Figure 7.13b, which is now always positive and is significantly lower in absolute terms, with a value of 6 mbar at the beginning and 1 mbar at the end of the test.
Thus, the pneumatic system can now be considered adequate for total pressure measures aswell.

7.5 Conclusions

The present chapter reported the results of a very extensive experimental campaign involving Pitot tubes in non-ideal subsonic flows of organic vapors having the primary objective of completing the commissioning of the dedicated pneumatic system. A total of 70 experimental runs were carried out, of which about 30 with siloxane MM and 40 with nitrogen.
The process of improving the pneumatic system to its best possible configuration was actually the most onerous and time consuming task of the whole campaign. Several positioning of components, as well as different line and coupling types, were evaluated to provide the minimum possible line

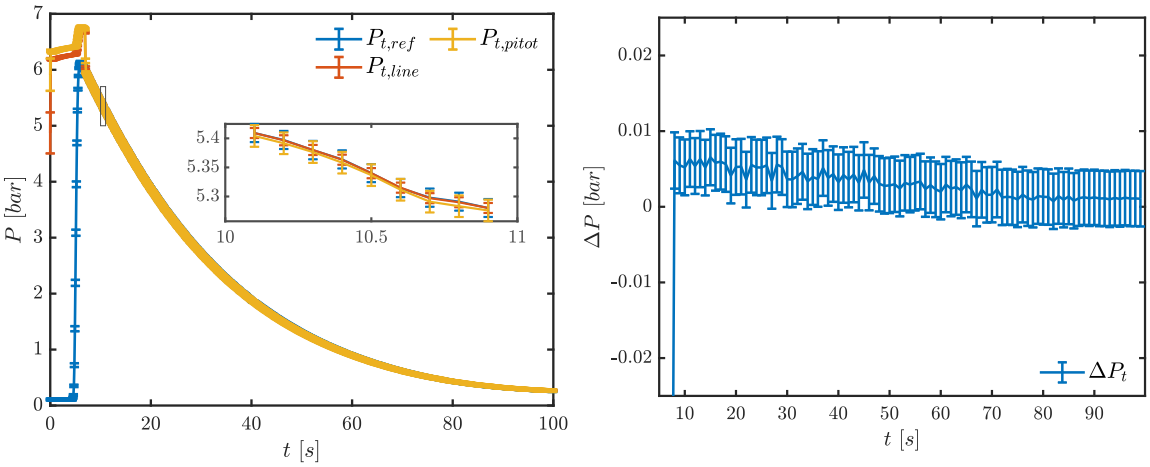

(a) Absolute total pressures.

(b) Total pressure difference.

Figure 7.13. Results concerning total pressure measures from test *206MM* with nozzle *cMM05*.

length. Moreover, unfortunately, many unsuccessful tests were repeated before the transducers inner volume was realized to be responsible for the measurement delay, and tests with the final improved configurations also had to be carried out after that.
This hard-earned expertise has allowed to establish several best practices concerning pressure measures involving pneumatic lines in transient non-ideal flows subject to condensation. For example, a dynamic testing procedure, such as the one previously presented, is essential prior to any experimental campaign involving transient flows to indicate if and how the pneumatic lines should be improved.

Both the choice of the type of probe and of subsonic conditions was deliberate, because it was only their combined testing that would have allowed to evaluate the performance of the complete pneumatic system against reference quantities. Indeed, a Pitot tube is the only type of probe that, in subsonic conditions, measures both total and static quantities that have a direct reference counterpart (be it flush-mounted or on a line). Had supersonic flows been directly considered, one would not have been able to discern measurement delay issues, given that total pressure shock losses would not have permitted any reference. Moreover, had directional pressure probes been used, no reference would have been available for static pressure measures, except perhaps preliminary campaigns with air in simpler facilities such as the *Safety Valves Test Rig*. Indeed, directional pressure probes often have a total pressure tap but do not have a static tap parallel to flow direction whose measure can be compared with reference readings from the wind tunnel. Identification of any possible issues with the static pressure pneumatic line would have therefore been impossible. Thus, although the final result of having achieved a 'simple' Pitot tube measure in the *TROVA* might not seem an extraordinary result, it is actually a feat in itself, which proved to be an essential preparatory step prior to directional pressure probes and shock losses measurements in non-ideal flows.

In a different regard, the present campaign allowed to experimentally verify, for the first time, the correct functioning of a Pitot tube in non-ideal flows of siloxane MM. Given the relatively limited variation in Pitot tube performance coefficients during tests, it can be concluded that the level of flow ideality does not significantly affect its behaviour. Thus, no particular calibration is required for Pitot tubes in non-ideal flows, but the instrument total and static pressure readings can be simply coupled with a total temperature measure and a suitable thermodynamic model

to calculate isentropic expansions in order to determine flow quantities, including local velocity, density and Mach number. This provides useful information for Pitot tubes use in engineering processes involving non-ideal flows. Under this aspect, the use of the total compressibility factor Z_T to parameterize pressure ratio trends in isentropic expansions (Section 2) might prove very useful to allow a faster calculation of flow quantities relevant in industrial applications. Isentropic flow relations or tables for a chosen fluid, analogous to those available for air at the back of any gasdynamics textbook, but with the additional parameter of total compressibility factor, could replace dedicated routines or spreadsheets requiring calls to an external thermodynamic library. This would reduce the computational burden in possible plant control systems involving PLCs, where the implementation of such simpler calculation with few parameters is useful considering the limited available computational power.

CHAPTER 8

PITOT TUBES IN NON-IDEAL SUPERSONIC FLOWS: NORMAL SHOCK LOSSES

This chapter documents the first ever experimental total pressure drop measurements across normal shock waves in non-ideal flows of siloxane MM vapor. Whilst consolidated theoretical and numerical tools are in place for shock losses calculation concerning non-ideal flows, direct experimental measures are lacking in literature due to the difficulties linked to running wind tunnels for such flows. The various operational complications are probably now quite evident after Sections 6 and 7.

The experimental campaign here presented builds upon the know-how developed in the two preceding sections and its aim is two-fold. The first objective is to provide experimental data for verification of theoretical and numerical tools for research and industrial applications. The investigated flow conditions, in terms of total temperature and pressure and of Mach number, are representative of real operating conditions in organic Rankine cycle (ORC) turbines, specifically of the supersonic stator row exit.

The second objective is to complete the pneumatic system assessment by considering supersonic flows after the already covered subsonic ones. This step is key to enable future testing of turbine blade cascades representative of those employed in ORCs. Given that the flow is often supersonic, the assessment of the blade row performance requires a pressure probe pneumatic system that can correctly operate in non-ideal supersonic flows of organic vapors.

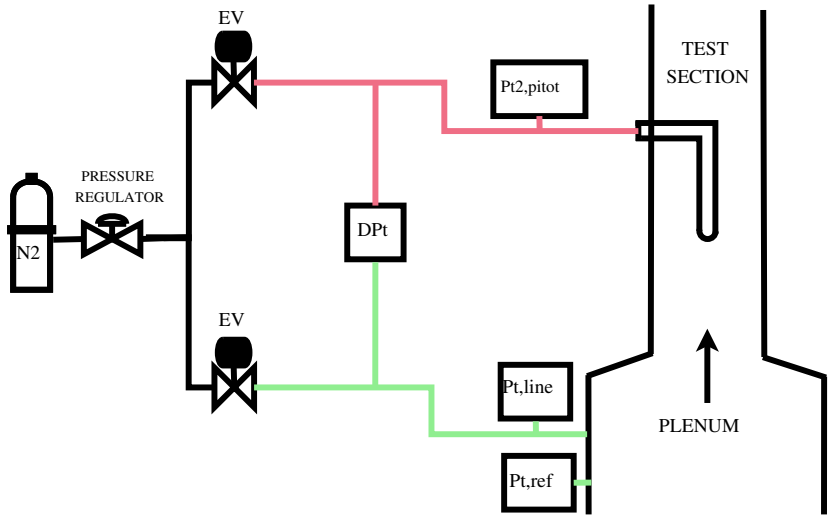

Figure 8.1. Pneumatic lines scheme in the *TROVA* for total pressure loss measurement across normal shocks with Pitot tubes.

8.1 Test Setup and Conditions

The experimental campaign was carried out using the *Wedge* rear plate and nozzle, described in better detail in Section 3 and illustrated in Figure 3.14. A new cylindrical insert was designed and produced to expose the probe to supersonic MM flow, with its tip in the uniform Mach number region, as illustrated in Figure 3.14.

Figure 8.1 illustrates the employed pneumatic system. Compared to the complete system in subsonic conditions, only the difference ΔP_t between the plenum total pressure (upstream of the shock) and the Pitot tube total pressure (downstream of the shock) is here considered. Quantity ΔP_t is now a direct measure of the total pressure loss across the shock. Absolute transducers are still present on each line to help with possible issues identification.

Preliminary tests with nitrogen were carried out prior to the experimental campaign with MM in order to assess the measurement system performance. One set of initial total conditions was considered for each fluid, as reported in Table 8.1 together with the name of the chosen exemplary test. Analogously to all previous experimental campaigns, tests were performed several times to ensure repeatability although the complete analysis is not shown here fore brevity. Results from only one test per condition will be further examined.

Considering the measurement delay issues covered in Section 7.2.3, all tests were performed with the *TotAle* probe due to its faster emptying dynamics with respect to the *Aeroprobe* Pitot tube. Unfortunately, the smaller *Kulite* transducers were not available for this campaign. The differential transducer used to measure ΔP_t is a *Schaevitz P2100 Series* having a full scale $FS = 2.0$ bar and an uncertainty of 3.6 mbar (1.8 ‰FS). Flush-mounted and pneumatic line absolute transducers were chosen according to the most suitable full-scale amongst those listed in Table 3.1.

In order to ensure that no delay issues on the probe total pressure line were infact present, subsonic testing using nozzle *cMM05* was carried out with this pneumatic system configuration (full details are not reported here for brevity). Despite the relatively large transducer volume, no measurement delays were present given that the probe total pressure was found to be always superposed with respect to the reference one.

Schlieren visualizations were performed employing the bench setup illustrated in Section 3 to

Test Set Name	P_t $[bar]$	T_t $[^\circ C]$	$Fluid$	Z_T	*Exemplary Test*
Sh-N2	9.70	25	N_2	1	*$N_2$179*
Sh-MM	12.76	233	MM	0.66	*MM182*

Table 8.1. Initial total conditions of the two sets of supersonic tests on the *TROVA* with Pitot tubes.

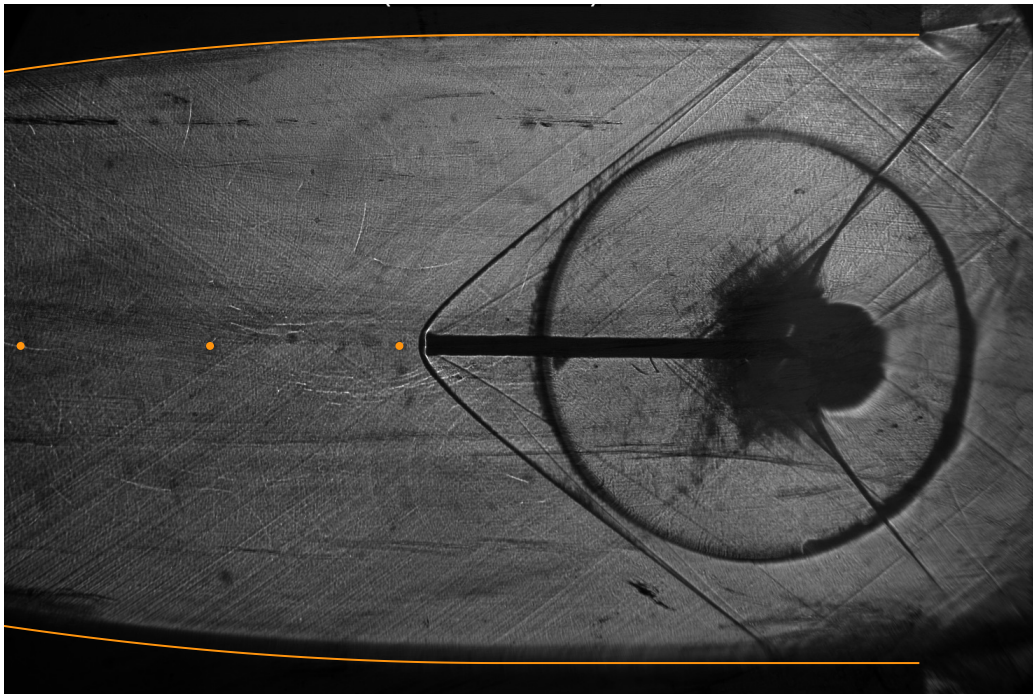

Figure 8.2. Schlieren image at $t = 8.5$ s during test *$N_2$179*. Nozzle contour and pressure taps are highlighted.

support pressure measurements.

8.2 Preliminary Experimental Campaign with Nitrogen

The schlieren image in Figure 8.2 shows that the wind tunnel operating regime is indeed the expected one, with supersonic flow impinging on the probe tip resulting in a bow shock that is locally normal to it.

Figure 8.3 illustrates pressures during test *$N_2$179*. It was performed with line flushing to test the full procedure for MM experimental runs, although it was unnecessary here due to the impossibility of condensation. Pressure $P_{t,line}$ is in perfect agreement with the reference total pressure in the plenum $P_{t,ref}$ after line flushing has ended, indicating no issues on the upstream total pressure line to the differential transducer. The two pressures are within errorbars of one another from test time $t = 6$ s, so less than 0.6 s after peak pressure was reached. Flushing pressure was chosen according to expected peak pressure with MM and is slightly high compared to the present nitrogen testing conditions.

Pressure P_a is larger with respect to P_b and P_{fs}, consistently with taps position along the nozzle. The free-stream pressure P_{fs} is instead larger than pressure P_b at the preceding tap. This is

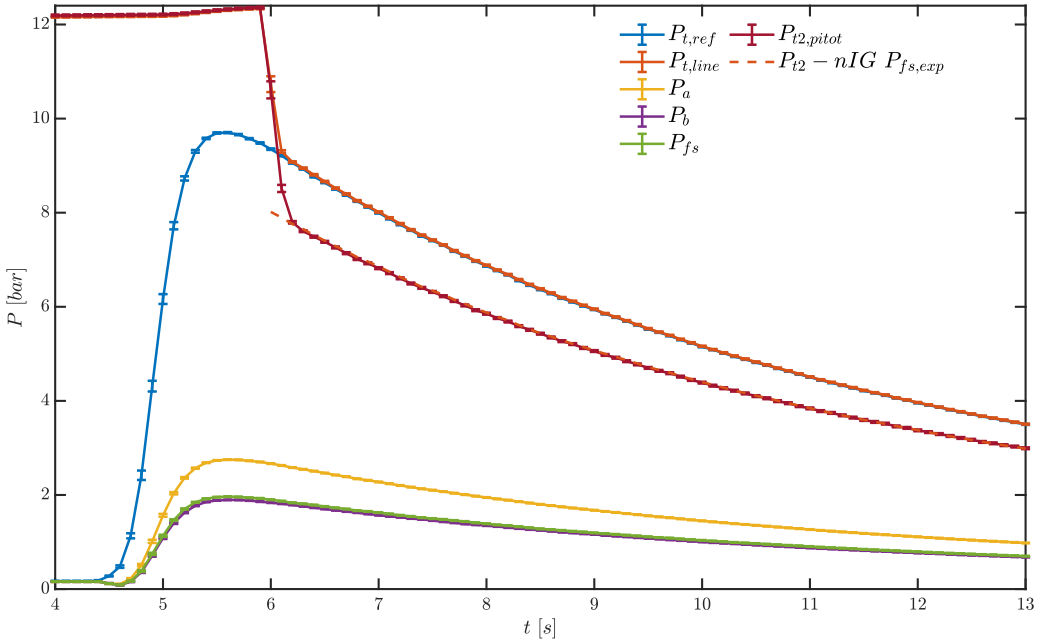

Figure 8.3. Absolute pressures during test N_2179. Line flushing is present until $t =\sim 6$ s for $P_{t,line}$ and $P_{t2,pitot}$.

attributed to a slight recompression occurring in the last portion of the nozzle linked to the off-design operation of the present geometry with nitrogen instead of design fluid MDM.

The absolute total pressure measured by the Pitot tube $P_{t2,pitot}$ is compared to the theoretical post-shock total pressure calculated from the experimental P_{fs} and assuming a normal shock at the probe tip (as it is evident from Figure 8.2). Post-shock pressure $P_{t2} - nIG\ P_{fs,exp}$ was determined by numerically solving mass, momentum and energy conservation equations across the shock coupled with the Span-Wagner thermodynamic model through the *FluidProp* library (Appendix A). Analytical Rankine-Hugoniot equations for a polytropic ideal gas with specific heats ratio $\gamma = 1.4$ were used to verify the above solution method, which is generalized to non-ideal flows, for following use with MM. As visible in Figure 8.4a, $P_{t2} - nIG\ P_{fs,exp}$ is within error bars of the measured $P_{t2,pitot}$ for most of the test, except for the initial time instants.
Figure 8.4b reports absolute and percentage differences between computed and measured post-shock total pressures, analogously to quantity $\Delta P_{CFD-exp}$ (Equation 4.5) employed in Sections 4 and 5 to evaluate the accordance between numerical and experimental results. The propagated uncertainty is also calculated with the assumption of no uncertainty in theoretical computations. The good agreement between measured and calculated post-shock pressures is evident, given that percentage differences are very close to 0 for most of the test.

Figure 8.4c shows total pressure loss across the shock ΔP_t directly measured with the differential transducer, together with the calculated total pressure difference. The two quantities exhibit absolute differences that are somewhat larger than what could be expected from the previous analysis on P_{t2}, where calculation was found very close or within errorbars of the measured quantity. This is linked to the fact that the measured differential pressure has a much lower associated uncertainty with respect to absolute transducers. Indeed, throughout the test, the uncertainty in the free-stream pressure transducer is $U_{P_{fs}} \sim 7$ mbar and $U_{P_{t2,pitot}} \sim 20$ mbar. Considering the differential transducer measuring ΔP_t, its uncertainty is instead only $U_{\Delta P_t} \sim 5$ mbar.

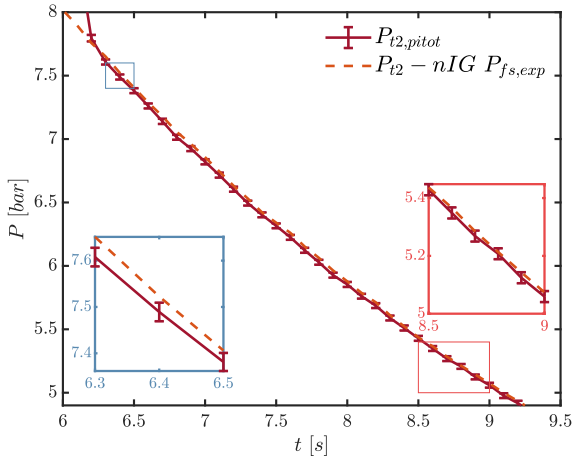

(a) Post-shock pressure P_{t2}.

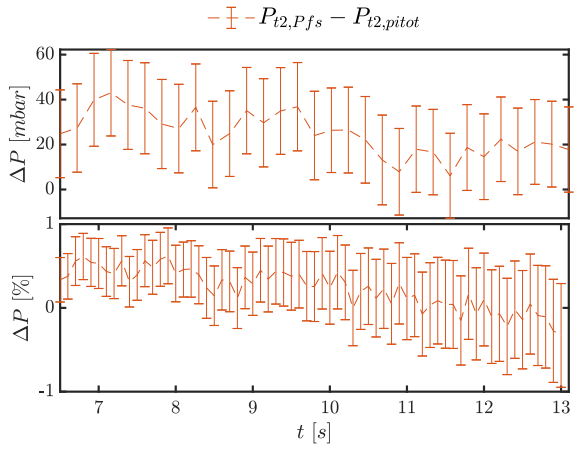

(b) Absolute and percentage differences between measured and calculated P_{t2}.

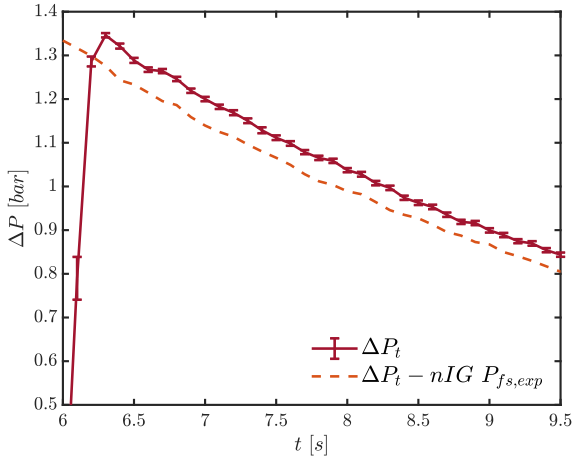

(c) Total pressure loss ΔP_t.

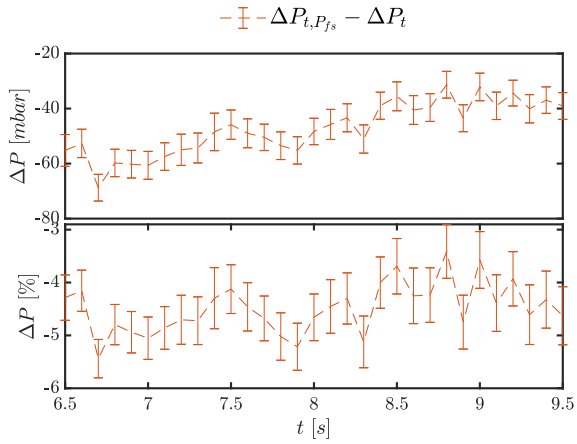

(d) Absolute and percentage differences between measured and calculated ΔP_t.

Figure 8.4. Zoom at $t = 6 - 9.5$ s of measured and calculated pressures during test *$N_2$179* with related absolute and percentage differences.

Figure 8.4d reports absolute and percentage differences between computed and measured total pressure losses. For graphical clarity, these are reported in the legend as $\Delta P_{t,P_{fs}} - \Delta P_t$.
The difference between the experimental and theoretical pressure drops is in the range $\sim 40-60$ mbar or $4 - 6\%$. In relative terms, the percentage discrepancy is higher than what was observed for absolute pressures since a ΔP is considered here instead, with lower values involved at the percentage difference denominator.

Overall, the measurement system performance seems to be satisfactory, given that the percentage difference between measured and calculated total pressure loss is never larger than 6%. Under this aspect, it must be pointed out that such a discrepancy might not be due to issues with the direct pressure loss measure, but might instead be linked to the experimental P_{fs} value employed in theoretical calculation to verify ΔP_t from the differential transducer.

The present nozzle was designed with the *method of characteristics* so as to yield a uniform flow at the axis starting several millimeters before the free-stream pressure tap in certain design conditions with fluid siloxane MDM. Testing with nitrogen, a fluid with significantly different molecular complexity, implies a different conformation of the expansion and of the turning region. The flow might still be accelerating or might be recompressed between the free-stream tap and the probe tip, resulting in a different pressure at the two positions. This could contribute to the evidenced differences between the pressure drop directly measured with a differential transducer and the one calculated with the experimental P_{fs}. This effect is thought to be relatively limited, given that probe tip and free-stream tap are only ~ 3 mm apart. Nevertheless, CFD calculation are envisaged in the near-future to better understand this aspect.
Moreover, although a complete numerical and experimental characterization of the present nozzle is not available, results on supersonic nozzle *nMM16* (Chapter 4) have shown that the *turning region* displays the largest discrepancies between measurement and CFD. This seems to indicate that achieving a high quality measure is here most difficult and should be further investigated.
Another possible explanation for the above differences between measured and calculated shock losses could be linked to a shock-boundary layer interaction occurring at the back plate, in the depth (z-direction) of the test section and thus unfortunately not visible from schlieren images. The shock wave produced by the probe tip impinges on the back wall at a certain distance downstream of the free-stream tap that depends on its slope. The distance between the center of the channel, where the probe tip is placed, and the wall is only 9.35 mm. As visual reference, this is about a third of the distance between the probe and the upper or lower nozzle profile in the vertical direction. It is thus possible that pressure increase by the shock wave at the wall propagates upstream of the shock itself through the subsonic portion of the boundary layer. This could result in a measured pressure at the wall tap that is larger than the free-stream pressure at the center of the channel at the probe tip. Thus, the free-stream Mach number calculated from the measured P_{fs} is actually lower than the one impinging on the probe, consistently with the lower calculated shock losses with respect to measured ones. Numerical simulations of the nozzle with the inserted probe are foreseen in the future to verify this hypothesis.

Mach lines in schlieren images were extracted in order to verify the P_{fs} measure. Unfortunately, as visible in Figure 8.5a, gradients in the image are quite faint because the whole optical apparatus was set for testing with MM, characterized by stronger density gradients and darker images. Only two Mach lines could be reliably identified, but they are fairly distant from the free-stream tap or the probe tip. The extracted Mach number is plotted against its axial position in Figure 8.5b, together with the values calculated from pressures at the taps. The two data-sets are in good agreement with each other, but the large error bars and the aforementioned axial distance do not allow to draw conclusive remarks on the reliability of the measured P_{fs}.

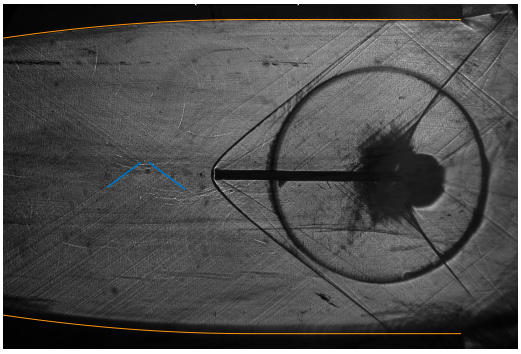

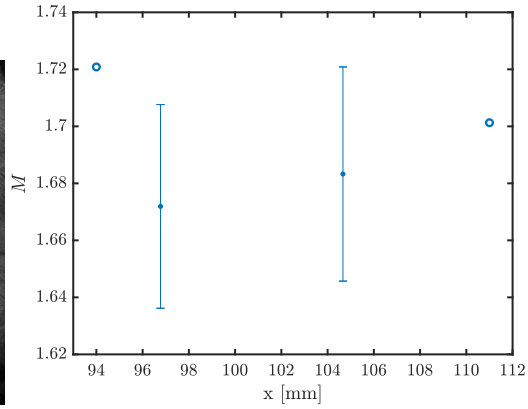

(a) Schlieren image with superposed identified Mach lines at $t = 8.5\ s$.

(b) Mach number from pressure measurements (empty dots) and Mach lines (with error bars). The plot is zoomed between the free-stream tap at $x = 111$ mm and the preceding one.

Figure 8.5. Mach number extraction from schlieren images for conditions at $t = 8.5\ s$ during test N_2179.

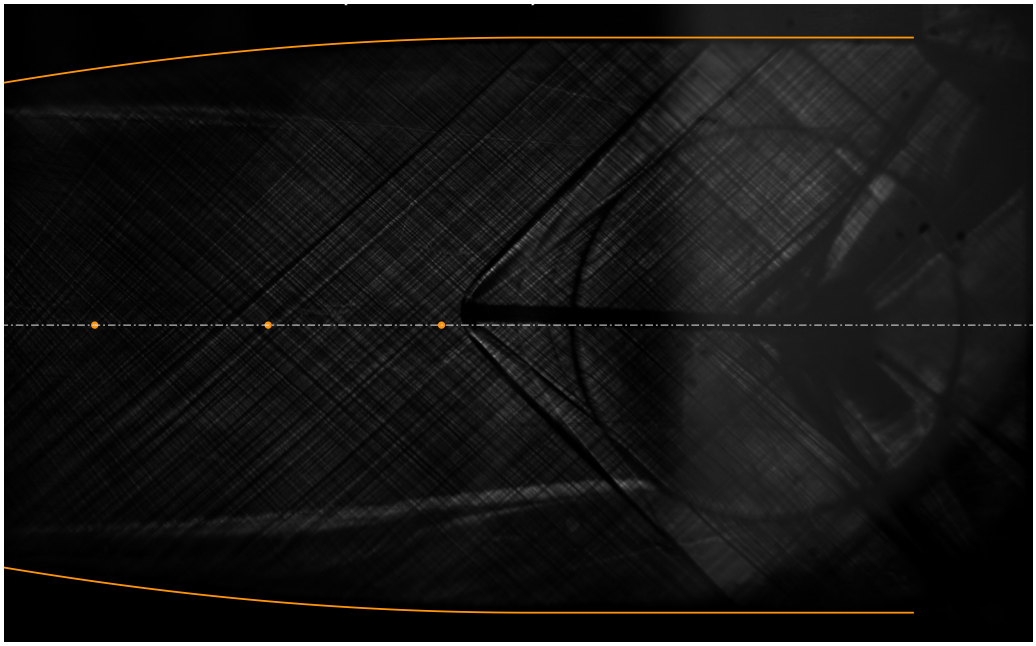

Figure 8.6. Schlieren image at $t = 10$ s, corresponding to $Z_T = 0.70$, during test *182MM*. Nozzle contour, axis and pressure taps are highlighted.

8.3 Experimental Campaign with Siloxane MM

The schlieren image in Figure 8.6 shows that, just like test *$N_2$179* with nitrogen, the wind tunnel operates as intended, with a supersonic flow and a bow shock at the probe tip.

Figure 8.7 reports absolute pressures during test *182MM*. Pressures $P_{t,line}$ and $P_{t,ref}$ are always within error bars of one another throughout the test after line flushing has ended, indicating no issues on the upstream total pressure line to the differential transducer. The line flushing time and pressure were much more appropriate for MM testing with respect to nitrogen and allowed to have the latter two pressures in perfect equilibrium exactly at the time instant at which the pressure peak was reached.

Pressure P_a is larger with respect to P_b and P_{fs}, consistently with taps position along the nozzle. The free-stream pressure P_{fs} is lower than pressure P_b at the preceding tap at the beginning of the test and becomes slightly larger after $t =\sim 25$ s. This was observed in all repeated tests with MM and is attributed to the off-design operation of the present geometry which causes a re-compression. With respect to nitrogen tests, the non-ideal dependence of the flow field on total conditions also plays a role, as it leads to the inversion occurring between P_b and P_{fs} as conditions become more ideal during the test.

1D calculation were performed to provide a theoretical comparison to experimental results. $P_{fs} - A^*/A$ is the free-stream pressure calculated by considering a one-dimensional isentropic expansion until the known geometrical area ratio where the corresponding pressure tap is located. Given the non-ideal dependence of A^*/A on total conditions, *1D* isentropic expansions were recalculated at each considered time instant. Due to the involved computational effort, calculations were performed only at selected $t = 10, 15, 20, 25, 30, 35, 40, 45, 50$ s.

Considering that the free-stream tap is located in the turning region where flow should become uniform and expansion at the axis has stopped, 1D calculation should provide a reasonable

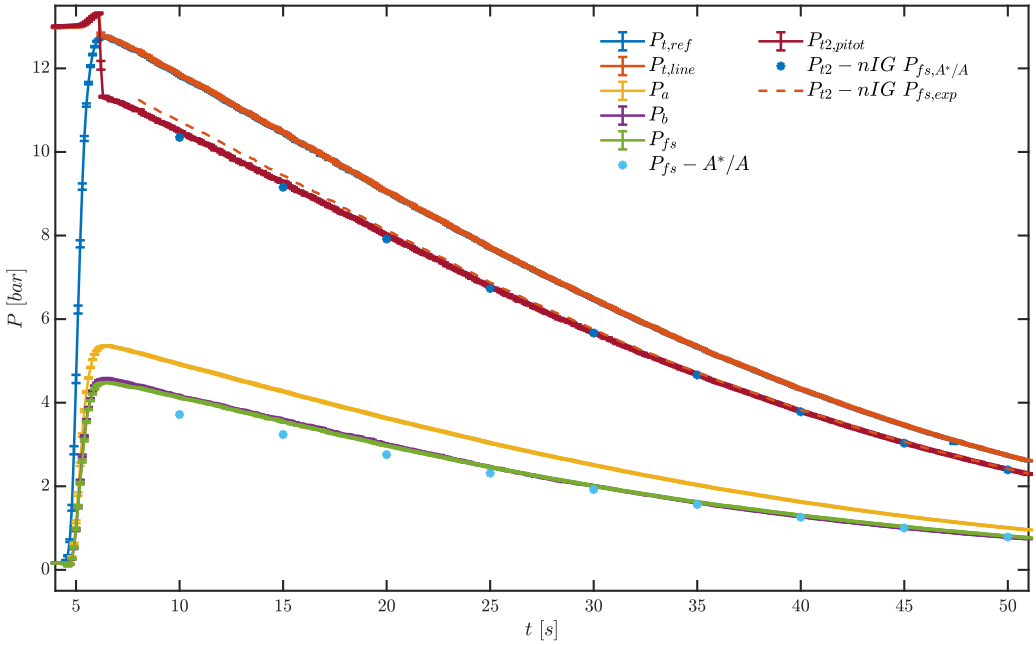

Figure 8.7. Absolute pressures during test *182MM*. Line flushing is present until $t =\sim 6$ s for $P_{t,line}$ and $P_{t2,pitot}$.

pre-shock pressure comparison for experimental results instead of CFD calculation, currently not available on this nozzle. This kind of analysis was not carried out for tests with nitrogen due to the dramatically different molecular complexity with respect to design fluid MDM, which implies a very different expansion evolution in a fixed geometry. As such, conditions at the free-stream tap are not necessarily approaching uniformity, as would instead occur for the design case. The hypothesis of 1D flow might not be accurate, resulting in possibly misleading values. Although siloxane MM is still characterized by a slightly lower molecular complexity than MDM in the same fluid family, the shape of the turning region is not expected to be markedly different with respect to design conditions leading to uniform flow.

A zoom on free-stream pressure can be seen in Figure 8.8a, with the related absolute and percentage differences between measured and calculated values in Figure 8.8b. At $t = 10$ s, calculated P_{fs} is 400 mbar lower than the measured one. The difference decreases to ~ 150 mbar at $t = 25$ s and down to ~ 20 mbar at $t = 50$ s. In percentage terms with reference to the measured quantity, the discrepancy between the two free-stream pressures is $\sim 10\%$ at $t = 10$ s, $\sim 6\%$ at $t = 25$ s and $\sim 3\%$ at $t = 50$ s.

This does not necessarily indicate that measured free-stream pressure is wrong, or that the measurement quality worsens as the flow is less ideal. In fact, in case of non-ideal flows, total conditions have an impact on the *turning* region of the nozzle aswell. Thus, the change in percentage differences during the test might only reflect the fact that flow conditions at the free-stream tap might be more or less uniform and consequently further away from the assumption of 1D flow depending on values of P_T and T_T.

Schlieren images at time instants $t = 10, 20, 40$ s were processed to provide a further comparison for the evaluation of P_{fs} through Mach lines extraction, as illustrated in Figure 8.9. The determined Mach number is plotted against its axial position in Figure 8.9d, together with the values calculated from measured P_{fs} at the taps and from the geometrical area ratio. The three data-sets show a

good qualitative agreement with each other, all capturing the non-ideal effects causing a change in Mach number depending on total conditions. Mach number from schlieren images seems to be overall higher with respect to the one calculated from measured P_{fs} at $x = 111$ mm, with a percentage difference that is anyways never larger than 3.5%. Data from Mach lines is actually closer to the one predicted from the geometrical area ratio, with a percentage difference $\leqslant 1.8\%$. Although percentage differences are fairly limited and error bars are relatively large, results seem to indeed indicate that $P_{fs} - A^*/A$ is a better representation of the actual free-stream pressure rather than the measured P_{fs}.

The measured post-shock total pressure $P_{t2,pitot}$ was compared to quantities $P_{t2} - nIG\ P_{fs,exp}$ and $P_{t2} - nIG\ P_{fs,A^*/A}$ determined from conservation equations coupled with the thermodynamic model implemented in *FluidProp*. The measured free-stream pressure P_{fs} and the previously calculated $P_{fs} - A^*/A$ were respectively employed. Since the latter pressure was only determined at specific time instants, then $P_{t2} - nIG\ P_{fs,A^*/A}$ is also only available at those test times. Measured and computed pressures are reported in Figure 8.8c and their absolute and percentage differences in Figure 8.8d.
Consistently with the fact that $P_{fs} - A^*/A$ is lower than the measured free-stream pressure, the predicted post-shock total pressure $P_{t2} - nIG\ P_{fs,A^*/A}$ is also lower with respect to $P_{t2,pitot}$. At $t = 10$ s, the difference with the experimental result is ~ 150 mbar, down to ~ 30 mbar at $t = 25$ s and ~ 15 mbar at $t = 50$ s. The calculated pressure enters within error-bars of $P_{t2,pitot}$ (having width ± 15 mbar) between $t = 25$ s and $t = 30$ s. Although the discrepancy is significant in absolute values, the agreement is actually quite good in percentage terms, with a $\leqslant 1.8\%$ difference with respect to the measured pressure throughout the test.
Calculated $P_{t2} - nIG\ P_{fs,exp}$ is instead always larger than $P_{t2,pitot}$. At $t = 10$ s, the difference with the experimental result is ~ 230 mbar, decreasing to ~ 110 mbar at $t = 25$ s and ~ 20 mbar at $t = 50$ s. The overall agreement with the measured post-shock pressure is thus slightly worse than using $P_{fs} - A^*/A$, but still satisfactory considering that discrepancies are always below $\leqslant 2.5\%$ with respect to the measured post-shock total pressure.

Figure 8.8e shows the total pressure loss across the shock. ΔP_t was directly measured with a differential transducer whilst $\Delta P_t - nIG\ P_{fs,exp}$ and $\Delta P_t - nIG\ P_{fs,A^*/A}$ were calculated consistently with the two methods previously explained. The related absolute and percentage differences are instead found in Figure 8.8f.
As expected given the absolute pressures trends, $\Delta P_t - nIG\ P_{fs,A^*/A}$ is larger than the measured ΔP_t by ~ 115 mbar at $t = 10$ s and ~ 7 mbar at $t = 25$ s. In percentage terms with respect to ΔP_t, this corresponds to a discrepancy of, respectively, $\leqslant 10\%$ and $\leqslant 1\%$. At the end of the test at $t = 50$ s, it is within error bars (± 5 mbar) of the experimental pressure drop. So, except for the initial time instants, the overall agreement in percentage terms is in line or even better than that observed for nitrogen testing.
Considering calculated quantity $\Delta P_t - nIG\ P_{fs,exp}$, it is always lower than the experimental value, with significantly worse discrepancies in line with those evidenced for pre-shock total pressure $P_{t2} - nIG\ P_{fs,exp}$, both in absolute and percentage terms. At $t = 10$ s the difference between the two pressure drops is ~ 250 mbar ($\sim 20\%$), decreasing to ~ 130 mbar ($\sim 15\%$) at $t = 25$ s and to ~ 30 mbar ($\sim 9\%$) at $t = 50$ s.
Consistently with all previous findings, this seems to point towards possible issues with the free-stream pressure measurement.
As already mentioned for nitrogen tests, shock-boundary layer interaction might be a possible root cause of P_{fs} issues, all the more in case of MM where discrepancies between calculated and measured pressure drops are larger than for nitrogen. Given the lower molecular complexity, nitrogen flow expands to a higher free-stream Mach number ($M \sim 1.7$) compared to siloxane MM ($M \sim 1.5$). As a consequence, and as visible if schlieren images of tests with the two fluids are

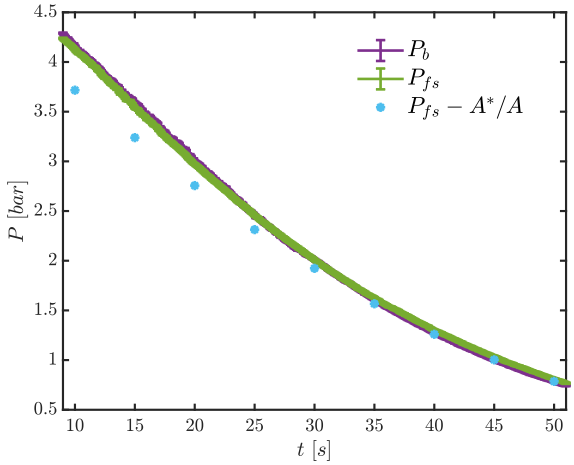

(a) Zoom after $t = 10$ s on free-stream pressure P_{fs}.

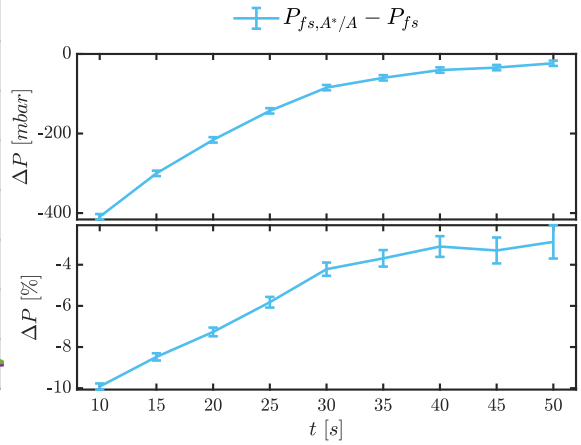

(b) Absolute and percentage differences between P_{fs} from geometric area ratio and the measured one.

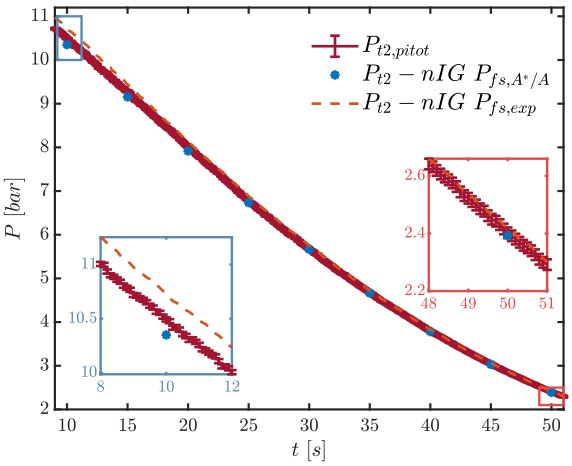

(c) Zoom after $t = 10$ s on post-shock pressure P_{t2}.

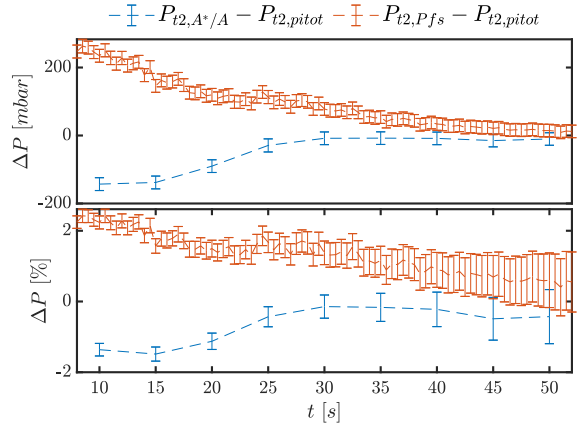

(d) Absolute and percentage differences between measured P_{t2} and those from calculated and measured P_{fs}.

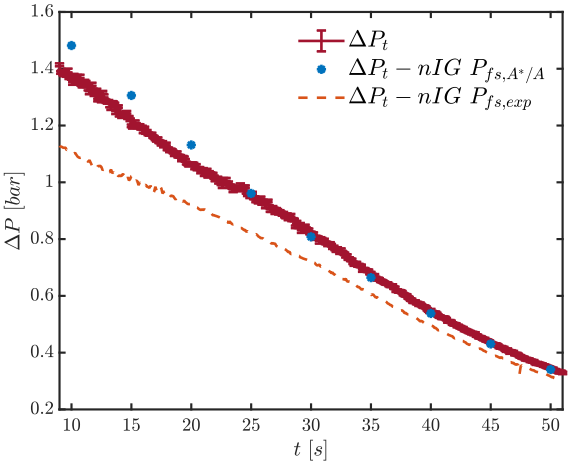

(e) Zoom after $t = 10$ s on total pressure loss ΔP_t.

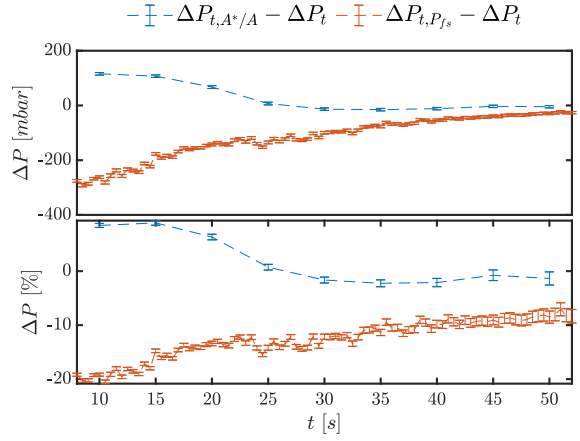

(f) Absolute and percentage differences between measured ΔP_t and those from calculated and measured P_{fs}.

Figure 8.8. Measured and calculated pressures during test *MM182*, with absolute and percentage differences.

superposed, the shock wave angle taken from the nozzle x-axis is larger for MM. This means that the shock wave should impinge on the rear plate closer to the wall tap than in case of nitrogen, resulting in a stronger pressure increase through the subsonic portion of the boundary layer with respect to flow pressure just in front of the probe tip at the center of the channel. CFD simulations will allow to verify this hypothesis. If it were true, then the measured pressure drop better agrees with the one calculated from $P_{fs} - A^*/A$ rather than from the measured free-stream pressure simply because 1D theory using the geometrical area ratio predicts a lower pre-shock pressure which is, incidentally, closer to the mid-channel value at the probe tip than the wall pressure affected by shock-boundary layer interaction.

It must also be pointed out that, as visible in Figure 8.6, the *TotAle* probe is not perfectly well aligned with the free-stream but is at an angle of $\sim 2.5\,^\circ$. This could contribute to differences between measured and calculated total pressure losses. It is advisable that tests with MM be repeated with an improved probe-flow alignment.

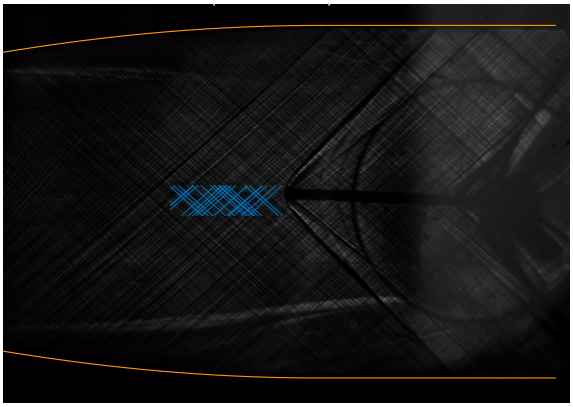

(a) Schlieren image with superposed identified Mach lines for condition $t = 10\ s$.

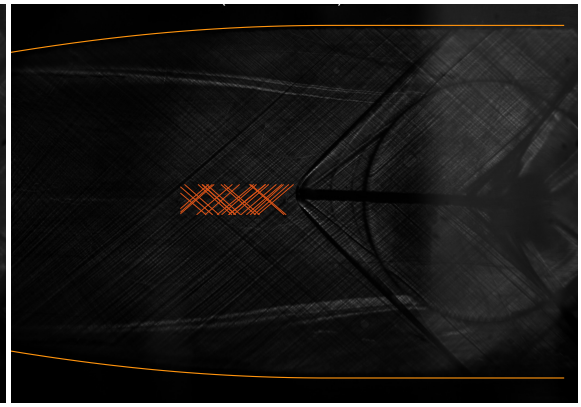

(b) Schlieren image with superposed identified Mach lines for condition $t = 20\ s$.

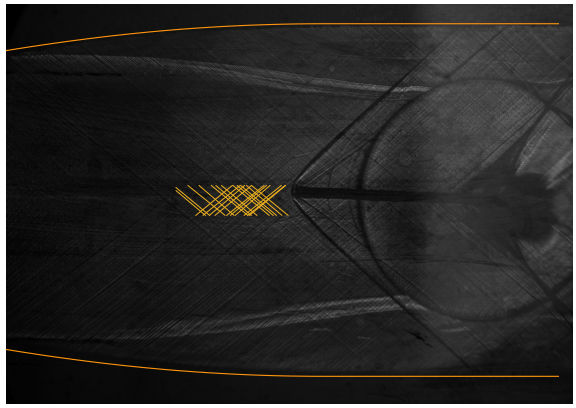

(c) Schlieren image with superposed identified Mach lines for condition $t = 40\ s$.

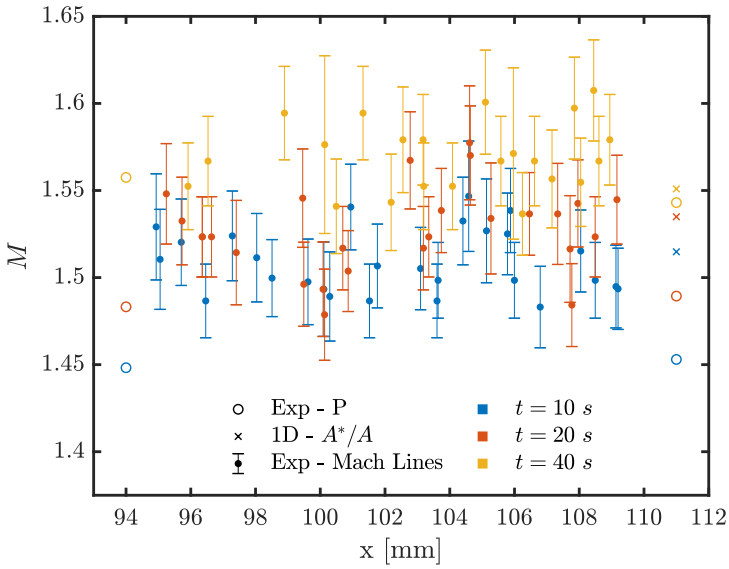

(d) Mach number from pressure measurements, geometrical area ratio and Mach lines. The plot is zoomed between the free-stream tap at $x = 111$ mm and the preceding one.

Figure 8.9. Mach number extraction from schlieren images for conditions at $t = 10, 20, 40\ s$ during test *182MM*.

8.4 Conclusions

The present experimental campaign has proven that the pneumatic measurement system is capable of correctly performing direct total pressure loss measurements across shocks in non-ideal flows of organic vapors with satisfactory agreement with theoretical calculation. However, it is evident that, for siloxane MM, the measured ΔP_t shows an unexpected better agreement with the one calculated from the free-stream pressure deduced from the area ratio and *1D* isentropic theory rather than using the measured P_{fs}. As already previously noted, this calls for further investigation on possible measurement issues at the free-stream pressure tap.
CFD calculation are recommended to better characterize the nozzle behaviour as wind tunnel. The complementary use of numerical simulation proved very important in case of subsonic testing, because it allowed to highlight possible boundary layer effects on the reference static pressure. Analogously, detailed knowledge of the free-stream flow in the nozzle turning region would allow to better assess total pressure loss measurements by the probe.
As further comparison for the direct experimental shock loss measure, CFD calculation on the probe head exploiting its axial symmetry are envisaged, as well as simulations of the nozzle with the inserted probe to explore the extent of shock wave-boundary layer interactions.
Near-future plans also include pressure probes testing at different Mach numbers, with purposely designed nozzles. Their overall size will be smaller with respect to nozzle *nMDMwedge*, which was indeed quite large to avoid blockage effects due to airfoil presence in previous experimental campaigns (Section 3.6). Possible blockage effects linked to pressure probes are instead significantly less problematic due to the much smaller occupied area. Thus, nozzles size for supersonic pressure probes testing can be scaled down to ensure a longer test time and a lower total pressure loss during valves opening transient. This will allow to reach less ideal pre-shock conditions with respect to those explored in this chapter. Moreover, tests with total conditions spanning a large portion of the vapor phase of siloxane MM will be carried out. All of this will enable to perform direct total pressure loss measures across shocks at different levels of non-ideality and assess the impact of total conditions.

CHAPTER 9

CONCLUSIONS AND OUTLOOK

9.1 Conclusions

The research presented in this work investigated several aspects concerning the field of non-ideal compressible fluid dynamics.

A theoretical approach based on 1D isentropic expansions was implemented to investigate the behaviour of several different fluids with varying degree of molecular complexity. Findings indicate that, for complex fluids in moderately high non-ideal conditions ($Z_T \geqslant 0.5$, representative of most engineering processes), expansions are similar if total conditions share the same total compressibility factor because, in these conditions, a similar volumetric behavior also implies a similar caloric one throughout the process.
The above was verified with one of the first ever experimental campaigns concerning supersonic non-ideal flows in a large part of the vapor phase of siloxane MM, from strongly non-ideal conditions at $Z_T = 0.39$ to dilute ones at $Z_T = 0.98$. Pressure measurements and Mach number extraction from schlieren visualizations performed in the *TROVA* not only highlighted the non-ideal dependance of isentropic expansions on total conditions, but most importantly confirmed the suitability of Z_T as a similarity parameter for conditions with $Z_T \geqslant 0.6$.
The focus was then shifted on choked subsonic nozzles at different Mach numbers operating with moderately non-ideal flows. Experimental results in synergy with numerical calculation were used to investigate key flow aspects. Non-ideal effects were verified to be more important where compressibility effects are also more relevant and the impact of boundary layer growth was assessed with the key help of CFD simulations. This multidisciplinary approach proved essential for the appropriate choice of the static pressure against which Pitot tube readings must be compared, allowing a better assessment of the pneumatic system functioning and establishing useful knowledge in view of future pressure probe calibration with non-ideal flows in the *TROVA*.
Building on the knowledge of experimental testing and numerical simulation of elementary nozzle flows in the non-ideal regime, the second part of this work was devoted to the development of experimental techniques for pressure probe testing in such flows.
First of all, several pneumatic lines configurations were assessed to overcome the most challenging experimental aspects, namely the transient nature of blow-down plant operation and vapor condensation in the lines, which was responsible for an undesirable mass sink effect. A pneumatic scheme with nitrogen flushing was thus implemented to allow pressure probes testing in subsonic and supersonic non-ideal flows.
Pitot tubes testing in non-ideal subsonic flows of organic vapors was carried out to complete the pneumatic system commissioning. Extensive experimental campaigns allowed to identify several best practices concerning pressure measures involving pneumatic lines in transient non-ideal flows subject to condensation. Lines length should be kept at the bare minimum, and the 'hidden' volume of any employed transducer must not be forgotten when choosing the most appropriate sensors. Moreover, a dynamic testing procedure on the complete line configuration is essential prior to any experimental campaign involving transient flows to indicate if and how the pneumatic lines should be improved. Also, reference pressures must be carefully chosen according to the flow features characterizing the wind tunnel, such as possible boundary layer effects.
In a different regard, the campaign allowed to experimentally verify that flow non-ideality does not affect the behaviour of a Pitot tube in non-ideal subsonic flows. Although not particularly surprising, its verification is actually important, as it indicates that no specific calibration is required for Pitot tubes in compressible subsonic non-ideal flows. Flow quantities such as local velocity, density and Mach number can be determined from the instrument total and static pressure readings complemented by a total temperature measure and a suitable thermodynamic model through calculation of 1D isentropic expansions. All of this is useful information for Pitot tubes use in relevant industrial applications involving non-ideal flows. Under this aspect, given the good

performance of total compressibility factor as a similarity quantity for complex fluids, isentropic flow tables/relations with the additional Z_T parameter could replace dedicated codes requiring calls to an external thermodynamic library. This would allow a faster and cheaper calculation of flow quantities where the implementation of simple relations with few parameters is useful, such as plant control contexts involving PLC systems with limited computational power.
Subsonic Pitot tube testing was an essential preparatory step, not only for future directional pressure probes calibration, but also for direct measures of total pressure losses across normal shocks in non-ideal flows, such as those performed in the experimental campaign presented in the last chapter of this work. The use of a Pitot tube in supersonic non-ideal flows has proven that the pneumatic measurement system is capable of correctly performing direct total pressure loss measurements with satisfactory agreement with theoretical calculation. Further investigation on possible measurement issues at the free-stream pressure tap is envisaged, including the complementary use of CFD calculation to better characterize the nozzle behaviour as wind tunnel, analogously to the case of choked subsonic nozzles, and to explore the extent of possible shock wave-boundary layer interactions at the back wall. As further comparison for the direct experimental shock loss measure, CFD calculation on the probe head exploiting its axial symmetry are also foreseen in the near-future.
On the experimental side, planned campaigns include pressure probes testing in non-ideal supersonic flows at various Mach numbers and with total conditions spanning a large portion of the vapor phase of siloxane MM. This will enable to perform direct total pressure loss measures across shocks at different levels of non-ideality and assess the impact of total conditions.

The present work represents a contribution to the general and fundamental knowledge of non-ideal compressible fluid dynamics with a holistic approach that includes theoretical computations, numerical calculation and experimental results.
Reliable experimental methodologies were established in the challenging environment of high pressure, high temperature non-ideal compressible flows, from detailed nozzle flow characterization to pressure probes testing in both subsonic and supersonic conditions. The developed methodologies should pave the way for future calibration of directional pressure probes and their use in blade cascade characterization concerning non-ideal flows.
Complementary use of CFD to understand detailed flow features and verify results has proven particularly useful and is suggested as common practice in cases where non-ideality introduces further complications in experimental testing.
Results from this work should allow to provide industry with the tools to perform reliable and inexpensive velocity, mass flow rate and performance measurements in real operating plants where non-ideal flows are involved, such as in the field of organic Rankine cycles.
Finally, the large experimental data-set produced within this research on non-ideal flows includes subsonic and supersonic nozzle expansions and direct measures of normal shock losses. This contributes to filling the current literature gap in available experimental results and provides useful information for numerical tools comparison.

9.2 Outlook

Future developments already planned to be 'locally' carried out at *CREA lab*, such as further supersonic Pitot tubes testing at other Mach numbers and total conditions or detailed CFD calculation on probe tips, have already been provided above. The present section instead suggests a general future direction on the three main research topics covered in this work, namely theoretical calculation, nozzle characterization and pressure probes testing concerning non-ideal flows.

If a polytropic ideal gas is considered, total pressure losses across normal shocks only depend on the free-stream Mach number. In case of non-ideal flow behaviour, total conditions instead also play a role. It would be interesting and practically useful to investigate whether the total compressibility factor is a good similarity parameter in case of shock losses as well, analogously to what was found for 1D isentropic expansions. To this end, a calculation framework similar to that employed in Section 2 could be implemented. Shock losses could be calculated for flows with same Mach number and different total conditions but same total compressibility factor. Given results from isentropic expansions, in case of complex fluids this should lead to flows having close pre-shock values of compressibility factor and fundamental derivative of gasdynamics, unless very strong non-ideality levels are considered. Thus, the similar caloric and volumetric pre-shock behavior is expected to result in similar shock losses, but this is to be rigorously verified through calculation. This analysis could be taken even further by considering oblique shocks and how their polars depend on the total compressibility factor.
Furthermore, calculations using the simple yet qualitatively accurate *van der Waals* model should be carried out to better highlight the role of molecular complexity in flow similarity (for both isentropic flows and shock losses) and possibly lead to a molecular interpretation of any similarity pattern.
The present work has allowed to verify the good performance of the total compressibility factor as a similarity parameter for isentropic expansions in moderately non-ideal conditions. This is precious information, because it allows to drastically reduce the number of non-ideal flows required for subsonic pressure probes calibration. Not all possible probe operating conditions would have to be experimentally reproduced, but only selected ones sharing the same total compressibility factor as real conditions are required, entailing very significant time and costs savings.
If future results, both theoretical (from the previously suggested 1D framework) and experimental (from near-future extended supersonic Pitot tube campaigns in the *TROVA*), were to indeed verify that total compressibility factor is a suitable similarity parameter for shock losses in non-ideal flows aswell, this would directly lead to a significantly reduced experimental effort for probes in supersonic conditions too.
Considering that calibration of directional pressure probes requires tests repetition at different incidence angles, all of this would be particularly impactful.

A consistent part of this work was devoted to the detailed characterization of subsonic and supersonic non-ideal nozzle flows. This was essential preparation in view of pressure probes and also allowed to provide literature with experimental data characterizing fundamental *NICFD* flows. Active nozzle-fitted facilities are now starting to be able to perform such measures routinely, thus nozzles are increasingly employed as wind tunnels for testing of other aspects (e.g. probes, aerodynamic profiles (Zocca et al., 2019), turbulence and thermodynamic models calibration (Gori et al., 2019a, 2020)) and are no longer a novel research contribution per se.
However, one last aspect of non-ideal nozzle flows of pure fluids that has not been experimentally reproduced yet is the non-monotonic Mach number trend along isentropic expansions. This is due to the fact that conditions leading to such a behaviour are extremely non-ideal, with very

high pressures and temperatures, with the latter possibly dangerously close or beyond the thermal stability limit of considered fluids.
In fact, a nozzle yielding a non-monotonic Mach number trend was designed for testing in the *TROVA* in the frame of a past MSc. thesis (Bottin, 2017). Chosen design conditions were $P_T = 31\,\text{bar}$ and $T_T = 266\,°\text{C}$ ($Z_T = 0.28$) for siloxane MM, and considered off-design ones were $P_T = 40\,\text{bar}$ and $T_T = 270\,°\text{C}$. Authors in Romei et al. (2020b,a) numerically investigating the impact of strongly non-ideal features on supersonic ORC turbine cascade flows of siloxane MM, considered non-monotonic Mach number trends of expansions with similar nominal total conditions of $P_T = 40\,\text{bar}$ and $T_T = 270 - 272.5\,°\text{C}$. Whilst this is at a relatively safe distance from the temperature of about $T = 310\,°\text{C}$, the limit suggested by Gallarini (2020) at which the fluid undergoes a still acceptable decomposition, reproducing this flow in the *TROVA*, and possibly in other plants aswell, is not trivial at all. Such high pressure levels might be too demanding for the mechanical resistance of certain plant components. Moreover, the desired isentropic expansion develops extremely close to the saturation curve ($< 5\,°\text{C}$ of superheating), especially at the nozzle location where the non-monotonic Mach number trend should occur. This requires an extremely precise total conditions regulation in order to avoid condensation in the nozzle, something which is not quite easily guaranteed in the *TROVA*. Hopefully, the experience acquired in the past years might allow to reproduce in the future such experimental conditions in the latter facility and in other active wind tunnels for non-ideal flows.

The main future developments concerning experimental campaigns with non-ideal flows will certainly involve pressure probes. Although in a relatively limited number, dedicated research wind tunnels across the world are finally becoming mature enough to move beyond nozzle characterization and towards pressure probes testing. Other than the work on the *TROVA* reported here, two other facilities to date have performed probes testing in non-ideal flows to the author's knowledge. As previously mentioned, a wedge probe was employed in cascade testing of non-ideal flows at Whittle Laboratories of Cambridge University (Baumgärtner et al., 2020). Preliminary results on the *CLOWT* plant at Muenster University on a rotatable cylinder Pitot probe in high subsonic flows with fluid Novec^{TM} 649 were also very recently presented (Reinker et al., 2020).
However, campaigns in both facilities were carried out at relatively ideal conditions ($Z_T \simeq 0.88$) and thus actually evaluated effects linked to molecular complexity rather than to flow non-ideality. Nevertheless, established procedures for probes calibration are not in place yet, and the present work has hopefully contributed to the foundations of systematic pressure probes testing in subsonic and supersonic non-ideal flows and their future use in research (e.g. ORC turbine cascade testing) and industrial contexts (e.g. ORC plant performance) where these occur.
A lot of key aspects of technical solutions enabling this on the *TROVA* have been widely discussed in this work already. However, some research ideas, general takeaways and best practices concerning the future development of the topic are addressed below.

Pressure probes testing is a combination of wind tunnel and probe behaviours. As widely experienced here, detailed knowledge of both the nozzle flow field and probe characteristics is important to achieve accurate results. As an example, reliable subsonic Pitot tube testing was achieved thanks to the preliminary characterization (both experimental and numerical) of the employed subsonic nozzles with no probe insertion. Considering supersonic conditions instead, experiment verification with numerical tools yielding detailed knowledge of the nozzle behaviour is unfortunately not available yet. Useful information on the shape of the turning region at different operating conditions is currently missing, as well as indications on the extent of possible shock wave-boundary layer interactions at the rear plate. As a consequence, the uncertainty in free-stream total pressure highlighted in Section 8 complicates measured shock loss comparison with theoretical calculation.
On the same note, preliminary probe testing in steady test rigs involving a simpler setup with

air (or any other incondensable having an ideal gas behaviour), should be carried out if possible. It is important to establish a reference probe behavior (especially in case of directional ones) in conditions where complications typical of non-ideal flows experimenting, such as high flow temperature and pressure, transient nature of the plant, line condensation or flow dependance on stagnation conditions, do not play a role. This helps to then accurately evaluate results in non-ideal setups and to understand the cause of possible unexpected experimental data.
For this reason, a preliminary campaign was carried out at the *Safety Valves Test Rig* of Politecnico di Milano before *TROVA* testing of Pitot tubes in subsonic conditions. It proved very useful because it allowed to immediately understand that one of the probes had important manufacturing issues and to assess insensitivity to flow angle, compressibility and Reynolds number effects. In fact, this should have also been performed before inserting Pitot tubes in non-ideal supersonic flows in the *TROVA*. Such tests are actually planned in the near future for more detailed comparison and evaluation of *TROVA* results.

A correct nozzle design is also of paramount importance. Concerning pressure probes calibration in non-ideal subsonic conditions, choked converging nozzles with a portion with constant cross section, such as those employed in this work, are the most suitable wind tunnel configuration whenever a fine control on nozzle total or back pressures is not possible. The size of the test section should be as large as possible in order to avoid any effects linked to probe blockage (although this significantly depends on the size and length of the probe stem and head) and to boundary layer effects. The latter were significant in the present work, especially close to sonic conditions, due to the small test section size. If it were possible to go back in time, effort would be devoted to enlarging the height of the constant area section by sacrificing the double concavity design of the first convergent, typically employed in all *TROVA* nozzles to ensure a smooth and gradual acceleration.
In case blow-down wind tunnels are considered, the downside of a larger nozzle is lower test time due to a larger minimum area and faster high pressure vessel discharge. The latter aspect might prove challenging for the pneumatic system response, which should be carefully evaluated with dynamic testing such as carried out in this work.
In supersonic conditions, nozzles should be designed so as to ensure that the free-stream tap is in the turning region and that no excessive re-compression might occur until the probe tip. Any test condition that leads to strong off-design nozzle operation should preferably be avoided due to the associated change in shape of the turning region. In fact, although this was carried out in the present work, operation with different fluids and/or at markedly different total conditions with respect to nozzle design ones is not recommended if the aim is to perform an accurate shock loss measure or to calibrate a probe in supersonic non-ideal conditions. If nozzle off-design operation were to occur, detailed knowledge on the turning region shape should be gathered through numerical tools, as previously suggested.
The importance of the turning region sparks interesting research ideas. It is perhaps evident that a nozzle geometry yielding such part of the flow field that is as invariant as possible with respect to non-ideal flow conditions (subject to experimental uncertainty) would prove very useful. To this end, a nozzle design framework could be developed involving uncertainty quantification and shape optimization methodologies coupled with CFD or *method of characteristics* calculations, analogously to increasingly common turbomachinery blades optimal design procedures. This would allow to at least mitigate the difficulties linked with the free-stream pressure measurement, especially in blow-down facilities where off-design operation is inevitable.

Directional probes calibration requires rotation with respect to flow direction. In case of blown-down facilities, this is of course not feasible during a single test run, which should therefore be repeated at different constant incidences. If steady test conditions are instead possible, rotation

can be performed during a test and might be automated with the use of slides. However, this is technically challenging. The probe tip must ideally be kept at the nozzle axis, especially in cases with reduced test section size, in order to ensure it is facing the isentropic core of the flow. This means that the probe cannot be simply rotated about the stem axis, but that the whole instrument needs to be translated along more than one direction. This would be hard to perform as the test is running without incurring in leakages out of the test section, which would be dangerous considering the high temperature and pressure generally involved in non-ideal flows experimental campaigns. Even if the necessary mechanical system to achieve this were actually designed and produced (e.g. rotating shaft with an eccentric hole for the probe stem), leakage-tight gaskets or o-rings might cause too much friction for the probe to be rotated. Also, as evidenced during preliminary subsonic tests at the *Safety Valves Test Rig*, probe stem bending due to aerodynamic load might make it further impossible to move the probe. This was observed with air at moderate total pressure and Mach number, and testing with dense vapors at strongly non-ideal supersonic conditions is expected to be worse.

Given all of these technical difficulties and considering the number of flows required for a complete testing at several incidence angles, virtual (numerical) calibration can be employed to reduce the experimental burden. Once probe behaviour is evaluated at a number of operating conditions and incidence angles, these experimental results can be used to run a shape-optimization routine with the use of CFD. Parameters defining the probe shape can be modified until a numerical domain yielding the same performance coefficients as the real probe is retrieved. Then, probe behaviour at other incidence or operating conditions (even involving different fluids than those the probe was tested with) can be determined from simulations on such numerical domain.

Virtual calibration of course requires that CFD is able to reproduce experimental results with extremely high fidelity. As perhaps evident after the numerical and experimental results presented here, this is not yet the case for non-ideal flows, even with relatively simple geometries such as nozzles. Thus, substantial work towards increasing agreement between experiment and numerics is needed before a virtual calibration procedure can be successfully put in place. This might involve numerous activities, from the improvement of thermodynamic models accuracy to the investigation of turbulent structures in non-ideal flows or the fine-tuning of turbulence model parameters for the specific non-ideal operating conditions.

Moreover, the numerical calibration procedure should also account for uncertainties associated with experimental data and should thus involve the use of uncertainty quantification methodologies, overall offering a challenging but possibly prolific research path.

Il vero non è una realtà che si presta ad essere scoperta né possiamo sapere a priori quali osservazioni sono rilevanti e quali non lo sono; ogni scoperta, ogni approfondimento della comprensione comincia come una predizione di quello che può essere. Questa immagine predittiva di un'ipotesi sorge come ogni atto creativo della mente; è un lavoro mentale, un'ispirazione dall'interno e non è la conseguenza di una ricerca programmata.

– Rita Levi-Montalcini, *Elogio dell'Imperfezione*

APPENDIX A

Thermodynamic Modeling

Within the frame of *NICFD*, appropriate thermodynamic modeling is clearly important to allow an accurate description of a fluid behaviour. A brief recall of the thermodynamic models relevant to the present work are reported below.

The *state principle* states the existance of a *fundamental relation* for a simple system in a stable equilibrium state relating all of its thermodynamic properties and thus providing a complete description of its behaviour (Gyftopoulos and Beretta, 1991). The *fundamental relation* can be expressed in the *energy form* as follows:

$$E = E(S, V, \mathbf{n}) \tag{A.1}$$

where E is the energy, expressed as a function of the independent variables S, V and $\mathbf{n}$. In case of simple systems, this is the internal energy. S is the entropy, V is the volume and $\mathbf{n}$ is the vector of the amount of constituents. This relation holds for all thermodynamic systems at stable equilibrium state and represents a hyper-surface in the space of thermodynamic variables. Once the function E is known for a system, all of its thermodynamic properties at a stable equilibrium state $(S, V, \mathbf{n})$ can be calculated by taking derivatives.
$E = E(S, V, \mathbf{n})$ is a convex function with respect to S and is strictly monotone with respect to it, except at the point of minimum energy where $\partial E / \partial S = 0$ by the III principle of thermodynamics. This function can therefore be inverted to give a *fundamental relation* in the *entropy form*:

$$S = S(E, V, \mathbf{n}) \tag{A.2}$$

which is a concave function with respect to E and contains the same information as the *energy form*.
Equivalent formulations of the *fundamental relation* can be obtained by defining other characteristic quantities via the Legendre transform. The most notable forms are the *Enthalpy form H*, the *Helmoltz free energy form A* and the *Gibbs free energy form G* (Gyftopoulos and Beretta, 1991).
For single-constituent simple systems, the above relations can also be expressed in the specific form:

$$e = e(s, v) \qquad s = s(e, v) \tag{A.3}$$

where e is the specific internal energy per unit mass, s is the specific entropy per unit mass and v is the specific volume per unit mass. A thermodynamic model is provided if a functional form of the *fundamental relation*, in any of its possible forms, is assigned.
Since all thermodynamic properties can be calculated from the *fundamental relation* through derivatives, an equivalent way of providing a thermodynamic model is to assign relations for said derivatives, the so-called *equations of state*. In case of a single constituent, *equations of state* from

the *energy form* are:

$$\left(\frac{\partial e(s,v)}{\partial s}\right)_v = T(s,v) \qquad \left(\frac{\partial e(s,v)}{\partial v}\right)_s = -P(s,v). \tag{A.4}$$

If the fundamental relation is expressed in the Helmoltz free energy form $\alpha = \alpha(T,v)$ and the Euler relation for a pure substance ($e = Ts - Pv + \mu$) is applied, the following equations of state are derived:

$$P = P(T,v) \qquad e = e(T,v) \tag{A.5}$$

where T and v are the independent variables. This formulation is very commonly employed in the description of the thermodynamic behaviour of fluids. $P = P(T,v)$ is referred to as *Thermal Equation of State* and $e = e(T,v)$ as *Caloric Equation of State* (Emanuel, 1987).

A.1 Ideal Gas Model

The ideal gas model is the simplest thermodynamic description of a fluid. It is sufficiently accurate at pressures and temperatures away from the critical point and the saturation curve but fails in describing the behaviour in the dense gas region. The model assumes that the gas is made of identical point particles interacting with each other only through elastic collisions and are not subject to forces of mutual attraction or repulsion. As a consequence, internal energy and specific heats only depend on temperature. The thermal and caloric equations of state are:

$$\begin{aligned} P(T,v) &= \frac{RT}{v} \\ e(T,v) &= e(T) = e_{ref} + \int_{T_{ref}}^{T} c_v(\tau)\, d\tau \end{aligned} \tag{A.6}$$

where *ref* indicates an arbitrary reference state, $c_v = \left(\frac{\partial e}{\partial T}\right)_v$ is the specific heat at constant volume and R is the specific gas constant calculated as $R = \mathcal{R}/M_m$, with $\mathcal{R} = 8.314\,\mathrm{kJ/(kmolK)}$ as the universal gas constant. If a constant specific heat is also assumed, the internal energy is linearly dependant on temperature and the model is called *Polytropic Ideal Gas* model (*PIG*).

A.2 van der Waals Model

The *van der Waals* model (van der Waals, nted) is the most simple model accounting for intermolecular forces and for the finite dimension of molecules: both of these aspects are fundamental when complex and heavy molecules, such as organic fluids, need to be modeled, because they have a strong impact on volumetric and caloric behaviours. It allows to model both the liquid and vapor phases, and it has a strong physical basis. Although it is not always quantitatively accurate, it is important for the physical explanation of non-ideal effects in single phase regions. The model is not valid in the two-phase region, where it predicts metastable states or does not satisfy thermodynamic stability.
The equations of state are:

$$\begin{aligned} P(T,v) &= \frac{RT}{v-b} - \frac{a}{v^2} \\ e(T,v) &= e_{ref} + \int_{T_{ref}}^{T} c_v(\tau)\, d\tau - \frac{a}{v} \end{aligned} \tag{A.7}$$

where a accounts for the long range attractive intermolecular forces. This term is always positive, meaning that the contribution of these forces reduces the pressure at given temperature and specific volume with respect to the ideal gas model. b instead accounts for the short range repulsive intermolecular forces, so for the *covolume effect* due to the finite volume of molecules. This term is positive too, and therefore leads to an increase in pressure at given temperature and specific volume compared to the ideal gas model. Both parameters are substance-specific and depend on critical temperature and pressure, and can be determined by imposing stability conditions at the critical point $\left(\frac{\partial P}{\partial v}\right)_T = 0$ and $\left(\frac{\partial^2 P}{\partial v^2}\right)_T = 0$ (Colonna and Guardone, 2006):

$$a = \frac{27}{64}\frac{(RT_c)^2}{P_c} \qquad b = \frac{1}{8}\frac{RT_c}{P_c} \tag{A.8}$$

It is common to assume constant specific heat, so that the polytropic van der Waals equations of state in its reduced form conveniently depends on the dimensionless isochoric specific heat c_v/R:

$$\begin{aligned} P(T_r, v_r) &= \frac{8}{3}\frac{T_r}{v_r - 1} - \frac{3}{v_r^2} \\ e(T_r, v_r) &= \frac{8}{3}\frac{c_v}{R}T_r - \frac{3}{v_r} \end{aligned} \tag{A.9}$$

where $P_r = P/P_c$, $v_r = v/v_c$, $T_r = T/T_c$ and $e_r = e/(P_c v_c)$, with P_c, T_c and v_c representing the critical pressure, temperature and volume respectively.

A.3 improved Peng-Robinson-Stryjek-Vera model (iPRSV)

The *iPRSV* model (van der Stelt et al., 2012) is an improved version of the *Peng-Robinson* model with *Stryjek-Vera* modifications, building upon the van der Waals model and allowing improved quantitative predictions of thermodynamic properties. The thermal equation of state has the following cubic form:

$$P(T, v) = \frac{RT}{v - b} - \frac{a}{v^2 + 2vb - b^2} \tag{A.10}$$

where parameters a and b depend on the gas constant, critical temperature, critical pressure, reduced temperature and acentric factor, with many substance-specific parameters obtained from experimental data regression. For the calculation of caloric properties, the ideal gas contribution to specific heat at constant volume is modeled as a polynomial function of temperature, with substance-dependent coefficients. Full details are found in (van der Stelt et al., 2012).

A.4 Span-Wagner Model

(Span and Wagner, 2003a,b) proposed a state-of-the-art multiparameter model for non-polar and weakly polar fluids that is able to provide accurate thermodynamic properties even close to the critical point. Differently to the previous thermodynamic models where equations of state were provided, a functional form is here provided for the fundamental relation in terms of the reduced Helmoltz free energy $\alpha_r(\tau, \delta) = \alpha/RT$ as a function of the inverse reduced temperature $\tau = T_c/T$ and reduced density $\delta = \rho/\rho_c$, where ρ is density and ρ_c is the critical density. The functional form for α_r is divided into an ideal gas contribution α_r^{id} and a residual part α_r^{nid} accounting for the effect of intermolecular forces:

$$\alpha_r(\tau, \delta) = \alpha_r^{id}(\tau, \delta) + \alpha_r^{nid}(\tau, \delta) \tag{A.11}$$

The ideal gas Helmoltz free energy is calculated as:

$$\alpha_r^{id} = \alpha_{r_0} + \int_{T_0}^{T} \left(c_{p,id}^0 - R \right) d\mathcal{T} - T \int_{T_0}^{T} \frac{c_{p,id}^0 - R}{T} d\mathcal{T} + RT \ln \left(\frac{\rho}{\rho_0} \right) \tag{A.12}$$

where the subscript 0 denotes a reference state and the isobaric specific heat in the ideal gas limit at said reference state $c_{p,id}^0$ is calculated analogously to the *iPRSV* model. The residual contribution to α_r is calculated as:

$$\begin{aligned} \alpha_r^{nid}(\tau,\delta) = \quad & n_1\delta\tau^{0.25} + n_2\delta\tau^{1.125} + n_3\delta\tau^{1.5} \\ & + n_4\delta^2\tau^{1.375} + n_5\delta^3\tau^{0.25} + n_6\delta^7\tau^{0.875} \\ & + n_7\delta^2\tau^{0.625}\mathrm{e}^{-\delta} + n_8\delta^5\tau^{1.75}\mathrm{e}^{-\delta} + n_9\delta\tau^{3.625}\mathrm{e}^{-\delta^2} \\ & + n_{10}\delta^4\tau^{3.625}\mathrm{e}^{-\delta^2} + n_{11}\delta^3\tau^{14.5}\mathrm{e}^{-\delta^3} + n_{12}\delta^4\tau^{12.0}\mathrm{e}^{-\delta^3} \end{aligned} \tag{A.13}$$

where n_i, $i = 1, \ldots, 12$ are substance-specific parameters resulting from experimental data fitting or extrapolation.
The most extensively considered fluids in the present work are siloxanes MM and MDM. The values for their n_i parameters were first reported in (Colonna et al., 2006, 2008) and were more recently improved by (Thol et al., 2016, 2017).

The *RefProp* (Lemmon et al., 2018) thermodynamic library implements the Span-Wagner model with the most up-to-date fluid parameters for siloxane MM and MDM and for a very large number of other substances of practical interest. Throughout the present work except for computational fluid dynamics simulations (*CFD*), thermodynamic properties are always calculated using the Span-Wagner model through the *RefProp* library, which is embedded in calculation with the use of the *FluidProp* interface (Colonna et al., 2004). The *iPRSV* model was instead employed for CFD calculation with the *SU2* suite because it is directly embedded in the code, considerably speeding simulations up with respect to external calls to the *RefProp* library.

REFERENCES

Antonini, C., G. Persico, and A. L. Rowe
2008. Prediction of the dynamic response of complex transmission line systems for unsteady pressure measurements. *Measurement Science and Technology*, 19(12):125401.

Arts, T., H. Boerrigter, M. Carbonaro, J. M. Charbonnier, G. Degrez, D. Olivari, M. L. Riethmuller, and R. Braembussche
2001. Measurement techniques in fluid dynamics. An introduction, von Karman institute for fluid dynamics. *Rhode-Saint-Genese*, Pp. 43–274.

Baumgärtner, D., J. J. Otter, and A. P. Wheeler
2019. The effect of isentropic exponent on supersonic turbine wakes. *Proceedings of NICFD 2020*, 2C-2019(Figure 2):1–6.

Baumgärtner, D., J. J. Otter, and A. P. S. Wheeler
2020. The Effect of Isentropic Exponent on Transonic Turbine Performance. *Journal of Turbomachinery*, 142(8):1–10.

Bottin, M. P. d. M.
2017. Non-ideal nozzle design and simulation for an organic vapour wind tunnel. *MSc. thesis*.

Brown, G.
2001. Henry darcy and the pitot tube. Pp. 360–366.

Cammi, G.
2019. *Measurement Techniques for Non-Ideal Compressible Fluid Flows: Applications to Organic Fluids*. Ph.d. thesis, Politecnico di Milano.

Cammi, G., C. Conti, A. Spinelli, and A. Guardone
2020. Experimental characterization of nozzle flow expansions of siloxane mm for orc turbines applications. *Energy*.

Cammi, G., C. C. Conti, A. Spinelii, F. Cozzi, and A. Guardone
2019. Experimental Characterization of Nozzle Flow Expansions of Siloxane MM for ORC Turbines Applications. *Proceedings of the 5th International Seminar on ORC Power Systems, 2019*, (2008):1–11.

Cammi, G., A. Spinelli, F. Cozzi, and A. Guardone
2021. Automatic detection of oblique shocks and simple waves in schlieren images of two-dimensional supersonic steady flows. *Measurement: Journal of the International Measurement Confederation*, 168:108260.

Colonna, P., E. Casati, C. Trapp, T. Mathijssen, J. Larjola, T. Turunen-Saaresti, and A. Uusitalo
2015. Organic Rankine Cycle Power Systems: From the Concept to Current Technology, Applications, and an Outlook to the Future. *Journal of Engineering for Gas Turbines and Power*, 137(10):1–19.

Colonna, P. and A. Guardone
2006. Molecular interpretation of nonclassical gas dynamics of dense vapors under the van der Waals model. *Physics of Fluids*, 18(5):1–14.

Colonna, P., N. R. Nannan, and A. Guardone
2008. Multiparameter equations of state for siloxanes: [(CH3)3-Si-O1/2]2-[O-Si-(CH3)2]i=1,...,3, and [O-Si-(CH3)2]6. *Fluid Phase Equilibria*, 263(2):115–130.

Colonna, P., N. R. Nannan, A. Guardone, and E. W. Lemmon
2006. Multiparameter equations of state for selected siloxanes. *Fluid Phase Equilibria*, 244(2):193–211.

Colonna, P., T. P. van der Stelt, and A. Guardone
2004. FluidProp: a program for the estimation of thermo physical properties of fluids.

Conti, C. C., A. Spinelli, G. Cammi, M. Zocca, F. Cozzi, and A. Guardone
2017. Schlieren Visualizations of Non-Ideal Compressible Fluid Flows. *13th International Conference on Heat Transfer, Fluid Mechanics and Thermodynamics (HEFAT 2017)*, (April):1–6.

Doeblin, E. O.
1990. *Measurement Systems - Application and Design*, 4th edition. McGraw-Hill.

Emanuel, G.
1987. *Advanced classical thermodynamics*. New York, NY: AIAA Education Series.

Gallarini, S.
2020. *High Temperature Non-ideal Compressible Flows of Siloxane Vapors*. Ph.d. thesis, Politecnico di Milano.

Gori, G., G. Iaccarino, and P. M. Congedo
2019a. Structural Uncertainty Estimation of Turbulence Models in Oganic Rankine Cycle Applications. In *Proceedings of the 5th International Seminar on ORC Power Systems, 2019*.

Gori, G., M. Zocca, G. Cammi, and A. Spinelli
2019b. Accuracy assessment of the Non-Ideal Computational Fluid Dynamics model for siloxane MDM from the open-source SU2 suite. *European Journal of Mechanics - B/Fluids*, (September).

Gori, G., M. Zocca, A. Guardone, O. P. Le Maître, and P. M. Congedo
2020. Bayesian inference of thermodynamic models from vapor flow experiments. *Computers and Fluids*, 205(May).

Guardone, A., A. Spinelli, and V. Dossena
2013. Influence of Molecular Complexity on Nozzle Design for an Organic Vapor Wind Tunnel. *Journal of Engineering for Gas Turbines and Power*, 135.

Gyftopoulos, E. P. and G. P. Beretta
1991. *Thermodynamics: Foundations and Applications*. New York: MacMillan Publishing Company.

Harinck, J., A. Guardone, and P. Colonna
2009. The influence of molecular complexity on expanding flows of ideal and dense gases. *Physics of Fluids*, 21(8).

Head, A., C. De Servi, E. Casati, M. Pini, and P. Colonna
2016. Preliminary design of the orchid: A facility for studying non-ideal compressible fluid dynamics and testing orc expanders. In *Proceedings of the ASME Turbo Expo*, volume 3.

Helfgen, B., M. Türk, and K. Schaber
2003. Hydrodynamic and aerosol modelling of the rapid expansion of supercritical solutions (RESS-process). *J. Supercrit Fluids*, 26(3):225–242.

Keulen, L., S. Gallarini, C. Landolina, A. Spinelli, P. Iora, C. Invernizzi, L. Lietti, and A. Guardone
2018. Thermal stability of hexamethyldisiloxane and octamethyltrisiloxane. *Energy*, 165.

Lemmon, E. W., I. Bell, M. L. Huber, and M. O. McLinden
2018. NIST Standard Reference Database 23: Reference Fluid Thermodynamic and Transport Properties-REFPROP, Version 10.0, National Institute of Standards and Technology.

Macchi, E. and M. Astolfi
2016. *Organic Rankine Cycle (ORC) Power Systems: Technologies and Applications*. Woodhead Publishing.

Merzkirch, W.
1987. *Flow Visualization*. Academic Press.

Reinker, F., E. Y. Kenig, M. Passmann, and S. Aus Der Wiesche
2017. Closed Loop Organic Wind Tunnel (CLOWT): Design, Components and Control System. *Energy Procedia*, 129:200–207.

Reinker, F., R. Wagner, M. Passmann, L. Hake, and S. Aus Der Wiesche
2020. Performance of a rotatable cylinder pitot probe in high subsonic non-ideal gas flows. In *Proceedings of NICFD 2020*.

Robertson, M., P. Newton, T. Chen, A. Costall, and R. Martinez-Botas
2020. Experimental and numerical study of supersonic non-ideal flows for organic rankine cycle applications. *Journal of Engineering for Gas Turbines and Power*, 142(8):1–10.

Romei, A., D. Vimercati, A. Guardone, and G. Persico
2020a. Amplification of operational uncertainty induced by nonideal flows in supersonic turbine cascades. *Journal of Engineering for Gas Turbines and Power*, 142(8).

Romei, A., D. Vimercati, G. Persico, and A. Guardone
2020b. Non-ideal compressible flows in supersonic turbine cascades. *Journal of Fluid Mechanics*, 882:A121–A1226.

Sauer, R.
1947. General characteristics of the flow through nozzles at near critical speeds. TM 1147, NACA.

Settles, G. S.
2001. *Schlieren and Shadowgraph techniques. Visualizing Phenomena in Transparent Media*. Springer.

Shawney, G.
2013. *Fundamentals of Fluid Mechanics*, 2nd edition. IK International Publishing House.

Span, R. and W. Wagner
2003a. Equations of state for technical applications. I. Simultaneously optimized functional forms for nonpolar and polar fluids. *Int. J. Thermophys.*, 24(1):1–39.

Span, R. and W. Wagner
2003b. Equations of state for technical applications. II. Results for nonpolar fluids. *Int. J. Thermophys.*, 24(1):41–109.

Spinelli, A., G. Cammi, C. C. Conti, S. Gallarini, M. Zocca, F. Cozzi, P. Gaetani, V. Dossena, and A. Guardone
2019. Experimental observation and thermodynamic modeling of non-ideal expanding flows of siloxane MDM vapor for ORC applications. *Energy*, 168:285–294.

Spinelli, A., M. Pini, V. Dossena, P. Gaetani, and F. Casella
2013. Design, simulation, and construction of a test rig for organic vapors. *Journal of Engineering for Gas Turbines and Power*, 135(4):1–10.

Standard, B.
2008. BS ISO 3966:2008 - Measurement of fluid flow in closed conduits: Velocity area method using Pitot static tubes. Technical report, British Standard.

Thol, M., F. H. Dubberke, E. Baumhögger, J. Vrabec, and R. Span
2017. Speed of sound measurements and fundamental equations of state for octamethyltrisiloxane and decamethyltetrasiloxane. *Journal of Chemical & Engineering Data*, 62(9):2633–2648.

Thol, M., F. H. Dubberke, G. Rutkai, T. Windmann, A. Köster, R. Span, and J. Vrabec
2016. Fundamental equation of state correlation for hexamethyldisiloxane based on experimental and molecular simulation data. *Fluid Phase Equilibria*, 418:133–151.

Thompson, P. A.
1971. A Fundamental Derivative in Gasdynamics. *Physics of Fluids*, 14(9).

Thompson, P. A.
1988. *Compressible Fluid Dynamics*. McGraw-Hill.

Tomasoni, G.
2012-2013. Prove preliminari su un banco prova per fluidi organici. Master's thesis, Politecnico di Milano, Milan, Italy.

Turunen-Saaresti, T., A. Uusitalo, and J. Honkatukia
2017. Design and testing of high temperature micro-ORC test stand using siloxane as working fluid. *Journal of Physics: Conference Series*, 821:012024.

van der Stelt, T. P., N. R. Nannan, and P. Colonna
2012. The iPRSV equation of state. *Fluid Phase Equilibria*, 330:24–35.

van der Waals, J.
1988, Reprinted. *On the continuity of gaseous and liquid states*, volume XIV. North-Holland, Amsterdam.

Vimercati, D., G. Gori, and A. Guardone
2018. Non-ideal oblique shock waves. *Journal of Fluid Mechanics*, 847:266–285.

Zanellato, L., M. Astolfi, A. Serafino, D. Rizzi, and E. Macchi
2017. Field Performance Evaluation of ORC Geothermal Power Plants Using Radial Outflow Turbines. *Energy Procedia*, 129:607–614.

Zocca, M., A. Guardone, G. Cammi, F. Cozzi, and A. Spinelli
2019. Experimental observation of oblique shock waves in steady non - ideal flows. *Experiments in Fluids*, Pp. 1–12.

Zucrow, M. H. and J. D. Hoffman
1977. *Gas dynamics: multidimensional flow*, volume 2. Wiley, John & Son.

LIST OF FIGURES

LIST OF TABLES